Universidade de São Paulo
Faculdade de Filosofia, Ciências e Letras de Ribeirão Preto
Departamento de Química
Programa de Pós-Graduação em Química

“Desenvolvimento de modelos biomiméticos para investigação do papel do estrôncio na mineralização óssea”

“Development of biomimetic models to investigate the role of strontium on bone mineralization”

Camila Bussola Tovani

Tese apresentada à Faculdade de Filosofia, Ciências e Letras de Ribeirão Preto da Universidade de São Paulo, como parte das exigências para a obtenção do título de Doutor em Ciências, Área: **Química**

RIBEIRÃO PRETO -SP

2020

Universidade de São Paulo
Faculdade de Filosofia, Ciências e Letras de Ribeirão Preto
Departamento de Química
Programa de Pós-Graduação em Química

"Desenvolvimento de modelos biomiméticos para investigação do papel do estrôncio na mineralização óssea"

Camila Bussola Tovani

Orientadora: Profª. Drª. Ana Paula Ramos

Tese apresentada à Faculdade de Filosofia, Ciências e Letras de Ribeirão Preto da Universidade de São Paulo, como parte das exigências para a obtenção do título de Doutor em Ciências, Área: **Química**

RIBEIRÃO PRETO - SP

2020

FICHA CATALOGRÁFICA

Tovani, Camila Bussola
Development of bioinspired models to investigate the role of strontium on bone mineralization. Ribeirão Preto, 2020.
169 p.: 74 il. ; 30 cm

Tese de Doutorado, apresentada à Faculdade de Filosofia, Ciências e Letras de Ribeirão Preto/USP – Área de concentração: Química.
Orientadora: Ramos, Ana Paula.

1. Bone. 2. Biomineralization. 3. Apatite. 4. Strontium. 5. Collagen.

"O correr da vida embrulha tudo.
A vida é assim: esquenta e esfria, aperta e daí
afrouxa, sossega e depois desinquieta.
O que ela quer da gente é coragem."

João Guimarães Rosa

À minha irmã Gabriela, minha fonte inesgotável de resiliência e amor.
Aos meus pais Maria Cristina e Readir Almeida, minhas referências de fortaleza, amor,
compreensão e apoio incondicional.

Pois sem vocês nada seria possível!

Agradecimentos

À minha irmã Gabriela Maria, um anjo que Deus me deu a dádiva de amar e conviver. Não importa como, você sempre estará comigo me dando força e inspiração para seguir.

Aos meus pais, Maria Cristina e Readir Almeida, pelo amor, dedicação e apoio incondicional durante toda minha vida, principalmente nos momentos de incerteza. Obrigada por me ensinarem o caminho da honestidade e persistência

Ao meu companheiro Paulo Cesar, pelo suporte, amor e dedicação que fazem minha vida ser mais leve. Obrigada por aceitar todos os desafios ao longo desses anos me fazendo acreditar incansavelmente que dias melhores viriam. Pelas discussões que me inspiram cientifica e pessoalmente. Sinto-me honrada em te ter ao meu lado.

Agradeço à professora Ana Paula Ramos, por toda contribuição científica, dedicação e paciência ao longo desses anos. Pelas inúmeras oportunidades, por me incentivar à independência, pelas palavras nos momentos de incerteza e principalmente por acreditar em mim. Seu apoio e amizade foram fundamentais para que eu chegasse até aqui. Tenho muito respeito e carinho pela história que construímos juntas. Além de química esses anos ao seu lado me fizeram ser uma pessoa melhor. Obrigada por ter possibilitado tantas mudanças e conquistas em minha vida. A você, minha eterna gratidão!

Aos amigos do Laboratório de Físico-Química de Superfícies e Coloides, Guilherme, João Pedro, Lari, Lucas Bahia e Lucas Urbano, Marcos e Tami. E aos que já por ele passaram. Mais do que o espaço de trabalho, pudemos compartilhar nossas vidas ao longo desses anos, criando laços que transpuseram os limites da USP. Obrigada pela parceria e convivência que enchem meu coração de amor e alegria. Agradeço especialmente à Tamires por ter me auxiliado nos experimentos de formação de fosfatos de cálcio e estrôncio em meio confinado.

Marcos, não tenho palavras para agradecê-lo por toda contribuição pessoal e profissional, por me incentivar a buscar minha melhor versão, mais forte, calma e grata. Lucas, obrigada por toda alegria e afeto que traz à minha vida, sempre disposto a ajudar com uma palavra amiga. Roberta, minha companheira não só de USP, mas de vida, grata por poder compartilhar com você, de forma surpreendente, as dores e alegrias desta caminhada. Claudio, obrigada por ter se tornado tão presente e especial. Mel, obrigada por todo carinho e apoio, você é luz em minha vida. Camila Fontes, obrigada pela força, companheirismo e inspiração nessa jornada tão desafiadora. Felipe Thomaz, pela paciência durante os primeiros experimentos no laboratório e pela amizade de longa data. Luiz

Fernando, obrigada pela alegria contagiante. Luiz Andrilli, obrigada por estar sempre disposto a ajudar. Profª. Drª. Juliana Fonseca de Lima, obrigada pelo carinho especial e por todos os conselhos.

Marcos, Claudio e Lucas, obrigada por gentilmente terem me auxiliado na formatação desta tese

Aos meus queridos amigos da Maison du Brésil, Luiz, Graycy, Thaíssa, Vinicius, Marcos, Lívia, Carol, Flávio e Elis. Vocês foram essenciais para que eu pudesse superar todas as adversidades de morar em outro país.

Amigos, agradecer é reconhecer a importância das pessoas em nossa vida, por isso serei eternamente grata a cada um de vocês, que tanto me fizeram crescer ao longo desses anos. Vocês foram o presente mais lindo que a USP me deu.

Aos meus tios Maria Lúcia, Ângela, Pedro, Rosane, Valdir, Sônia, Sandra, Sandro e avós Aparecida, Cássio, Valdin e Maria pelo carinho e incentivo.

À Meire, Paulo e Mariana, por me receberem com tanto carinho na família de vocês da qual tenho muita alegria de fazer parte.

À professora Maria Elizabete Zaniquelli, com quem tive o privilégio de trabalhar durante a iniciação científica. Obrigada pelos ensinamentos, oportunidades, confiança e paciência. Tenho muito orgulho em tê-la como amiga.

À professora Rogéria Rocha Gonçalves, que com suas aulas encantadoras foi minha primeira referência dentro da universidade. Obrigada pelos ensinamentos, carinho e principalmente por me inspirar a aprender cada vez mais.

Ao professor Pietro Ciancaglini pelos ensinamentos, oportunidades e colaboração com os experimentos de cultura de osteoblastos.

À professora Sandra Y. Fukada e à Mariana P. R. Soares pela colaboração com os experimentos de cultura de osteoclastos.

Ao Prof. Dr. Osvaldo Serra pelo uso dos equipamentos.

A todos os professores do DQ pelos ensinamentos.

A todos os funcionários do Departamento de Química, pelo serviço prestado na secretária, à Lâmia e André por toda disposição e auxílio. Aos técnicos Lourivaldo, Rodrigo e Mércia, pela ajuda e colaboração durante esta trajetória

À Fapesp pelas bolsas de estudos concedidas para o desenvolvimento deste trabalho (2014/24249-0 e 2017/24827-2) e à CAPES e ao CNPq pelo suporte financeiro.

Acknowledgments

I will never be able to express all my gratefulness and appreciation to Dr. Nadine Nassif, who I had the honor to have as academic advisor in the Biomineralization team at Sorbonne Université. Thank you for your trust since my first day in the laboratory, always giving me independence and support to go further. Thank you for everything that I have learned from you and all the opportunities, that for sure have changed my life; you gave me much more than I could expect! And the most important, thank you for teaching me search for "crazy things" in life and in science. I promise you: I will never forget about it.

I also would like to thank Dr. Thierry Azaïs for having accepted me in the Biomineralization team, introduced me to the solid-state NMR, and for the fruitful discussions about biomineralization. Dr Marie Alberic, my friend since the first day at LCMCP. Thank you for your kind attention, for all the coffees at Jardin des Plantes or at the kitchen in the lab. Dr Miléna Lama and Elora Bessot for the friendship, patience and help with collagen. For sure I could not face collagen without you girls. Next, I would like to show my gratitude to the other members from LCMCP Mohamed, Isabelle, Patrick and Guillaume that formed me to use the instruments

Dr Alexandre Gloter from LPS Paris Sud, for all the opportunities that you gave me and valuable scientific contribution along this journey.

My dear friends Laurence and Philippe, your friendship was essential during my time in Paris. Thank you for everything! Thanks also to all my friends from "DOMLUX", for your patience to help me with the French language, I really had good moments with all of you.

“And once the storm is over, you won’t remember how you made it through, how you managed to survive. You won’t even be sure, whether the storm is really over. But one thing is certain. When you come out of the storm, you won’t be the same person who walked in. That’s what this storm’s all about.”

Haruki Murakami

TABLE OF CONTENTS

CHAPTER 1

General introduction and motivation

CHAPTER 2

Sr^{2+}-substitution in biomimetic apatite: possible effects on bone mineral

CHAPTER 3

Investigating the stability of Sr^{2+}- rich amorphous calcium phosphate in physiological environment and the role of Sr^{2+} on the early stages of bone formation

CHAPTER 4

Towards new insights about the effect of Sr^{2+} on collagen network in bone tissue

CHAPTER 5

Using confinement to study the crystallization pathway of calcium phosphate in the presence of Sr^{2+}

CHAPTER 6

Sr^{2+}-substituted $CaCO_3$ rod-like particles: structural characterization and in vitro osteogenic activity

CHAPTER 7

Conclusions and perspectives

Appendix

Curriculum Vitæ

LIST OF FIGURES

LIST OF TABLES

LIST OF ABREVIATIONS

ACC	Amorphous calcium carbonate
ACP	Amorphous calcium phosphate
ALP	Alkaline phosphatase
ATR-FTIR	Attenuated total reflection – Fourier Transformed Infrared Spectroscopy
ATP	Adenosine triphosphate
α-MEM	Minimum essential medium
CN	Classical nucleation theory
CP	Cross polarized
CaP	Calcium phosphate
DTG	Derivative thermogravimetry
EDS	Energy dispersive X-ray spectroscopy
EELS	Electron energy loss spectroscopy
FWHM	Full width at the half maximum
HA	Apatite
HRTEM	High resolution transmission electron microscopy
HetCor	Heteronuclear correlation
LW	Line width
LPOM	Light polarized optical microscopy
MAS NMR	Magic angle spinning nuclear magnetic resonance spectroscopy
MTT	(3-(4,5-Dimethylthiazol-2-yl)-2,5-Diphenyltetrazolium Bromide)
NCN	Non-classical nucleation theory
NMR	Nuclear magnetic resonance spectroscopy
PAA	Poly(acrylic acid)
PBS	Phosphate buffer saline
PEG	Poly(ethylene glycol)
PNPP	4-Nitrophenyl phosphate disodium salt hexahydrate
PILP	Polymer-induced liquid-precursor
SAED	Selected area electron diffraction
SBF	Simulated body fluid
SEM	Scanning electron microscopy
STEM	Scanning transmission electron microscopy
ssNMR	Solid-state nuclear magnetic resonance
TEM	Transmission electron microscopy
TGA	Thermogravimetric analysis
XRD	X-ray diffraction

RESUMO

Íons estrôncio (Sr^{2+}) são o componente ativo do fármaco ranelato de estrôncio, uma droga que reduz fraturas vertebrais e não-vertebrais em pacientes com osteoporose. Isso, por sua vez, tem incentivado a incorporação deste íon em biomateriais e moléculas orgânicas visando à regeneração óssea. No entanto, os mecanismos envolvidos na ação osteogênica do Sr^{2+}, bem como os possíveis efeitos resultantes de seu acúmulo no tecido, são raramente considerados. Estudos clínicos relatam o desenvolvimento de mineralização patológica devido ao excesso de Sr^{2+} reforçando a necessidade de investigações mais profundas sobre a ação desse íon no nível molecular do osso. Nesse sentido, esta tese apresenta um estudo abrangente dos impactos de Sr^{2+} nas propriedades estruturais do tecido ósseo, compreendendo os componentes orgânicos e inorgânicos tais como apatita e colágeno. Três modelos biomiméticos foram estabelecidos: (i) apatita carbonatada exibindo as principais características estruturais descritas no mineral ósseo, isto é, cristais com morfologia em forma de placa e orientação cristalográfica preferencial ao longo do eixo c; (ii) matrizes de colágeno densas, organizadas e mineralizadas que reproduzem a hierarquia do osso no nível do tecido e (iii) membranas de policarbonato com poros cilíndricos e nanométricos que reproduzem os espaços confinados onde a biomineralização ocorre. Embora a substituição de Ca^{2+} por Sr^{2+} em apatitas sintéticas seja comumente descrita como isomórfica para toda a faixa de concentração, inesperadamente observamos uma fase secundária em concentrações intermediárias de Sr^{2+}. Caracterizada como fosfato de cálcio amorfo rico em Sr^{2+} [Sr(ACP)], esta fase forma-se juntamente com apatita substituída com Sr^{2+}. Este resultado questiona o conhecimento atual sobre a substituição de Ca^{2+} por Sr^{2+} em apatitas sintéticas. Ainda, a formação de [Sr(ACP)] pode ser vista como uma evidência da interferência físico-química do Sr^{2+} na formação de apatita óssea como observado em patologias decorrentes de altas concentrações deste íon. Também foi demonstrado que em elevadas concentrações de Sr^{2+} ocorre a desestabilização do arranjo supramolecular das fibrilas de colágeno, que são as estruturas básicas da matriz orgânica óssea. O uso de meio confinado forneceu informações sobre os estágios iniciais da mineralização de apatita, mostrando que Sr^{2+} e confinamento agem em sinergismo para estabilizar os intermediários cinéticos deste mineral. Todos esses resultados foram obtidos com base em diversas de técnicas de caracterização tais como microscopia eletrônica de transmissão, difração de elétrons, espectroscopia por perda de energia de elétrons, ressonância magnética nuclear de estado sólido e espectroscopia Raman. De forma geral, os resultados apresentados nesta tese fornecem novas informações do ponto de vista físico-químico para a compreensão dos múltiplos efeitos do Sr^{2+} no tecido ósseo.

ABSTRACT

Strontium ions (Sr^{2+}) are the active component of strontium ranelate, a drug which reduces bone fractures in osteoporotic patients. This finding has in turn encouraged the incorporation of Sr^{2+} into biomaterials and organic molecules aiming at bone healing. Although the widespread interest in Sr^{2+}-based biomaterials has emerged over the last years, the mechanisms underlying its involvement as well as the possible effects resulting from its accumulation in bone tissue have received by far less attention. Clinical studies have reported the development of pathological mineralization due to the excess of Sr^{2+} reinforcing the need of deeper investigations on the action of this ion at the molecular level of bone. To address this shortcoming, this thesis presents a comprehensive investigation of the impacts of Sr^{2+} on the structural properties of bone comprising its organic and inorganic parts. Therefore, three biomimetic models were stablished: (i) carbonated apatite displaying the main structural features found in bone mineral *i.e.* crystals with plate-like morphology and preferential crystallographic orientation along the c axis, (ii) dense and anisotropic mineralized type-I collagen matrices which reproduce the hierarchy of bone at the tissue level and (iii) polycarbonate membranes with cylindrical pores mimicking the confined spaces where biomineralization takes place. While the substitution of Ca^{2+} by Sr^{2+} in synthetic apatite is commonly described as isomorphic in the whole range of concentration, we unexpectedly observed a secondary phase. Such phase was characterized as a Sr^{2+}-rich amorphous calcium phosphate [Sr(ACP)] and was formed simultaneously with Sr^{2+}-substituted apatite. This finding opens questions on the current knowledge concerning the substitution of Ca^{2+} by Sr^{2+} in synthetic apatite. Moreover, the detection of Sr(ACP) is an evidence of the physicochemical interference of Sr^{2+} on the formation of bone apatite and therefore its adverse effects at the regime of high doses observed *in vivo*. Interestingly, the self-assembly of collagen fibrils, the basic building blocks of bone extracellular matrix, was also impaired at high concentrations of Sr^{2+}. The use of confinement provided information regarding the early stages of bone formation, showing that Sr^{2+} and the physical environment act in synergism to stabilize kinetic intermediates of apatite. All these results were obtained relying on a panel of techniques, i.e., transmission electron microscopy, selected area electron diffraction, energy electron loss spectroscopy, solid state nuclear magnetic resonance and Raman spectroscopy. Overall, by using biomimetic models, this thesis gives clues from the physicochemical standpoint to understand the multiple effects of Sr^{2+} on bone tissue.

Chapter 1

General introduction and motivation

Abstract

The observation of nature and the outstanding properties of naturally found materials led to considerable advances in materials science. Specially, biomineralization is a ubiquitous and tightly regulated process which gives rise to functional organic–inorganic hybrid materials such as bone, teeth, and shells. The remarkable structures and morphology found in mineralized organisms have fascinated and intrigued scientist from different fields. It has also improved the understanding about pathological mineralization and bone regenerative therapies. In the context of osteoporosis treatments, Sr^{2+} has emerged in 2004 as the bioactive component of the drug strontium ranelate which is used in more than 70 countries. However, it is intriguing that the same element is involved in bone disorders, *i.e,* osteomalacia and rickets. This has turned our attention to investigate the possible effects of this element in bone using models able to mimic its organic and inorganic parts in terms of structure and composition. In this chapter we present a comprehensive view of the main mechanisms used by living organisms to produce biominerals and that were adopted to control the formation of the biomimetic models developed in this thesis.

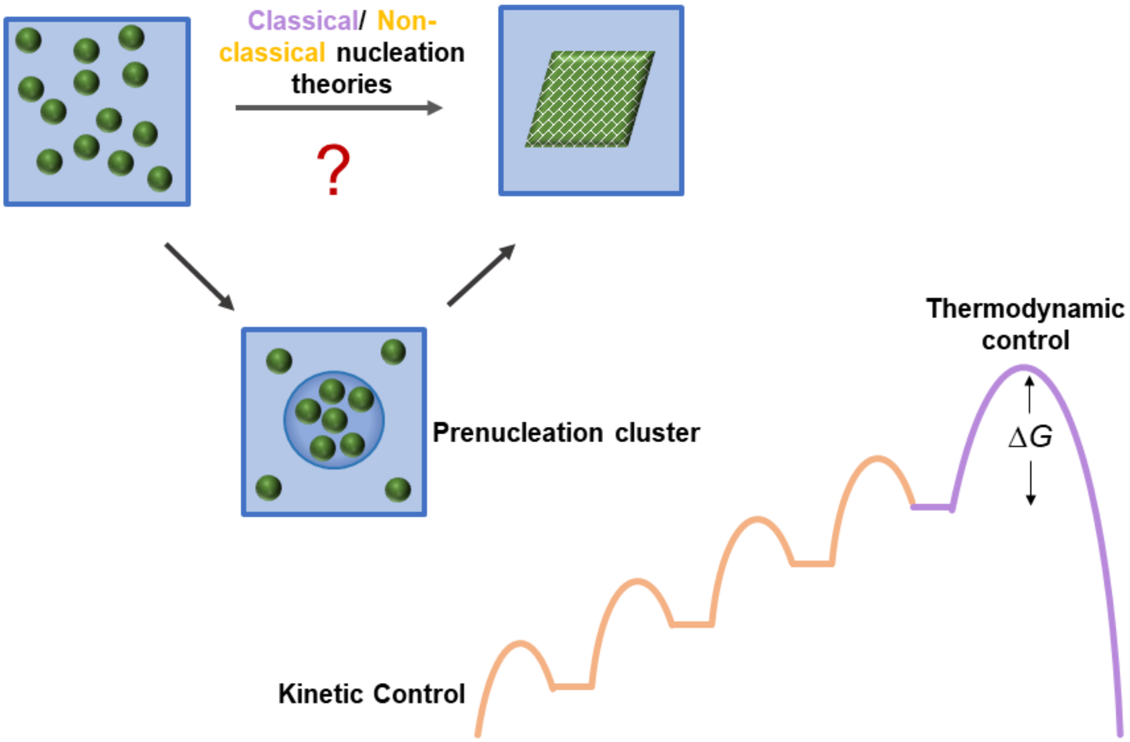

1.1 | An overview of biomineralization

Biomineralization is a complex process whereby organisms create fascinating multifunctional hybrid structures with hierarchical organization. Biominerals contrast with their synthetic and geological counterparts by the ability to control structural parameters namely crystal size, morphology, spatial orientation and polymorphs selection under ambient conditions and aqueous environment. Moreover, the synergism between the inorganic precursors and the macromolecules present in the biomineralization medium leads to materials with enhanced mechanical resistance and distinctive optical properties with respect to their constituents.[1] This is greatly exemplified by bone tissue and nacre which are basically constituted by calcium phosphate/collagen and carbonate/chitin, respectively. Biominerals are widespread in nature and more than 60 different types of mineralized structures are present in bacteria, plants, and animals playing structural and biochemical roles.[2] Among them, we can highlight silica, iron oxide, calcium carbonate and phosphate as well-known examples.

Iron oxides and sulfides are produced as magnetite (Fe_3O_4) and greigite (Fe_3S_4) by magnetotactic bacteria and used for different functions including hardening of teeth, sensing of magnetic fields, navigation and iron storage.[3,4] The unicellular algae diatoms and radiolarians are fascinating examples of biosilicifying organisms exhibiting a variety of sophisticated shapes which were not synthetically reproduced to date (Figure 1.1).[5,6]

Calcium carbonate based are the most abundant biogenic minerals being present in the hard parts out of marine organisms including corals, echinoderms (sea urchins and stars), mollusks, sponges, crustaceans, and certain algae (coccolithophores) (Figure 1.2).[7] This mineral occurs in the form of three anhydrous crystalline polymorphs *i.e* vaterite, aragonite, and calcite, with different thermodynamic stability under ambient conditions (vaterite<aragonite<calcite).[8,9] Two crystalline hydrated forms are also reported: monohydrocalcite ($CaCO_3.1H_2O$) and ikaite ($CaCO_3.6H_2O$). In 2019 a third crystalline hydrated form named hemi-hydrate ($CaCO_3.\frac{1}{2}H_2O$) was reported by the group of Peter Fratzl.[10] In addition to these crystalline phases, calcium carbonate is also stabilized by macromolecules and inorganic ions in the form of amorphous calcium carbonate (ACC).[11]

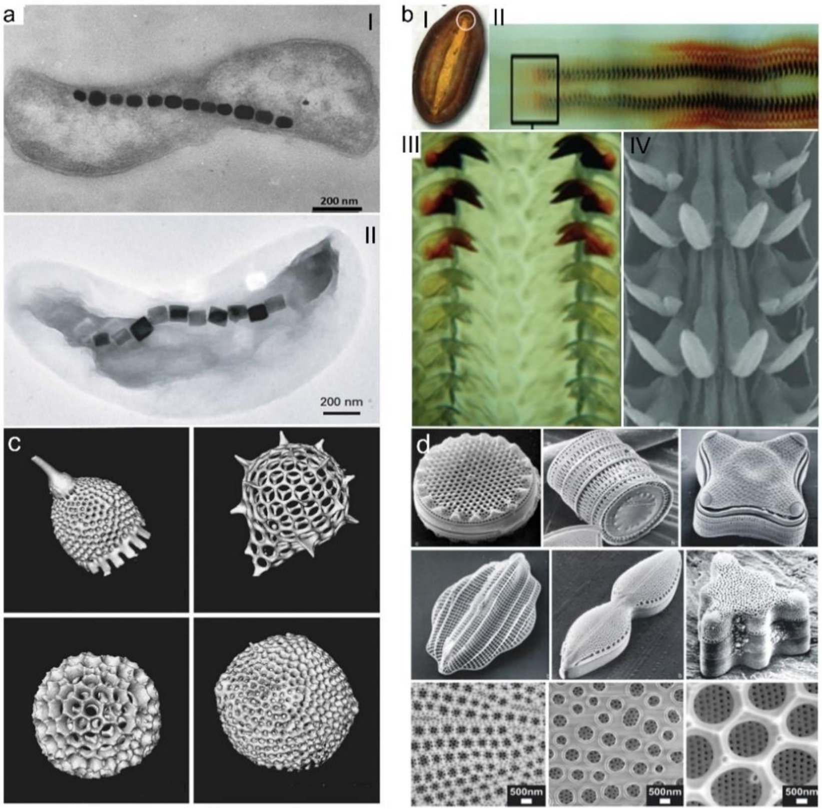

Figure 1.1 | Highly controlled morphology of biominerals based on Fe_3O_4 and SiO_2. (a) Transmission electron microscopy (TEM) image of magnetotactic_bacteria with single chain of mineralized spherical (i) and cubic (ii) magnetosomes. (b) Chiton radula, (i) image of the chiton (*Cryptochiton stelleri*) indicating its mouth (which contains the radula) by a white circle, (ii) optical microscopy image of an entire radula from *C. stelleri* containing more than 70 rows of parallel mineralized teeth, (iii) zone in the radula with a gradual change in tooth color from transparent to black demonstrating the earliest stages of biomineralization and (iv) scanning electrons microscopy (SEM) image of six mineralized teeth in each row. (c) X-ray tomograms of radiolarians exhibiting highly resolved, sharply defined surface elements. (d) SEM images of cell walls from different diatom species showing hierarchical distribution of pores. Images in top and middle rows show overviews of single silica cell walls, and images in bottom row show details of diatom silica cell walls. Reprinted with permission from: (a) Ref. 12, Copyright 2016 Royal Society of Chemistry, (b) i-iii Ref. 13, Copyright 2013 WILEY-VCH, iv Ref. 14, Copyright 2007 Elsevier, (c) Ref. 6, Copyright 2015 Microscopy Society of America and (d) Ref. 15, Copyright 2007 Elsevier.

While vaterite is rare in nature, ACC is found in combination to single crystals of calcite in calcareous sponges, sea urchin and stars, while aragonite is found in nacre where the organization of the crystals leads to the high mechanical resistance. The most well-known examples of calcium phosphate-based biominerals are bone and teeth.[16]

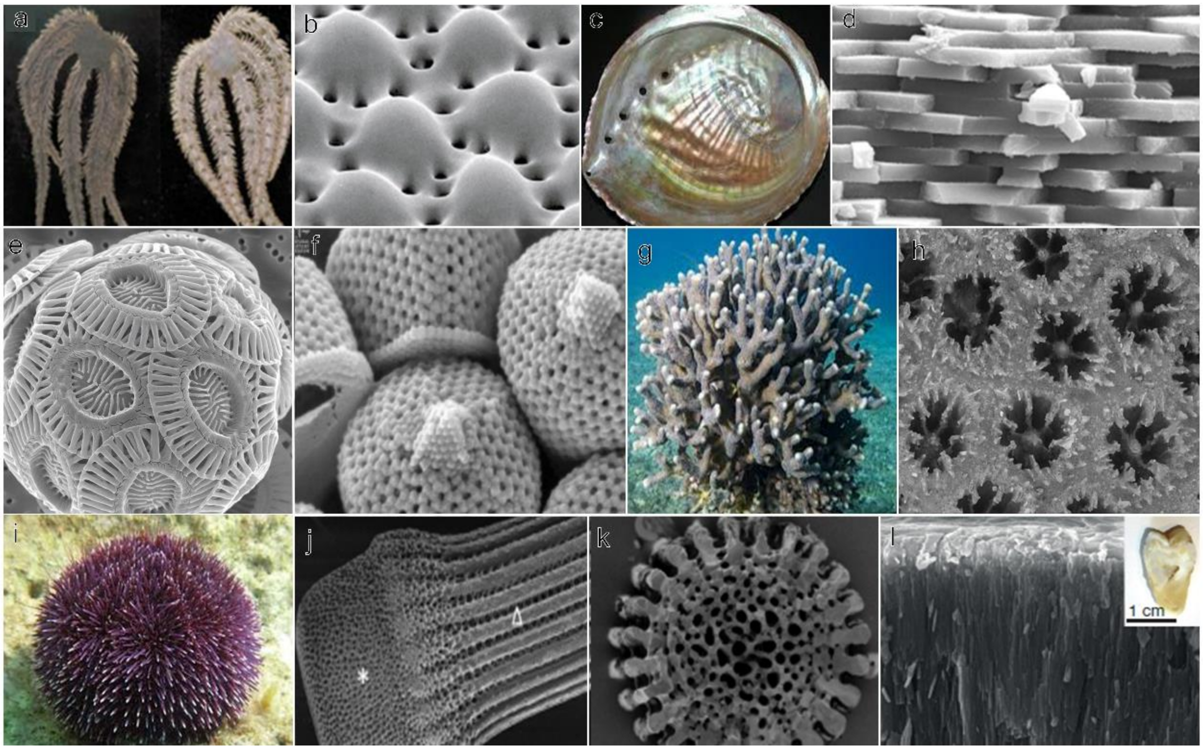

Figure 1.2 | (a) Brittle star *Ophiocoma wendtii,* a light-sensitive specie which changes the color from day (left) to night (right) and (b) SEM image showing the periodic arrangement of its calcitic structure. (c) Illustration of a nacreous layer of abalone shell and (d) SEM image showing its typical brick-and-mortar structure of aragonite tablets. (e) SEM images of coccolithophores formed by calcite plates and (f) spherical particles whose elements are composed of single crystals. (g) Illustration of aragonitic coral and (h) SEM image showing the morphological skeletal features common to all stony corals. (i) Illustration of sea urchin and (j) SEM image of a spine and (k) cross-section of a spine perpendicular to its long axis and (l) SEM image of enamel of human tooth with cross-section of specimen shown in inset photograph. Reprinted with permission from: (a-b) Ref. 17, Copyright 2001 Springer Nature, (e-f) Ref. 19, Copyright 2016 Elsevier, (h) Ref. 20, Copyright 2017 AAAS, (j-k) Ref. 124, Copyright 2018 American Chemical Society and (l) Ref. 21, Copyright 2017 Springer Nature.

It is believed that along the evolution the organisms developed their own strategies for producing different patterns of minerals adjusted to the function required.[22] Even though several mechanisms are involved in biomineralization, Stephen Mann proposed that many organisms share some basic approaches to regulate such exquisite process.[23] These approaches are summarized as (i) supramolecular preorganization, (ii) interfacial molecular recognition; (iii) vectorial regulation and (iv) cellular processing. Basically, these stages comprise the self-assembly of the organic matrix *i.e.* lipid vesicles, proteins and polysaccharides in arrays (i) which control the inorganic nucleation from aqueous solution (ii). The specific interaction between the ionic precursors and the functional groups of the organic templates is the key to the controlled nucleation of crystals at specific sites within the matrix. As the first nucleus forms within the organic hosts the mineral assembly starts with the spatially regulated growth process (iii). Finally, the last step of biomineralization comprises several constructional processes driven by cellular activity, i.e, assembly of crystals (iv).[24] This step gives rise to biominerals with unusual morphologies and is by far the most challenge aspect of biomineralization to reproduce in synthetic systems.[25] This series of processes was termed by Mann as molecular tectonics or synthesis with construction. A multitude of cells and macromolecules are involved in these processes to regulate the accurate deposition of mineral thus avoiding undesirable precipitations from the supersaturated biological fluids.[23]

Besides the chemical interactions, the organic matrix also controls the feature of biominerals by providing restricted spaces whereby the nucleation and growth processes take place.[26] Therefore, an intrinsic feature of biomineralization is the formation of materials in well-defined spaces rather than in bulk solution.[27] It is worth noting that a system is defined as confined if (i) the nucleation and growth processes occur in small volumes and (ii) the transport of the building blocks of one phase is prevented between these volumes.[28]

Despite the relevance of confinement on biominerals formation, this is an often-overlooked aspect in the investigations aiming at understanding biomineralization. This is mainly because of the challenge of undertake precipitation in small volumes and set up devices with controlled size. Moreover, the complex environment *in vivo* including cells, proteins and macromolecules also hinder the study of exclusive effects of confinement.[29] Thus, synthetic models are needed to go further in this respect.

The group of Fiona Meldrum has systematically investigated how confinement influences the formation of several biominerals namely calcium carbonate, calcium phosphate, calcium sulfate and calcium oxalate.[30–33] To this end, track-etched membranes containing cylindrical pores with controlled size were settled as model of confined systems in biomineralization. The group showed in elegant accounts that confinement by itself influences the formation of minerals on many levels including morphology, size, orientation, polycrystallinity, and polymorphism. For example, crystals of hydroxyapatite nucleated within 25–300 nm pores displayed preferred orientation as compared to those formed in bulk solution (Figure 1.3a).[34] In this case, the restricted volume was able to reproduce the bioapatite found in bones and teeth. It was also suggested that confinement provides a novel way of identifying metastable intermediary phases during the precipitation of biominerals.[35] In confinement, the intermediate products (*e.g,* amorphous phases) are kinetically stabilized as consequence of their reduced contact with the solution and other nucleus which in turn hind aggregation, redissolution and reprecipitation processes towards crystallization. It is worth noting that several theories are proposed to account for the mechanism by which confinement affects the kinetics of precipitation, including the slower transport of ions, and the reduced convection.[36–40]

The same group also explored the use of confinement to shed light into the selectivity of calcite and aragonite in organisms, a fascinating topic that has been the focus of research for decades.[41] While calcite was the main product when the precipitation was carried out in bulk, aragonite single crystals were formed within the cylindrical pores of track-etched membranes (Figure 1.3b). Although this report significantly improved our understanding about the strategies exploited by organisms to regulate the formation of bominerals in nature, the mechanism by which confinement facilitates aragonite growth for now remains unknown.[42] Therefore, these reports strength the idea that organisms can use constrained spaces to biologically control the diversity of shapes and textures exhibited by biominerals.

Other systems namely micelles, liposomes and polysaccharide matrices have also been used to investigate the effect of confinement in biomineralization.[43,43]

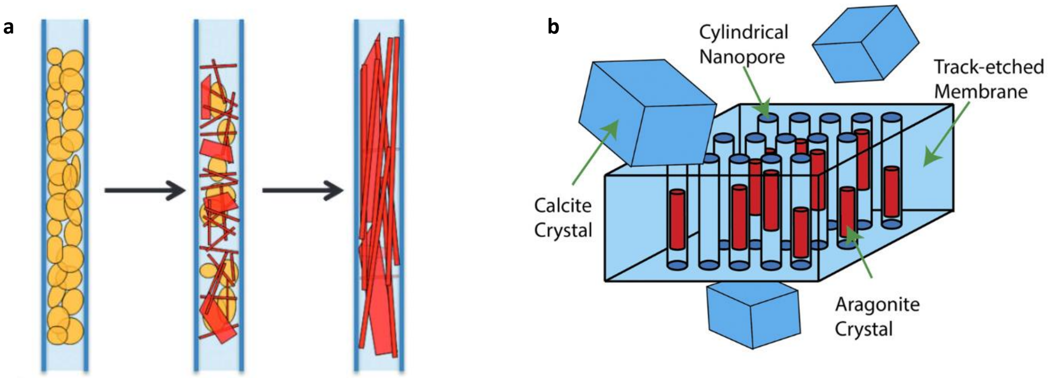

Figure 1.3 | Scheme of (a) apatite and (b) $CaCO_3$ crystallization within the cylindrical nanopores of track-etched membranes. (a) The amorphous calcium phosphate particles(yellow) is formed within the pores and then converted into apatite (red), which is parallelly oriented to the long axis of the pore. (b) Calcite crystals are formed in the bulk solution while aragonite single crystals oriented to the membrane axis are formed within the nanopores. Reprinted with permission from: (a) Ref. 34, Copyright 2013 WILEY-VCH Verlag GmbH & Co and (b) Ref. 42, Copyright 2018 National Academy of Sciences.

Nature has served as a source of inspiration to design innovative materials with optimized functions in different fields, i.e., hard tissues implants, catalysts, optical devices.[44] In this sense, the attention of the scientific community was turned towards deciphering the mechanisms behind the biogenic principles of building materials. This has challenging the frontiers of the classical divisions in science of inorganic, organic, physical chemistry, physics, and biology. Moreover, the study of biomineralization and bio-inspired materials has boosted the development of characterization techniques in special *in situ* ones. [45] Overall, the investigation of biogenic materials has improved the concept of bioinspiration and shed new lights on materials science.[46] Specially, calcium carbonates and phosphates have attracted enormous attention in the field of biomaterials science. Our group have shown its applications to improve the bioactivity of Ti implants and design innovative bioactive materials.[47–49]

Fundamental questions including the putative existence of an amorphous precursor, and how mineral is delivered to the crystallization site are yet unanswered. From these, the process of bone formation is by far one of the most investigated natural process and will be discussed in more detail in the next sections.

1.2 | Bone tissue: structure and composition

Bone is a complex hybrid material that comprises cells and an extracellular matrix formed by mineralized collagen fibrils, non-collagenous proteins and water.[50] The hierarchical assembly of these components occurs in a bottom-up manner giving rise to a complex architecture responsible by the stiffness and toughness of bone.[51] Such structure/function relationship is intriguing and has been investigated for more than 320 years without a consensus. In fact, the paradigm of bone hierarchy was originally elaborated in 1691 by the English physician Clopton Havers who proposed a model comprising five structural levels of organization in bone.[52]

However, details of the architecture of the organic and inorganic constituents of bone have become available with the development of X-ray diffraction and electron microscopy techniques. In 1998 Weiner and Wagner described seven hierarchical levels of organization in bone.[53] Further insights into bone organization were obtained by using nanoscale 3D-imaging. These revealed two distinct assemblies in bone: (i) an ordered array of mineralized collagen fibrils as the higher percentage of bone (80% wt.), and (ii) a less ordered material referred also as diffuse lamellae, comprising highly spaced collagen fibrils associated with a high amount of non-collagenous proteins and crystals located inside and between the fibrils.[54] This finding has in turn motivated Weiner and Reznikov to update in 2014 the previous model of bone organization and 9 hierarchical levels were proposed considering these two different arrangements of collagen fibrils.[55] Finally, in 2018 the fractal-like model was proposed by Reznikov showing that the hierarchical organization of bone begins at the nanoscale.[56] For the first time it was shown that the hierarchical motifs pertain to both collagen and mineral and not only to collagen as described in the previous models. Thus, this adaptation of the Weiner and Wagner model resulted into 12 organization levels in bone (Fig.1.4). Accordingly, at the fundamental level there are atoms (I) that form both amino acids (II) and the first acicular crystals (II). So, focusing first in the organic matrix the amino acids residues are linked through peptide bonds to form molecular chains (III) arranged in triple helical structures referred to as tropocollagen molecules (IV). Interactions between tropocollagen molecules leads to its self-organization into fibrils (V) of about 80–120 nm where carbonated apatite nucleates. Focusing on the mineral, the first acicular crystals are combined to form platelets (III) that further assemble parallelly forming stacks (IV). Then, these stacks form bigger aggregates of minerals (V) that span over the cross-section of collagen fibril thus giving rise to the basic building block of bone, i.e., mineralized fibrils (VI).The parallel assembly of mineralized fibrils gives rise to continuous arrays that self-assemble in different ways forming ordered and less ordered motifs (VII). These are then packed into bundles of fibrils (VIII) that are further arranged in geometrical patterns (twisted plywood geometry) forming lamella (IX). Lamellar packets form trabeculae or are concentrically disposed around a canal forming the osteons (X), that in turn origin trabecular and compact bone respectively (XI), resulting the whole bone tissue (XII).

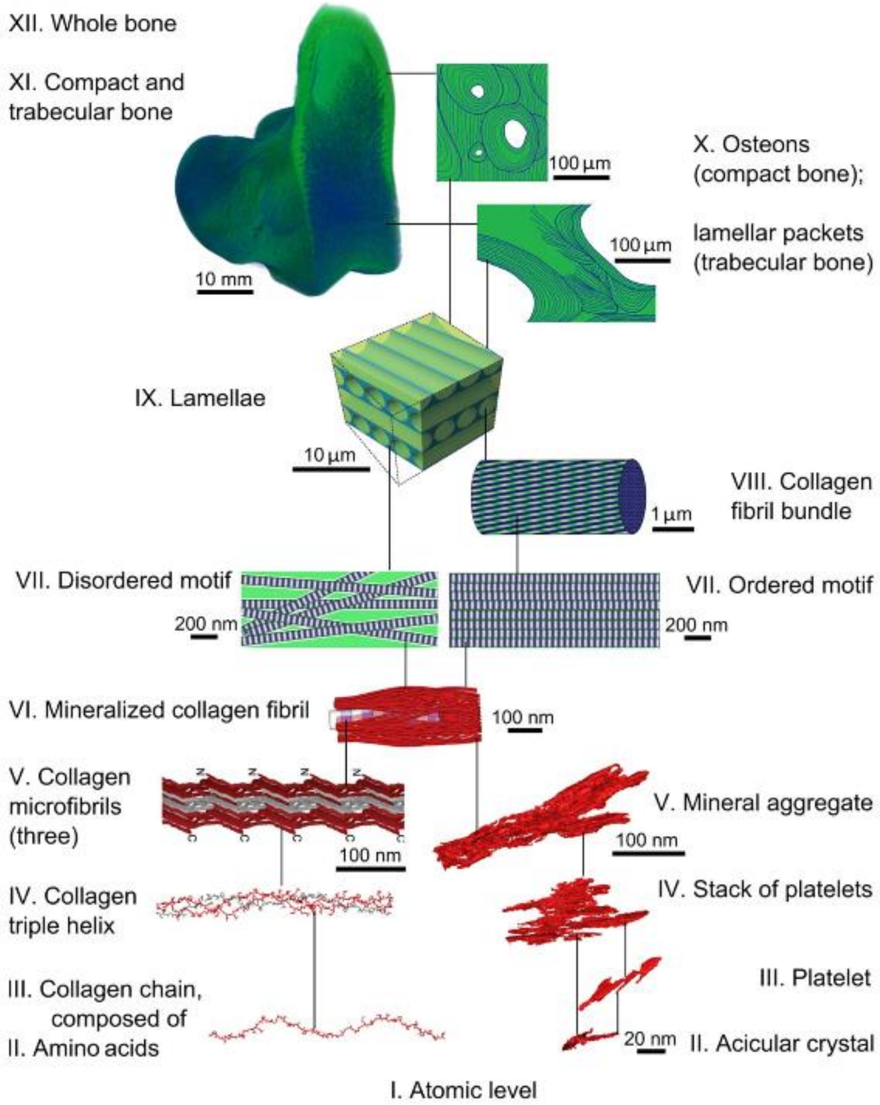

Figure 1.4 | Scheme showing the hierarchical organization of bone. Initially apatite crystals and collagen molecules are put apart to show their nested structural motifs, and so listed in according to the structural motifs complexity. Both ordered and disordered domains of lamellar bone comprise mineralized collagen fibrils that are 80 to 120 nm thick and form a continuous network. Reprinted with permission from Ref. 56, Copyright 2018 AAAS.

1.2.1 | Collagen self-assembly in bone: from triple helix to liquid crystalline geometries

Collagen is a generic name for a group of 28 proteins whose hallmark is the formation of triple helix between the polypeptide chains.[57] The amino-acid sequence (Gly-X-Y) in which X and Y are frequently proline and hydroxyproline is also a common characteristic of these proteins (Figure 1.5). This motif of amino acids is in turn responsible for the assembly of the polypeptide chains of collagen into triple helix.[58]

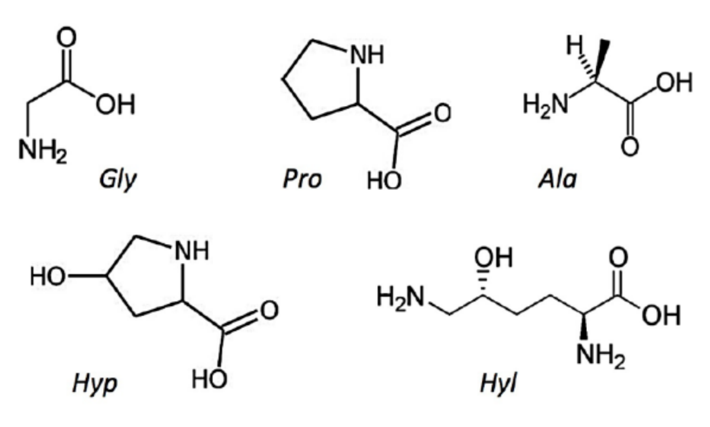

Figure 1.5 | Chemical structure of the amino acids present in collagen molecules.

Collagens are synthesized by tissue specific cells, i.e., fibroblasts, osteoblasts, chondrocytes and differ from each other in terms of structure, assembly and functions. Among the different families, the most abundant (about 90% wt. of the total collagen) is the fibril-forming, including collagen types II (present in cartilage), III (present in arteries), V (present in cornea), and XI (present in cartilage) and type I, the most abundant in the human body (present in skin, tendon, cornea and bone extracellular matrix). These proteins are characterized by their ability to assemble into highly orientated supramolecular structures with a characteristic fibril-array with diameters ranging from 25 to 400 nm.[59]

In vivo, the formation of collagenous matrices follows a multistep pathway involving intracellular and extracellular processes (Figure 1.6). Briefly, the cells produce procollagen molecules which are packed into secretory vesicles in the Golgi apparatus. Then, this precursor molecule is released in the extracellular space where the enzymatic cleavage of the extremities (N and C propeptides) takes place forming collagen molecules also referred as tropocollagen. Because of the negative charge of these terminal groups the procollagen molecule is soluble at physiological pH.[60] Therefore, is only after the processing of procollagen that fibrillogenesis is initiated. The process of collagen self-assembly is often compared to crystallization with initial nucleation and subsequent aggregation.[61]

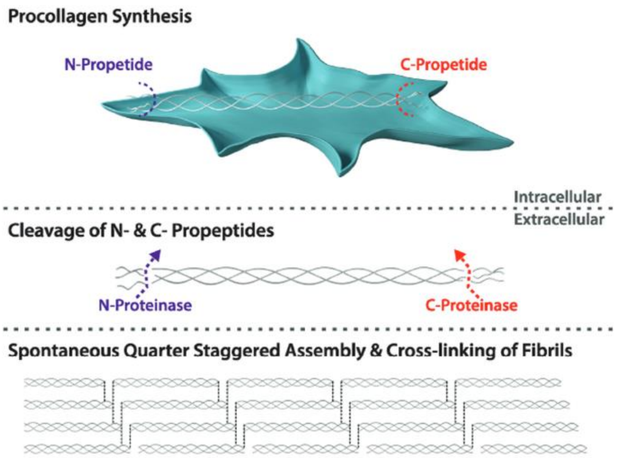

Figure 1.6 | Biosynthesis of collagen. Procollagen is synthesized intracellularly and secreted to the extracellular space where the specific cleavage of the N and C propeptides extensions takes place giving rise to tropocollagen molecules. N and C proteinases are responsible for procollagen processing. Afterwards collagen molecules assemble into fibrils through crosslinking. Reprinted with permission from Ref. 62, 2018 WILEY-VCH Verlag GmbH & Co.

Type-I collagen fibrils are the most important building blocks of connective tissues. Therefore, the structure and assembly of collagen molecules are fundamental for the stability, physical and biochemical properties of these tissues.[63] The triple helix of type-I collagen is formed by two α_1 and one α_2 folded polypeptide chains and has of about 300 nm in length and 1.5 nm in diameter. Initially, 5 collagen molecules aggregate into microfibrils, which in turn assemble into fibrils and then fibers. Hydrogen bonding, hydrophobic and electrostatic interactions and covalent cross-links between the collagen monomers are involved in the stabilization of the fibrils network.[64]

Several models have been proposed to explain the assembly of tropocollagen into collagen fibrils forming the typical banding pattern. One of the initial models was proposed in 1963 by Hodge and Petruska supported by electron microscopy.[65] Accordingly, in order to form a fibril 5 tropocollagen molecules assemble parallelly with an offset of 67 nm between rows resulting in a 40 nm gap or hole zone and a 27 nm overlap zone. This is known as the quarter stagger model because neighboring collagen molecules are displaced one quarter (67 nm) of its length (300 nm) (Figure 1.7). Covalent cross-links are stablished near the N- and C-termini to connect the molecules within a fibril. This model was further refined and extended to the three-dimensional assembly of microfibrils. Smith proposed that five tropocollagen molecules are arranged forming a fibril precursor called microfibril.[66] Using X-ray diffraction, Orgel presented in 2006 a revised microfibrillar model showing five staggered tropocollagen molecules arranged with a right-handed tilt, rather than axially staggered.[67] Then, one microfibril was defined as a unit cell of collagen fibrils. It is important to note that the association of collagen molecules reaching an intermediate state between the unit triple helix and fibril *in vivo* is a matter of debate to date.

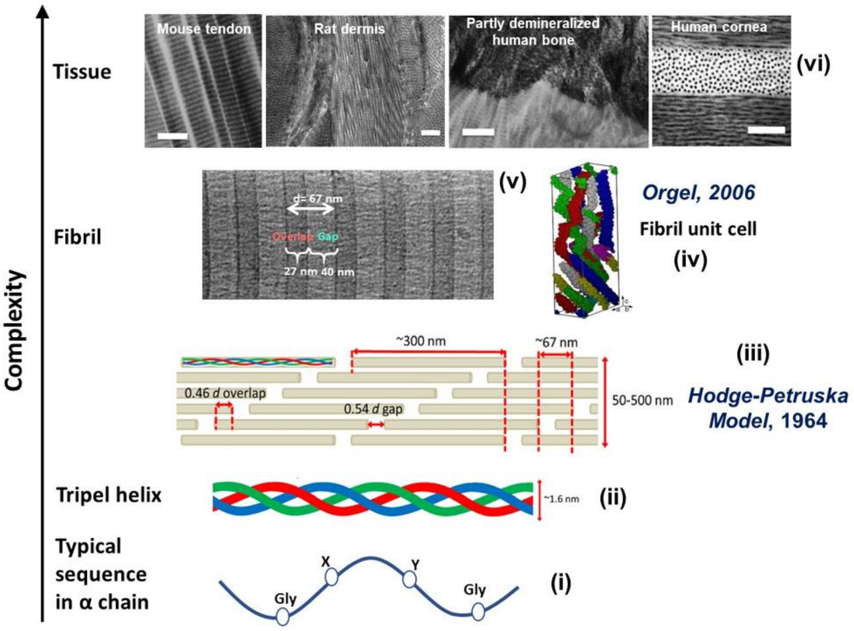

Figure 1.7 | Hierarchical structure of collagen and models of collagen fibril. (i) Amino acid sequence in the α-chains, (ii) collagen molecule, (iii) schematic representation of the Hodge-Petruska model accounting for the banding pattern of a collagen fibril, (iv) unit cell of collagen fibril comprising one 67 nm repeat proposed by Orgel, (v) cryo-TEM image of a collagen fibril and (vi) TEM images of connective tissues showing the dense packing of collagen fibrils. Adapted with permission from (ii-iii) Ref. 68, Copyright 2015 Elsevier, (iv) Ref. 67, Copyright 2006 National Academy of Sciences, (v) Ref. 69, Copyright 2016 National Academy of Sciences, and (vi) Ref. 70, Copyright 2013 Royal Society of Chemistry.

Collagen fibrils are highly ordered in vertebrate organisms displaying typical geometries according to the tissue. Typical examples are the plywood geometry in lamellar bone and the parallel arrays of fibers in tendons.[71] Moreover, these motifs found in the tissues namely dermis, tendon, cornea and bone are described as analogous to that of liquid crystals, a physical state of matter between liquid and solid.[72] Some authors, however, prefer the term mesomorphic state rather than liquid crystal to emphasize that this is in fact an intermediate state of these phases.

The classifications of liquid crystals into three major mesophases according to their molecular organization was proposed by Friedel in 1922.[73] Nematic is the simplest geometry in which there is a long-range order and the molecules tend to align parallel to each other but without translational order. In the cholesteric or chiral nematic phase the molecules are parallel aligned in successive planes forming layers which rotate regularly from one plane to the next. The cholesteric axis is perpendicular to the stratification. Therefore, we can say that this phase corresponds to a rotation in the nematic geometry (Figure 1.8). The nomenclature thermotropic is used when the transition from isotropic to liquid crystals geometries is reached by changing the temperature. When the transition is reached by changing the concentration of solvent or solute the liquid crystal is called lyotropic.

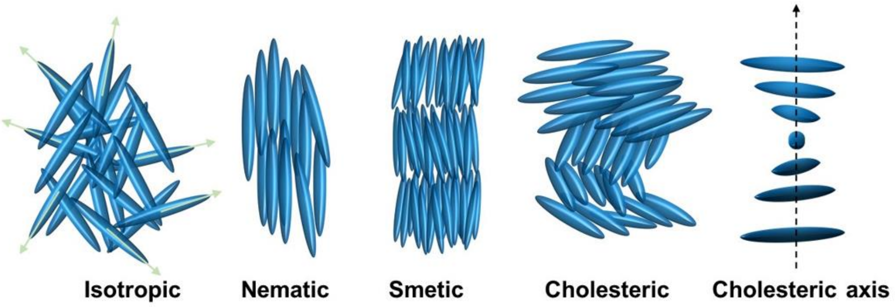

Figure 1.8 | Scheme showing different arrangements from isotropic to liquid-crystal geometries comprising the nematic, smetic and cholesteric mesophases.

TEM and SEM analysis of ultrathin sections of decalcified human compact bone revealed that collagen is organized in regular patterns of parallel nested arcs (Figure 1.9a-c).[74] This was firstly interpreted as curved fibrils. Afterwards, Yves Bouligand showed that, in fact, this resulted from the 3D arrangement of collagen fibrils lying in successive plans with specific rotations.[75] Then, in analogy to the cholesteric mesophase of liquid crystals a model known as Bouligand's twisted plywood was proposed (Figure 1.9 d-g). This consists in a pyramid in which the molecular directions are represented by parallel and equidistant lines in a series of rectangles representing the planes (Figure 1.9g). The lines rotate from one rectangle to the next by small and constant angles. It is noteworthy that the mineralization and molecular cross-links limit the fluidity of collagen fibrils in the matrices. Therefore, this organization is described as analogous to liquid crystals.

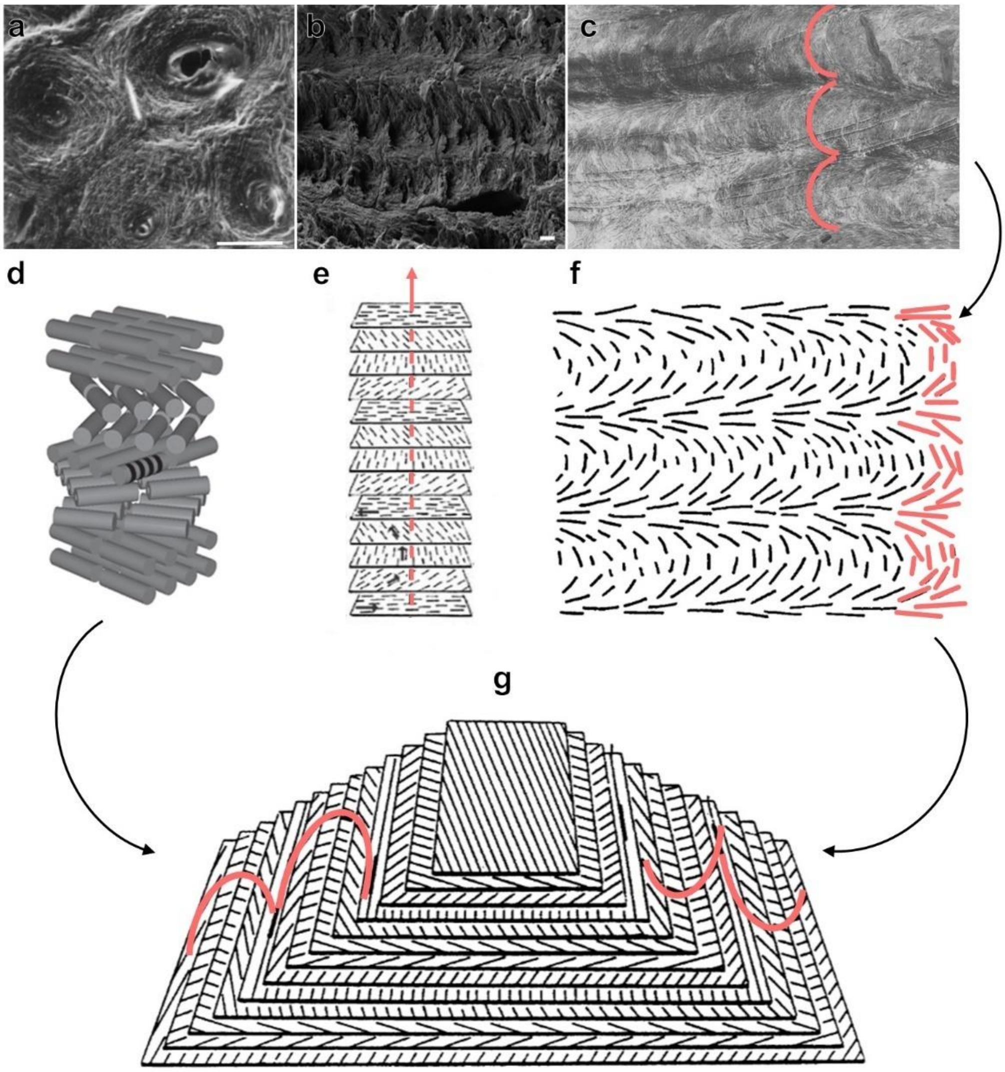

Figure 1.9 | (a) SEM image of compact bone showing the osteons. (b) SEM image of fractured bone perpendicular to its long axis. The lamellae are composed by mineralized collagen fibrils aligned parallelly and perpendicularly to the fracture surface. Scale bars: 1 μm. (c) TEM image of ultrathin section of human demineralized compact bone displaying typical arched pattern (red line). (d) Diagram of rotating collagen fibrils. (e-f) Drawing of arced patterns as they can be observed in electron micrographs of several extracellular matrices. (g) 3D Bouligand's model of twisted plywood geometry. Bouligand curves (red line) were drawn to identify the geometric motifs. Reprinted with permission from:(a) Ref. 72, Copyright 1996 Elsevier, (b) Ref. 55, Copyright 2014 Elsevier, (c)Ref. 76, Copyright 1988 Springer Nature, (d) Ref. 70, Copyright 2013 Royal Society of Chemistry, (e) Ref. 77, Copyright 2006 Elsevier, (f) Ref. 78, Copyright 1992 Elsevier and (g) Ref. 79, Copyright 1995 Elsevier.

The lyotropic properties of soluble collagen were widely investigated to validate the involvement of liquid crystalline arrangements in the morphogenesis of bone tissue.[80,78] Marie-Madeleine Giraud-Guille studied the self-assembly of collagen molecules in acidic solutions showing the formation of different liquid-crystals mesophases according to their concentration (Figure 1.10a).[81] At 40 mg mL^{-1} type-I collagen undergoes phase transition from isotropic to nematic phase. Increasing the concentration between 50-70 mg mL^{-1} the precholesteric phase is triggered and cholesteric above 80 mg mL^{-1}. Then, Giraud-Guille showed that these liquid crystal geometries of collagen molecules could be stabilized *in vitro* by increasing the pH using ammonia vapor (Figure 1.10b).[79] Initially, in the concentrated acidic solution, the amino acids residues are positively charged maintaining the molecules in the liquid state due to the repulsion between the chains. As the pH increases due to the ammonia diffusion, the net charge of the collagen monomers is decreased, and hydrophobic interactions dominate. Therefore, the triple-helices aggregate leading to the precipitation of the fibrils. Basically, this process involves the passage from the molecular to the fibrillar state by a sol-gel transition which takes place without disturbing the liquid crystal organization.[82]

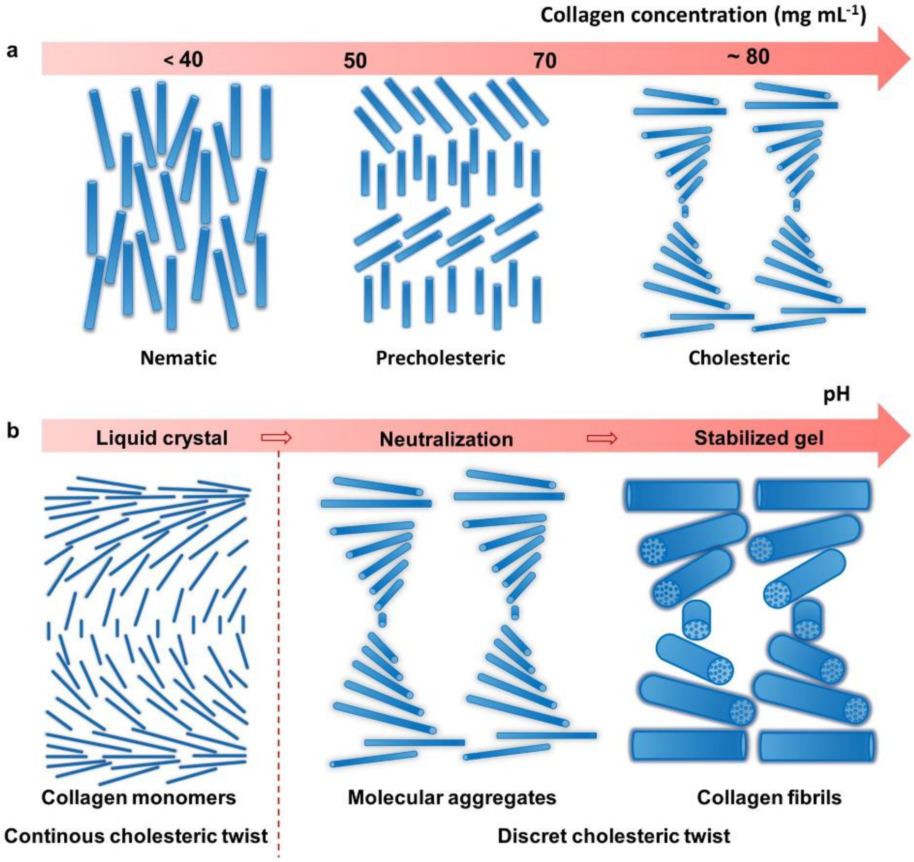

Figure 1.10 | Scheme of *in vitro* stabilization of liquid crystal mesophases of the collagen. (a) The first step is the concentration of the collagen solution according to the mesophase. (b) sequence, the exposition of the gel to ammonia vapor increases the pH leading to the stabilization of the liquid crystalline mesophase. Adapted with permission from Ref. 79, Copyright 1995 Elsevier.

Collagen is secreted by the cells in concentrations nearly to 40 mg ml^{-1} which therefore strengths the idea of a molecular liquid crystal phase preceding the fibril assembly in the tissues.[83] In this context, one important question which persists is whether the liquid crystals arrangements start with the procollagen molecules in confined spaces inside the cells or in the extracellular matrix. The fact that procollagen molecules also assemble into cholesteric geometries *in vitro* has suggested that this molecule assumes a similar organization in the cellular compartments.[84] However, further investigations in native tissues are still needed as a proof of concept.

Although these investigations have improved our understanding about the supramolecular assembly of collagen in human body it is still challenging to handle high concentrated collagen materials. Consequently, biomineralization investigations and biomaterials design have been undertaken using collagen at low concentration which does not represent the organization and mechanical properties found in the connective tissues (Figure 1.11).[85] In this context, the group of Nadine Nassif has contributed to bridge this gap by developing several models to reproduce the collagen architecture found in living tissues *i.e.* cholesteric liquid crystals. The approaches used by the group involve collagen concentration by evaporation, reverse dialysis and spray-drying. [85–88] This has improved the knowledge towards the fabrication of biomimetic 3D materials in the contexts of biomineralization and tissue engineering.

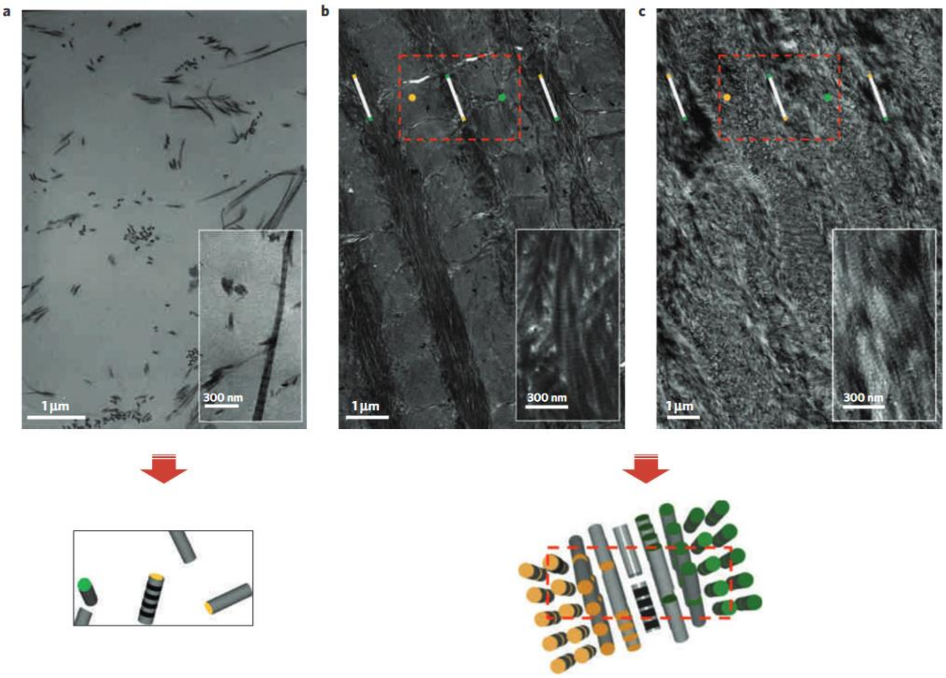

Figure 1.11 | TEM images of ultrathin sections of (a) low-concentration collagen matrix (5 mg ml^{-1}), (b) demineralized compact bone and (c) high-concentration collagen matrix (250 mg ml^{-1}). In the low-concentration collagen matrix, collagen fibrils appear with no-preferred orientation. In contrast, the pattern observed in the high-concentration collagen matrix mimics the organization of the organic extracellular matrix of bone in terms of density and organization, i.e, long-range twisted plywood geometry. The periodic rotation of collagen fibrils is illustrated by white bars, corresponding to fibrils positioned in the section plane, and yellow and green dots corresponding to fibrils normal to this plane. Schematic representations of the organization of collagen fibrils in a, and in b are shown below (as indicated by the red arrows). The green and orange colors illustrate the opposite extremities (N- and C-terminal) of the collagen fibrils. Reprinted with permission from Ref. 85, Copyright 2012 Springer Nature.

Strikingly, plywood-like architectures are ubiquitous in nature and can be identified in animals and plants (Fig.1.12). These observations have suggested that a common mechanism of tissues morphogenesis involving liquid crystals precursors phases emerged along the evolutionary process leading to the complex architecture of these materials. Besides mechanical strength and flexibility, such arrangement provides distinct optical properties, i.e, structural colors to these biogenic materials. Inspired on these materials, nanofibrillar biopolymers have emerged as potential candidates for the development of sustainable and biocompatible materials for technological applications.[89] Nevertheless, reproducing such a specific long-range ordering in dense matrices is still challenging.

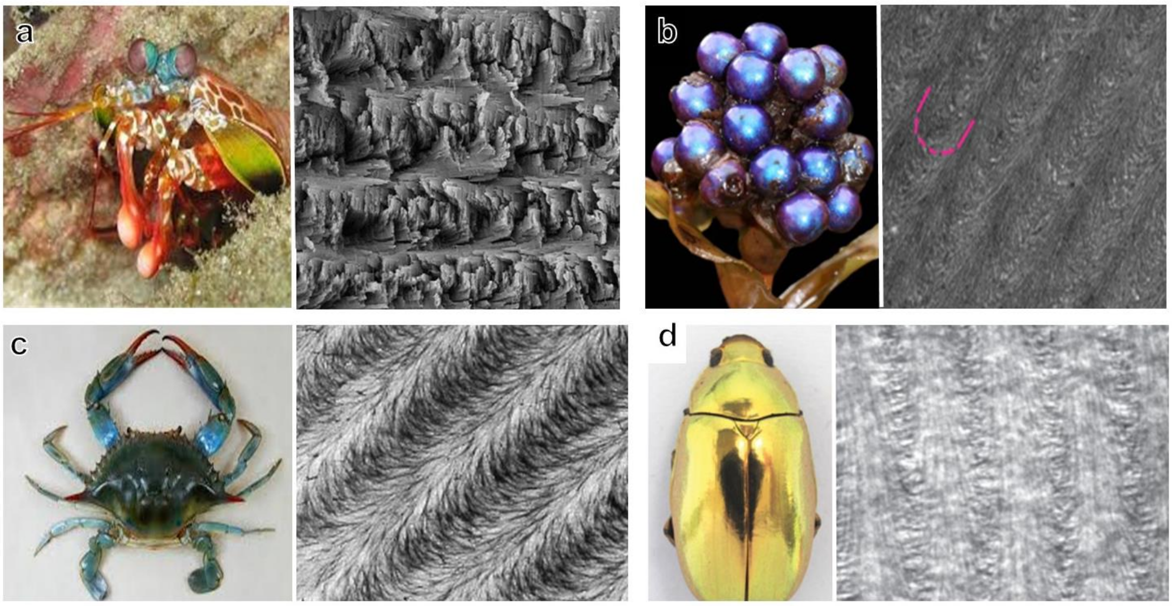

Figure 1.12 | Twisted plywood structures in nature. (a) Peacock mantis shrimp *Odontodactylus scyllarus*. SEM image of a sectioned club sowing the chitin fibrils mineralized with mixed calcium phosphate and carbonate. (b) Fruit of *Pollia condensate*. TEM image of the cellulose matrix that constitute the outer layers of the cell walls of the epicarp. (c) Crab. TEM image of sectioned decalcified cuticle showing the chitin matrix. (d) Beetle *Chrysina resplendens*. TEM of an oblique section of the cuticle made of chitin. Reprinted with permission from (a) Ref. 90, Copyright 2012 AAAS, (b) Ref. 91, Copyright 2012 National Academy of Sciences, (c) Ref. 82 Copyright 2006 IOP Publishing, and (d) Ref. 92, Copyright 2017 Royal Society.

1.2.2 | Formation of bone tissue: from prenucleation clusters to mineralized collagen fibrils

Even though the composition of bone apatite derives from synthetic hydroxyapatite $Ca_{10}(PO_4)_6(OH)_2$, this biomineral has its own structural signature ascribed to ionic substitutions, poor structural ordering and preferential crystallographic orientation along the c-axis (Figure 1.13a-c).[93] The most common ionic substitution in bone is the replacement of PO_4^{3-} and/or OH^- by CO_3^{2-} which is named B-type (the most common in bone) and A-type substitution, respectively, or AB-type when both occur (Figure 1.13d).[94] Additionally, other foreign ions, i.e., Na^+, Zn^{2+}, Mg^{2+}, Sr^{2+}, F^- and HPO_4^{2-} are also found in smaller fraction in bone mineral. [53]

Recently, it was shown that bioapatite displays distinct mineral domains characterized as a crystalline core and an amorphous hydrated layer which accommodates Ca^{2+}, HPO_4^- and CO_3^{2-} (Figure 1.3b).[95] In addition to the chemical composition, ionic substitutions and collagen are responsible for the different characteristics of these domains specially the size, degree of disordering of the crystalline part and the ratio crystalline core/amorphous layer.[96]

The physicochemical properties of apatite contribute not only for the mechanical properties of bone but also for its biochemical function. The low degree of crystallinity is reported to support the resorption/remodeling processes whereas the hydrated disordered surface layer is proposed to act as an ion reservoir.[97,98]

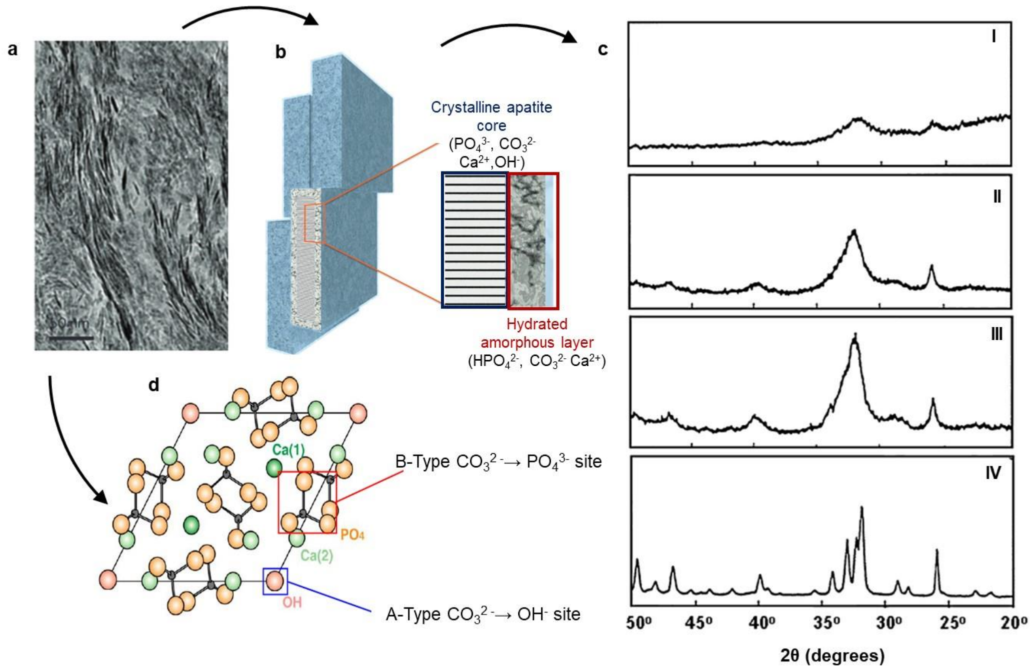

Figure 1.13 | TEM image of ultrathin section of sheep bone showing the alignment of apatite crystals inside the organic matrix (a). Schematic representation of apatite platelet showing the crystalline core and the hydrated amorphous layer (b). X-ray diffraction patterns of bones from (I) seventeen-day-old (II) five-week, (III) two-year-old chick and (IV) highly crystalline synthetic hydroxyapatite (c). The bone mineral become more crystalline with the extent of mineralization. Bioapatite and synthetic apatite are structurally different. (d) Representation of apatite structure showing the possible ionic substitutions. Spheres in orange represent oxygen and calcium in green. Reprinted with permission from: (a-b) Ref. 95, Copyright 2013 Springer Nature and (c) Ref. 99, Copyright 2009 Springer Nature.

The mechanisms governing the nucleation and growth of bone apatite is a long-standing paradigm. Several models based on different pathways have been proposed resulting in controversies regarding the involvement of the extracellular matrix and the existence of precursor species, i.e, prenucleation clusters, amorphous phase.[100] Usually, the biomineralization process is described on the basis of classical (CN) and non-classical nucleation theories (NCN).[101] According to the CN the minerals are directly nucleated from the assemble of atomic/molecular building units. The growth process occurs only by the attachment of these building block (Figure 1.14a-b). Conversely, the NCN considers that kinetically accessible phases are formed before the thermodynamic product. Therefore, rather than the direct nucleation from ions in solution, this model considers that minerals are formed via a multistep process involving redissolution, reprecipitation and aggregation of secondary phases.[102]

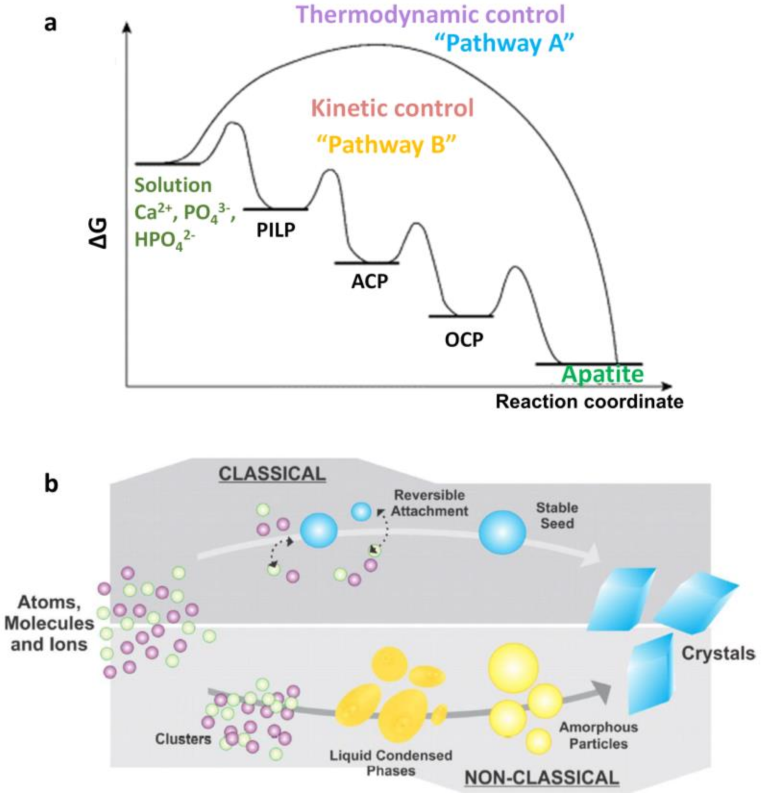

Figure 1.14 | Reaction coordinate diagram representing different pathways to form apatite (a). The pathway A represents the classical crystallization mechanism, without involving intermediate phases. The pathway B demonstrates the mineralization via a multistep mechanism forming different phases. The first step requires a $\Delta G_{Nucleation}$+ ΔG_{Growth}, while the subsequent steps only require a $\Delta G_{Phase\ Transformation}$. Scheme illustrating the CN and NCN theories (c). Figure (b) extracted with permission from Ref.103, Copyright 2018 The Chemical Society of Japan & Wiley-VCH Verlag GmbH & Co and Ref.104, Copyright 2008 AAAS .

The unconventional composition, structure and habits of mineralized organisms have questioned the CN. Then, models based on NCN emerged to explain such exquisite biominerals.[105] The so-called transient precursor theory considers the formation of an amorphous phase which is then converted into more stable crystalline phases following Ostwald-Lussac step rule.[106,107] According to these principles, Posner described in 1966 an amorphous precursor during the formation of biological apatite.[108] In 1974, Betts and Posner proposed that ACP is an aggregate of $Ca_9(PO_4)_6$ subunits with ~1 nm, later named

Posner's cluster.[108] Accordingly, ACP should dissociate into these clusters rather than into the ionic precursors which in turn suggests important role of Posner's cluster during apatite formation. Since then, in analogy to the Posner's cluster, prenucleation clusters have been proposed to take part in the formation of several biominerals which follows an amorphous precursor pathway, i.e, calcium carbonate, calcium oxalate and calcium phosphate.[109] However, due to the nanometric size the visualization of this subunits is challenging making them a matter of debate so far.[110]

Recent accounts from the group of Nico Sommerdjik based on cryo-TEM and computational simulations have supported the proposition of Posner. The group showed that in a buffered solution under constant ionic strength, apatite nucleation starts with the aggregation of prenucleation clusters (Figure 1.15).[111] These aggregates in turn densify forming polymeric assemblies from which ACP is nucleated and ultimately transformed into crystalline apatite. It is important to note that, in this study, the authors found that the composition of the clusters differs from the originally proposed by Posner.[112]

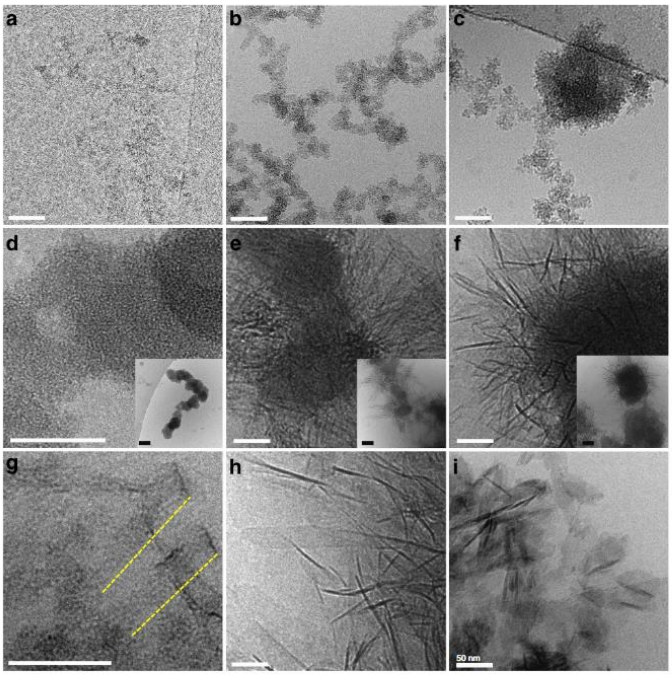

Figure 1.15 | *In situ* cryo-TEM observation of calcium phosphate transformation. (a) polymeric network from nanometre-sized units (0-2 min), (b) branched polymeric assemblies (2–20 min), (c) nodules (10–20 min), (d) amorphous spheres (15–60 min), (e) aggregated spheres+ribbons (60–80 min), (f) ribbons (80–110 min), (g) direct assembly of ribbons from polymeric aggregates (60–110 min) (lines denote alignment of complexes), (h) elongated plates (4110 min), (i) plates (1 month), scale bar, 50 nm (insets are lower magnification images: scale bar, 100 nm). Figures Reprinted with permission from Ref. 112, Copyright 2013 Springer Nature.

Apart from these *in vitro* demonstrations, the formation of a transient amorphous phase is thought to be a common strategy in biomineralization to transport the ionic precursors to the crystallization site. A transient ACP phase was identified in zebrafish fish bones, mouse enamel, in rat calvaria, and long bones.

The function of collagen and non-collagenous proteins used to be neglect during the first investigations of bone mineralization. Only over the last decades these proteins started to be considered as active components rather than only matrices for mineral deposition.[113] With respect to collagen, it remains a matter of debate whether the nucleation starts within the confined spaces provided by the gap-zone, i.e, intrafibrillar mineralization, or between the fibrils, i.e, extrafibrillar mineralization.[100] According to the intrafibrillar model, in the early stages of calcification, apatite or an amorphous precursor is deposited within the gap zones and then spanned across the fibrils giving rise to banding patterns.[114]

Even though non-collagenous proteins are not related to the mechanical features of bone they are considered as important regulators of osteogenesis.[115] In a general way, non-collagenous proteins are thought to be needed for inhibiting the pathological calcification in solution and promoting the intrafibrillar mineralization.[116,117] These functions have been ascribed to their acidic residues, which accumulate calcium ions and interact with collagen. Therefore, polyanionic molecules rich in carboxylate groups, specially poly-aspartate, have been used in biomineralization studies as analogous of non-collagenous proteins.[118] These molecules were shown to stabilize ACP promoting its infiltration within the intrafibrillar spaces of collagen.[119]

Laurie Grower developed a polymer-induced liquid-precursor (PILP) hypothesis for calcium carbonate mineralization which was extended for calcium phosphate collagen systems.[120] Accordingly, charged polymers stabilize ACP as a fluid (PILP) in a liquid medium leading to liquid-liquid phase separation. By means of capillarity this ACP precursor infiltrates into the gap zones of collagen fibrils and then solidifies and crystallizes into apatite. In this context, several studies have reported the needing of polyanionic analogs of non-collagenous proteins to guide the intrafibrillar mineralization.[120]

Fabio Nudelman from Nico Sommerdjik group has undertaken cryo-TEM investigations relying on low concentrated fibrillar collagen to show that non-collagenous proteins and collagen act in synergy to control the intrafibrillar mineralization (Figure 1.16).[121] The study showed that non-collagenous proteins (represented by polyaspartic acid) form negatively charged complexes with ACP which infiltrates the gaps within the fibrils by interaction with the positively charged domains of the collagen molecules. The gap zones act as structural template for controlling the conversion of ACP into oriented apatite crystals along the axis of the fibril. Conversely, Deshpande and Beniash showed that non collagenous proteins attach to collagen promoting local supersaturation of calcium ions thus suggesting that nucleation of apatite takes place directly in the fibril and not in complexes in solution.[122]

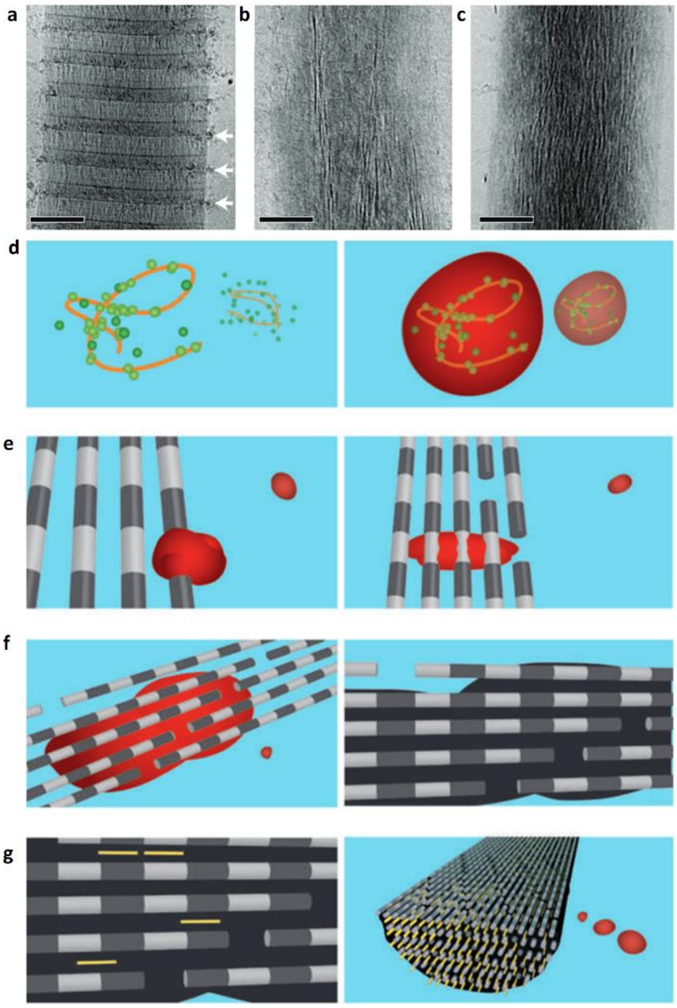

Figure 1.16 | Cryo-TEM images of collagen at different stages of mineralization in the presence of 10 μg ml^{-1} of poly(aspartic acid): after 24 h of mineralization calcium phosphate particles were found outside the fibril (a), after 48 h, apatite crystals started to develop within the fibril (b) and after 72 h, elongated crystals extended over the fibril (c). The collagen fibrils deformed as de mineral developed and the banding patterns were not visible. Scale bars: 100 nm. Mechanism of collagen fibril mineralization (d-g). The mineralization of collagen fibril starts with the formation of calcium phosphate clusters (green) which complex with the polyaspartate (orange line), forming stable mineral droplets (d). Mineral droplets bind to a distinct region on the collagen and enter the fibril (e). Once inside the collagen, the mineral in a liquid state diffuses through the interior of the fibril and solidifies into a disordered an amorphous phase (black) (f). Finally, directed by the collagen, the amorphous mineral is converted into oriented apatite crystals (yellow) (g). Reprinted with permission from (a-c) Ref.121, Copyright 2010 Springer Nature and (d-g) Ref.123, Copyright 2010 Springer Nature.

Strikingly, the group of Nadine Nassif achieved biomimetic intrafibrillar mineralization without the involvement of calcium binding polyelectrolytes *i.e* non-collagenous proteins (Figure 1.17).[85] Under a classical theory perspective, the group showed that the three-dimensional organization of collagen scaffold can initiate and orientate the growth of carbonated apatite. This was the first study to accomplish the mineralization of apatite in a tissue-like matrix of type I collagen displaying the twisted plywood geometry of bone tissue.

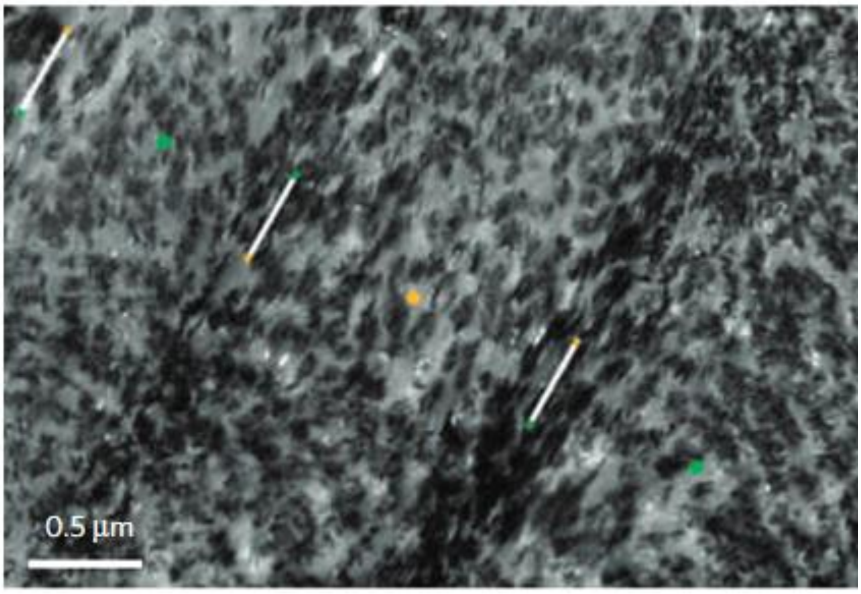

Figure 1.17 | TEM image of ultra-thin section of unstained mineralized high-concentration collagen matrix. The nanometric apatite crystals are coaligned with the collagen fibrils as indicated by the white lines. Reprinted with permission from Ref. 85, Copyright 2012 Springer Nature.

To sum up, Figure 1.18 shows the major mechanisms (including some not discussed herein) proposed by contemporary theorists to account for the mineral formation and organization within the collagen matrix in bone. These represent different means, i.e, classical and non-classical in achieving the same end: unveiling the process of bone formation.

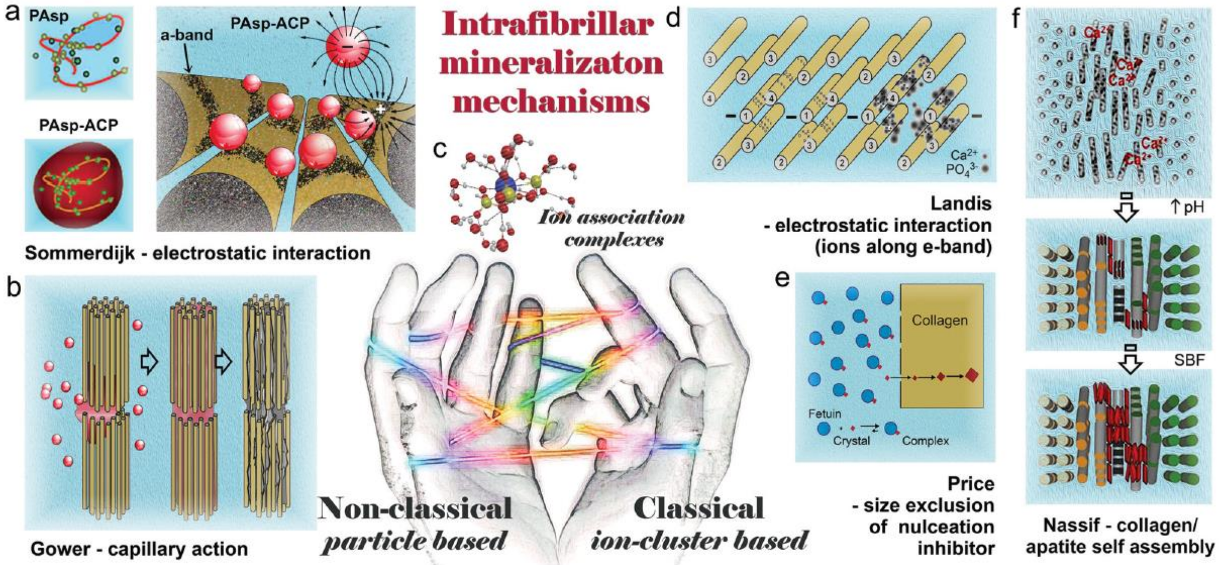

Figure 1.18 | The most important mechanisms proposed by contemporary theorists to account for the phenomenon of intrafibrillar collagen mineralization. The two hands symbolically represent the classical and non-classical nucleation theories. The colored fluorescent string that intertwines between the fingers symbolically depicts how the discovery of ion association complexes offers a potential link to unite the two nucleation theories. Of these mechanisms, the electrostatic attraction mechanism proposed by the Landis, size exclusion of nucleation inhibitors proposed by Price and the mechanism of collagen/apatite self-assembly proposed by Nassif are more inclined to be related to the classical nucleation theory, as represented by the right hand in the figure. By contrast, the capillary action of mineralization precursors proposed by Gower and the electrostatic interaction mechanism proposed by Sommerdijk are perceivably accountable by the non-classical crystallization theory, as represented by the left hand in the figure. PAsp: poly(aspartic acid). Reprinted with permission from Ref. 100, 2016 Copyright WILEY-VCH Verlag GmbH & Co.

1.3 | Objectives

General objectives

1. To develop biomimetic models to understand the impact of Sr^{2+} on (i) the mechanisms of bone mineralization (ii) the physicochemical properties of bone.

2. To synthesize and characterize bioactive Sr^{2+} phosphates and carbonates and to evaluate their effects on osteoblasts

Specific objectives

1. To evaluate the impacts of Sr^{2+} on the physicochemical properties of biomimetic apatite

2. To study the formation of dense and organized collagen matrices mineralized with biomimetic apatite in the presence of Sr^{2+}

3. To evaluate the role of Sr^{2+} on the formation of calcium phosphates and carbonates in confined environment provided by the pores of polycarbonate track-etched membranes

4. To synthesize Sr^{2+} containing calcium phosphate and carbonate particles with controlled morphology and size to design bioactive particle potentially applied for bone regeneration

This thesis was organized in 7 chapters. In the **Chapter 1** we presented the basic principles of biomineralization that drove this investigation. Next, in the **Chapter 2** we developed a biomimetic model of Sr^{2+}- containing apatite in which high concentrations of this ion led to the formation of an amorphous calcium strontium phosphate phase Sr(ACP). In the **Chapter 3** we evaluated the response of Sr(ACP) to physiological environment. In the **Chapter 4** we investigated the impacts of Sr^{2+} on a model based on a mineralized collagen matrix which mimics the bone tissue in terms of density and organization. In the **Chapter 5** we described the role of $Sr^{2+}$and confinement in the formation of apatite. In the **Chapter 6** the formation of calcium carbonate in confinement in the presence of Sr^{2+} was investigated. Moreover, the particles formed in confinement had their bioactivity and toxicity evaluated. Finally, the major achievements and perspectives of this thesis were outlined in the **Chapter 7.**

1.4 | References

(1) Lowenstam, H. A., and Weiner, S. *On Biomineralization.*; Oxford University Press on Demand, 1989.

(2) Addadi, L.; Weiner, S. Biomineralization: Mineral Formation by Organisms. *Phys. Scr.* **2014**, *89* (9), 0980003.

(3) Arakaki, A.; Nakazawa, H.; Nemoto, M.; Mori, T.; Matsunaga, T. Formation of Magnetite by Bacteria and Its Application. *J. R. Soc. Interface* **2008**, *5* (26), 977–999.

(4) Lefèvre, C. T.; Menguy, N.; Abreu, F.; Lins, U.; Pósfai, M.; Prozorov, T.; Pignol, D.; Frankel, R. B.; Bazylinski, D. A. A Cultured Greigite-Producing Magnetotactic Bacterium in a Novel Group of Sulfate-Reducing Bacteria. *Science.* **2011**, *334* (6063), 1720–1723.

(5) Hildebrand, M. Diatoms, Biomineralization Processes, and Genomics. *Chem. Rev.* **2008**, *108* (11), 4855–4874.

(6) Wagner, R. C.; Jungck, J. R.; Van Loo, D. Sub-Micrometer X-Ray Tomography of Radiolarians: Computer Modeling and Skeletonization. *Micros. Today* **2015**, *23* (5), 18–23.

(7) Meldrum, F. C. Calcium Carbonate in Biomineralisation and Biomimetic Chemistry. *Int. Mater. Rev.* **2003**, *48* (3), 187–224.

(8) Plummer, L. N.; Busenberg, E. The Solubilities of Calcite, Aragonite and Vaterite in CO_2-H_2O Solutions between 0 and 90°C, and an Evaluation of the Aqueous Model for the System $CaCO_3$-CO_2-H_2O. *Geochim. Cosmochim. Acta* **1982**, *46* (6), 1011–1040.

(9) Jamieson, J. C. Phase Equilibrium in the System Calcite-Aragonite. *J. Chem. Phys.* **1953**, *21* (8), 1385–1390.

(10) Zou, Z.; Habraken, W. J. E. M.; Matveeva, G.; Jensen, A. C. S.; Bertinetti, L.; Hood, M. A.; Sun, C.; Gilbert, P. U. P. A.; Polishchuk, I.; Pokroy, B.; et al. A Hydrated Crystalline Calcium Carbonate Phase: Calcium Carbonate Hemihydrate. *Science.* **2019**, *363* (6425), 396–400.

(11) Addadi, L.; Raz, S.; Weiner, S. Taking Advantage of Disorder: Amorphous Calcium Carbonate and Its Roles in Biomineralization. *Advanced Materials*. **2003**,15 (12), 959–970.

(12) Mirabello, G.; Lenders, J. J. M.; Sommerdijk, N. A. J. M. Bioinspired Synthesis of Magnetite Nanoparticles. *Chem. Soc. Rev.* **2016**, *45* (18), 5085–5106.

(13) Wang, Q.; Nemoto, M.; Li, D.; Weaver, J. C.; Weden, B.; Stegemeier, J.; Bozhilov, K. N.; Wood, L. R.; Milliron, G. W.; Kim, C. S.; et al. Phase Transformations and Structural Developments in the Radular Teeth of Cryptochiton Stelleri. *Adv. Funct. Mater.* **2013**, *23* (23), 2908–2917.

(14) Sone, E. D.; Weiner, S.; Addadi, L. Biomineralization of Limpet Teeth: A Cryo-TEM Study of the Organic Matrix and the Onset of Mineral Deposition. *J. Struct. Biol.* **2007**, *158* (3), 428–444.

(15) Kröger, N. Prescribing Diatom Morphology: Toward Genetic Engineering of Biological Nanomaterials. *Curr. Opin. Chem. Biol.* **2007**, *11* (6), 662–669.

(16) Vallet-Regí, M.; Arcos, D. A. Biological Apatites in Bone and Teeth. *Nanoceramics in clinical use: From materials to applications*. **2016**, 39, 1–24.

(17) Aizenberg, J.; Tkachenko, A.; Weiner, S.; Addadi, L.; Hendler, G. Calcitic Microlenses as Part of the Photoreceptor System in Brittlestars. *Nature* **2001**, *412* (6849), 819–822.

(18) Addadi, L.; Joester, D.; Nudelman, F.; Weiner, S. Mollusk Shell Formation: A Source of New Concepts for Understanding Biomineralization Processes. *Chem. - A Eur. J.* **2006**, *12* (4), 980–987.

(19) Naleway, S. E.; Taylor, J. R. A.; Porter, M. M.; Meyers, M. A.; McKittrick, J. Structure and Mechanical Properties of Selected Protective Systems in Marine Organisms. *Mater. Sci. Eng. C* **2016**, *59*, 1143–1167.

(20) Von Euw, S.; Zhang, Q.; Manichev, V.; Murali, N.; Gross, J.; Feldman, L. C.; Gustafsson, T.; Flach, C.; Mendelsohn, R.; Falkowski, P. G. Biological Control of Aragonite Formation in Stony Corals. *Science* . **2017**, *356* (6341), 933–938.

(21) Yeom, B.; Sain, T.; Lacevic, N.; Bukharina, D.; Cha, S. H.; Waas, A. M.; Arruda, E. M.; Kotov, N. A. Abiotic Tooth Enamel. *Nature* **2017**, *543* (7643), 95–98.

(22) Knoll, A. H. Biomineralization and Evolutionary History. *Rev. Mineral. Geochemistry* **2003**, *54* (1), 329–356.

(23) Mann, S. Molecular Tectonics in Biomineralization and Biomimetic Materials Chemistry. *Nature* **1993**, *365* (6446), 499–505.

(24) Walsh, D.; Hopwood, J. D.; Mann, S. Crystal Tectonics: Construction of Reticulated Calcium Phosphate Frameworks in Bicontinuous Reverse Microemulsions. *Science (80-.).* **1994**, *264* (5165), 1576–1578.

(25) Mann, S. Molecular Recognition in Biomineralization. *Nature* **1988**, *332* (6160), 119–124.

(26) Gower, L. B. Biomimetic Model Systems for Investigating the Amorphous Precursor Pathway and Its Role in Biomineralization. *Chem. Rev.* **2008**, *108* (11), 4551–4627.

(27) Wang, Y. W.; Christenson, H. K.; Meldrum, F. C. Confinement Increases the Lifetimes of Hydroxyapatite Precursors. *Chem. Mater.* **2014**, *26* (20), 5830–5838.

(28) Whittaker, M. L.; Dove, P. M.; Joester, D. Nucleation on Surfaces and in Confinement. *MRS Bull.* **2016**, *41* (5), 388–392.

(29) Gong, X.; Wang, Y. W.; Ihli, J.; Kim, Y. Y.; Li, S.; Walshaw, R.; Chen, L.; Meldrum, F. C. The Crystal Hotel: A Microfluidic Approach to Biomimetic Crystallization. *Adv. Mater.* **2015**, *27* (45), 7395–7400.

(30) Loste, E.; Park, R. J.; Warren, J.; Meldrum, F. C. Precipitation of Calcium Carbonate in Confinement. *Adv. Funct. Mater.* **2004**, *14* (12), 1211–1220.

(31) Ihli, J.; Wang, Y.-W.; Cantaert, B.; Kim, Y.-Y.; Green, D. C.; Bomans, P. H. H.; Sommerdijk, N. A. J. M.; Meldrum, F. C. Precipitation of Amorphous Calcium Oxalate in Aqueous Solution. *Chem. Mater.* **2015**, *27* (11), 3999–4007.

(32) Wang, Y. W.; Christenson, H. K.; Meldrum, F. C. Confinement Leads to Control over Calcium Sulfate Polymorph. *Adv. Funct. Mater.* **2013**, *23* (45), 5615–5623.

(33) Cantaert, B.; Beniash, E.; Meldrum, F. C. The Role of Poly(Aspartic Acid) in the Precipitation of Calcium Phosphate in Confinement. *J. Mater. Chem. B* **2013**, *1* (48), 6586–6595.

(34) Cantaert, B.; Beniash, E.; Meldrum, F. C. Nanoscale Confinement Controls the Crystallization of Calcium Phosphate: Relevance to Bone Formation. *Chem. - A Eur. J.* **2013**, *19* (44), 14918–14924.

(35) Stephens, C. J.; Ladden, S. F.; Meldrum, F. C.; Christenson, H. K. Amorphous Calcium Carbonate Is Stabilized in Confinement. *Adv. Funct. Mater.* **2010**, *20* (13), 2108–2115.

(36) Anduix-Canto, C.; Kim, Y. Y.; Wang, Y. W.; Kulak, A.; Meldrum, F. C.; Christenson, H. K. Effect of Nanoscale Confinement on the Crystallization of Potassium Ferrocyanide. *Cryst. Growth Des.* **2016**, *16* (9), 5403–5411.

(37) Ha, J. M.; Wolf, J. H.; Hillmyer, M. A.; Ward, M. D. Polymorph Selectivity under Nanoscopic Confinement. *J. Am. Chem. Soc.* **2004**, *126* (11), 3382–3383.

(38) Kim, Y. Y.; Hetherington, N. B. J.; Noel, E. H.; Kröger, R.; Charnock, J. M.;

Christenson, H. K.; Meldrum, F. C. Capillarity Creates Single-Crystal Calcite Nanowires from Amorphous Calcium Carbonate. *Angew. Chemie - Int. Ed.* **2011**, *50* (52), 12572–12577.

(39) Wang, Y.; Zeng, M.; Meldrum, F. C.; Christenson, H. K. Using Confinement to Study the Crystallization Pathway of Calcium Carbonate. *Cryst. Growth Des.* **2017**, *17* (12), 6787–6792.

(40) Schenk, A. S.; Albarracin, E. J.; Kim, Y.-Y.; Ihli, J.; Meldrum, F. C. Confinement Stabilises Single Crystal Vaterite Rods. *Chem. Commun.* **2014**, *50* (36), 4729–4732.

(41) Zeng, M.; Kim, Y. Y.; Anduix-Canto, C.; Frontera, C.; Laundy, D.; Kapur, N.; Christenson, H. K.; Meldrum, F. C. Confinement Generates Single-Crystal Aragonite Rods at Room Temperature. *Proc. Natl. Acad. Sci. U. S. A.* **2018**, *115* (30), 7670–7675.

(42) Xu, Y.; Sommerdijk, N. A. J. M. Aragonite Formation in Confinements: A Step toward Understanding Polymorph Control. *Proc. Natl. Acad. Sci. U. S. A.* **2018**, *115* (34), 8469–8471.

(43) Tester, C. C.; Wu, C.-H.; Weigand, S.; Joester, D. Precipitation of ACC in Liposomes—a Model for Biomineralization in Confined Volumes. *Faraday Discuss.* **2012**, *159*, 345.

(44) Greil, B. P. Advanced Materials Progress Report on Microporous and Mesoporous Material. *Adv. Mater.* **2002**, *14* (10), 709–716.

(45) De Yoreo, J. J.; N. A. J. M., S. Investigating Materials Formation with Liquid-Phase and Cryogenic TEM. *Nat. Rev. Mater.* **2016**, *1* (8), 16035.

(46) Liu, Z.; Zhang, Z.; Ritchie, R. O. On the Materials Science of Nature's Arms Race. *Adv. Mater.* **2018**, *30* (32), 1–16.

(47) de Souza, I. D.; Cruz, M. A. E.; de Faria, A. N.; Zancanela, D. C.; Simão, A. M. S.; Ciancaglini, P.; Ramos, A. P. Formation of Carbonated Hydroxyapatite Films on Metallic Surfaces Using Dihexadecyl Phosphate-LB Film as Template. *Colloids Surf. B. Biointerfaces* **2014**, *118*, 31–40.

(48) Tovani, C. B.; Faria, A. N.; Ciancaglini, P.; Ramos, A. P. Collagen-Supported $CaCO_3$ Cylindrical Particles Enhance Ti Bioactivity. *Surf. Coatings Technol.* **2019**, *358*, 858–864.

(49) Tovani, C. B.; Zancanela, D. C.; Faria, A. N.; Ciancaglini, P.; Ramos, A. P. Bio-Inspired Synthesis of Hybrid Tube-like Structures Based on $CaCO_3$ and Type I-Collagen. *RSC Adv.* **2016**, *6* (93), 90509–90515.

(50) Weiner, S.; Traub, W.; Wagner, H. D. Lamellar Bone: Structure-Function Relations. *J. Struct. Biol.* **1999**, *126* (3), 241–255.

(51) Su, X.; Sun, K.; Cui, F. Z.; Landis, W. J. Organization of Apatite Crystals in Human Woven Bone. *Bone* **2003**, *32* (2), 150–162.

(52) Reznikov, N.; Bilton, M.; Lari, L.; Stevens, M. M.; Kröger, R. Fractal-like Hierarchical Organization of Bone Begins at the Nanoscale. *Science.* **2018**, *360* (6388), eaao2189.

(53) Weiner, S.; Wagner, H. D. The Material Bone: Structure-Mechanical Function Relations. *Annu. Rev. Mater. Sci.* **1998**, *28* (1), 271–298.

(54) Ruth, E. B. Bone Studies. I. Fibrillar Structure of Adult Human Bone. *Am. J. Anat.* **1947**, *80* (1), 35–53.

(55) Reznikov, N.; Shahar, R.; Weiner, S. Three-Dimensional Structure of Human Lamellar Bone: The Presence of Two Different Materials and New Insights into the Hierarchical Organization. *Bone* **2014**, *59*, 93–104.

(56) Reznikov, N.; Bilton, M.; Lari, L.; Stevens, M. M.; Kröger, R. Fractal-like Hierarchical Organization of Bone Begins at the Nanoscale. *Science* **2018**, *360* (6388), eaao2189.

(57) Ricard-Blum, S. The Collagen Family. *Cold Spring Harb. Perspect. Biol.* **2011**, *3* (1), 1–19.

(58) Charvolin, J.; Sadoc, J. F. Type-I Collagen Fibrils: From Growth Morphology to Local Order. *Eur. Phys. J. E* **2019**, *42* (4), 1–9.

(59) Exposito, J. Y.; Valcourt, U.; Cluzel, C.; Lethias, C. The Fibrillar Collagen Family. *Int. J. Mol. Sci.* **2010**, *11* (2), 407–426.

(60) Fessler, J. H.; Fessler, L. I. Biosynthesis of Procollagen. *Annu. Rev. Biochem.* **1978**, *47* (1), 129–162.

(61) Comper, W. D.; Veis, A. Characterization of Nuclei in *in Vitro* Collagen Fibril Formation. *Biopolymers* **1977**, *16* (10), 2133–2142.

(62) Sorushanova, A.; Delgado, L. M.; Wu, Z.; Shologu, N.; Kshirsagar, A.; Raghunath, R.; Mullen, A. M.; Bayon, Y.; Pandit, A.; Raghunath, M.; et al. The Collagen Suprafamily: From Biosynthesis to Advanced Biomaterial Development. *Adv. Mater.* **2018**, *31* (1), 1–39.

(63) Myllyharju, J.; Kivirikko, K. I. Collagens and Collagen-Related Diseases. *Ann. Med.* **2001**, *33* (1), 7–21.

(64) Ottani, V.; Martini, D.; Franchi, M.; Ruggeri, A.; Raspanti, M. Hierarchical Structures in Fibrillar Collagens. *Micron* **2002**, *33* (8), 587–596.

(65) Petruska, J. A; Hodge, A J. A subunit model for the tropocollagen macromolecule. *Proc. Natl. Acad. Sci.* **1964**, *51* (5), 871–876.

(66) Smith, J. W. Packing Arrangement of Tropocollagen Molecules. *Nature* **1965**, *205* (4969), 356–358.

(67) Orgel, J. P. R. O.; Irving, T. C.; Miller, A.; Wess, T. J. Microfibrillar Structure of Type I Collagen in Situ. *Proc. Natl. Acad. Sci. U. S. A.* **2006**, *103* (24), 9001–9005.

(68) Sherman, V. R.; Yang, W.; Meyers, M. A. The Materials Science of Collagen. *J. Mech. Behav. Biomed. Mater.* **2015**, *5*, 22–50.

(69) Solomonov, I.; Zehorai, E.; Talmi-Frank, D.; Wolf, S. G.; Shainskaya, A.; Zhuravlev, A.; Kartvelishvily, E.; Visse, R.; Levin, Y.; Kampf, N.; et al. Distinct Biological Events Generated by ECM Proteolysis by Two Homologous Collagenases. *Proc. Natl. Acad. Sci.* **2016**, *113* (39), 10884–10889.

(70) Giraud Guille, M. M.; Nassif, N.; Fernandes, F. M. Collagen-based Materials for Tissue Repair, from Bio-inspired to Biomimetic. In *Materials Design Inspired by Nature: Function through Inner Architecture*; 2013,107–127.

(71) Weiner, S.; Wagner, H. D. The Material Bone: Structure-Mechanical Function Relations. *Annu. Rev. Mater. Sci.* **1998**, *28* (1), 271–298.

(72) Giraud-Guille, M. M. Twisted Liquid Crystalline Supramolecular Arrangements in Morphogenesis. *Int. Rev. Cytol.* **1996**, *166*, 59–101.

(73) Friedel, G. Les États Mésomorphes de La Matière. *Ann. Phys. (Paris).* **1922**, *9* (18), 273–474.

(74) Garden, R. S. The structure and function of the proximal end of the femur. *J. Bone Joint Surg. Br.* **1961**, *43* (3), 576–589.

(75) Bouligand, Y. Twisted Fibrous Arrangements in Biological Materials and Cholesteric Mesophases. *Tissue Cell* **1972**, *4* (2), 189–217.

(76) Giraud-Guille, M. M. Twisted Plywood Architecture of Collagen Fibrils in Human Compact Bone Osteons. *Calcif. Tissue Int.* **1988**, *42* (3), 167–180.

(77) Mosser, G.; Anglo, A.; Helary, C.; Bouligand, Y.; Giraud-Guille, M. M. Dense Tissue-like Collagen Matrices Formed in Cell-Free Conditions. *Matrix Biol.* **2006**, *25* (1), 3–13.

(78) Giraud-Guille, M. M. Liquid Crystallinity in Condensed Type I Collagen Solutions. A Clue

to the Packing of Collagen in Extracellular Matrices. *J. Mol. Biol.* **1992**, *224* (3), 861–873.

(79) Besseau, L.; Giraud-Guille, M. M. Stabilization of Fluid Cholesteric Phases of Collagen to Ordered Gelated Matrices. *J. Mol. Biol.* **1995**, *251* (2), 197–202.

(80) Bouligand, Y.; Giraud-Guille, M.-M. Spatial Organization of Collagen Fibrils in Skeletal Tissues: Analogies with Liquid Crystals. In *Biology of Invertebrate and Lower Vertebrate Collagens*; Springer US: Boston, MA, 1985,15–134.

(81) Giraud-Guille, M. M.; Besseau, L. Banded Patterns in Liquid Crystalline Phases of Type I Collagen: Relationship with Crimp Morphology in Connective Tissue Architecture. *Connect. Tissue Res.* **1998**, *37* (4), 183–193.

(82) Belamie, E.; Mosser, G.; Gobeaux, F.; Giraud-Guille, M. M. Possible Transient Liquid Crystal Phase during the Laying out of Connective Tissues: α-Chitin and Collagen as Models. *J. Phys. Condens. Matter* **2006**, *18* (13).

(83) Hulmes, D. J.; Bruns, R. R.; Gross, J. On the State of Aggregation of Newly Secreted Procollagen. *Proc. Natl. Acad. Sci.* **1983**, *80* (2), 388–392.

(84) Martin, R.; Farjanel, J.; Eichenberger, D.; Colige, A.; Kessler, E.; Hulmes, D. J. S.; Giraud-Guille, M. M. Liquid Crystalline Ordering of Procollagen as a Determinant of Three-Dimensional Extracellular Matrix Architecture. *J. Mol. Biol.* **2000**, *301* (1), 11–17.

(85) Wang, Y.; Azaïs, T.; Robin, M.; Vallée, A.; Catania, C.; Legriel, P.; Pehau-Arnaudet, G.; Babonneau, F.; Giraud-Guille, M. M.; Nassif, N. The Predominant Role of Collagen in the Nucleation, Growth, Structure and Orientation of Bone Apatite. *Nat. Mater.* **2012**, *11* (8), 724–733.

(86) Nassif, N.; Gobeaux, F.; Seto, J.; Belamie, E.; Davidson, P.; Panine, P.; Mosser, G.; Fratzl, P.; Giraud Guille, M. M. Self-Assembled Collagen-Apatite Matrix with Bone-like Hierarchy. *Chem. Mater.* **2010**, *22* (11), 3307–3309.

(87) Wang, Y.; Silvent, J.; Robin, M.; Babonneau, F.; Meddahi-Pellé, A.; Nassif, N.; Giraud Guille, M. M. Controlled Collagen Assembly to Build Dense Tissue-like Materials for Tissue Engineering. *Soft Matter* **2011**, 7 (20), 9659–9664.

(88) Lama, M.; Fernandes, F. M.; Marcellan, A.; Peltzer, J.; Trouillas, M.; Banzet, S.; Grosbot, M.; Sanchez, C.; Giraud-Guille, M. M.; Lataillade, J. J.; et al. Self-Assembled Collagen Microparticles by Aerosol as a Versatile Platform for Injectable Anisotropic Materials. *Small* **2019**, *1902224*, 1–8.

(89) Ling, S.; Kaplan, D. L.; Buehler, M. J. Nanofibrils in Nature and Materials Engineering. *Nat. Rev. Mater.* **2018**, *3 (4)*, 1–15.

(90) Weaver, J. C.; Milliron, G. W.; Miserez, A.; Evans-Lutterodt, K.; Herrera, S.; Gallana, I.; Mershon, W. J.; Swanson, B.; Zavattieri, P.; DiMasi, E.; et al. The Stomatopod Dactyl Club: A Formidable Damage-Tolerant Biological Hammer. *Science.* **2012**, *336* (6086), 1275–1280.

(91) Vignolini, S.; Rudall, P. J.; Rowland, A. V.; Reed, A.; Moyroud, E.; Faden, R. B.; Baumberg, J. J.; Glover, B. J.; Steiner, U. Pointillist Structural Color in Pollia Fruit. *Proc. Natl. Acad. Sci. U. S. A.* **2012**, *109* (39), 15712–15715.

(92) Finlayson, E. D.; McDonald, L. T.; Vukusic, P. Optically Ambidextrous Circularly Polarized Reflection from the Chiral Cuticle of the Scarab Beetle Chrysina Resplendens. *J. R. Soc. Interface* **2017**, *14* (131), 20170129.

(93) Rey, C.; Combes, C.; Drouet, C.; Glimcher, M. J. Bone Mineral: Update on Chemical Composition and Structure. *Osteoporos. Int.* **2009**, *20* (12), 2155–2155.

(94) Penel, G.; Leroy, G.; Rey, C.; Bres, E. MicroRaman Spectral Study of the PO_4 and CO_3

Vibrational Modes in Synthetic and Biological Apatites. *Calcif. Tissue Int.* **1998**, *63* (6), 475–481.

(95) Wang, Y.; Von Euw, S.; Fernandes, F. M.; Cassaignon, S.; Selmane, M.; Laurent, G.; Pehau-Arnaudet, G.; Coelho, C.; Bonhomme-Coury, L.; Giraud-Guille, M. M.; et al. Water-Mediated Structuring of Bone Apatite. *Nat. Mater.* **2013**, *12* (12), 1144–1153.

(96) Wang, Y.; Von Euw, S.; Laurent, G.; Crevant, C.; Bonhomme-Coury, L.; Giraud-Guille, M. M.; Babonneau, F.; Nassif, N.; Azaïs, T. Impact of Collagen Confinement vs. Ionic Substitutions on the Local Disorder in Bone and Biomimetic Apatites. *Mater. Horizons* **2014**, *1* (2), 224–231.

(97) Bembey, A. K.; Bushby, A. J.; Boyde, A.; Ferguson, V. L.; Oyen, M. L. Hydration Effects on the Micro-Mechanical Properties of Bone. *J. Mater. Res.* **2006**, *21* (8), 1962–1968.

(98) Cowin, S. C. Bone Poroelasticity. *J. Biomech.* **1999**, *32* (3), 217–238.

(99) Rey, C.; Combes, C.; Drouet, C.; Glimcher, M. J. Bone Mineral: Update on Chemical Composition and Structure. *Osteoporos. Int.* **2009**, *20* (6), 1013–1021.

(100) Jiao, K.; Niu, L. N.; Ma, C. F.; Huang, X. Q.; Pei, D. D.; Luo, T.; Huang, Q.; Chen, J. H.; Tay, F. R. Complementarity and Uncertainty in Intrafibrillar Mineralization of Collagen. *Adv. Funct. Mat*. 2016, 26(38) 6858–6875.

(101) Erdemir, D.; Lee, A. Y.; Myerson, A. S. Nucleation of Crystals from Solution: Classical and Two-Step Models. *Acc. Chem. Res.* **2009**, *42* (5), 621–629.

(102) De Yoreo, J. J.; Gilbert, P. U. P. A.; Sommerdijk, N. A. J. M.; Penn, R. L.; Whitelam, S.; Joester, D.; Zhang, H.; Rimer, J. D.; Navrotsky, A.; Banfield, J. F.; et al. Crystallization by Particle Attachment in Synthetic, Biogenic, and Geologic Environments. *Science.* **2015**, *349* (6247), 0006760.

(103) Rao, A.; Cölfen, H. From Solute, Fluidic and Particulate Precursors to Complex Organizations of Matter. *Chem. Rev.* **2018**, *18* (8), 1203–1221.

(104) Meldrum, F. C.; Sear, R. P. Now You See Them. *Science* **2008**, *322* (5909), 1802–1803.

(105) Meldrum, F. C.; Cölfen, H. Controlling Mineral Morphologies and Structures in Biological and Synthetic Systems. *Chem. Rev.* **2008**, *108* (11), 4332–4432.

(106) Nancollas, G. H. Phase Tranformation During Precipitation of Calcium Salts. In *Biological Mineralization and Demineralization*; Springer Berlin Heidelberg: Berlin, Heidelberg, 1982,79–99.

(107) Zhang, T. H.; Liu, X. Y. How Does a Transient Amorphous Precursor Template Crystallization. *J. Am. Chem. Soc.* **2007**, *129* (44), 13520–13526.

(108) Termine, J. D.; Posner, A. S. Infrared Analysis of Rat Bone: Age Dependency of Amorphous and Crystalline Mineral Fractions. *Science* **1966**, *153* (3743), 1523–1525.

(109) Gebauer, D.; Kellermeier, M.; Gale, J. D.; Bergström, L.; Cölfen, H. Prenucleation Clusters as Solute Precursors in Crystallisation. *Chem. Soc. Rev.* **2014**, *43* (7), 2348–2371.

(110) Smeets, P. J. M.; Finney, A. R.; Habraken, W. J. E. M.; Nudelman, F.; Friedrich, H.; Laven, J.; De Yoreo, J. J.; Rodger, P. M.; Sommerdijk, N. A. J. M. A Classical View on Nonclassical Nucleation. *Proc. Natl. Acad. Sci. U. S. A.* **2017**, *114* (38), 7882–7890.

(111) Dey, A.; Bomans, P. H. H.; Müller, F. A.; Will, J.; Frederik, P. M.; De With, G.; Sommerdijk, N. A. J. M. The Role of Prenucleation Clusters in Surface-Induced Calcium Phosphate Crystallization. *Nat. Mater.* **2010**, *9* (12), 1010–1014.

(112) Habraken, W. J. E. M.; Tao, J.; Brylka, L. J.; Friedrich, H.; Bertinetti, L.; Schenk, A. S.; Verch, A.; Dmitrovic, V.; Bomans, P. H. H.; Frederik, P. M.; et al. Ion-Association Complexes Unite Classical and Non-Classical Theories for the Biomimetic Nucleation of

Calcium Phosphate. *Nat. Commun.* **2013**, *4* (1),1-12.

(113) Nudelman, F.; Lausch, A. J.; Sommerdijk, N. A. J. M.; Sone, E. D. *In Vitro* Models of Collagen Biomineralization. *J. Struct. Biol.* **2013**, *183* (2), 258–269.

(114) Niu, L. N.; Jee, S. E.; Jiao, K.; Tonggu, L.; Li, M.; Wang, L.; Yang, Y. D.; Bian, J. H.; Breschi, L.; Jang, S. S.; et al. Collagen Intrafibrillar Mineralization as a Result of the Balance between Osmotic Equilibrium and Electroneutrality. *Nat. Mater.* **2017**, *16* (3), 370–378.

(115) Ibsen, C. J. S.; Gebauer, D.; Birkedal, H. Osteopontin Stabilizes Metastable States Prior to Nucleation during Apatite Formation. *Chem. Mater.* **2016**, *28* (23), 8550–8555.

(116) Brylka, L.; Jahnen-Dechent, W. The Role of Fetuin-A in Physiological and Pathological Mineralization. *Calcif. Tissue Int.* **2013**, *93* (4), 355–364.

(117) Boskey, A. L. Noncollagenous Matrix Proteins and Their Role in Mineralization. *Bone Miner.* **1989**, *6* (2), 111–123.

(118) Krogstad, D. V.; Wang, D.; Lin-Gibson, S. Polyaspartic Acid Concentration Controls the Rate of Calcium Phosphate Nanorod Formation in High Concentration Systems. *Biomacromolecules* **2017**, *18* (10), 3106–3113.

(119) Wu, Z.; Wang, X.; Wang, Z.; Shao, C.; Jin, X.; Zhang, L.; Pan, H.; Tang, R.; Fu, B. Self-Etch Adhesive as a Carrier for ACP Nanoprecursors to Deliver Biomimetic Remineralization. *ACS Appl. Mater. Interfaces* **2017**, *9* (21), 17710–17717.

(120) Palmer, L. C.; Newcomb, C. J.; Kaltz, S. R.; Spoerke, E. D.; Stupp, S. I. Biomimetic Systems for Hydroxyapatite Mineralization Inspired by Bone and Enamel. *Chem. Rev.* **2008**, *108* (11), 4754–4783.

(121) Nudelman, F.; Pieterse, K.; George, A.; Bomans, P. H. H.; Friedrich, H.; Brylka, L. J.; Hilbers, P. A. J.; De With, G.; Sommerdijk, N. A. J. M. The Role of Collagen in Bone Apatite Formation in the Presence of Hydroxyapatite Nucleation Inhibitors. *Nat. Mater.* **2010**, *9* (12), 1004–1009.

(122) Deshpande, A. S.; Beniash, E. Bioinspired Synthesis of Mineralized Collagen Fibrils. *Cryst. Growth Des.* **2008**, *8* (8), 3084–3090.

(123) Cölfen, H. A Crystal-Clear View. *Nat. Mater.* **2010**, *9* (12), 960–961.

(124) Albéric, M.; Caspi, E. N.; Bennet, M.; Ajili, W.; Nassif, N.; Azaïs, T.; Berner, A.; Fratzl, P.; Zolotoyabko, E.; Bertinetti, L.; et al. Interplay between Calcite, Amorphous Calcium Carbonate, and Intracrystalline Organics in Sea Urchin Skeletal Elements. *Cryst. Growth Des.* **2018**, *18* (4), 2189–2201.

CHAPTER 2

Sr^{2+}- substitution in biomimetic apatite: possible effects on bone mineral

Abstract

Sr^{2+} is a key element in osteoporosis treatments, a bone disease which affects millions of people worldwide. While the effects of Sr^{2+} at the cell level have been described, the underlying impacts on the crystalline structure of bone are still unclear. To address this shortcoming, we describe in this chapter a simple and versatile procedure to study the Sr^{2+} incorporation in bone mineral. Relying on a bioinspired pathway, a series of Sr^{2+} substituted apatite that combines the major bone mineral features such as size, morphology, crystalline structure and CO_3^{2-} substitution is depicted as model to investigate how Sr^{2+} may affect chemical and physical properties of bone. Unexpectedly, at high Sr^{2+} concentrations an amorphous phase (Sr(ACP)) is stabilized rather than Sr^{2+} substituted apatite which may explain the development of skeletal diseases such as osteomalacia related to the accumulation of Sr^{2+} in bone tissue. As expected for the lower doses of Sr^{2+}, the products presented lower crystallinity and expanded cell parameters in comparison to the pure apatite. These results suggest that the heterogeneous distribution of Sr^{2+} in bone is associated with regions of low structural organization. Going further, such observations give clues from the physicochemical standpoint to understand the possible impacts of Sr^{2+}on bone mineral, thus providing insights for its use in treatment of osteoporosis. (The results presented in this Chapter were obtained during the internship at LCMCP (BEPE-FAPESP) advised by Dr. Nadine Nassif).

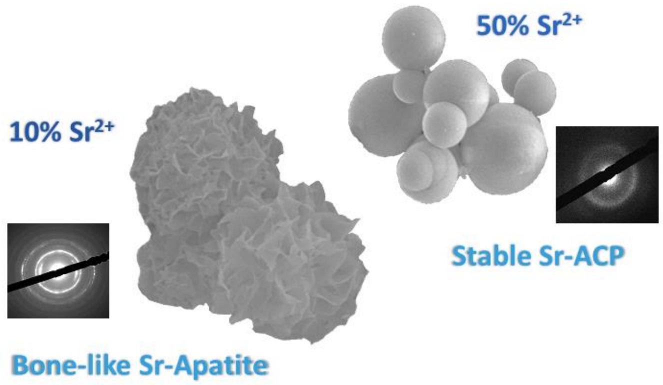

The results presented in this chapter are reproduced with permission from: Bussola Tovani, C.; Gloter, A.; Azaïs, T.; Selmane, M.; Ramos, A. P.; Nassif, N. Formation of Stable Strontium-Rich Amorphous Calcium Phosphate: Possible Effects on Bone Mineral. Acta Biomater. 2019, 92, 315–324. Copyright 2019 Elsevier.

2.1 | Introduction

Bone is a complex tissue that undergoes continuous remodeling through action of osteoblasts and osteoclasts.[1] The remodeling cycle regulates the bone architecture and mechanical properties by repairing small damages and removing old tissue.[2] Cells produce growth factors, cytokines, and proteins, which regulate the remodeling cycle.[3] Trace elements also play a role in bone mineral remodeling.[4] Among such elements, strontium has been shown to exert a dual effect on the bone regeneration dynamics: it reduces bone resorption and increases bone formation. [5] Sr^{2+} preferentially accumulates in the bone tissue (99% of the total amount of Sr^{2+} in the body): Sr^{2+} and Ca^{2+} have similar charge-to-size ratio, so the former ion replaces the latter ion in apatite.[6] A maximum of 10-12% of Sr^{2+} is found in biological apatite after its administration.[7,8] Notably, Sr^{2+} can also substitute Ca^{2+} in the crystalline structure of other biominerals such as carbonates. [9,10]

Although Sr^{2+} is a non-essential trace element found in the human body and behaves similarly to Ca^{2+} and Mg^{2+} in physiological environment, administration of Sr^{2+} as strontium ranelate has a dual effect on bone metabolism: it stimulates osteoblast proliferation while decreasing osteoclast activity, thereby increasing bone mineral density. Such effect has not been observed for other divalent cations.[11] On the basis of this dual effect, several Sr^{2+}-based medicines and biomaterials have been developed to treat osteoporosis, a bone disease that affects hundreds of millions of people worldwide.[12–18] However, administration of Sr^{2+} has a dose-dependent impact on bone formation and high Sr^{2+} doses have been associated with the development of skeletal diseases like osteomalacia in rats with renal failure.[19–21]

Sr^{2+} incorporation into bone is heterogeneous. Higher Sr^{2+} concentrations can be found in newly formed bone and are related to locally higher metabolism. [22] For example, Sr^{2+} is exclusively incorporated into new bone of patients treated with strontium ranelate. [23] Besides its impact at the cellular level, one question remains: how does Sr^{2+} affect the mineralized bone matrix? In an attempt to understand how Sr^{2+} influences bone apatite (HA) at the crystalline structure level, several syntheses of Sr^{2+}-substituted HA have been described.[24–27]Nevertheless, bone mineral and synthetic HA have distinct features, which limits correlation between *in vitro* and *in vivo* results.

Bone HA, formed under physiological conditions, bears a hydrated amorphous shell and a core consisting of nanometric crystals with plate-like morphology [28] and preferential crystallographic orientation along the *c*-axis.[29] Furthermore, bone apatite is nonstoichiometric and can host different ions in its crystalline lattice and/or outer layer.[30]

Indeed, the structural features of bone mineral are strongly related to ion substitutions, especially replacement of PO_4^{3-} and OH^- by CO_3^{2-}, and the presence of water.[31–33]

Reproducing such bone mineral features *in vitro* remains a challenge and is vitally important for better comprehension of *in vivo* phenomena. Different attempts have been made to obtain biomimetic apatite. However, the non-physiological conditions used during the synthesis including high temperature, microwave radiation, high pressure, solid-state diffusion, organic solvents, and stabilizing agents, may give rise to products with distinct crystallinity, surface area, crystal size, and composition as compared to bioapatite.[34–39] Moreover, the experimental conditions may promote kinetic and thermodynamic controls over the reaction and select different phases and polymorphs.[31] Indeed, isomorphic Ca^{2+} substitution for Sr^{2+} in the apatite crystalline structure has been reported *in vitro* up to 100% of substitution, but the formation of such strontium apatite has not been described in biological systems.[24,40]

Heterogeneous Sr^{2+} distribution at atomic scale is another factor that hinders the evaluation of the Sr^{2+} impact on bone apatite.[6] In this sense, controlled *in vitro* bone-like systems are necessary to mimic this event and to provide insights in this regard.

To address these shortcomings, a simple and versatile procedure to study the incorporation of Sr^{2+} into bone mineral is described in this chapter. The strategy consists in using bioinspired conditions described in bone remodeling process, i.e., water at room pressure and temperature and initial low pH, to mimic the environment at the mineralizing front.[41] The influence of Sr^{2+} on the formation of biomimetic apatite was investigated by substituting Ca^{2+} ranging from 0 up to 100%. Using a combination of energy electron loss spectroscopy (EELS), ^{31}P solid state nuclear magnetic resonance spectroscopy (NMR), Raman spectroscopy, X-ray diffraction (XRD), transmission electron microscopy (TEM), and selected area electron diffraction (SAED), the resulting phosphate phases were characterized providing clues to understand the presence of bone defects upon high Sr^{2+}doses.

2.2 | Experimental procedure

2.2.1 | Synthesis of biomimetic apatite containing different amount of Sr^{2+}

Biomimetic apatite was synthesized on the basis of an approach developed by Nassif et al.[32] Briefly, stock $CaCl_2$ (110 mmol L^{-1}), $SrCl_2$ (110 mmol L^{-1}), NaH_2PO_4 (33 mmol L^{-1}), and $NaHCO_3$ (33 mmol L^{-1}) solutions were prepared by dissolving $CaCl_2.2H_2O$ (Sigma), $SrCl_2.6H_2O$ (Sigma), $NaHCO_3$ (Sigma), and NaH_2PO_4 (Sigma) in aqueous acetic acid (500 mM) solution. Mixtures containing different Sr^{2+} molar percentages (namely 0, 5, 10, 25, 50, 75, and 100%) in relation to the total number of mols of divalent cations (Ca^{2+} + Sr^{2+}) were prepared. The (Ca + Sr)/(P + C) ratio was kept constant and equal to 1.67 and pH ~ 3.5.Two flasks (35 mL, height = 50 mm) containing these solutions (20 mL) and covered with perforated (four holes) parafilm were placed in a closed desiccator. A third flask containing fresh aqueous ammonia solution (30% wt., 8 mL) was placed in the desiccator. Diffusion of $NH_3(g)$ into the flasks slowly increases the pH of the solution and triggered Sr-Ca phosphate precipitation. After reaction for one or six days (pH~11), the solids were filtered and washed with deionized water and then ethanol, to remove soluble salts, and centrifuged (6000 rpm, 10 min). The recovered powders were dried at 37 °C for three days before characterization.

2.2.2 | Characterization of the samples

X-ray diffraction analysis was carried out on a Bruker D8 X-ray diffractometer operating in the reflection mode with CuKα radiation, beam voltage of 40 kV, and beam current of 40 mA (Sorbonne Université, CNRS, Collège de France, Laboratoire Chimie de la Matière Condensée de Paris, LCMCP).The data were collected in the 2θ range of 5-80°, with steps of 0.01° and a counting time of 9 s. The interplanar distances (d-spacing) and the coherent domain length (d) were estimated in the direction of the (002) plane using the *Checkcell* software and the Scherrer equation respectively. The crystal lattice parameters were calculated using the *Checkcell* software according to the position of the diffraction peaks. Fourier-transform infrared spectra with attenuated total reflectance (ATR-FTIR) were obtained on a Perkin Elmer Spectrum One spectrophotometer in the range of 4100-550 cm^{-1} with a resolution of 1 cm^{-1} (LCMCP). Raman spectra were recorded in the range of 1200-300 cm^{-1} on a spectrophotometer Kaiser Optical Systems with a diode laser operating at λ = 785 nm as excitation source (LCMCP). Thermogravimetric analysis

(TGA) experiments were performed on a thermo-microbalance instrument (NETZSCH STA409PC) (LCMCP). The measurements were performed from room temperature to 1000°C in air atmosphere with a heating rate of 5°C/min. Scanning electron microscopy (SEM) images and energy dispersive spectroscopy (EDS) were conducted on a microscope Hitachi S-3400N under accelerating voltage of 10 kV. To this end, samples were covered with a 10-nm gold layer (LCMCP). EDS was performed using an Oxford instruments X-MAX detector (20 mm^2). To this end the samples were coated with a 10-nm carbon layer. A transmission electron microscope (TEM JEOL 2011) operating at 100 keV was used to obtain the TEM and high-resolution (HRTEM) images and the selected area electron diffraction patterns (SAED), (Université Paris Sud, Laboratoire de Physique des Solides, LPS). EDS mapping of the elements Ca, Sr, O and P was performed on a single particle by using a TEM microscope FEI TECNAI G2 F20 HRTEM operating at 200 kV. To this end, the samples were dispersed in ethanol and some drops were deposited on a lacey carbon film on copper grid. EELS spectra were acquired in a Nion STEM microscope at 200 keV (LPS). ^{1}H and ^{31}P solid-state nuclear magnetic resonance (ss NMR) experiments were conducted on an Avance 300 Bruker spectrometer operating at $\nu(^1H)$ = 300.13 MHz and $\nu(^{31}P)$ = 121.5 MHz (LCMCP). The powders were packed in 4 mm zirconia rotors and spun at 14 kHz. ^{31}P direct aquisition spectra were recorded in quantitatve conditions used a recycle delay (RD) of 60 s and a 30° pulse, the number of scans (NS) were set to 80. The 2D ^{1}H-^{31}P HetCor (hetero nuclear correlation) spectra were recorded using the following parameters RD = 2 s; contact time t_{CP} = 1 ms, NS = 32-80 for each 40-120 t_1 increments depending on the sample. The Double CP (cross polarized) $^1H \rightarrow ^{31}P \rightarrow ^1H$ MAS (magic angle spinning) NMR experiment is described elsewhere in the literature and the following parameters were used: RD = 2, $t_{CP}1$ = $t_{CP}2$ = 1 ms, NS = 2000-3000 depending on the sample.[42] The chemical shifts were referenced to H_3PO_4 85% wt. for ^{31}P (0 ppm) and adamantane for ^{1}H (0 ppm).

2.3 | Results and discussion

2.3.1 | Ca^{2+} substitution for Sr^{2+} in biomimetic HA leads to Sr(ACP) formation

This investigation started with bioinspired synthesis of HA, during which we tried to reproduce the chemical conditions found *in vivo*. The vapor diffusion approach allowed us to control pH increase through NH_3(g) dissolution in the precursor acidic solution containing the PO_4^{3-}, CO_3^{2-}, Sr^{2+}, and Ca^{2+} ions, thereby producing nanocrystalline carbonated apatite that resembled the structure of apatite found in bone and teeth.[32] Moreover, the initial low pH enabled us to study the incorporation of Sr^{2+} into HA in conditions that mimicked those found in the acidic extracellular environment where osteoclasts act during bone remodeling.[43] Table 2.1 summarizes the amount (%Sr^{2+}) incorporated into the solids as determined by SEM-EDS. Sr^{2+} incorporation was proportional to the Sr^{2+} amount added to the starting solutions.

Table 2.1 | Sr^{2+} molar percentages (% Sr^{2+}) in relation to the total number of mols of divalent cations (Ca^{2+} + Sr^{2+}) in the starting solutions and in the products, determined by SEM-EDS

%Sr^{2+} in the solution	%Sr^{2+} in the product
0	0
5	3
10	10
25	20
50	40
75	60
100	100

XRD, ATR-FTR, SEM, TEM, and Raman spectroscopy were combined to follow the Sr^{2+} impact on the HA structure. The diffraction peaks (Figure 2.1) reveal that the series of samples 0%Sr^{2+}–25%Sr^{2+} correspond to hexagonal HA (space group P63/m). The XRD patterns of the samples exhibit broad peaks, related to small crystallite size and to the presence of CO_3^{2-} ions, which are a source of structural disorder in bone (see next sections).[29] Moreover, the higher intensity of the 002 peak in relation to the pattern suggests preferential orientation and larger coherent domain along the c-axis. Such features confirm structural similarity between the bone mineral and the HA model adopted in this study, which is crucial to understand the *in vitro* results and *in vivo* events and to correlate them.

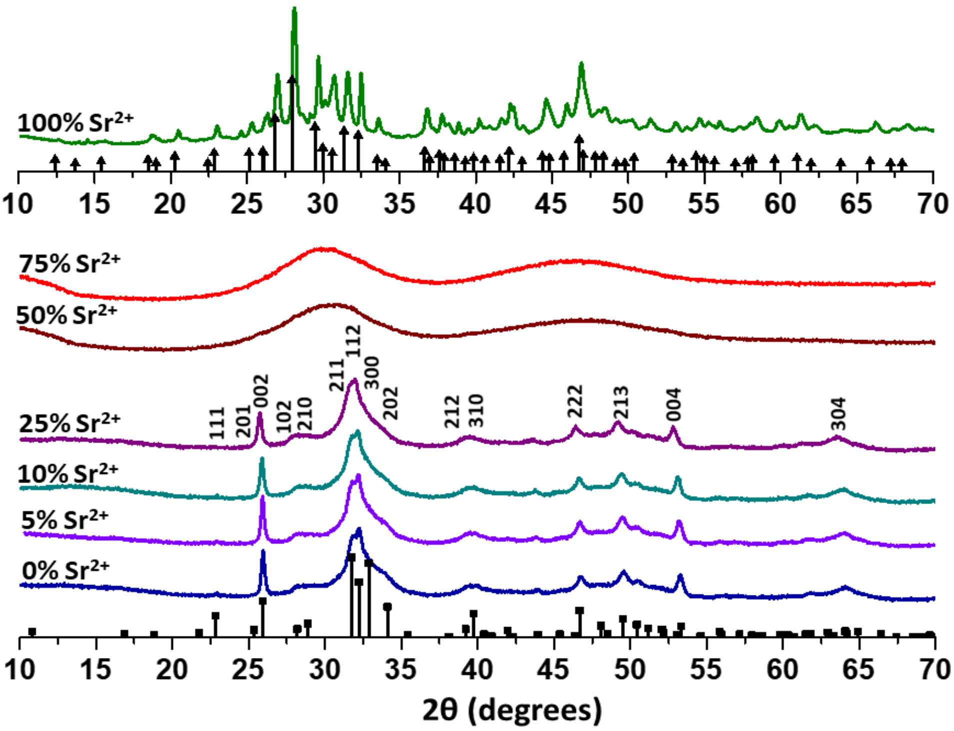

Figure 2.1 | XRD patterns for the series of samples 0–100%Sr^{2+} after six days of reaction. The peaks of the 0–25% Sr^{2+} samples are indexed with the hydroxyapatite structure (JCPDS 9-432). Sr(ACP) is observed upon increasing Sr^{2+} content in the samples (50–75% Sr^{2+}). The peaks of 100%Sr^{2+} sample are indexed with the Collin's salt structure (JCPDS 01-074-1867).

Surprisingly, the 50%Sr^{2+} and 75%Sr^{2+} samples do not display Bragg reflections, indicating the precipitation of an amorphous phase and inhibition of HA formation. In the case of the 100%Sr^{2+} sample, a well crystallized phase indexed as Collin's salt ($Sr_6H_3(PO_4)_5.2H_2O$) arose instead of the fully Sr^{2+}-substituted HA. The (002) Bragg reflections in the XRD patterns (Figure 2.2) of the samples 0%Sr^{2+}–25%Sr^{2+} shifted linearly to lower 2θ values with increased Sr^{2+} content, indicating that the interplanar distances and hence the lattice parameters augmented.

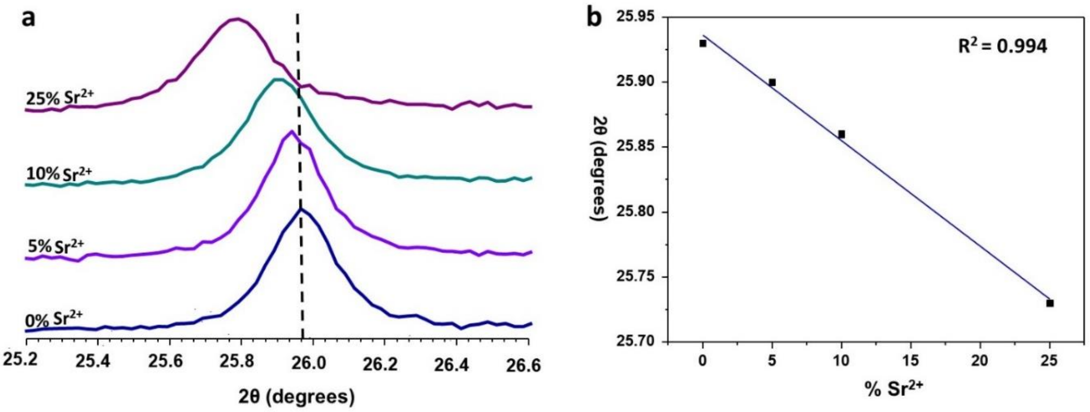

Figure 2.2 | (a) Enlarged XRD patterns of the series of samples 0-25%Sr^{2+} showing the displacement of the 002 peak to lower 2θ values upon increasing Sr^{2+} content in the samples. (b) Position of the 002 peaks as a function of the Sr^{2+} content (molar percentage).

Indeed, estimation of the interplanar distance (Table 2.2) along the 002 plane and the lattice parameters demonstrates that Ca^{2+} replacement with Sr^{2+} in apatite expands the unit cell, which agrees with the larger Sr^{2+}ionic radius. Even though Ca^{2+} replacement with Sr^{2+} provokes crystal strain, the apatite structure is maintained up to the 25%Sr^{2+} sample.

Table 2.2 | Crystallite Size (d), interplanar distance (d-spacing), lattice parameter (a and c), and unit cell volume (V) obtained from the XRD patterns of the series of samples 0-25%Sr^{2+} after six days of reaction

Sample	d (nm)	d-spacing (Å)	a(Å)	c(Å)	V(Å^3)
0% Sr^{2+}	32.3	3.43	9.43	6.87	529
5% Sr^{2+}	31.4	3.44	9.43	6.88	530
10% Sr^{2+}	30.5	3.44	9.43	6.89	531
25% Sr^{2+}	27.6	3.45	9.46	6.91	537

The Raman spectra of the HA samples, 5%Sr^{2+}, 10%Sr^{2+}, and 25%Sr^{2+}, (Figure 2.3a) evidences a linear shift in the wavenumber values of the ν_1 band assigned to the symmetric stretching of PO_4^{3-}, as compared to the spectrum of pure HA (0%Sr^{2+}) (Figure 2.3b-d). Although total incorporation of Sr^{2+} on the HA surface layer could have occurred, these results corroborate heteroionic Ca^{2+}substitution for Sr^{2+} in the crystalline lattice. With respect to structural changes, the broadening of the bands assigned to PO_4^{3-} after addition of Sr^{2+} suggests that this ion causes progressive crystalline disorder, which agrees with XRD observations. This trend is characterized by linear correlation between the full width at the half maximum (FWHM) values and the Sr^{2+} content in the samples (Figure 2.3c). Noticeably, the Raman spectra of the 50%Sr^{2+} and 75%Sr^{2+} samples display broader bands as compared to the crystalline products thus strengthening their amorphous nature. Similar effects have been described in synthetic particles, as well as in minerals arising in cell cultures after treatment with Sr^{2+}.[24,40,44] In fact, Sr^{2+} uptake by minerals synthesized by osteoblasts has been shown to occur in a dose-dependent manner and to be accompanied by a linear increase in cell parameters.[45] Substitution of Ca^{2+} for Sr^{2+} up to 25% in the lattice of synthetic HA has been reported to cause structural disorder, whereas higher Sr^{2+} concentrations have been shown to increase HA crystallinity.[24,25] As revealed by *in vivo* studies, small changes in the structural properties of the 5%Sr^{2+} sample can be related to no marked effects in the bone mineral density of rats treated with low Sr^{2+} dosages.[46] According to previous reports showing that the bone mineral mechanical properties are inversely related to its crystallinity, the structural disordering observed for Sr^{2+} concentrations of up to 25% may be related to increased bone rigidity in osteoporotic patients.[47,48]

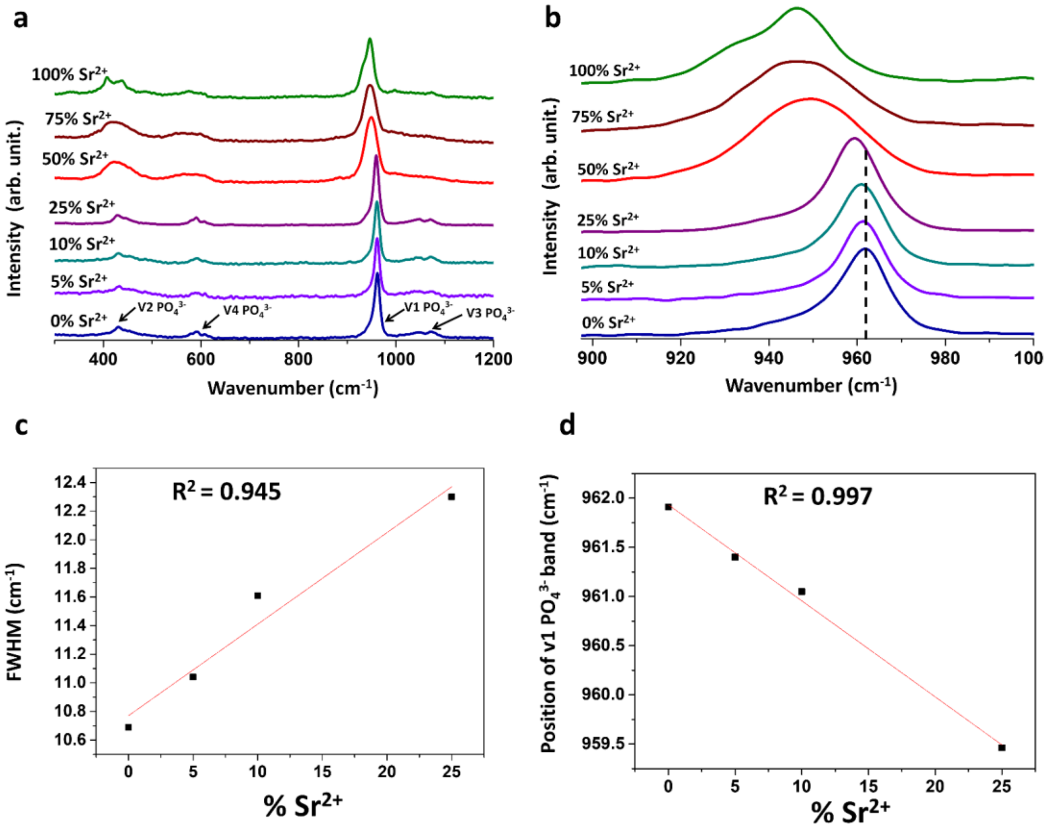

Figure 2.3 | (a) Raman spectra of the series of samples 0-100% Sr^{2+} (b) Enlarged ν_1 PO_4^{3-} Raman bands showing the broadening and displacement of the band upon increasing Sr^{2+} content. (c) Correlation between the FWHM values of the ν_1 PO_4^{3-} Raman band and %Sr^{2+}. (d) Correlation between the ν_1 PO_4^{3-} Raman band position as function of %Sr^{2+}.

In accordance with the XRD and Raman results, the ATR-FTIR spectra of the 0–25%Sr^{2+} samples display sharper bands ascribed to the PO_4^{3-} vibration modes, whilst the 50%Sr^{2+} and 75%Sr^{2+} samples exhibit marked broad bands as expected to amorphous phosphates (Figure 2.4a). The band observed near 3330 cm^{-1} is related to OH stretch of hydroxide groups and adsorbed water (Figure 2.4b). This band and the one at 1600 cm^{-1}, which is related to the bending mode of water molecule, are relatively more intense for the 50%Sr^{2+} and 75%Sr^{2+} samples. This is in agreement with the higher degree of hydration in amorphous phosphate phases.[29] Additionally, a weak band attributed to structural OH vibration (assigned by *) is observed in the spectra of the series of samples 0–25%Sr^{2+} as a result of hydroxide ions in crystalline apatite environments (Figure 2.4b).[49] The presence of typical CO_3^{2-} bands in the regions of 870 cm^{-1} and 1360–1580 cm^{-1} (ν_2 symmetric and ν_3 asymmetric stretching respectively) confirms that the samples have carbonated nature and resemble biological apatite found in bone tissue and tooth enamel.[30] Notably, such bands are less intense in the spectra of the amorphous particles. CO_3^{2-} ions can be hosted in the disordered hydrated layer of bone apatite or in its crystalline core by lattice substitution of PO_4^{3-} ions (B-type), OH^- ions (A-type), or both (AB-type).[50] Further analysis of the CO_3^{2-} bands reveals less intense ν_3 bands, related to B-type substitution, and a more intense ν_3 band, related to A-type substitution, as indicated by the dashed lines (Figure 2.4b).[51] A-type substitution is a mechanism that facilitates CO_3^{2-} charge balance and spatial accommodation.[52] In this sense, this result suggests that Ca^{2+} substitution for Sr^{2+} may influence charge distribution in HA, which in turn affects the CO_3^{2-} substitution site. Furthermore, in biological apatite, such substitution influences the local disorder and promotes formation of an amorphous layer in the bone mineral.[29] Although bone aging and biological activity are known to affect the CO_3^{2-} amount, this relationship is not yet completely understood.[53] In this context, besides the impact on crystalline properties, the influence on CO_3^{2-} substitution suggests further effects of Sr^{2+} in bone mineral.

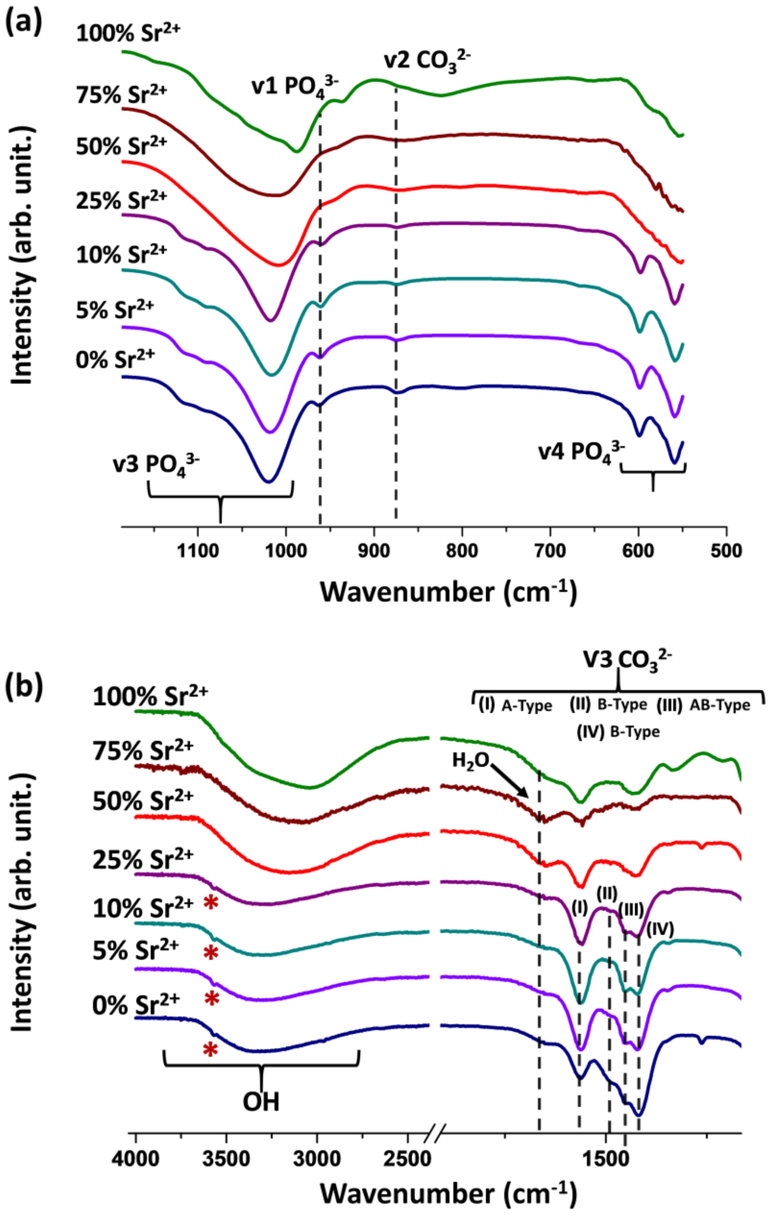

Figure 2.4| ATR-FTIR spectra of the series of samples 0–75%Sr^{2+} after six days of reaction displaying typical bands of (a) PO_4^{3-} (ν_1, ν_3 and ν_4 vibrational modes) and CO_3^{2-} (ν_2 vibrational mode) and (b) CO_3^{2-} (ν_3 vibrational mode), OH^- groups and H_2O molecules.

TGA was performed on the 0%Sr^{2+}, 50%Sr^{2+} and 75%Sr^{2+} samples to investigate their water content (Figure 2.5a) The TGA and DTG curves (Figure 2.5b-d), reveal two weight loss events in the range of 25-400°C related to the dehydration processes: adsorbed (surface) and structural water molecules are released in the range of 25-200 °C and 200-400 °C, respectively. Moreover, a higher content of water was found in 50%Sr^{2+} and 75% Sr^{2+}samples (18.9 and 16.6% wt., respectively) as compared to 0% Sr^{2+} (9.8% wt) in agreement with the ATR-FTIR data.

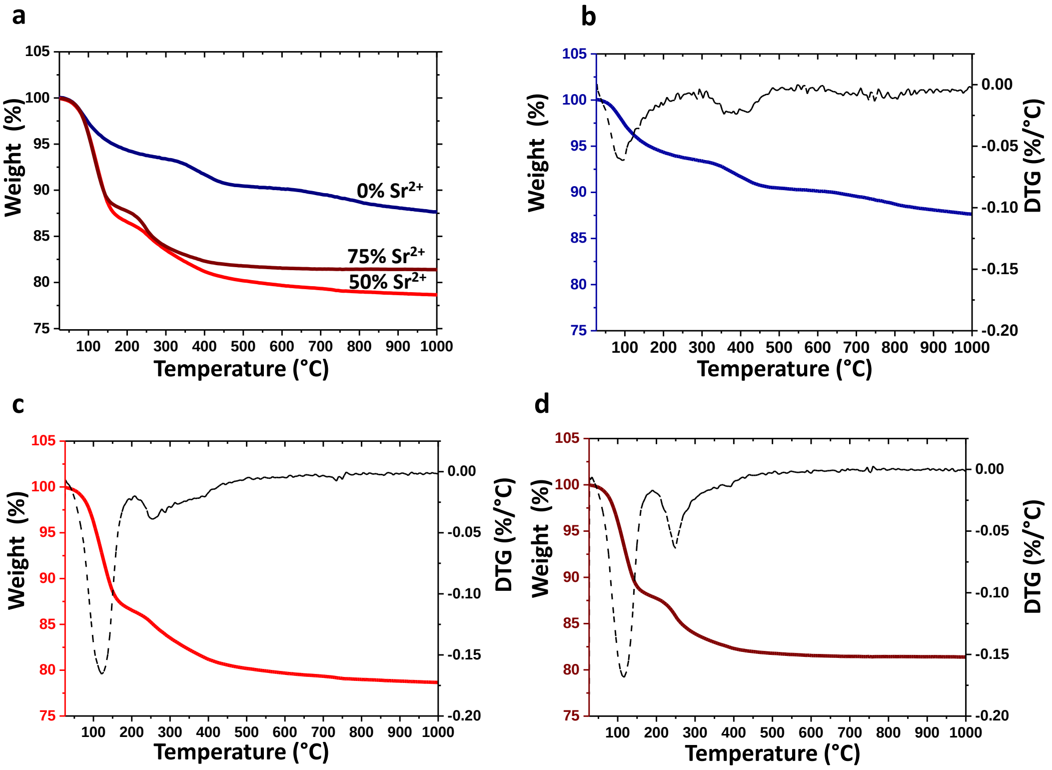

Figure 2.5 | (a) TGA curves of the 0%Sr^{2+}, 50%Sr^{2+} and 75%Sr^{2+} samples. TGA (left axis, solid curves) and DTG (dashed black curves, right axis) of the (b) 0%Sr^{2+}, (c) 50%Sr^{2+}and (d) 75%Sr^{2+} samples reveal two weight loss events range of 25-400 °C ascribed to dehydration processes.

Typical spherulitic aggregates are observed in the SEM images of the series of samples with apatite structure (Figure 2.6a-c). The samples containing less than 50%Sr^{2+} do not differ significantly in terms of morphology. The 50%Sr^{2+} and 75%Sr^{2+} samples (characterized as amorphous in the previous discussion) display regular and spherical morphology (Figure 2.6d-e). The sample identified as Collin's salt exhibits plate-like morphology (Figure 2.6f). The morphological differences evidenced by SEM attest to the structural/compositional changes previously described.

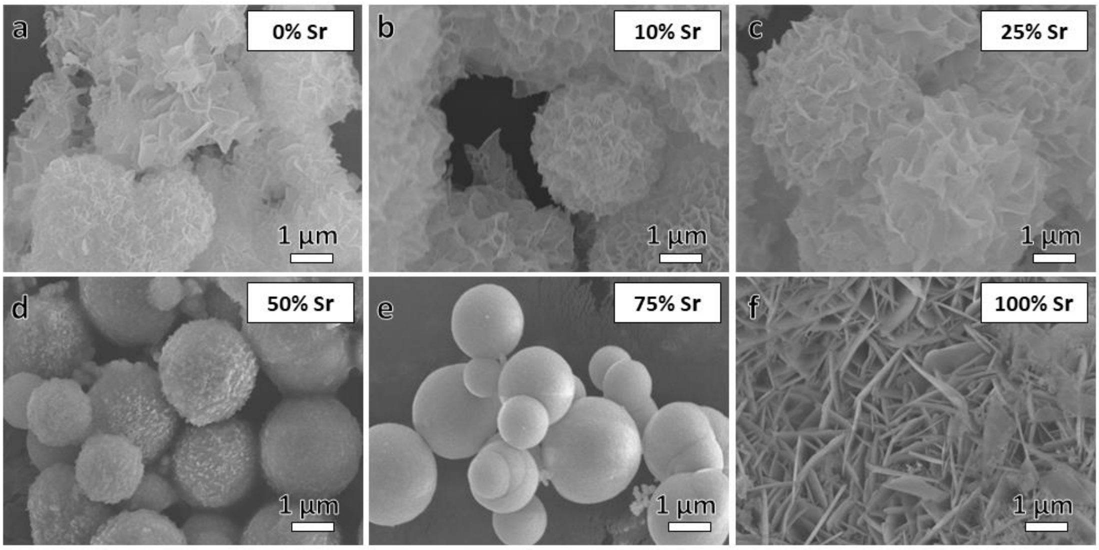

Figure 2.6 | SEM images of the (a) 0%Sr^{2+}, (b) 10%Sr^{2+}, (c) 25%Sr^{2+}, (d) 50%Sr^{2+}, (e) 75%Sr^{2+} and (f) 100%Sr^{2+} samples after six days of reaction. Particles with typical flower- like morphology are observed for the samples with apatitic structure (0–25%Sr^{2+}). Spherical particles are observed in the amorphous samples (50–75%Sr^{2+}).

TEM performed on the series of samples 0–25%Sr^{2+} reveals that the spherulites observed by SEM are formed by the aggregation of nanometric crystals with plate-like morphology with thickness of 3-6 nm similar to that one found in bone (Figure 2.7a-d).[32,54] Notably, SAEDs confirm the preferential radial orientation of the (002) planes in the spherulitic HA particles (Figure 2.7e- f).

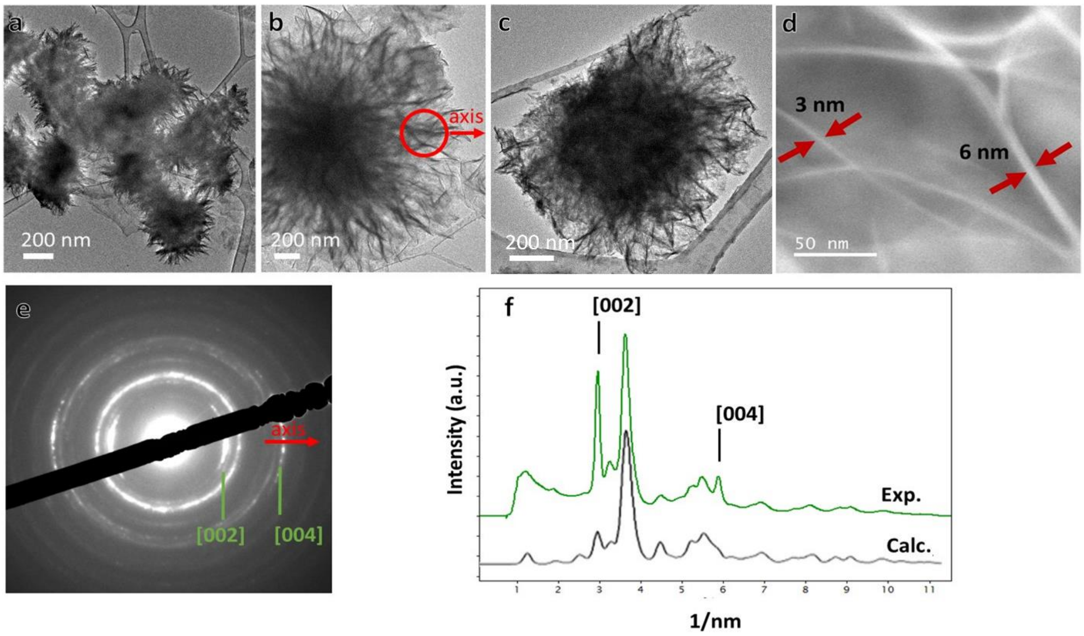

Figure 2.7 | (a-c) TEM images of the 0%Sr^{2+}, 5%Sr^{2+} and 25%Sr^{2+} samples. (d) STEM image of 25%Sr^{2+} samples showing crystalline thin leaves composed of slabs of 3-6 nm of thickness. (e) SAED from the encircled area of the 5%Sr^{2+} sample. The orientation of the SAED with respect to the image is indicated by the radial axis. SAED exhibits a (002) planes preferential radial orientation. (f) Radial integration of the SAED of (e) (green line) and the isotropic electron diffraction of HA calculated (grey line). The preferential growth direction results in a stronger (002) and (004) planes contributions in the experimental curve.

Although XRD identified HA as the major phase in the 25%Sr^{2+} sample, TEM reveals additional presence of a low amount of amorphous particles (Figure 2.8a-d). Crystals surrounding the amorphous aggregates suggests that the latter can be converted into HA.

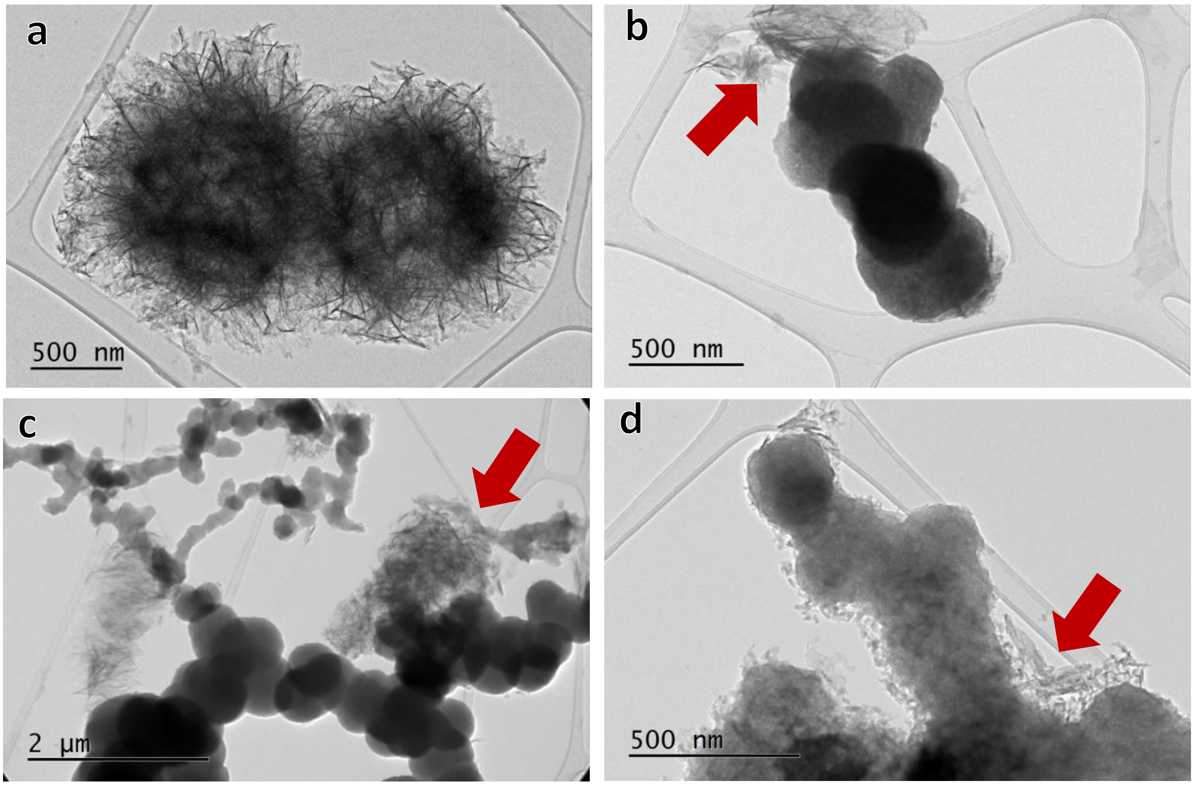

Figure 2.8 | TEM images of the 25%Sr^{2+} sample showing (a) HA and (b-d) amorphous particles coexisting.

Elementary TEM mapping performed on the two type of particles present in the 25% Sr^{2+} system show that the elements Ca, Sr, P, and O are homogeneously distributed in the HA and amorphous particles, confirming that Sr^{2+} and Ca^{2+} are incorporated into both crystalline (Figure 2.9a) and amorphous (Figure 2.9b) particles.

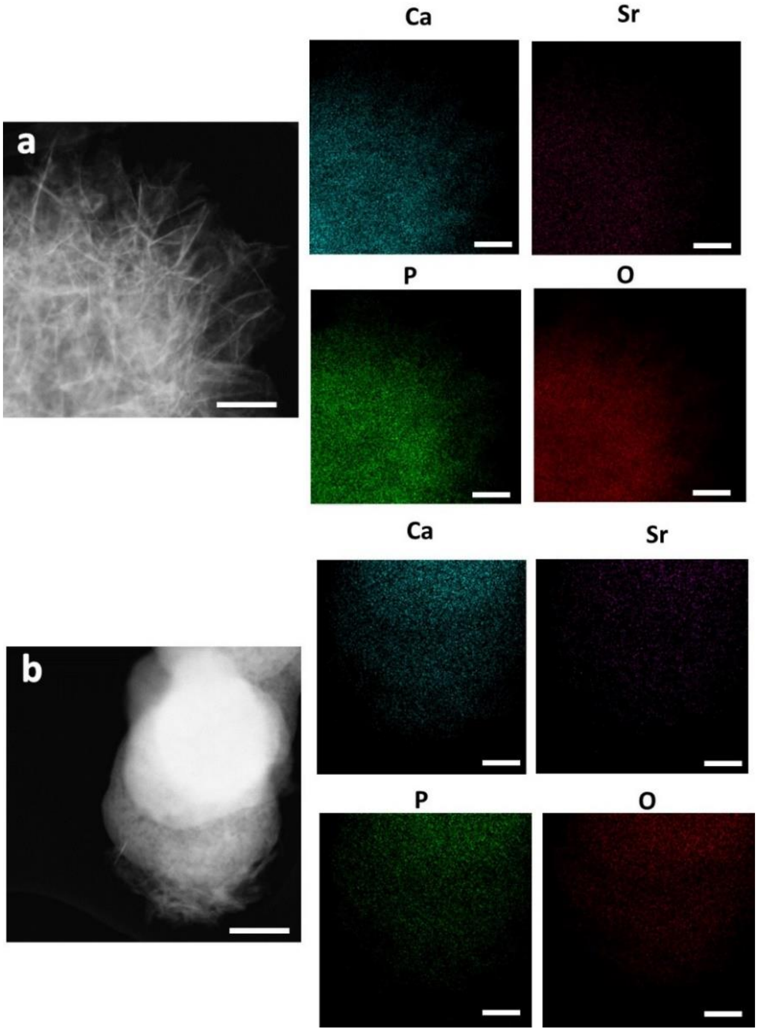

Figure 2.9| TEM images and EDS mapping of the 25%Sr^{2+} sample showing the distribution of Sr, Ca, P, and O over the apatite (a) and amorphous (b) particles. Scale bar in all panels is 200 nm.

Overall, these results contrast with findings reported for synthetic HA, for which isomorphic Ca^{2+} substitution for Sr^{2+} is described up to 100% of Sr^{2+}.[24,26,27,40] Regardless of the administered dose, bone mineral has been shown to incorporate a maximum of 12.3% Sr^{2+} in the lattice; any excess Sr^{2+} is loaded on the bone surface by adsorption and ion exchange.[55,23]

The formation of such amorphous phases can be seen as evidence of Sr^{2+} physicochemical interference on apatite formation and could account for the adverse effects of the administration of high Sr^{2+} doses observed *in vivo* and in cell cultures *in vitro*.[56,19] In fact, high Sr^{2+} doses have been reported to induce mineralization defect in rats with normal renal functions and osteomalacia (a bone disease caused by defective mineralization) in rats with chronic renal failures.[56,57] Collin's salt formation is in line with the presence of insoluble salts in animals with high Sr^{2+} dietary.[58] Still in this regard, rather than Sr^{2+}- HA, a mixture of minerals containing $SrHPO_4$ has been reported to arise in the presence of high Sr^{2+} concentrations in the mineralization medium containing matrix vesicles.[59] Similarly, different Sr^{2+}-phosphate phases together with amorphous precipitate have been found in mineralized cell cultures exposed to high Sr^{2+} doses.[45] Interestingly, these outcomes highlight the different impact that Sr^{2+} has on biological apatite and synthetic HA. Such differences may be due to the use of non-physiological conditions that often favor formation of products with high degree of crystallinity.[36]

2.3.2 | Understanding Sr^{2+} incorporation and its impact on biomimetic HA local order

^1H and ^{31}P solid state NMR were performed to probe the local environment in the phosphates. Sharp resonance peaks centered around 3 ppm, which are characteristic of PO_4^{3-} ions in crystalline HA, are found in the quantitative ^{31}P MAS NMR spectra for the series of samples 0–25% Sr^{2+}(Figure 2.10a). Increasing Sr^{2+} content broadened the resonance signal and shifted it toward downfield (Table 2.3). These findings show that Ca^{2+} substitution for Sr^{2+} in the HA lattice increases the distribution of environments around the phosphates, thereby confirming the structural disorder induced by Sr^{2+}. Such strains in the HA crystalline lattice could also influence bond lengths and angles in the phosphate group changing its chemical environment.[60] The pronounced broadening observed for the 25%Sr^{2+} sample (Figure 2.10 a, purple line) could also result from the presence of amorphous particles, as discussed above. A similar behavior was observed in the ^{31}P NMR spectra of Mg^{2+}-substituted HA, which was also related to structural disorder caused by the ionic substitution.[61] The 50%Sr^{2+} and 75%Sr^{2+} samples exhibit broad signals characterized by Gaussian line shapes with typical line widths (LW) values of amorphous phosphate environments (~ 630 Hz).[31] This result once again confirms that the apatite environment is disrupted and gives place to a huge distribution of chemical environments by increasing Sr^{2+} concentration.

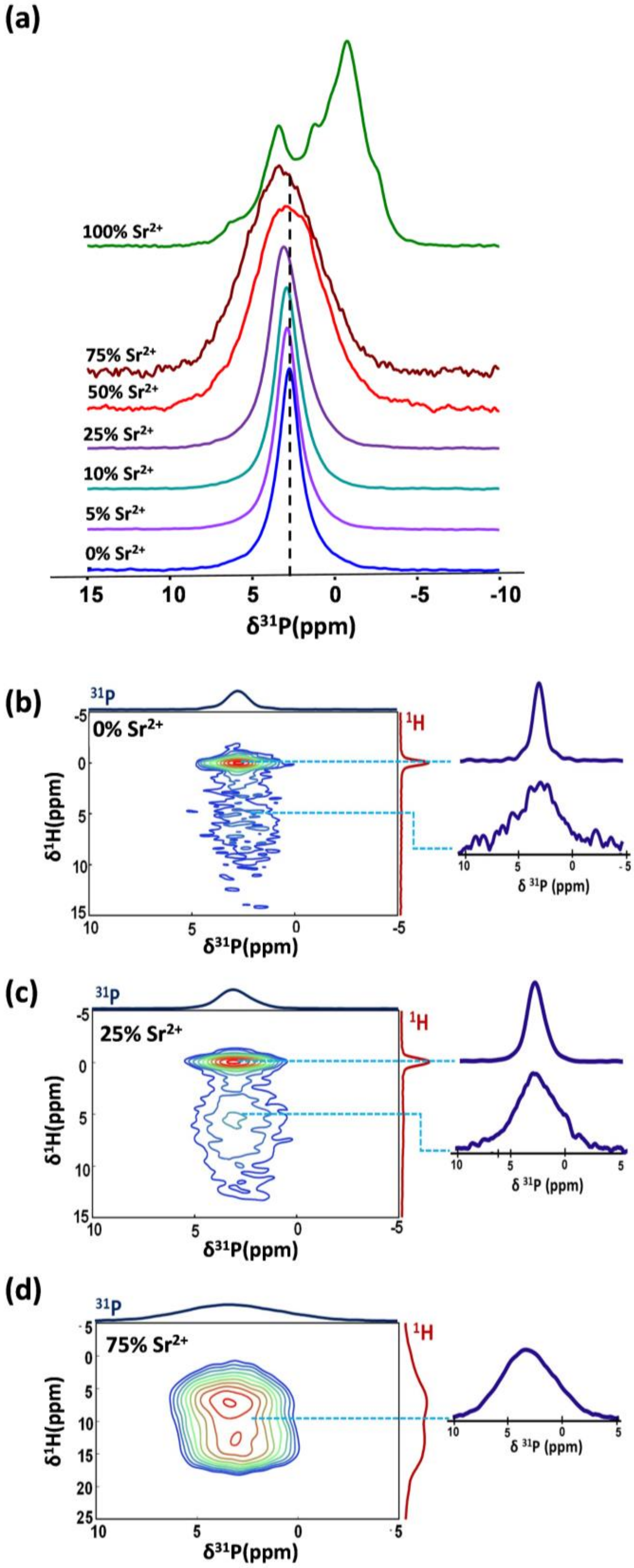

Figure 2.10 | (a) ^{31}PMAS spectra of the series of samples 0–100%Sr^{2+} after six days of reaction (b-d)^{1}H-^{31}P HetCor spectra of the 0%Sr^{2+}, 25%Sr^{2+}, and 75%Sr^{2+} samples and extracted ^{31}P slices corresponding to the resonance at δ(^{1}H) = 0 and 4.85 ppm due to the apatitic core and the hydrated disordered layer domains, respectively.

2D $^{1}H^{31}P$ HetCor spectra were recorded in order to obtain further information about Sr^{2+} distribution in both surface and core of the HA particles (Figure 2.10b-d). This experiment allows the correlation of phosphate and proton chemical environments leading to the identification of possible local structural differences in the samples. The 0%Sr^{2+} and 25%Sr^{2+} samples exhibit two cross peaks ($\delta(^{31}P) \sim 3$ ppm) revealing two distinct chemical environments: one related to the apatitic PO_4^{3-} (correlation with OH^- ions ($\delta(^{1}H) = 0$ ppm), and another correlated with water ($\delta(^{1}H) = 5$ ppm) and HPO_4^{2-} ($\delta(^{1}H) = 12.5$ ppm) on the HA surface (Figure 2.10b,c). The low content of strontium in samples 0 to 25%Sr^{2+} precipitate under the form of spherulites, which consist of core-layer nanoplatelets. Such core-layer organization (crystalline *vs.* amorphous) is characteristic of biomimetic apatite.[29] In the 25%Sr^{2+} sample, micrometric amorphous material is revealed by TEM but its NMR signal cannot be distinguished from the one of the HA particles (i.e., amorphous layer).

The ^{31}P slices extracted from each correlation peak revealed a sharper resonance typical of crystalline apatite ($\delta(^{31}P) \sim 3.0$ ppm and LW ~ 150 Hz) and a broad resonance characteristic of amorphous phosphate ($\delta(^{31}P) \sim 3.2$ ppm and LW~ 500 Hz)). These characteristic features of biomimetic apatite thereby highlight the great potential of this model to investigate Sr^{2+} incorporation in bone. Indeed, the proposed mechanism for Sr^{2+} incorporation in bone involves two steps: first, the Sr^{2+} ions are weakly and reversibly adsorbed on the apatite hydrated amorphous layer. Then, they are subsequently incorporated into the crystalline lattice by substituting Ca^{2+} positions typically at a maximum of 10%, whereas excess Sr^{2+} accumulates on the bone surface.[62,8] The ^{31}P projections of the crystalline core and hydrated disordered layer reveal that the LW values increase progressively with Sr^{2+} concentration in the crystalline core and in the hydrated layer, thereby confirming Sr^{2+} incorporation in both HA sites (Table 2.3).

The 2D ^{1}H ^{31}P HetCor MAS NMR spectrum of the 75%Sr^{2+} sample (Figure 1.10d) shows typical signatures of amorphous phosphate: a broad signal in the δ (^{1}H) range of ~ 5–15 ppm, corresponding to water and HPO_4^{2-}. The absence of cross peak related to OH^- ions confirms that this amorphous phase is homogeneous. These results support the currently accepted mechanism for Sr^{2+} incorporation into bone in terms of localization in different regions (surface and crystalline lattice) and limited ratio of Ca^{2+}replacement with Sr^{2+} in biological apatite.[6,14,63,64]

Table 2.3 | ^{31}P shifts (δ) and line widths (LW) of the apatitic core and disordered hydrated layer determined from ^{31}P slices (δ(^{1} H) = 0 and 4.85 ppm respectively) extracted from the ^{1}H-^{31}P HetCor spectra of the 6 days samples

Sample	**^{31}P apatitic core**		**^{31}P amorphous layer**	
	δ(^{31}P) ±0.05 ppm	**LW ±10 Hz**	**δ(^{31}P) ±0.05 ppm**	**LW ±10 Hz**
0% Sr^{2+}	2.71	153	2.52	415
5% Sr^{2+}	2.81	170	2.61	472
10% Sr^{2+}	2.87	180	2.72	485
25% Sr^{2+}	3.06	238	2.91	527
75% Sr^{2+}	-	-	3.33	699

To gain insight into the chemical environments of protons, double CP $^{1}H \rightarrow {}^{31}P \rightarrow {}^{1}H$ MAS NMR spectra were recorded for the series of samples 0–25%Sr^{2+} (Figure 2.11). The spectra exhibit a narrow and intense peak around 0 ppm, which is characteristic of OH^- ions in the crystalline apatitic environment, and two peaks, at 5.5 and 15 ppm, corresponding to adsorbed water and HPO_4^{2-}, respectively. The position of the OH^- peak does not change with Ca^{2+} substitution for Sr^{2+} in HA. Nevertheless, such peak broadened slightly with Sr^{2+} addition, suggesting that the distribution of chemical environments around the hydroxyl groups increased. Interestingly, compared to OH^-, the relative intensity of the H_2O and HPO_4^{2-} resonance peaks increase upon Sr^{2+} addition, suggesting the augment in the ratio of HA hydrated layer and crystalline core.

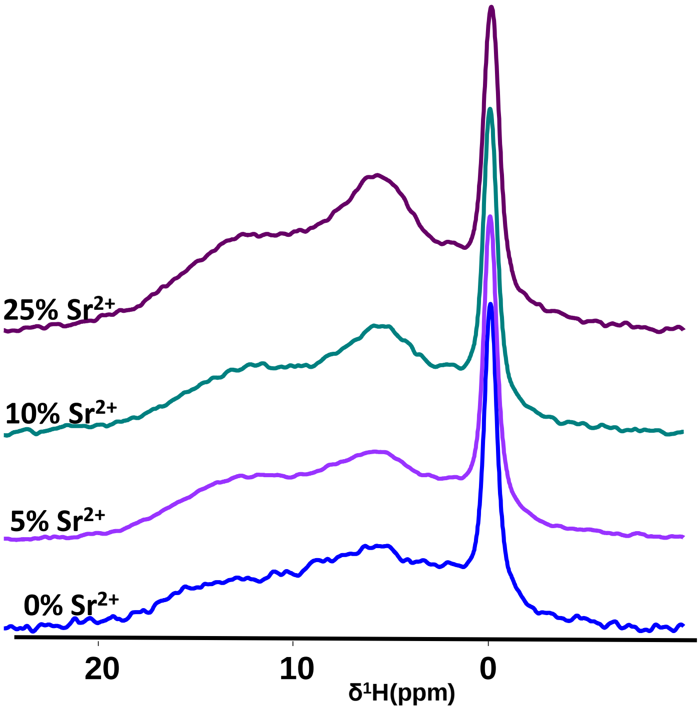

Figure 2.11 | Double CP $^{1}H \rightarrow ^{31}P \rightarrow ^{1}H$ MAS NMR spectra of the series of samples 0-25%Sr^{2+}.

2.3.3 | Understanding Sr^{2+} distribution between crystalline and amorphous phases

Shorter experiments (one day) were conducted to investigate the Sr^{2+} effects on amorphous particle formation. Spheres with rough surfaces and diameters of several micrometers are observed in the SEM images for the 50%Sr^{2+} (Figure 2.12a) and 75%Sr^{2+} (Figure 2.12e) samples. Remarkably, the surface of the 50%Sr^{2} sample is rougher when compared to the 75%Sr^{2+} sample. Further TEM investigation was performed revealing the presence of two dominant structures in both systems: <100-nm homogeneous spheres with smooth surface (Figure 2.12c and Figure 2.12g) and dense, bigger particles with needles emanating from the surface (Figure 2.12b and Figure 2.12f), which are less frequent in the 75%Sr^{2+} sample and agreed with the SEM observations.

Although XRD confirms formation of an amorphous phase, SAED patterns taken from the surface of the 50%Sr^{2+} sample exhibit narrow rings (Figure 2.12d, inset), revealing the presence of crystalline domains, whereas the inner part of the sphere displayed broad diffraction rings (Figure 2.12b, inset), confirming its amorphous nature. Similar investigations were performed on the 75%Sr^{2+} sample and found that both the core and surface are characterized by diffraction patterns with broad rings (Figure 2.12f, and Figure 2.12h, inset), confirming absence of crystalline domains in contrast with the 50%Sr^{2+}

sample. The smaller smooth spheres present in both systems display SAED patterns with broad rings. Diffraction fringes are absent in the HRTEM images, which is typical of amorphous materials (Figure 2.12g, inset). The presence of crystalline domains on the surface of the 50%Sr^{2+} amorphous particles suggests that the Sr^{2+} content in the starting solutions plays a role in the dynamics of ion exchange between the particle surface and the reaction medium. At 50% Sr^{2+}, more Ca^{2+} ions can accumulate on the particle surface as compared to the 75%Sr^{2+} sample, thus favoring local HA precipitation.

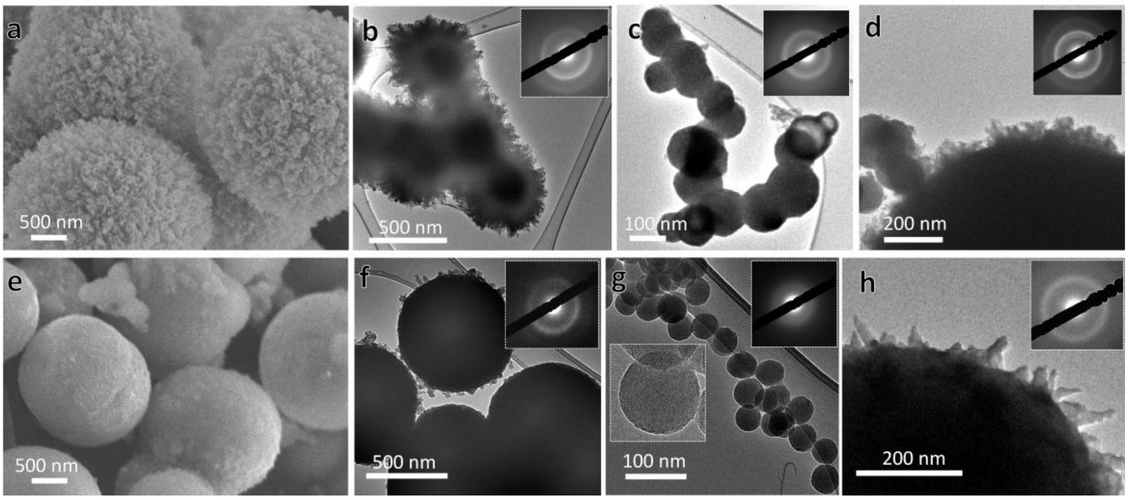

Figure 2.12 | (a) SEM and (b-d) TEM images with SAED in insert of the 50%Sr^{2+} sample after one day of reaction. (e) SEM and TEM (f-h) images with SAED and HRTEM (inset g) of the 75%Sr^{2+} sample after one day of reaction.

To gain further insights into Sr^{2+} distribution in HA and Sr(ACP) and into their mechanism of formation, the 25%Sr^{2+} system (characterized as a mixture of both structures) was studied by STEM-EELS. Such technique allows to acquire spatially resolved mappings that show the elemental distribution. This is an important starting point to obtain a link between the different structures found in this system and Sr^{2+} incorporation. EELS spectra were obtained for HA and Sr(ACP) particles (Figure 2.13). The spectra were collected for an energy range spanning from 300 to 2500 eV, enabling a simultaneous measurement of Ca-L (346 eV), O-K (530 eV), Sr-L (1940eV), and P-K (2146 eV). Comparison between the spectra of both particles shows that the main difference is the weaker Ca peak for the amorphous phase. On the other hand, both phases exhibit Sr-L and P-K edges with similar intensities (Figure 2.14, inset). Quantifications based on EELS result in approximate Sr/Ca ratios of ca. 0.16 for the Sr^{2+} substituted HA and of ca. 0.27 for the Sr(ACP). These results confirm that the amorphous phase has much higher %Sr^{2+} than the apatitic phase.

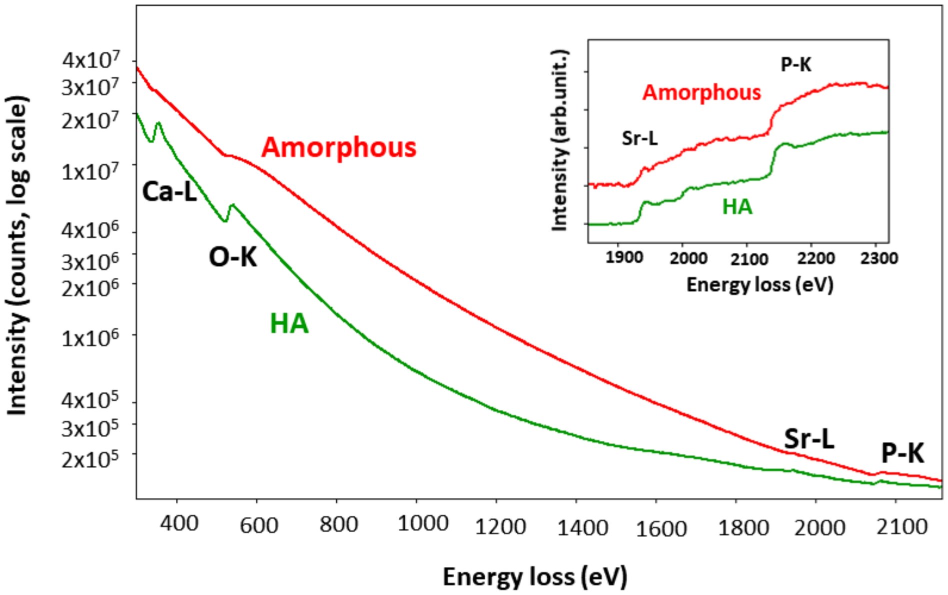

Figure 2.13 | EELS spectra of the Sr^{2+}-doped HA and Sr(ACP) present in the 25%Sr^{2+} sample after one day of reaction (300-2500 eV energy range and 1900-2300 eV energy range in the inset).

STEM-EELS with nanometric resolution was performed on the amorphous particle containing crystalline needles (Figure 2.14). The EELS spectra recorded from 100 to 700 eV and comprising the P-L (132 eV), Sr-M (133 eV), C-K (285eV), Ca-L (346 eV), and O-K (530 eV) edges can be seen for the inner part of the amorphous particle and the outer layer. EELS mapping also evidences that the outer needles and amorphous core have different calcium compositions. This confirms our hypothesis that Ca^{2+} accumulates on the surface of the amorphous phase by ion exchange with the reaction medium.

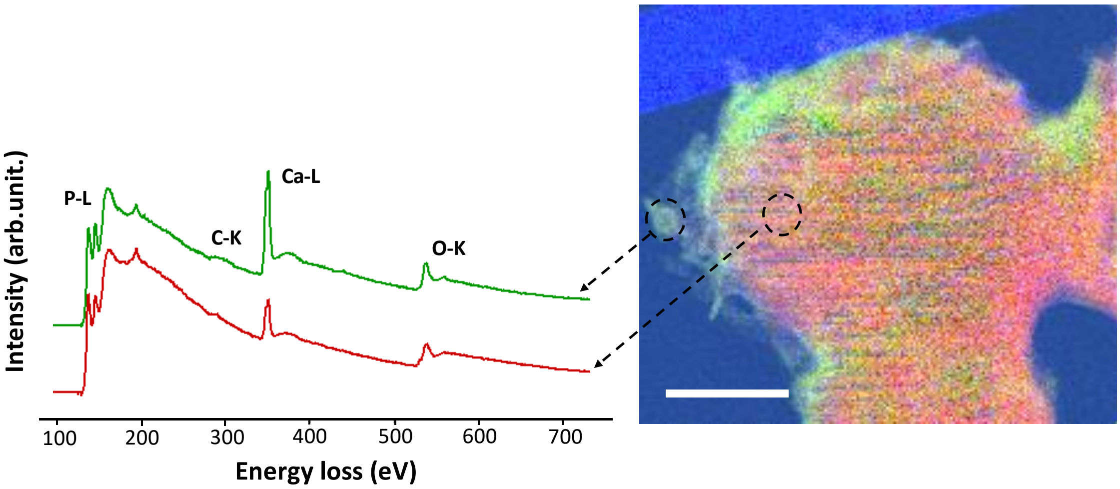

Figure 2.14 | EELS spectra (100-700 eV) extracted at the surface and an inner part of an amorphous particle with crystalline apatitic domains found in the 25%Sr^{2+} sample after one day of reaction. The image is composed by the intensity of the P-L (red), the C-K (blue), and the Ca-L (green) edges. Scale bar = 100 nm.

2.3.4 | The impact of Sr^{2+} on the pathway of HA mineralization

Herein, the approach adopted to synthesize HA avoided precipitation of other phases like octacalcium phosphate, brushite, and amorphous calcium phosphate by using acidic pH (3.5) at the start of the reaction and slow crystallization rate through NH_3(g) diffusion. As shown by XRD, solid state NMR and TEM, HA and Sr^{2+}-substituted HA were the only phases in the series of samples 0–10%Sr^{2+}, whereas a small amount of amorphous particles emerged in the 25%Sr^{2+} sample, as evidenced by TEM. These findings indicate an amorphous phase-mediated pathway in HA precipitation. Sr^{2+} progressively stabilizes this amorphous precursor and, at higher Sr^{2+} incorporation (50%Sr^{2+} and 75%Sr^{2+}), its conversion into HA did not occur even after six days of reaction.

As shown before, incorporation of Sr^{2+} elicits structural strains in HA thereby limiting its amount into the HA hexagonal structure. On the other hand, amorphous structures have high ability to accommodate ions and molecules. Indeed, enhanced Sr^{2+} uptake in calcite via an amorphous precursor pathway has been demonstrated.[65] Recently, the synergic effect of Sr^{2+} and Mg^{2+} on amorphous calcium phosphate stabilization has been reported and shown to retard its conversion into HA.[66] In the present study Sr(ACP) particles originated in the absence of additives. This was different from the amorphous particles currently described as transient phases, which are rapidly converted into HA.[67] Here, the Sr(ACP) persisted in the reaction medium, suggesting high stability.

Amorphous phases are ubiquitous in nature. They occur in carbonate silicates and phosphate biominerals and play a pivotal role in biomineralization.[68] Even though the Ostwald rule of stages that predicts that metastable amorphous phases are typically converted into the most thermodynamically stable polymorphs, amorphous precursors can be thermodynamically and kinetically stabilized by use of organic additives, confined volumes, and trace elements such as Mg^{2+} and also Sr^{2+}, as shown here.[69,70,71,72]

Recently, it was shown that Mg^{2+} is heterogeneously distributed in the bone tissue; it accumulates in the boundary regions of human enamel in the form of Mg^{2+} bearing amorphous calcium phosphate.[73] The formation of highly stable Sr(ACP) under physiological conditions suggests that Sr^{2+}may also be heterogeneously distributed in bone within regions of low structural order. In addition to the structural incompatibility between HA and high Sr^{2+} concentrations, the surface energy effect must be considered.[74] Particle size and hydration are key parameters to understand the thermodynamic stability of polymorphs and their occurrence in natural systems.[75,76] An increase in surface area can lead to kinetically stabilized polymorphs instead of the thermodynamic products usually obtained at ambient conditions. As a result, complex crossovers of polymorphs are observed at the nanoscale.[77] It was demonstrated that particles with larger surface area allow hydrated phases to exist as a consequence of the decrease in surface energy due to water adsorption.[78] In this sense, the presence of totally amorphous nanometric particles (as shown by TEM, SAED, and HRTEM) strongly suggests additional stabilization of the Sr(ACP) particles by surface energy and formation of bigger particles most probably by coalescence and attachment of smaller particles.

2.4 | Conclusions

Overall, the co-existence of Sr^{2+} substituted HA and Sr(ACP) is described which questions the limit of Sr^{2+} solubility into HA under biomimetic conditions. Moreover, at specific concentrations, Sr^{2+} can effectively stabilize ACP, similarly to another important stabilizing agent of amorphous precursors, Mg^{2+}. These intriguing results suggest that heterogeneous Sr^{2+} distribution in bone may be associated with regions of low structural order.

In general terms, by setting biomimetic conditions, this study provides physicochemical understanding of the effect of Sr^{2+} on HA mineralization and substantial insights into its impact on the bone tissue. Additionally, the presented model is comprehensive and can be adopted to describe the effect of other ions and molecules of biological interest on the bone mineralization pathway. The next chapters will be dedicated to understand the stability of Sr(ACP) in bone environment.

2.5 | References

(1) Taylor, D.; Hazenberg, J. G.; Lee, T. C. Living with Cracks: Damage and Repair in Human Bone . *Nat. Mater.* **2007**, *6* (4), 263–268.

(2) Hadjidakis, D. J.; Androulakis, I. I. Bone Remodeling. *Ann. N. Y. Acad. Sci.* **2006**, *1092*, 385–396.

(3) Mundy, G. R. Cytokines and Growth Factors in the Regulation of Bone Remodeling. *J. Bone Miner. Res.* **1993**, *8 (S2)*, S505-S510.

(4) Quarles, L. D. Cation Sensing Receptors in Bone: A Novel Paradigm for Regulating Bone Remodeling? *J. Bone Miner. Res.* **1997**, *12* (12), 1971–1974.

(5) Bonnelye, E.; Chabadel, A.; Saltel, F.; Jurdic, P. Dual Effect of Strontium Ranelate: Stimulation of Osteoblast Differentiation and Inhibition of Osteoclast Formation and Resorption in Vitro. *Bone* **2008**, *42* (1), 129–138.

(6) Dahl, S. G.; Allain, P.; Marie, P. J.; Mauras, Y.; Boivin, G.; Ammann, P.; Tsouderos, Y.; Delmas, P. D.; Christiansen, C. Incorporation and Distribution of Strontium in Bone. *Bone* **2001**, *28* (4), 446–453.

(7) Cabrera, W. E.; Schrooten, I.; De Broe, M. E.; D'haese, P. C Strontium and Bone. *J. Bone Miner. Res.* **1999**, *14* (5).

(8) Boivin, G.; Deloffre, P.; Perrat, B.; Panczer, G.; Boudeulle, M.; Mauras, Y.; Allain, P.; Tsouderos, Y.; Meunier, P. J. Strontium Distribution and Interactions with Bone Mineral in Monkey Iliac Bone after Strontium Salt (S 12911) Administration. *J. Bone Miner. Res.* **2009**, *11* (9), 1302–1311.

(9) Allison, N.; Finch, A. A.; Sutton, S. R.; Newville, M. Strontium Heterogeneity and Speciation in Coral Aragonite: Implications for the Strontium Paleothermometer. *Geochim. Cosmochim. Acta* **2001**, *65* (16), 2669–2676.

(10) Tovani, C. B.; Oliveira, T. M.; Gloter, A.; Ramos, A. P. Sr2+-Substituted $CaCO_3$ Nanorods: Impact on the Structure and Bioactivity. *Cryst. Growth Des.* **2018**, *18* (5), 2932–2940.

(11) Habibovic, P.; Barralet, J. E. Bioinorganics and Biomaterials: Bone Repair. *Acta Biomater.* **2011**, 7 (8), 3013–3026.

(12) Reginster, J. Y.; Seeman, E.; De Vernejoul, M. C.; Adami, S.; Compston, J.; Phenekos, C.; Devogelaer, J. P.; Curiel, M. D.; Sawicki, A.; Goemaere, S.; et al. Strontium Ranelate Reduces the Risk of Nonvertebral Fractures in Postmenopausal Women with Osteoporosis: Treatment of Peripheral Osteoporosis (TROPOS) Study. *J. Clin. Endocrinol. Metab.* **2005**, *90* (5), 2816–2822.

(13) Seeman, E.; Vellas, B.; Benhamou, C.; Aquino, J. P.; Semler, J.; Kaufman, J. M.; Hoszowski, K.; Varela, A. R.; Fiore, C.; Brixen, K.; et al. Strontium Ranelate Reduces the Risk of Vertebral and Nonvertebral Fractures in Women Eighty Years of Age and Older. *J. Bone Miner. Res.* **2006**, *21* (7), 1113–1119.

(14) Boivin, G.; Farlay, D.; Khebbab, M. T.; Jaurand, X.; Delmas, P. D.; Meunier, P. J. In Osteoporotic Women Treated with Strontium Ranelate, Strontium Is Located in Bone Formed during Treatment with a Maintained Degree of Mineralization. *Osteoporos. Int.* **2010**, *21* (4), 667–677.

(15) Gentleman, E.; Fredholm, Y. C.; Jell, G.; Lotfibakhshaiesh, N.; O'Donnell, M. D.; Hill, R. G.; Stevens, M. M. The Effects of Strontium-Substituted Bioactive Glasses on Osteoblasts and Osteoclasts in Vitro. *Biomaterials* **2010**, *31* (14), 3949–3956.

(16) Leite, Á. J.; Gonçalves, A. I.; Rodrigues, M. T.; Gomes, M. E.; Mano, J. F. Strontium-Doped Bioactive Glass Nanoparticles in Osteogenic Commitment. *ACS Appl. Mater. Interfaces* **2018**, *10* (27), 23311–23320.

(17) Riggs, B. L.; LJ, M. The Worldwide Problem of Osteoporosis : By Epidemiology. *Bone* **1995**, *17* (5), 505S-511S.

(18) Odén, A.; McCloskey, E. V.; Kanis, J. A.; Harvey, N. C.; Johansson, H. Burden of High Fracture Probability Worldwide: Secular Increases. *Osteoporos. Int.* **2015**, *26* (9), 2243–2248.

(19) Verberckmoes, S. C.; De Broe, M. E.; D'Haese, P. C. Dose-Dependent Effects of Strontium on Osteoblast Function and Mineralization. *Kidney Int.* **2003**, *64* (2), 534–543.

(20) Schrooten, I.; Cabrera, W.; Goodman, W. G.; Dauwe, S.; Lamberts, L. V.; Marynissen, R.; Dorriné, W.; De Broe, M. E.; D'Haese, P. C. Strontium Causes Osteomalacia in Chronic Renal Failure Rats. *Kidney Int.* **1998**, *54* (2), 448–456.

(21) Morohashi, T.; Sano, T.; Yamada, S. Effects of Strontium on Calcium Metabolism in Rats. I. A Distinction between the Pharmacological and Toxic Doses. *Jpn. J. Pharmacol.* **1994**, *64* (3), 155–162.

(22) Boivin, G.; Farlay, D.; Khebbab, M. T.; Jaurand, X.; Delmas, P. D.; Meunier, P. J. In Osteoporotic Women Treated with Strontium Ranelate, Strontium Is Located in Bone Formed during Treatment with a Maintained Degree of Mineralization. *Osteoporos. Int.* **2010**, *21* (4), 667–677.

(23) Li, C.; Paris, O.; Siegel, S.; Roschger, P.; Paschalis, E. P.; Klaushofer, K.; Fratzl, P. Strontium Is Incorporated into Mineral Crystals Only in Newly Formed Bone during Strontium Ranelate Treatment. *J. Bone Miner. Res.* **2010**, *25* (5), 968–975.

(24) O'Donnell, M. D.; Fredholm, Y.; de Rouffignac, A.; Hill, R. G. Structural Analysis of a Series of Strontium-Substituted Apatites. *Acta Biomater.* **2008**, *4* (5), 1455–1464.

(25) Li, Z. Y.; Lam, W. M.; Yang, C.; Xu, B.; Ni, G. X.; Abbah, S. A.; Cheung, K. M. C.; Luk, K. D. K.; Lu, W. W. Chemical Composition, Crystal Size and Lattice Structural Changes after Incorporation of Strontium into Biomimetic Apatite. *Biomaterials* **2007**, *28* (7), 1452–1460.

(26) Geng, Z.; Cui, Z.; Li, Z.; Zhu, S.; Liang, Y.; Lu, W. W.; Yang, X. Synthesis, Characterization and the Formation Mechanism of Magnesium- and Strontium-Substituted Hydroxyapatite. *J. Mater. Chem. B* **2015**, *3* (18), 3738–3746.

(27) Terra, J.; Dourado, E. R.; Eon, J. G.; Ellis, D. E.; Gonzalez, G.; Rossi, A. M. The Structure of Strontium-Doped Hydroxyapatite: An Experimental and Theoretical Study. *Phys. Chem. Chem. Phys.* **2009**, *11* (3), 568–577.

(28) Reznikov, N.; Bilton, M.; Lari, L.; Stevens, M. M.; Kröger, R. Fractal-like Hierarchical Organization of Bone Begins at the Nanoscale. *Science.* **2018**, *360,* 6388.

(29) Wang, Y.; Von Euw, S.; Laurent, G.; Crevant, C.; Bonhomme-Coury, L.; Giraud-Guille, M. M.; Babonneau, F.; Nassif, N.; Azaïs, T. Impact of Collagen Confinement vs. Ionic Substitutions on the Local Disorder in Bone and Biomimetic Apatites. *Mater. Horizons* **2014**, *1* (2), 224–231.

(30) Astala, R.; Stott, M. J. First Principles Investigation of Mineral Component of Bone: CO_3 substitutions in Hydroxyapatite. *Chem. Mater.* **2005**, *17* (16), 4125–4133.

(31) Wang, Y.; Von Euw, S.; Fernandes, F. M.; Cassaignon, S.; Selmane, M.; Laurent, G.; Pehau-Arnaudet, G.; Coelho, C.; Bonhomme-Coury, L.; Giraud-Guille, M. M.; et al. Water-Mediated Structuring of Bone Apatite. *Nat. Mater.* **2013**, *12* (12), 1144–1153.

(32) Nassif, N.; Martineau, F.; Syzgantseva, O.; Gobeaux, F.; Willinger, M.; Coradin, T.; Cassaignon, S.; Azaïs, T.; Giraud-Guille, M. M. In Vivo Inspired Conditions to Synthesize Biomimetic Hydroxyapatite. *Chem. Mater.* **2010**, *22* (12), 3653–3663.

(33) Wu, Y.; Ackerman, J. L.; Chesler, D. A.; Graham, L.; Wang, Y.; Glimcher, M. J. Density of Organic Matrix of Native Mineralized Bone Measured by Water- and Fat-Suppressed Proton Projection MRI. *Magn. Reson. Med.* **2003**, *50* (1), 59–68.

(34) An, G. H.; Wang, H. J.; Kim, B. H.; Jeong, Y. G.; Choa, Y. H. Fabrication and Characterization of a Hydroxyapatite Nanopowder by Ultrasonic Spray Pyrolysis with Salt-Assisted Decomposition. *Mater. Sci. Eng. A* **2007**, *449–451* (3), 821–824.

(35) Liu, J.; Li, K.; Wang, H.; Zhu, M.; Xu, H.; Yan, H. Self-Assembly of Hydroxyapatite Nanostructures by Microwave Irradiation. *Nanotechnology* **2005**, *16* (1), 82–87.

(36) Gupta, H. S.; Guitia, F. An Effective Morphology Control of Hydroxyapatite Crystal via Hydrothermal Synthesis. *Cryst. Growth Des.* **2009**, *9*, 466–474.

(37) Yeong, K. C. B.; Wang, J.; Ng, S. C. Mechanochemical Synthesis of Nanocrystalline Hydroxyapatite from CaO and $CaHPO_4$. *Biomaterials* **2001**, *22* (20), 2705–2712.

(38) Bose, S.; Saha, S. K. Synthesis and Characterization of Hydroxyapatite Nanopowders by Emulsion Technique. *Chem. Mater.* **2003**, *15* (23), 4464–4469.

(39) Uota, M.; Arakawa, H.; Kitamura, N.; Yoshimura, T.; Tanaka, J.; Kijima, T. Encapsulées Dans Stéarate de Calcium Synthesis of High Surface Area Hydroxyapatite Nanoparticles by Mixed Surfactant-Mediated Approach. *Langmuir* **2005**, *21* (11), 4724–4728.

(40) Bigi, A.; Boanini, E.; Capuccini, C.; Gazzano, M. Strontium-Substituted Hydroxyapatite Nanocrystals. *Inorganica Chim. Acta* **2007**, *360* (3), 1009–1016.

(41) Akiva, A.; Kerschnitzki, M.; Pinkas, I.; Wagermaier, W.; Yaniv, K.; Fratzl, P.; Addadi, L.; Weiner, S. Mineral Formation in the Larval Zebrafish Tail Bone Occurs via an Acidic Disordered Calcium Phosphate Phase. *J. Am. Chem. Soc.* **2016**, *138* (43), 14481–14487.

(42) Folliet, N.; Roiland, C.; Bégu, S.; Aubert, A.; Mineva, T.; Goursot, A.; Selvaraj, K.; Duma, L.; Tielens, F.; Mauri, F.; et al. Investigation of the Interface in Silica-Encapsulated Liposomes by Combining Solid State NMR and First Principles Calculations. *J. Am. Chem. Soc.* **2011**, *133* (42), 16815–16827.

(43) Baron, R.; Neff, L.; Louvard, D.; Courtoy, P. J. Acidification and Bone Cell-Mediated Extracellular Evidence for a Low PH in Resorbing Lacunae Resorption : Of a 100-KD Lysosomal Membrane Protein and Localization at the Osteoclast Ruffled Border. *J. Cell Biol.* **1985**, *101* (6), 2210–2222.

(44) Querido, W.; Campos, A. P. C.; Martins Ferreira, E. H.; San Gil, R. A. S.; Rossi, A. M.; Farina, M. Strontium Ranelate Changes the Composition and Crystal Structure of the Biological Bone-like Apatite Produced in Osteoblast Cell Cultures. *Cell Tissue Res.* **2014**, *357* (3), 793–801.

(45) Verberckmoes, S. C.; Behets, G. J.; Oste, L.; Bervoets, A. R.; Lamberts, L. V.; Drakopoulos, M.; Somogyi, A.; Cool, P.; Dorriné, W.; De Broe, M. E.; et al. Effects of Strontium on the Physicochemical Characteristics of Hydroxyapatite. *Calcif. Tissue Int.* **2004**, *75* (5), 405–415.

(46) Fuchs, R. K.; Allen, M. R.; Condon, K. W.; Reinwald, S.; Miller, L. M.; McClenathan, D.; Keck, B.; Phipps, R. J.; Burr, D. B. Strontium Ranelate Does Not Stimulate Bone Formation in Ovariectomized Rats. *Osteoporos. Int.* **2008**, *19* (9), 1331–1341.

(47) Paschalis, E. P.; Betts, F.; DiCarlo, E.; Mendelsohn, R.; Boskey, A. L. FTIR Microspectroscopic Analysis of Human Iliac Crest Biopsies from Untreated Osteoporotic

Bone. *Calcif. Tissue Int.* **1997**, *61* (6), 487–492.

(48) Paschalis, E. P.; Fratzl, P.; Gamsjaeger, S.; Hassler, N.; Brozek, W.; Eriksen, E. F.; Rauch, F.; Glorieux, F. H.; Shane, E.; Dempster, D.; et al. Aging Versus Postmenopausal Osteoporosis: Bone Composition and Maturation Kinetics at Actively-Forming Trabecular Surfaces of Female Subjects Aged 1 to 84 Years. *J. Bone Miner. Res.* **2016**, *31* (2), 347–357.

(49) Koutsopoulos, S. Synthesis and Characterization of Hydroxyapatite Crystals: A Review Study on the Analytical Methods. *J. Biomed. Mater. Res.* **2002**, *62* (4), 600–612.

(50) Chickerur, N. S.; Tung, M. S.; Brown, W. E. A Mechanism for Incorporation of Carbonate into Apatite. *Calcif. Tissue Int.* **1980**, *32* (1), 55–62.

(51) Fleet, M. E. Infrared Spectra of Carbonate Apatites: N2-Region Bands. *Biomaterials* **2009**, *30* (8), 1473–1481.

(52) Antonakos, A.; Liarokapis, E.; Leventouri, T. Micro-Raman and FTIR Studies of Synthetic and Natural Apatites. *Biomaterials* **2007**, *28* (19), 3043–3054.

(53) Rey, C.; Renugopalakrishnan, V.; Collins, B.; Glimcher, M. J. Fourier Transform Infrared Spectroscopic Study of the Carbonate Ions in Bone Mineral during Aging. *Calcif. Tissue Int.* **1991**, *49*, 251–258.

(54) Wang, Y.; Azaïs, T.; Robin, M.; Vallée, A.; Catania, C.; Legriel, P.; Pehau-Arnaudet, G.; Babonneau, F.; Giraud-Guille, M. M.; Nassif, N. The Predominant Role of Collagen in the Nucleation, Growth, Structure and Orientation of Bone Apatite. *Nat. Mater.* **2012**, *11* (8), 724–733.

(55) Farlay, D.; Boivin, G.; Panczer, G.; Lalande, A.; Meunier, P. J. Long-Term Strontium Ranelate Administration in Monkeys Preserves Characteristics of Bone Mineral Crystals and Degree of Mineralization of Bone. *J. Bone Miner. Res.* **2005**, *20* (9), 1569–1578.

(56) Oste, L.; Bervoets, A. R.; Behets, G. J.; Dams, G.; Marijnissen, R. L.; Geryl, H.; Lamberts, L. V.; Verberckmoes, S. C.; Van Hoof, V. O.; De Broe, M. E.; et al. Time-Evolution and Reversibility of Strontium-Induced Osteomalacia in Chronic Renal Failure Rats. *Kidney Int.* **2005**, *67* (3), 920–930.

(57) D'Haese, P. C.; Schrooten, I.; Goodman, W. G.; Cabrera, W. E.; Lamberts, L. V.; Elseviers, M. M.; Couttenye, M. M.; De Broe, M. E. Increased Bone Strontium Levels in Hemodialysis Patients with Osteomalacia. *Kidney Int.* **2000**, *57* (3), 1107–1114.

(58) Jokes, J. F. H.; Chemistry, P. The metabolism of calcium and phosphorus as influenced by the addition to the diet of salts of metals which form insoluble phosphates. *Am. J. Physiol.* **1938**, 124 (1),230–237.

(59) Bechkoff, G.; Radisson, J.; Bessueille, L.; Bouchekioua-Bouzaghou, K.; Buchet, R. Distinct Actions of Strontium on Mineral Formation in Matrix Vesicles. *Biochem. Biophys. Res. Commun.* **2008**, *373* (3), 378–381.

(60) Brooks, B. R.; III, C. L. B.; A. D. Mackerell, J.; Nilsson, L.; Petrella, R. J.; Roux, B.; Won, Y.; Archontis, G.; Bartels, C.; Boresch, S.; et al. CHARMM: The Biomolecular Simulation Program B. *J. Comput. Chem.* **2009**, *30* (10), 1545–1614.

(61) Laurencin, D.; Almora-Barrios, N.; de Leeuw, N. H.; Gervais, C.; Bonhomme, C.; Mauri, F.; Chrzanowski, W.; Knowles, J. C.; Newport, R. J.; Wong, A.; et al. Magnesium Incorporation into Hydroxyapatite. *Biomaterials* **2011**, *32* (7), 1826–1837.

(62) Bazin, D.; Dessombz, A.; Nguyen, C.; Ea, H. K.; Lioté, F.; Rehr, J.; Chappard, C.; Rouzière, S.; Thiaudière, D.; Reguer, S.; et al. The Status of Strontium in Biological Apatites: An XANES/EXAFS Investigation. *J. Synchrotron Radiat.* **2014**, *21* (1), 136–142.

(63) Boivin, G.; Meunier, P. J. The Mineralization of Bone Tissue: A Forgotten Dimension in

Osteoporosis Research. *Osteoporos. Int.* **2016**, *14* (3), 19–24.
(64) Marie, P. J.; Ammann, P.; Boivin, G.; Rey, C. Mechanisms of Action and Therapeutic Potential of Strontium in Bone. *Calcif. Tissue Int.* **2001**, *69* (3), 121–129.
(65) Littlewood, J. L.; Shaw, S.; Peacock, C. L.; Bots, P.; Trivedi, D.; Burke, I. T. Mechanism of Enhanced Strontium Uptake into Calcite via an Amorphous Calcium Carbonate Crystallization Pathway. *Cryst. Growth Des.* **2017**, *17* (3), 1214–1223.
(66) Kim, T. G.; Park, B. Synthesis and Growth Mechanisms of One-Dimensional Strontium Hydroxyapatite Nanostructures. *Inorg. Chem.* **2005**, *44* (26), 9895–9901.
(67) Zhang, T. H.; Liu, X. Y. How does a transient amorphous precursor template crystallization. *J. Am. Chem. Soc.* **2007**, 129 (44), 13520–13526.
(68) Gower, L. B. Biomimetic Model Systems for Investigating the Amorphous Precursor Pathway and Its Role in Biomineralization. *Chem. Rev.* **2008**, *108* (11), 4551–4627.
(69) Chung, S. Y.; Kim, Y. M.; Kim, J. G.; Kim, Y. J. Multiphase Transformation and Ostwalds Rule of Stages during Crystallization Of a metal Phosphate. *Nat. Phys.* **2009**, *5* (1), 68–73.
(70) Addadi, L.; Raz, S.; Weiner, S. Taking Advantage of Disorder: Amorphous Calcium Carbonate and Its Roles in Biomineralization. *Adv. Mater.* **2003**, *15* (12), 959–970.
(71) Whittaker, M. L.; Sun, W.; Derocher, K. A.; Jayaraman, S.; Ceder, G.; Joester, D. Structural Basis for Metastability in Amorphous Calcium Barium Carbonate (ACBC). *Adv. Funct. Mater.* **2018**, 28 (2), *1704202*.
(72) Zou, Z.; Habraken, W. J. E. M.; Matveeva, G.; Jensen, A. C. S.; Bertinetti, L.; Hood, M. A.; Sun, C.; Gilbert, P. U. P. A.; Polishchuk, I.; Pokroy, B.; et al. A Hydrated Crystalline Calcium Carbonate Phase: Calcium Carbonate Hemihydrate. *Science* **2019**, *363* (6425), 396–400.
(73) Fontaine, A. La; Zavgorodniy, A.; Liu, H.; Zheng, R.; Swain, M.; Cairney, J. Atomic-Scale Compositional Mapping Reveals Mg-Rich Amorphous Calcium Phosphate in Human Dental Enamel. *Sci. Adv.* **2016**, *2* (9), e1601145.
(74) Luther, G. W.; Rickard, D. T.; Navrotsky, A.; Navrotsky, A.; Navrotsky, A.; Mazeina, L.; Majzlan, J.; Tang, R. K.; Wang, L. J.; Nancollas, G. H.; et al. Iron Oxides. *Science* **2008**, *319* (3), 1635–1639.
(75) Navrotsky, A. Energetic Clues to Pathways to Biomineralization: Precursors, Clusters, and Nanoparticles. *Proc. Natl. Acad. Sci.* **2004**, *101* (33), 12096–12101.
(76) De Yoreo, J. J.; Gilbert, P. U. P. A.; Sommerdijk, N. A. J. M.; Penn, R. L.; Whitelam, S.; Joester, D.; Zhang, H.; Rimer, J. D.; Navrotsky, A.; Banfield, J. F.; et al. Crystallization by Particle Attachment in Synthetic, Biogenic, and Geologic Environments. *Science* **2015**, *349* (6247), aaa6760.
(77) Navrotsky, A. Nanoscale Effects on Thermodynamics and Phase Equilibria in Oxide Systems. *ChemPhysChem* **2011**, *12* (12), 2207–2215.
(78) Mchale, J. M.; Auroux, A.; Perrotta, A. J.; Navrotsky, A. Surface Energies and Thermodynamic Phase Surface Energies and Thermodynamic Phase Stability in Nanocrystalline Aluminas. **2008**, *788* (1997), 788–792.

CHAPTER 3

Investigating the stability of Sr^{2+}- rich amorphous calcium phosphate in physiological environment and the role of Sr^{2+} on the early stages of bone formation

Abstract

A multistep mechanism involving calcium phosphates transient phases is proposed for bone mineral formation. Amorphous calcium phosphate (ACP) is described as a key intermediate in this process and the way it crystallizes into apatite has attracted enormous attention due to the possibility of investigating the early stages of apatite deposition. In Chapter 2, we presented the incorporation of Sr^{2+} in biomimetic apatite by performing the precipitation in homogeneous medium which revealed the formation of a Sr^{2+}- rich amorphous calcium phosphate (Sr(ACP)). Herein, in order to clarify the possible role of Sr^{2+}on the early stages of bone apatite formation, we investigated the limit of Sr^{2+} incorporation on this phase as well as its behavior in a physiological environment. Sr(ACP) was found to be stable against crystallization with increased Sr^{2+} concentration which reinforce the notion of impaired mineralization at high Sr^{2+} dosages revealed in Chapter 2. At lower Sr^{2+} concentrations, biomimetic apatite was formed incorporating higher levels of Sr^{2+} as compared to the one-step precipitation performed in homogeneous medium. This may account for the higher concentrations of Sr^{2+} where the new bone tissue forms thus suggesting the involvement of an amorphous precursor in this process. Overall, these observations shed light on the mechanisms of physiological and pathological mineralization driven by Sr^{2+}. (The results presented in this Chapter were obtained during the internship at LCMCP (BEPE-FAPESP) advised by Dr. Nadine Nassif).

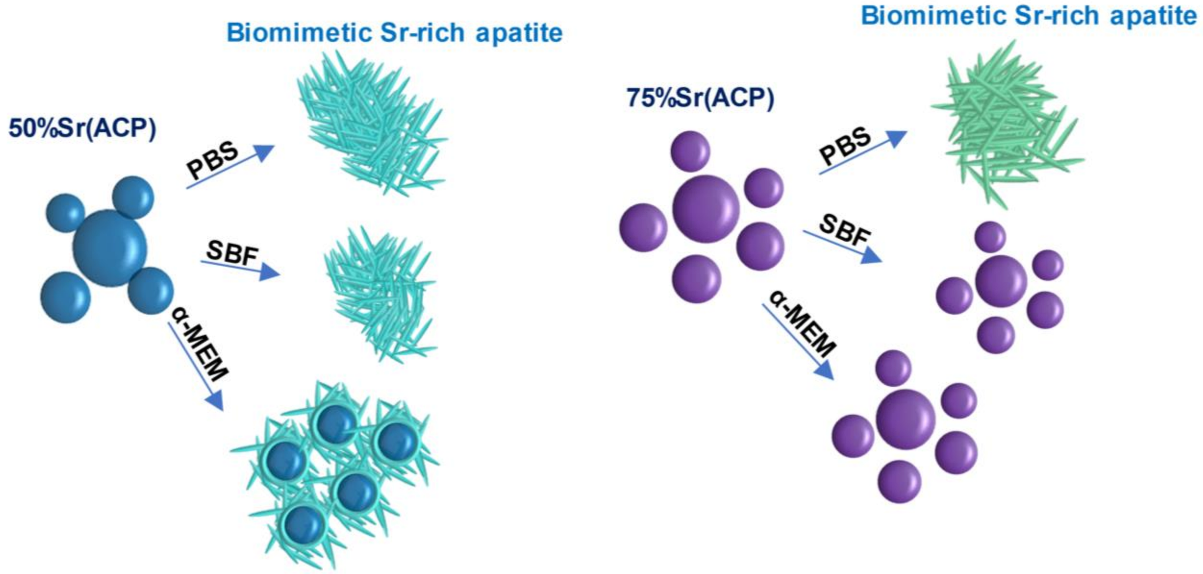

3.1 | Introduction

Unraveling the mechanisms underlying the precipitation of biomimetic apatite plays a fundamental role in understanding physiological and pathological calcifications. Studies of the nucleation and growth processes based on *in situ* cryo-transmission electron microscopy have shown that apatite forms *in vitro* through a multistep mechanism involving prenucleation cluster, amorphous precursor and solid-state reactions.[1,2] *In vivo* investigations have strengthened the notion of a disordered phosphate phase mediating bone formation by means of a non-classical mechanism as earlier proposed Termine and Posner.[3,4,5,6] Beyond bone mineralization, the formation of an amorphous precursor is believed to be an ubiquitous strategy in the biomineralization pathways of different organisms from various phyla. The crystallization of this precursor phase is regarded as the crucial step for determining the complex features of biogenic crystals *i.e.* composition, polymorph, morphology.[7,8,9] However, the molecular mechanisms modulating the lifetime of amorphous intermediates and its subsequent destabilization towards a crystalline mature product remains a matter of debate.

Organic molecules and ions like citrate, ATP, fetuin, Mg^{2+}, Zn^{2+}, $Sr^{2+}$are believed to control the early stages of bone mineralization by interacting with mineral intermediates.[10–14] Of these, the paradigm for Sr^{2+} incorporation in bone has emerged due to its widespread use in osteoporosis treatments and the realization of its distinct effects according to the dose.[15,16] Moreover, the fact that Sr^{2+} is selectively found in the regions of new bone formation suggests its involvement on the earliest stages of bioapatite deposition.[17,18] Indeed, previous studies have pointed out the formation of Sr^{2+} bearing ACP granules within the mitochondria of rats in agreement with recent evidences of the intracellular formation of ACP during bone mineralization.[19,20, 21] This notion is further supported by the fact that likewise Ca^{2+}, Sr^{2+} may be stored and transported to the extracellular matrix *via* transcellular pathways.[22,23] However, it was only recently that *in vitro* experiments have evidenced that Sr^{2+} stabilizes ACP under physiological conditions.[14,24]

Although the involvement of Sr^{2+} in the early stages of bone biomineralization is presumed, most of the investigations still rely on the mature phase of bone, i.e., apatite leading to a gap in the understanding about the role of Sr^{2+} on the pathway of bone mineralization. This is ascribed to both the challenge of probing the dynamic process of bone maturation *in vivo* and the metastability of amorphous phases which readily undergo crystallization making difficult its isolation from mature crystals.[25,26] Therefore, developing *in vitro* biomimetic models to investigate the initial phases by which Sr^{2+} is incorporated in bone is critical to clarify how this element may alters the pathway of bioapatite deposition in the scenario of physiological and pathological mineralization as well as the physicochemical basis of its therapeutic effects. Moreover, inorganic additives modulate the mineralization of many organisms. Thus, addressing the role of Sr^{2+} on the formation of bioapatite may also provide insights on the mechanisms by which nature controls the nucleation and growth of other biominerals thereby improving the current understanding and applications of biomineralization strategies.[27,28] Note also that Sr^{2+} has been reported to play a key role in the biomineralization of carbonate in marine organisms.[29,30]

Although the crystallization of ACP has been described, most of the investigations are undertaken in pure water or in saturated solutions, i.e, PBS which does not represent the biological environment where bone is formed.[31] Herein we investigated the formation of bone-like apatite from amorphous calcium phosphate stabilized by the incorporation of different amounts of Sr^{2+} (Sr(ACP)) in a physiological-like environment (alpha-MEM) where proteins, organic and inorganic ions are present. Sr(ACP) crystallizes giving rise to apatite with enhanced amount of incorporated into its lattice as compared to the direct nucleation from solution which. suggests the involvement of disordered phases during the uptake of Sr^{2+} by bone. Conversely, increased Sr^{2+} concentration in Sr(ACP) hinders its crystallization which may account for bone disorders caused by Sr^{2+} accumulation.[32,33] These results raise the possibility that the role of Sr^{2+} on bone mineralization may begin earlier than previously though. Overall this study provide insights into (i) the pathways by which Sr^{2+} is involved in physiological and pathological mineralization (ii) the formation of Sr^{2+}-rich regions in bone and (iii) the possibility of its intracellular accumulation in the form of Sr(ACP).

3.2 | Experimental procedure

3.2.1 | Mineral precipitation in homogeneous medium

Mineral precipitation was carried out on the basis of an approach developed by Nassif et al.[34] Briefly, stock $CaCl_2$ (110 mmol L^{-1}), $SrCl_2$ (110 mmol L^{-1}), NaH_2PO_4 (33 mmol L^{-1}), and $NaHCO_3$ (33 mmol L^{-1}) solutions were prepared by dissolving $CaCl_2.2H_2O$ (Sigma), $SrCl_2.6H_2O$ (Sigma), $NaHCO_3$ (Sigma), and NaH_2PO_4 (Sigma) in aqueous acetic acid (500 mmol L^{-1}) solution. 6.6 mL of $CaCl_2$, $NaHCO_3$ and NaH_2PO_4 solutions were used to prepare biomimetic apatite (HA). To prepare the Sr^{2+} bearing amorphous calcium phosphate particles (Sr(ACP)) the volume of $CaCl_2$ solution was then tuned forming $SrCl_2/CaCl_2/NaH_2PO_4/NaHCO_3$ mixtures containing different Sr^{2+} molar percentages (40, 50, 60, 75 and 80 mol%) in relation to the total number of mols of divalent cations (Ca^{2+} + Sr^{2+}). The (Ca + Sr)/(P + C) ratio was kept constant and equal to 1.67. Two flasks (35 mL, height = 50 mm) containing these solutions (20 mL) and covered with perforated (four holes) Parafilm were placed in a closed desiccator. A third flask containing fresh aqueous ammonia solution (30% wt., 8 mL) was placed in the desiccator. NH_3(g) diffusion into the flasks slowly increases the solution pH and triggered Sr-Ca phosphate precipitation. After reaction for 6 days (pH~11), the solids were filtered and washed with distilled water and then ethanol, to remove soluble salts, and centrifuged (6000 rpm, 10 min). The recovered powders were dried at 37 °C for three days before characterization.

3.2.2 | Stability of Sr(ACP) in different media

The amorphous particles containing 50 mol% of Sr^{2+}(50%Sr(ACP)) and 75% mol of Sr^{2+} (75%Sr(ACP) were suspended for 6 days in phosphate buffered saline solution (PBS), simulated body fluid (SBF) and cell culture medium (minimum essential medium, α-MEM, Gibco) supplemented with 10% (v/v) fetal bovine serum and 1% (v/v) penicillin/streptomycin. The reactants used to prepare SBF ($CaCl_2$, NaCl, $NaHCO_3$, KCl, $MgCl_2$, Na_2HPO_4, Na_2SO_4 and $C_4H_{11}NO_3$ (tris(hydroxymethyl)aminomethane)) were all analytical grade; the concentrations of the reactants and the procedure used to prepare the solution are described elsewhere.[35] In order to keep the pH constant and simulate the cell culture experiments the particles immersed in the cell culture medium were incubated in air at 37 ºC and 5% CO_2. All the suspensions were kept at 37ºC at a constant pH of 7.4.

Table 3.1 shows the composition of all the solutions used to evaluate the stability of the particles.

Table 3.1 | Ionic compositions of PBS, SBF, α-MEM and human blood plasma

Ion	**PBS (mmol L^{-1})**	**SBF (mmol L^{1})**	**α-MEM (mmol L^{1})**	**Human blood plasma (mmol L^{-1})**
Na^+	142	142	144	142
K^+	5.0	5.0	5.3	5.0
Mg^{2+}	-	1.5	0.8	1.5
Ca^{2+}	-	2.5	1.8	2.5
Cl^-	103	103	120	103
HCO_3^-	-	27	26	27.0
HPO_4^{2-}	1.0	1.0	1.0	1.0
SO_4^{2-}	-	0.5	0.8	0.5

3.2.3 | Characterization of the samples

The samples were characterized using Raman spectroscopy, infrared spectroscopy, energy dispersive spectroscopy, transmission electron microscopy and selected area diffraction as described in Chapter 2.

3.3 | Results and discussion

3.3.1 | Setting the limits of Sr^{2+} concentration for HA amorphization

Initially, we evaluated the possibility of incorporating different amounts of Sr^{2+} within the Sr(ACP) particles by performing experiments with Sr^{2+} concentration (mol %) ranging from 40% to 80% in the starting solutions.

The sample 40%Sr^{2+} displays an amorphous typical wavy background together with few diffraction peaks, suggesting the coexistence of an amorphous phase and poorly crystalline HA (Figure 3.1[aii]). As expected, the complete inhibition of HA formation was observed at 50% Sr^{2+}, thus setting the lower limit of Sr^{2+} incorporation to trigger the complete amorphization of HA (Figure 3.1a[iii]). By increasing the Sr^{2+} concentration it was found that 80 mol % was the highest limit of Sr^{2+} incorporation within the ACP phase (Figure 3.1a[vi]). After that a crystalline phase emerged, as observed in the diffractogram (Figure 3.1a[vii]). The infrared spectra of the 40% (Figure 3.1b[ii]) and 90% Sr^{2+} (Figure 3.1b[vii]) samples display sharper band nearly at 1100 cm^{-1} ascribed to the ν_3 asymmetric stretching of PO_4^{3-} groups as compared to the 50%, 60%, 75% and 80% Sr^{2+} samples (Figure 3.1b[iii-vi]). Moreover, the unfolding of the PO_4^{3-} ν_4 asymmetric bending at ~ 600 cm^{-1}, which is typical from crystalline phosphate, is not observed for the latter samples as expected from XRD data (Figure 3.1c[iii-vi]). Raman spectra were obtained to support the loss of long-range order in the samples (Figure 3.1d and Figure 3.1e). The 40%Sr^{2+} sample displays sharp bands similarly to HA while the other samples display broad bands typical from amorphous phosphate (Figure 3.1d[ii] and Figure 3.1e[ii]). The splitting in the band of the 90%Sr^{2+} sample suggests the formation of secondary phosphate phase (Figure 3.1e[vii]).

Overall, these results show the higher ability of amorphous phosphate in incorporating foreign ions as compared to apatite. After setting the limit range of Sr^{2+} incorporation within Sr(ACP), we studied their behavior in a physiological context.

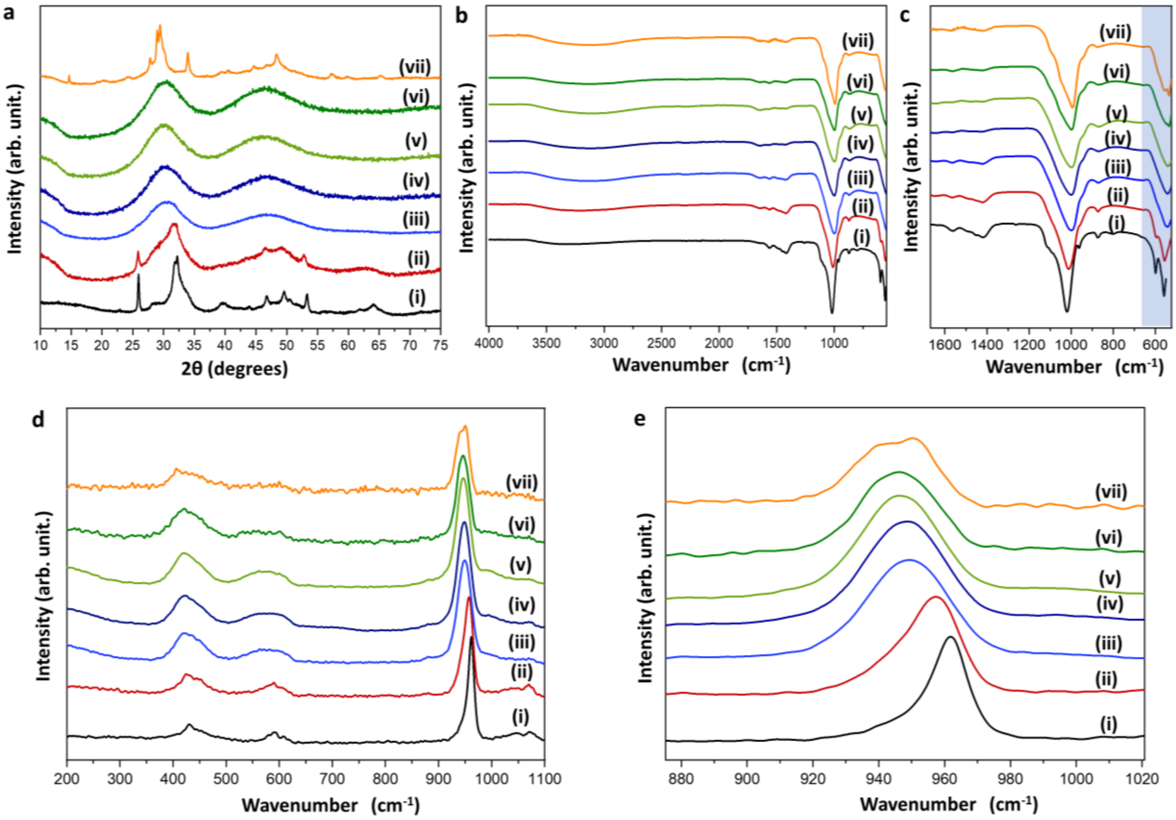

Figure 3.1 | XRD patterns (a), FTIR spectra (b) with enlarged view between the region from 1600 to 600 cm^{-1} with the ν_4 vibrational mode highlighted in blue (c), Raman spectra (d) with enlarged view showing the ν_1 vibrational mode (e) of the samples: 0% Sr^{2+} (i), 40% Sr^{2+} (ii), 50% Sr^{2+} (iii), 60% Sr^{2+} (iv), 75 % Sr^{2+} (v), 80% Sr^{2+} (vi) and 90% Sr^{2+} (vii). Diffractogram and spectra of biomimetic apatite (HA, 0% Sr^{2+}) were shown to highlight its formation in the samples.

3.3.2 | The stability of Sr(ACP) depends on the Sr^{2+} concentration and the composition of environment

The stability of the Sr(ACP) particles was investigated in different media to gain insights towards their behavior in bone tissue environment (e.g., extracellular matrix). Therefore, to understand the influence of ionic composition and macromolecules on this process, the particles were dispersed in different solutions ranging from simple PBS until the complex cell culture medium. We have chosen the 50%Sr(ACP) and 75%Sr(ACP) samples because they differ considerably in the amount of Sr^{2+} and were previously characterized (Chapter 2).[14]

After exposure to the different media, diffractograms from 50%Sr(ACP) and 75%Sr(ACP) particles bring an interesting result: while 50%Sr(ACP) invariably undergoes crystallization into biomimetic apatite(Figure3.2a), 75%Sr(ACP) crystallizes only after contact with PBS (Figure 3.2c). This suggests that the stability of Sr(ACP) depends on the

Sr^{2+} concentration and the composition of the environment. Moreover, the shift of the 002 peaks in the XRD patterns to smaller angles in comparison to the 0%Sr^{2+} sample indicates the incorporation of Sr^{2+} into lattices of the apatite products (Figure 3.2b). This is ascribed to the Ca^{2+} (114 pm) substitution by Sr^{2+} (132 pm) in the apatite lattice which in turn leads to the increase of the interplanar distances.[36] Such a displacement is even higher for the apatite formed *via* the conversion of 75%Sr(ACP) upon immersion in PBS thus suggesting a higher degree of Sr^{2+} incorporation (Figure 3.2d).

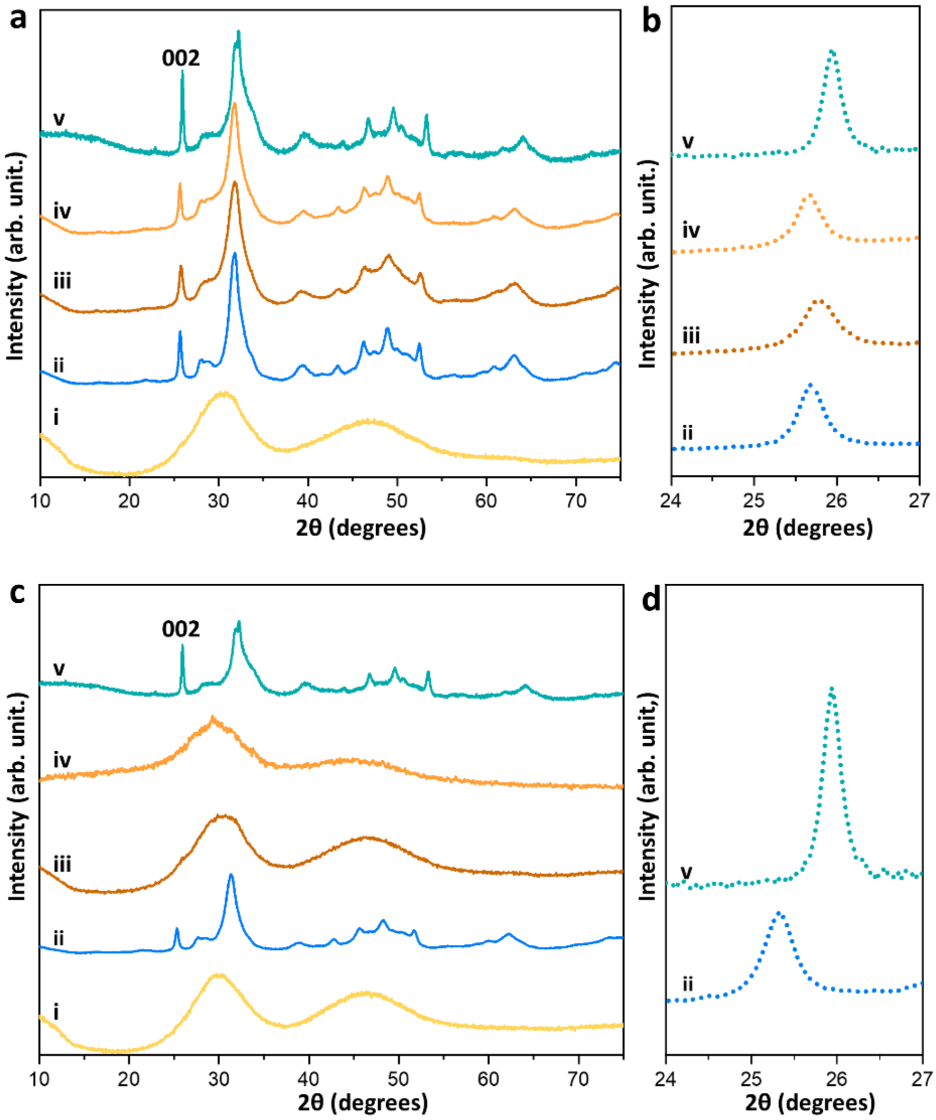

Figure 3.2 | XRD patterns of 50%Sr(ACP) (a-b) and 75%Sr(ACP) (c-d) before (i) and after 6 days of immersion in PBS (ii), SBF (iii) and cell culture medium (iv). The diffractogram of pure apatite (v) synthesized by precipitation in homogeneous medium is displayed to characterize the structural changes in the products from Sr(ACP) crystallization. The 002 peak was displaced towards smaller values of 2θ in the products obtained from 50%Sr(ACP) (b) and 75%Sr(ACP) (c) crystallization confirming the incorporation of Sr^{2+} into the apatite lattice.

Narrower bands typical of PO_4^{3-} in apatite structure are observed in the Raman spectra after immersion of 50%Sr(ACP) into all the media (Figure 3.3a[ii-iii]) and 75%Sr(ACP) into PBS (Figure 3.3c[ii]), strengthening the crystallization of the amorphous particles. The Sr^{2+} incorporation in the apatite lattice is further supported by the displacement of ν_1 band towards lower wavenumbers (Figure 3.3b[ii-iii] and Figure 3.3 d[ii]). Noticeably, no changes were noted in the broad PO_4^{3-} Raman bands of 75%Sr(ACP) after exposure to SBF therefore supporting its stability towards crystallization.

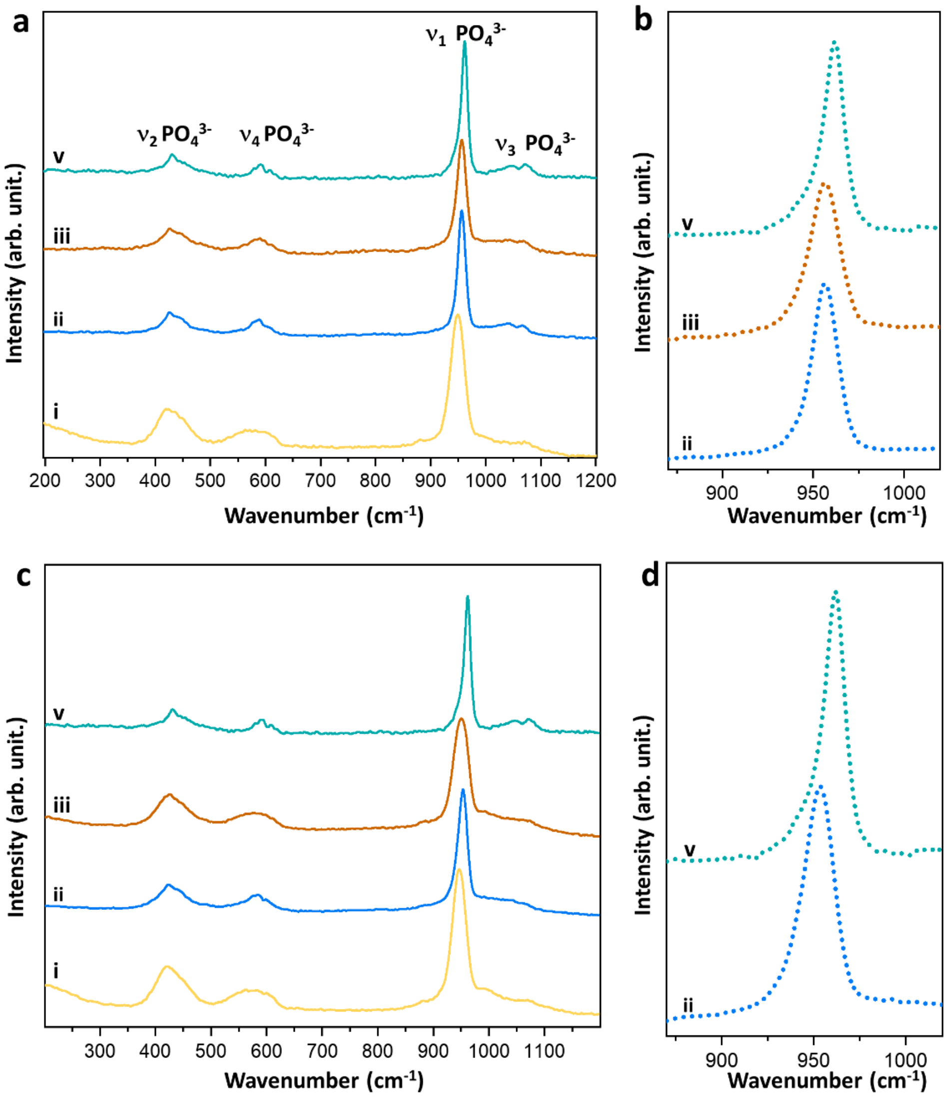

Figure 3.3| Raman spectra of 50%Sr(ACP) (a-b) and 75%Sr(ACP) before (i) and after 6 days immersion in PBS (ii) and SBF (iii). The spectrum of pure apatite is also displayed (v). The ν_1 band associated to the symmetric stretching of PO_4^{3-} is displaced towards smaller wavenumber values due to Sr^{2+} incorporation into the apatite lattice of the products from (b) 50%Sr(ACP) and (d) 75%Sr(ACP) crystallization.

The broad ν_3 and ν_4 PO_4^{3-} bands in the infrared spectra also confirm that 75%Sr(ACP) did not crystallize within SBF and cell culture medium (Figure 3.4b[iii-iv]). Conversely, these bands are sharper in the spectra of 50%Sr(ACP) after immersion in both PBS and SBF, and 75%Sr(ACP) after immersion in PBS, resembling those from apatite.[37] Additionally, the absorptions bands at 870 cm^{-1} and 1360–1580 cm^{-1} indicate the presence of CO_3^{2-} in the samples (CO_3^{2-} ν_2 out of plane deformation and ν_3 asymmetric stretching, respectively). Carbonate substitution is a fingerprint of the mineral phase found in bone tissue and tooth enamel being the B-type (replacement of phosphate) the most common.[38,39] Interestingly, this ion is also present as additive in biological amorphous calcium phosphate and is thought to influence its stability and conversion pathway. [40]

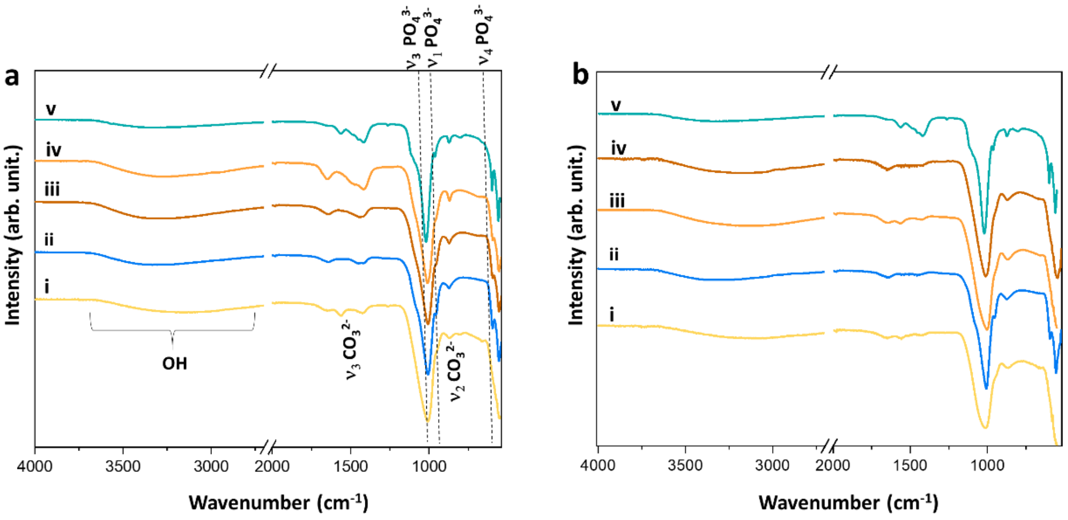

Figure 3.4 | Infrared spectra of 50%Sr(ACP) (a) and 75%Sr(ACP) (b) before (i) and after 6 days immersion in PBS (ii), SBF (iii) and cell culture medium (iv). The spectrum of pure apatite is also displayed (v). The ν_4 band associated to asymmetric bending of PO_4^{3-} is unfolded as Sr(ACP) crystallizes.

The mechanism of amorphous to crystalline conversion has been subject of a long debate. Dissolution/recrystallization, direct solid-state transformation and even a combination of multiple mechanisms have been proposed.[26,41]

In PBS, Ca^{2+} and Sr^{2+} ions released from the surface of the 50%Sr(ACP) and 75%Sr(ACP) particles are expected to react with PO_4^{3-} from the medium triggering locally the supersaturation towards apatite which is the more thermodynamically stable phase.[42] As the crystalline phase nucleates, the amorphous precursors are continuously consumed ensuring the formation and growth of new crystals nuclei.[43] However, when foreign ions and macromolecules are present in the medium such processes may be altered leading to different conversion rates and products, as observed for herein.[44]

The unexpected high stability of 75%Sr(ACP) within SBF and cell culture medium may be a matter of ionic force and carbonate content. In fact, SBF contains carbonate ions. In addition, the samples exposed to the culture medium were maintained in a CO_2 flux to keep the pH constant reproducing the conditions used in the cell culture experiments. It is described in the literature that carbonate species act as inhibitors of ACP dissolution by complexing Ca^{2+} present at the surface. [45,46] By means of solution speciation calculations, it was shown that the effect of carbonate on ACP crystallization is a competing mechanism through the formation of ion pairs with Ca^{2+}.[47] Finally, it should be noted that Mg^{2+}, which is also shown to stabilize ACP is present in both, SBF and cell culture media. [45,48]

Besides inorganic ions, the cell culture medium contains organic molecules including citrate and serum proteins which may also account to the enhanced stability of the 75%Sr(ACP) sample in SBF when compared to PBS. As usually proposed, an explanation is that such molecules bind to ACP mainly by the interactions between its negatively charged moieties and interfacial Ca^{2+} leading to a reduced exposure of ACP to the solution.[49,50] Consequently, the dissolution rate is decreased. Organic molecules are also shown to hinder the motion and aggregation of amorphous particles.[10] Another possible mechanism is the formation of complexes between organic molecules and Ca^{2+} and Sr^{2+} released from the particles lowering the free ion concentration needed to reach the critical supersaturation.[51,52] Notably, serum ions and proteins play a fundamental role in inhibiting apatite precipitation in non-calcified regions avoiding pathological mineralization.[12,53]

In order to understand the mechanisms of 50%Sr(ACP) and 75%Sr(ACP) conversion, TEM images were recorded before and after their exposure to each medium. The 50%Sr(ACP) and 75%Sr(ACP) particles display spherical morphology with diameters ranging from 200-500 nm (Figure 3.5a[i-iii] and 3.5b[i-iii] respectively). SAED patterns display diffuse rings strengthening their amorphous nature (insert Figure 3.5a[ii] and 3.5b[ii]). As shown in Chapter 2 by TEM images, the 50%Sr(ACP) spheres display some poorly crystalline apatitic domains at the surface (Figure 3.5a[iii]), contrasting to the bare surface of the 75%Sr(ACP) particles (Figure 3.5b[iii]). Because the formation of the first crystalline nucleus is regarded as the activation for ACP crystallization, the 50%Sr(ACP) spheres may experience a lower energetic barrier towards crystallization as compared to the 75%Sr(ACP).[54,55] This mechanism was characterized by Eanes and Posner as autocatalytic.[56] Given such thermodynamic aspect, it is reasonable that 50% Sr^{2+}(ACP) is converted into apatite regardless the medium. This finding suggests that the ongoing mechanism of Sr(ACP) conversion into apatite is driven by heterogeneous nucleation at the surface of the amorphous particles followed by the propagation of the crystalline phase *via* secondary nucleation from one domain to the next one.[57] However, non-classical mechanism involving particles aggregation cannot be excluded.[58]

The products of 50%Sr(ACP) and 75%Sr(ACP) crystallization form spherulitic aggregates composed of nanometric platelets typical of biological apatite (Figure 3.5a[iv-x]). The higher contrast in the outer layer suggests that the apatite spherulites are hollow and that the crystals nucleated on the Sr(ACP) surface grew by material diffusion from the inner towards the surface, thereby supporting the mechanism proposed for Sr(ACP) conversion. Additionally, TEM images of the 50%Sr(ACP) sample after immersion in the cell culture medium reveal that amorphous spherical particles remain together with the apatite spherulites. This suggests a slower conversion rate in this medium (Figure 3.5a[vi] and 3.5a[ix]) that is most likely due to the adsorption of organic components at the surface of the particles as previously discussed. As expected, the morphology of the 75%Sr(ACP) sample was not altered after the exposition to SBF and cell culture medium (Figure 3.5b(v-vi)].

The pathways of Sr(ACP) crystallization rises interesting insights into the paradigm of Sr^{2+} signature in bone mineral.[59] The limited incorporation rate of Sr^{2+} in bone irrespective of the administrated dose is a classic example of how efficient mineralized organisms are in differentiate Ca^{2+} and Sr^{2+}.[60] However, herein we demonstrate that such selection did not take place in ACP. The incorporation of Sr^{2+} was proportional to the amount added in the precursor solution thus reaching values even higher than that of Ca^{2+}. Considering the current models of bone biomineralization suggesting that the formation of apatite is preceded by an acidic disordered calcium phosphate phase, our results tends to show that the discrimination against Sr^{2+} in bone occurs with the tissue maturation.[3] This may account for the heterogeneous distribution of Sr^{2+} in bone with the highest concentration in regions of newly formed mineral.[17,61] In agreement with this idea, the amount of Sr^{2+} in bone decreases as the mineral phases evolves towards mature apatite where only faintly adsorbed ions are found.[59] Besides precursor for bone mineral, there is a consensus in literature over the presence of ACP at the surface of biological apatite which may explains partially why Sr^{2+} is often found superficially bounded rather than in the crystalline lattice of bone. [15,39, 59,62,]

The unexpected high stability of 75%Sr(ACP) in physiological environment can be rationalized in terms of the Sr^{2+}dose dependent effect on bone. At high levels, Sr^{2+} retards apatite crystallization leading to bone disorders such as osteomalacia and rickets.[33,63] It also opens new possibilities about how Sr^{2+} is transported with phosphates inside the cells at a high concentration regime.

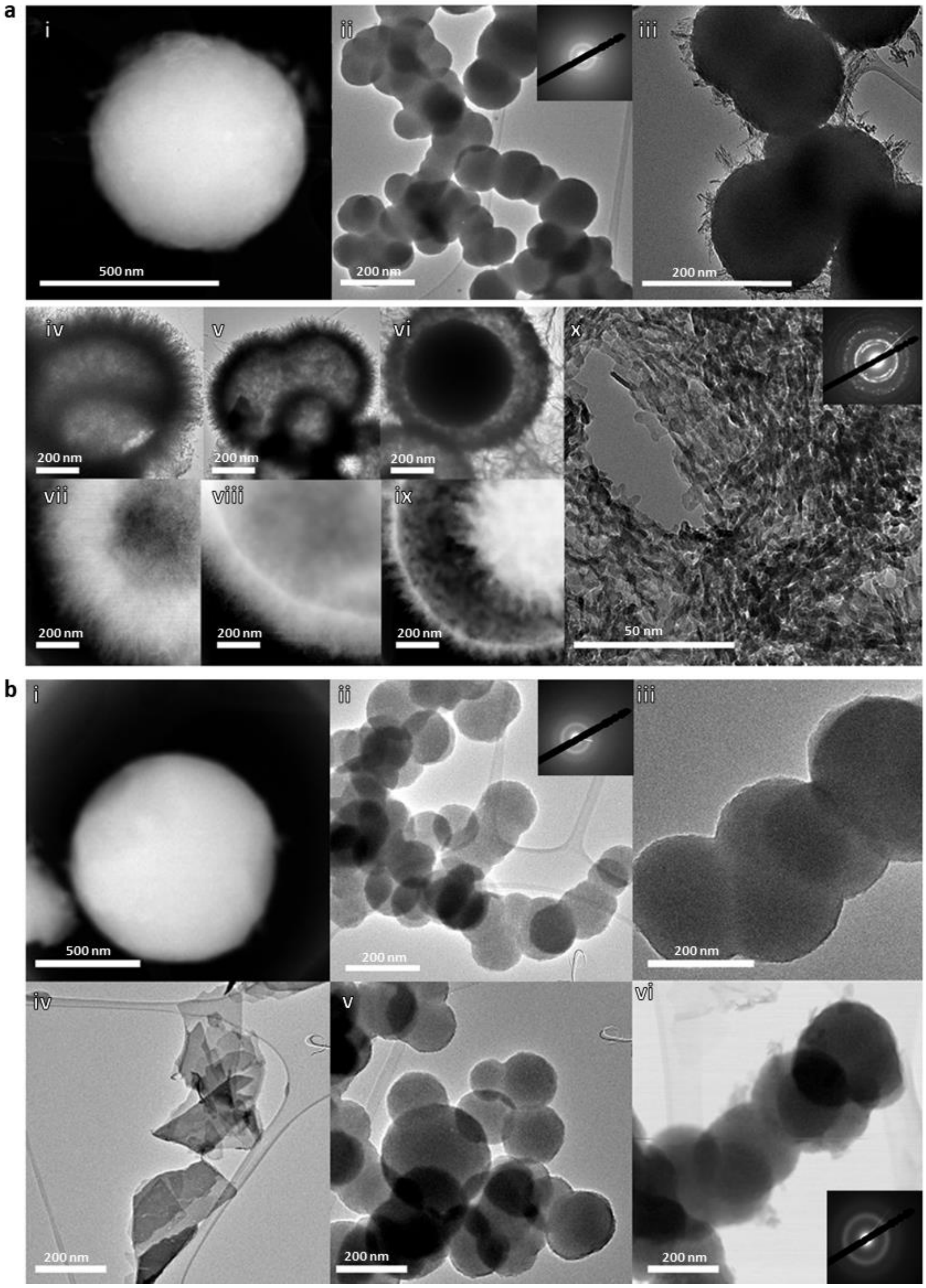

Figure 3.5 | TEM images of 50%Sr(ACP) (a) before (i-iii) and after 6 days immersion in PBS (iv-vii), SBF (v-viii) and cell culture medium (vi-ix). Bright (iv-vi) and dark (vii-ix) field images reveal that the apatite platelets form hollow spheres. (x) High magnification image of 50%Sr(ACP) after crystallization in PBS. Insets in images are typical SAED patterns from amorphous and apatite samples. TEM images of 75%Sr(ACP) (b) before (i-iii) and after 6 days immersion in PBS (iv), SBF (v) and cell culture medium (vi).

3.3.3 | *In vitro* synthesis of high Sr^{2+} doped biomimetic apatite under ambient conditions and its implication for biomineralization process

To understand the relationship between the concentration of Sr^{2+} incorporated within ACP and the structural properties of its crystallization products, we investigated in more detail the apatite samples formed after the immersion of 50%Sr(ACP) and 75% Sr(ACP) in PBS.

EDS analysis reveal a Sr content (mol%) of 40% and 60% in the 50%Sr(ACP) and 75%Sr(ACP) samples, respectively. After crystallization, EDS analysis show a Sr content of 30% and 60% in the apatite samples formed from the crystallization of the 50%Sr(ACP) and 60% Sr(ACP) samples respectively. This reveals that Sr^{2+} is transferred from the amorphous particles to its crystallization products i.e. biomimetic apatite. This was also confirmed by the shift in the Raman and XRD reflections as previously shown. EDS mappings show that Ca and Sr were homogeneously distributed throughout the apatite crystals without evidence of phase segregation (Figure 3.6).

Our results show that by using an amorphous precursor phase it is possible to enhance the Sr^{2+} incorporation into the lattice of biomimetic apatite at physiological conditions giving rise to crystals with Sr^{2+} concentration up to 60 mol%. This is an interesting result since in the Chapter 2 we found that (i) no more than 10 mol% of Sr^{2+} could be incorporated into biomimetic apatite without phase segregation and (ii) an amorphous phase was the only product when the precipitation was undertaken in homogeneous medium at 50 mol% Sr^{2+}. Thus, it turns out to be easier to control the formation of Sr^{2+}-rich apatite (40-60 mol%) by performing apart the precipitation and crystallization of Sr(ACP) in a two-step process. Likewise, some mineralized organisms seem to control the biomineralization process to accumulate ions such as Mg^{2+} and Zn^{2+} through non-classical mechanism involving a transient amorphous phase.[8] This is classically exemplified by the sea urchin teeth which contains high amounts of magnesium substituting calcium in the crystal lattice. Contrarily to *in vitro* experiments in which high Mg^{2+} doped calcite is hardly formed under ambient conditions this is achieved biologically through the formation of Mg^{2+}-rich amorphous calcium carbonate as an intermediate. Hence, its crystallization into calcite within confined environment decreases the likelihood of Mg^{2+} loss. However, it is challenging to reproduce this synthetic route due to the metastability of amorphous phases. Moreover, the ionic content (Mg^{2+}, Sr^{2+}, Zn^{2+}) is usually not preserved upon crystallization.[7]

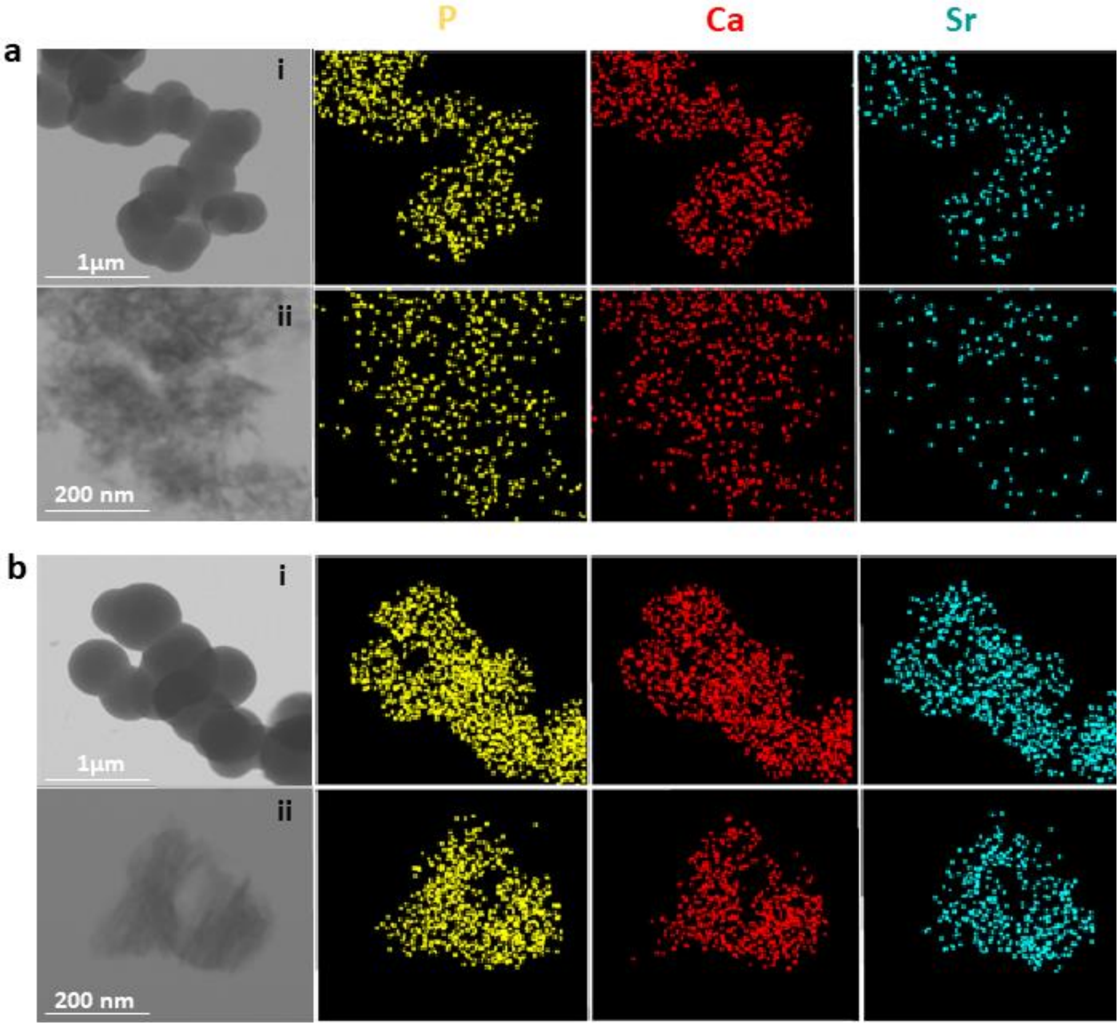

Figure 3.6 | TEM images of 50%Sr(ACP) (a) and 75%Sr(ACP) (b) before (i) and after (ii) 6 days immersion in PBS. TEM- EDS mappings show the homogeneous distribution of P (yellow), Ca (red) and Sr (cyan) elements within the samples.

Although the amount of Sr^{2+} (mol%) used herein is rather far from the physiological condition, our results provide some insights into the initial phases and underlying mechanisms by which Sr^{2+} is transported and accumulated in bone. Moreover, this simple approach leads to the design of Sr^{2+} bearing biomimetic apatite potentially applicable in osteoporosis treatments without the need of using organic additives or high temperatures.

3.4 | Conclusions

The stability of Sr(ACP) in physiological medium was found to be highly dependent upon (i) the environment composition and (ii) Sr^{2+} concentration. While 50%Sr(ACP) undergoes crystallization into biomimetic apatite irrespectively of the medium, 75%Sr(ACP) displayed enhanced stability in the medium with composition similar to the environment of bone formation, i.e., SBF and cell culture medium. Considering the mechanism of bone apatite formation, which involves an amorphous precursor, this result suggests the involvement of Sr^{2+} in the early stages of bone mineralization. Moreover, the crystallization of 50%Sr(ACP) resulted in the formation of biomimetic apatite containing high amounts of Sr^{2+}. This result contrasted with those obtained from the direct precipitations in solution in which a maximum of 10 mol% Sr^{2+} could be incorporated within apatite without phase segregation. This suggests that the formation of Sr^{2+}-rich regions in bone may transverse an amorphous precursor pathway in agreement with the contemporary theories of mineralization.

3.5 | References

(1) Wang, X.; Yang, J.; Andrei, C. M.; Soleymani, L.; Grand, K. Biomineralization of Calcium Phosphate Revealed by in Situ Liquid-Phase Electron Microscopy. *Commun. Chem.* **2018**, *1* (1), 80.

(2) Dey, A.; Bomans, P. H. H.; Müller, F. A.; Will, J.; Frederik, P. M.; De With, G.; Sommerdijk, N. A. J. M. The Role of Prenucleation Clusters in Surface-Induced Calcium Phosphate Crystallization. *Nat. Mater.* **2010**, *9* (12), 1010–1014.

(3) Akiva, A.; Kerschnitzki, M.; Pinkas, I.; Wagermaier, W.; Yaniv, K.; Fratzl, P.; Addadi, L.; Weiner, S. Mineral Formation in the Larval Zebrafish Tail Bone Occurs via an Acidic Disordered Calcium Phosphate Phase. *J. Am. Chem. Soc.* **2016**, *138* (43), 14481–14487.

(4) Mahamid, J.; Sharir, A.; Addadi, L.; Weiner, S. Amorphous Calcium Phosphate Is a Major Component of the Forming Fin Bones of Zebrafish: Indications for an Amorphous Precursor Phase. *Proc. Natl. Acad. Sci. U. S. A.* **2008**, *105* (35), 12748–12753.

(5) Posner, A. S.; Betts, F. Synthetic Amorphous Calcium Phosphate and Its Relation to Bone Mineral Structure. *Acc. Chem. Res.* **1975**, *8* (8), 273–281.

(6) Termine, J. D.; Posner, A. S. Infrared Analysis of Rat Bone: Age Dependency of Amorphous and Crystalline Mineral Fractions. *Science* **1966**, *153* (3743), 1523–1525.

(7) Gower, L. B. Biomimetic Model Systems for Investigating the Amorphous Precursor Pathway and Its Role in Biomineralization. *Chem. Rev.* **2008**, *108* (11), 4551–4627.

(8) Weiner, S.; Mahamid, J.; Politi, Y.; Ma, Y.; Addadi, L. Overview of the Amorphous Precursor Phase Strategy in Biomineralization. *Front. Mater. Sci. China* **2009**, *3* (2), 104–108.

(9) Addadi, L.; Raz, S.; Weiner, S. Taking Advantage of Disorder: Amorphous Calcium Carbonate and Its Roles in Biomineralization. *Adv. Mat.* **2003**, 15(12), 959–970.

(10) Chatzipanagis, K.; Iafisco, M.; Roncal-Herrero, T.; Bilton, M.; Tampieri, A.; Kröger, R.; Delgado-López, J. M. Crystallization of Citrate-Stabilized Amorphous Calcium Phosphate to Nanocrystalline Apatite: A Surface-Mediated Transformation. *CrystEngComm* **2016**, *18* (18), 3170–3173.

(11) Posner, A. S. Intramitochondrial storage of stable amorphous calcium phosphate. *Ann. N. Y. Acad. Sci.* **1978**, *307* (1), 248–249.

(12) Heiss, A.; Eckert, T.; Aretz, A.; Richtering, W.; Van Dorp, W.; Schäfer, C.; Jahnen-Dechent, W. Hierarchical Role of Fetuin-A and Acidic Serum Proteins in the Formation and Stabilization of Calcium Phosphate Particles. *J. Biol. Chem.* **2008**, *283* (21), 14815–14825.

(13) Procopio, A.; Malucelli, E.; Pacureanu, A.; Cappadone, C.; Farruggia, G.; Sargenti, A.; Castiglioni, S.; Altamura, D.; Sorrentino, A.; Giannini, C.; et al. Chemical Fingerprint of Zn–Hydroxyapatite in the Early Stages of Osteogenic Differentiation. *ACS Cent. Sci.* **2019**, *5* (8), 1449–1460.

(14) Bussola Tovani, C.; Gloter, A.; Azaïs, T.; Selmane, M.; Ramos, A. P.; Nassif, N. Formation of Stable Strontium-Rich Amorphous Calcium Phosphate: Possible Effects on Bone Mineral. *Acta Biomater.* **2019**, *92*, 315–324.

(15) Marie, P. J.; Ammann, P.; Boivin, G.; Rey, C. Mechanisms of Action and Therapeutic Potential of Strontium in Bone. *Calcif. Tissue Int.* **2001**, *69* (3), 121–129.

(16) D'Haese, P. C.; Schrooten, I.; Goodman, W. G.; Cabrera, W. E.; Lamberts, L. V.;

Elseviers, M. M.; Couttenye, M. M.; De Broe, M. E. Increased Bone Strontium Levels in Hemodialysis Patients with Osteomalacia. *Kidney Int.* **2000**, *57* (3), 1107–1114.

(17) Li, C.; Paris, O.; Siegel, S.; Roschger, P.; Paschalis, E. P.; Klaushofer, K.; Fratzl, P. Strontium Is Incorporated into Mineral Crystals Only in Newly Formed Bone during Strontium Ranelate Treatment. *J. Bone Miner. Res.* **2010**, *25* (5), 968–975.

(18) Boivin, G.; Farlay, D.; Khebbab, M. T.; Jaurand, X.; Delmas, P. D.; Meunier, P. J. In Osteoporotic Women Treated with Strontium Ranelate, Strontium Is Located in Bone Formed during Treatment with a Maintained Degree of Mineralization. *Osteoporos. Int.* **2010**, *21* (4), 667–677.

(19) Skoryna, S. C. Effects of Oral Supplementation with Stable Strontium. *Can. Med. Assoc. J.* **1981**, *125* (7), 703–712.

(20) Somlyo, A. P.; Somlyo, A. V.; Devine, C. E.; Peters, P. D.; Hall, T. A. Electron Microscopy and Electron Probe Analysis of Mitochondrial Cation Accumulation in Smooth Muscle. *J. Cell Biol.* **1974**, *61* (3), 723–742.

(21) Boonrungsiman, S. The Role of Intracellular Calcium Phosphate in Osteoblast-Mediated Bone Apatite Formation. *Proc. Natl. Acad. Sci.* **2012**, *109* (35), 14170–14175.

(22) PEACHEY, L. D. Electron Microscopic Observations on the Accumulation of Divalent Cations in Intramitochondrial Granules. *J. Cell Biol.* **1964**, *20*, 95–111.

(23) Selwyn, M. J.; Dawson, A. P.; Dunnett, S. J. Calcium Transport in Mitochondria. *FEBS Lett.* **1970**, *10* (1), 1–5.

(24) Jin, W.; Liu, Z.; Wu, Y.; Jin, B.; Shao, C.; Xu, X.; Tang, R.; Pan, H. Synergic Effect of Sr^{2+} and Mg^{2+} on the Stabilization of Amorphous Calcium Phosphate. *Cryst. Growth Des.* **2018**, *18* (10), 6054–6060.

(25) Mahamid, J.; Aichmayer, B.; Shimoni, E.; Ziblat, R.; Li, C.; Siegel, S.; Paris, O.; Fratzl, P.; Weiner, S.; Addadi, L. Mapping Amorphous Calcium Phosphate Transformation into Crystalline Mineral from the Cell to the Bone in Zebrafish Fin Rays. *Proc. Natl. Acad. Sci. U. S. A.* **2010**, *107* (14), 6316–6321.

(26) Lotsari, A.; Rajasekharan, A. K.; Halvarsson, M.; Andersson, M. Transformation of Amorphous Calcium Phosphate to Bone-like Apatite. *Nat. Commun.* **2018**, *9* (1), 4170.

(27) Littlewood, J. L.; Shaw, S.; Peacock, C. L.; Bots, P.; Trivedi, D.; Burke, I. T. Mechanism of Enhanced Strontium Uptake into Calcite via an Amorphous Calcium Carbonate Crystallization Pathway. *Cryst. Growth Des.* **2017**, *17* (3), 1214–1223.

(28) Albéric, M.; Bertinetti, L.; Zou, Z.; Fratzl, P.; Habraken, W.; Politi, Y. The Crystallization of Amorphous Calcium Carbonate Is Kinetically Governed by Ion Impurities and Water. *Adv. Sci.* **2018**, *5* (5), 1701000.

(29) Allison, N.; Finch, A. A.; Sutton, S. R.; Newville, M. Strontium Heterogeneity and Speciation in Coral Aragonite: Implications for the Strontium Paleothermometer. *Geochim. Cosmochim. Acta* **2001**, *65* (16), 2669–2676.

(30) Tovani, C. B.; Oliveira, T. M.; Gloter, A.; Ramos, A. P. Sr^{2+}-Substituted CaCO3Nanorods: Impact on the Structure and Bioactivity. *Cryst. Growth Des.* **2018**, *18* (5), 2932–2940.

(31) Buckwalter, J. A.; Glimcher, M. J.; Cooper, R. R.; Recker, R. Bone Biology. *Instr. Course Lect.* **1996**, *45*, 371–386.

(32) Oste, L.; Bervoets, A. R.; Behets, G. J.; Dams, G.; Marijnissen, R. L.; Geryl, H.; Lamberts, L. V.; Verberckmoes, S. C.; Van Hoof, V. O.; De Broe, M. E.; et al. Time-Evolution and Reversibility of Strontium-Induced Osteomalacia in Chronic Renal Failure Rats. *Kidney Int.* **2005**, *67* (3), 920–930.

(33) Storey, E. Strontium “ rickets ” : bone, calcium and strontium changes. *Australas. Ann. Med.* **1961**, *10* (3), 213–222.

(34) Nassif, N.; Martineau, F.; Syzgantseva, O.; Gobeaux, F.; Willinger, M.; Coradin, T.; Cassaignon, S.; Azaïs, T.; Giraud-Guille, M. M. In Vivo Inspired Conditions to Synthesize Biomimetic Hydroxyapatite. *Chem. Mater.* **2010**, *22* (12), 3653–3663.

(35) Kokubo, T.; Takadama, H. How Useful Is SBF in Predicting in Vivo Bone Bioactivity? *Biomaterials* **2006**, *27* (15), 2907–2915.

(36) Bigi, A.; Boanini, E.; Capuccini, C.; Gazzano, M. Strontium-Substituted Hydroxyapatite Nanocrystals. *Inorganica Chim. Acta* **2007**, *360* (3), 1009–1016.

(37) Koutsopoulos, S. Synthesis and Characterization of Hydroxyapatite Crystals: A Review Study on the Analytical Methods. *J. Biomed. Mater. Res.* **2002**, *62* (4), 600–612.

(38) Rey, C.; Collins, B.; Goehl, T.; Dickson, I. R.; Glimcher, M. J. The Carbonate Environment in Bone Mineral : A Resolution-Enhanced Fourier Transform Infrared Spectroscopy Study. **1989**, 157–164.

(39) Wang, Y.; Von Euw, S.; Laurent, G.; Crevant, C.; Bonhomme-Coury, L.; Giraud-Guille, M. M.; Babonneau, F.; Nassif, N.; Azaïs, T. Impact of Collagen Confinement vs. Ionic Substitutions on the Local Disorder in Bone and Biomimetic Apatites. *Mater. Horizons* **2014**, *1* (2), 224–231.

(40) Nitiputri, K.; Ramasse, Q. M.; Autefage, H.; McGilvery, C. M.; Boonrungsiman, S.; Evans, N. D.; Stevens, M. M.; Porter, A. E. Nanoanalytical Electron Microscopy Reveals a Sequential Mineralization Process Involving Carbonate-Containing Amorphous Precursors. *ACS Nano* **2016**, *10* (7), 6826–6835.

(41) Boskey, A. L.; Posner, A. S. Conversion of Amorphous Calcium Phosphate to Microcrystalline Hydroxyapatite. A PH-Dependent, Solution-Mediated, Solid-Solid Conversion. *J. Phys. Chem.* **1973**, *77* (19), 2313–2317.

(42) Eanes, E. D.; Termine, J. D.; Nylen, M. U. An Electron Microscopic Study of the Formation of Amorphous Calcium Phosphate and Its Transformation to Crystalline Apatite. *Calcif. Tissue Res.* **1973**, *12* (1), 143–158.

(43) Wang, C. G.; Liao, J. W.; Gou, B. Di; Huang, J.; Tang, R. K.; Tao, J. H.; Zhang, T. L.; Wang, K. Crystallization at Multiple Sites inside Particles of Amorphous Calcium Phosphate. *Cryst. Growth Des.* **2009**, *9* (6), 2620–2626.

(44) Termine, J. D.; Peckauskas, R. A.; Posner, A. S. Calcium Phosphate Formation in Vitro. II. Effects of Environment on Amorphous-Crystalline Transformation. *Arch. Biochem. Biophys.* **1970**, *140* (2), 318–325.

(45) Cao, X.; Harris, W. Carbonate and Magnesium Interactive Effect on Calcium Phosphate Precipitation. *Environ. Sci. Technol.* **2008**, *42* (2), 436–442.

(46) Kapolos, J.; Koutsoukos, P. G. Formation of Calcium Phosphates in Aqueous Solutions in the Presence of Carbonate Ions. *Langmuir* **1999**, *15* (19), 6557–6562.

(47) Song, Y.; Hahn, H. H.; Hoffmann, E. The Effect of Carbonate on the Precipitation of Calcium Phosphate. *Environ. Technol.* **2002**, *23* (2), 207–215.

(48) Gelli, R.; Ridi, F.; Baglioni, P. The Importance of Being Amorphous: Calcium and Magnesium Phosphates in the Human Body. *Adv. Colloid Interface Sci.* **2019**, *269*, 219–235.

(49) Rees, S. G.; Hughes Wassell, D. T.; Shellis, R. P.; Embery, G. Effect of Serum Albumin on Glycosaminoglycan Inhibition of Hydroxyapatite Formation. *Biomaterials* **2004**, *25* (6), 971–977.

(50) Sharma, V. K.; Johnsson, M.; Nancollas, G. H.; Johnsson, M.; Nancollas, G. H.; Sallis, J.

D. Influence of Citrate and Phosphocitrate on the Crystallization of Octacalcium Phosphate. *Langmuir* **1992**, *8* (2), 676–679.

(51) Martins, M. A.; Santos, C.; Almeida, M. M.; Costa, M. E. V. Hydroxyapatite Micro- and Nanoparticles: Nucleation and Growth Mechanisms in the Presence of Citrate Species. *J. Colloid Interface Sci.* **2008**, *318* (2), 210–216.

(52) Chen, Y.; Gu, W.; Pan, H.; Jiang, S.; Tang, R. Stabilizing Amorphous Calcium Phosphate Phase by Citrate Adsorption. *CrystEngComm* **2014**, *16* (10), 1864–1867.

(53) Garnett, J.; Dieppe, P. The Effects of Serum and Human Albumin on Calcium Hydroxyapatite Crystal Growth. *Biochem. J.* **1990**, *266* (3), 863–868.

(54) Meyer, J.L. Eanes, E. D. A Thermodynamic Analysis of the Amorphous to Crystalline Calcium Phosphate Transformation. *Calcif. Tiss. Res.* **1978**, *25*, 59–68.

(55) Jiang, S.; Pan, H.; Chen, Y.; Xu, X.; Tang, R. Amorphous Calcium Phosphate Phase-Mediated Crystal Nucleation Kinetics and Pathway. *Faraday Discuss.* **2015**, *179*, 451–461.

(56) Eanes, E. D.; Posner, A. S. Division of biophysics: kinetics and mechanism of conversion of noncrystalline calcium phosphate to crystalline hydroxyapatite. *Trans. N. Y. Acad. Sci.* **1965**, *28* (2), 233–241.

(57) Pan, H.; Liu, X. Y.; Tang, R.; Xu, H. Y. Mystery of the Transformation from Amorphous Calcium Phosphate to Hydroxyapatite. *Chem. Commun.* **2010**, *46* (39), 7415–7417.

(58) De Yoreo, J. J.; Gilbert, P. U. P. A.; Sommerdijk, N. A. J. M.; Penn, R. L.; Whitelam, S.; Joester, D.; Zhang, H.; Rimer, J. D.; Navrotsky, A.; Banfield, J. F.; et al. Crystallization by Particle Attachment in Synthetic, Biogenic, and Geologic Environments. *Science* **2015**, *349* (6247), aaa6760.

(59) Dahl, S. G.; Allain, P.; Marie, P. J.; Mauras, Y.; Boivin, G.; Ammann, P.; Tsouderos, Y.; Delmas, P. D.; Christiansen, C. Incorporation and Distribution of Strontium in Bone. *Bone* **2001**, *28* (4), 446–453.

(60) Boivin, G.; Deloffre, P.; Perrat, B.; Panczer, G.; Boudeulle, M.; Mauras, Y.; Allain, P.; Tsouderos, Y.; Meunier, P. J. Strontium Distribution and Interactions with Bone Mineral in Monkey Iliac Bone after Strontium Salt (S 12911) Administration. *J. Bone Miner. Res.* **2009**, *11* (9), 1302–1311.

(61) Boivin, G.; Farlay, D.; Khebbab, M. T.; Jaurand, X.; Delmas, P. D.; Meunier, P. J. In Osteoporotic Women Treated with Strontium Ranelate, Strontium Is Located in Bone Formed during Treatment with a Maintained Degree of Mineralization. *Osteoporos. Int.* **2010**, *21* (4), 667–677.

(62) Wang, Y.; Von Euw, S.; Fernandes, F. M.; Cassaignon, S.; Selmane, M.; Laurent, G.; Pehau-Arnaudet, G.; Coelho, C.; Bonhomme-Coury, L.; Giraud-Guille, M. M.; et al. Water-Mediated Structuring of Bone Apatite. *Nat. Mater.* **2013**, *12* (12), 1144–1153.

(63) Schrooten, I.; Elseviers, M. M.; Lamberts, L. V.; De Broe, M. E.; D'Haese, P. C. Increased Serum Strontium Levels in Dialysis Patients: An Epidemiological Survey. *Kidney Int.* **1999**, *56* (5), 1879–1885.

CHAPTER 4

Towards new insights about the effect of Sr^{2+} on collagen network in bone tissue

Abstract

Clinical reports of pathological mineralization are described for excess of Sr^{2+}.Whilst synthetic apatites are extensively used in attempts to unveil the effect of Sr^{2+} on bone, studies comprising the effect of this ion on both the organic and mineral parts of this tissue have not been accomplished to date. In this Chapter, we present the incorporation of Sr^{2+} in a biomimetic model based on dense and organized mineralized collagen matrices which reproduce the hierarchical architecture of bone at the ultrastructural level. The formation of such matrices is based on the self-assembly process of collagen/apatite in which collagen fibrillogenesis and apatite coprecipitation are trigged *in vitro*. In Chapter 2, it was shown that high Sr^{2+} doses destabilize the crystalline structure of apatite leading to the formation of an amorphous phase Sr(ACP). Going further, here, we show that this process is accompanied by destabilization of collagen network bringing unexplored to date effects of Sr^{2+} at bone organization. These findings provide new insights into the understanding of Sr^{2+}-based therapies unveiling the mechanisms governing bone disorders caused by excess of Sr^{2+} such as osteomalacia and rickets. (The results presented in this Chapter were obtained during the internship at LCMCP (BEPE-FAPESP) advised by Dr. Nadine Nassif).

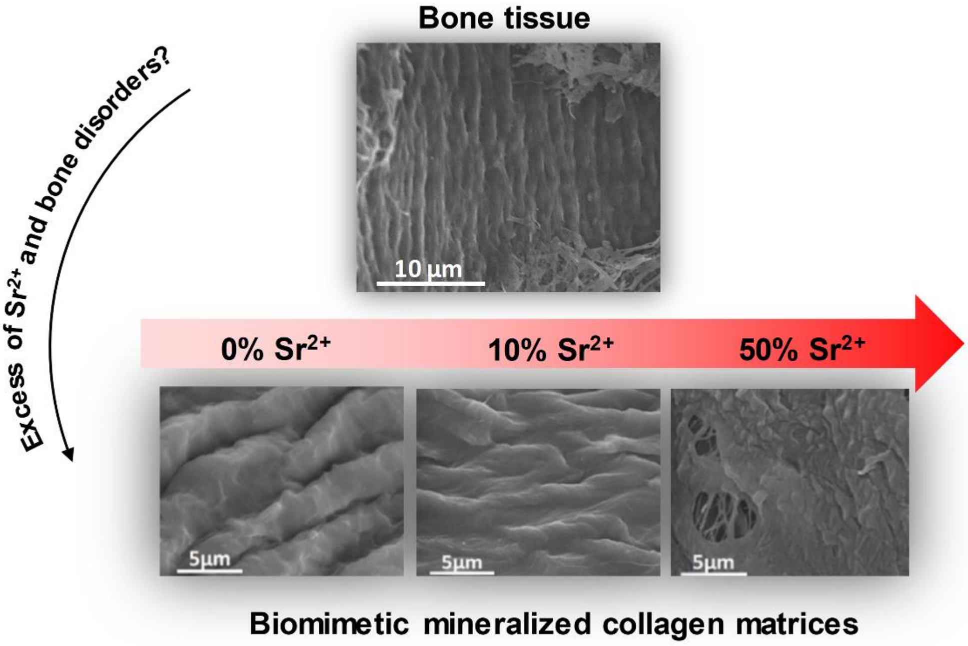

4.1 | Introduction

Strontium ions are the active component of strontium ranelate, a drug which reduces vertebral and nonvertebral fractures in osteoporotic patients.[1] This finding has in turn encouraged the incorporation of Sr^{2+} into biomaterials and organic molecules aiming at bone healing.[2] Although the widespread interest in Sr^{2+}-based biomaterials has emerged over the last years the mechanisms underlying its involvement in the formation of bone tissue as well as the possible effects resulting from its accumulation in the tissue has received by far less attention. Clinical studies have reported the development of pathological mineralization due to the excess of Sr^{2+} reinforcing the need of deeper investigations on the action of this ion at the molecular level of bone.[3] In fact, while the effects of Sr^{2+} in animals with normal renal functions depend on the administrated dose, this element is readily accumulated in the bone of patients with impaired renal functions leading to the mineralization defects, i.e., osteomalacia and rickets.[4,5] Therefore, investigating the possible effects of Sr^{2+} accumulation in bone is of paramount significance since elderly people who may present decreased renal function are the main target of osteoporosis treatments.[6]

The oral intake increases the level of Sr^{2+} in serum; however, little is known about its intracellular uptake and even less about the impacts behind its incorporation in the bone extracellular matrix.[7] Although essentially found in the mineral phase of bone, Sr^{2+} is also present in the extracellular matrix bonded on the surface and, in both inter and intrafibrillar spacings of collagen fibrils.[8] Apart this consideration, the possible involvement of Sr^{2+} in the organic/inorganic interface of bone has been neglected so far. In fact, the use of Sr^{2+} is mostly described and thought as beneficial, with the reported effect being the reduction of bone fracture by increasing bone density.[9]

Numerous studies rely on the mineral phases of bone, i.e., apatite, produced mainly by *in vitro* precipitation and in mineralized cell cultures.[10,11,12] In these cases, the effects of Sr^{2+} are described in terms of structural strains at the crystal level of apatite. Hence, discarding the role of Sr^{2+} in a biologically relevant model which mimics the hierarchical and organic/inorganic hybrid characteristic of bone tissue.

Bone mineralization is a complex process which involves cells and a multitude of ions, proteins and lipids in orchestrated mechanisms to build a hybrid material described with a fractal-like organization.[13] Type I collagen is the preponderant organic component of the bone extracellular matrix and is fundamental for the hierarchical organization and strength in this tissue.[14,15] During bone formation, collagen molecules self-assemble into fibrils, which are mineralized by apatite crystals. The distribution and size of apatite crystals found in the osteogenesis imperfecta bone disease stresses out the relevance of having a hierarchically organized collagen matrix for mineral deposition.[16,17]

Given the fundamental role of collagen on bone mineralization the development of models able to reproduce the main structural features of this tissue, i.e, dense and organized collagen matrix with co-aligned apatite nanoplatelets, is essential for an holistic understanding about the effects of Sr^{2+} on bone.[14,18] Nevertheless, reproducing *in vitro* such a complex architecture of bone is not straightforward and oversimplified systems may yield a limited overview. The use of a too low collagen concentration (below 40 mg mL^{-1}) leads to a lack of order and only the level of individual mineralized collagen fibrils can be reproduced.[14,19,20]

Here, we present the mineralization of biomimetic collagen matrices in the presence of different content of Sr^{2+} (mol%) in relation to Ca^{2+} namely 10% Sr^{2+} which is the physiological limit of incorporation in bone, and 50% Sr^{2+} mimicking a situation of pathological excess. By doing so, we found that excess of Sr^{2+} lead to the simultaneous destabilization of apatite and collagen network bringing unexplored to date effects of Sr^{2+} at bone organization. Complementary, preosteoblastic cells cultured on the collagen matrices mineralized at 0% Sr^{2+} and 10%Sr^{2+} displayed normal activity while impaired adhesion and mineralization was found at 50%Sr^{2+} in agreement with the scenario of bone disorders caused by Sr^{2+} accumulation.[21,22,23] Therefore, our biomimetic model reproduces the multiple effects of Sr^{2+} found *in vivo*.[24,25,26]

Overall, our results contribute to unveil the physicochemical mechanisms governing the role of Sr^{2+} on bone at therapeutic and pathological dosages.

4.2 | Experimental procedure

4.2.1 | Collagen extraction

Type I collagen monomers were extracted from rat tail tendons following a classical procedure.[27] Briefly, fresh tendons were washed with phosphate buffered saline (PBS) solution to remove traces of cells and blood and then solubilized in 0.5 mol.L^{-1} acetic acid. The crude solution was centrifuged, and the supernatant selectively precipitated with 0.7 mol L^{-1} NaCl. Precipitated type I collagen was solubilized in 0.5 mol L^{-1} acetic acid and desalted by dialysis against 0.5 mol L^{-1} acetic acid. The collagen concentration in the stock solution was determined as follow and then adjusted to 3 mg ml^{-1}.

4.2.2 | Determination of collagen concentration

The concentration of type I collagen solutions was assessed by hydroxyproline titration.[28] Briefly, 50 μL of the collagen solution (or 50 mg of collagen matrix) was mixed with 50 μL of 33% (v/v) aqueous HCl. After homogenization, the mixture was kept at 110 ºC. This step allows the cleavage of peptic bonding in the collagen molecule thus releasing the hydroxyproline residues. Sequentially, 1 mL of H_2O was added to the mixture followed by the addition of aqueous solution of 7% (v/v) chloramine-T ($CH_3C_6H_4SO_2NClNa$) which oxidizes the hydroxyproline residues. The reaction is then stopped by the addition of a solution of 66% (v/v) dimethylamino-4-benzaldehyde prepared in 60% (v/v) aqueous perchloric acid. While the perchloric acid stops the reaction, the dimethylamino-4-benzaldehyde leads to the formation of a purple complex. Parallelly, the same procedure was performed using hydroxy-L-proline standard solutions to build a calibration curve. Finally, the absorbance was read at 557 nm for the colored solutions and the concentration of collagen was determined by using the Lambert-Beer law.

4.2.3 | Preparation of mineralized collagen matrices

Disk-shaped collagen matrices with a thickness of ~3 mm and width of ~12 mm were prepared by the combination of continuous injection and reverse dialysis.[29] 15 mL of 1 mg mL^{-1} collagen acidic solution was mixed with $SrCl_2/CaCl_2/NaH_2PO_4/NaHCO_3$ acidic solution (0.5 mol L^{-1} acetic acid). Mixtures containing different Sr^{2+} molar percentages (namely 0, 10 and 50%) in relation to the total number of moles of divalent cations (Ca^{2+} + Sr^{2+}) were prepared. The (Ca + Sr)/(P + C) ratio was kept constant and equal to 1.67 and pH ~ 3.5. The concentrations of the salt precursors were $CaCl_2$ (46.1 mmol L^{-1}), $SrCl_2$ (46.1 mmol L^{-1}), NaH_2PO_4 (13.8 mmol L^{-1}) and $NaHCO_3$ (13.8 mmol L^{-1}). The collagen/salts mixtures were continually injected in a closed dialysis mold (Figure 4.1a). The bottom of the chamber was a dialysis membrane with a molecular weight cut off of 12–14 kDa (Figure 4.1b). Reverse dialysis process was performed against polyethylene glycol (PEG, 35 kDa, Fluka) dissolved in 0.5 mol L^{-1} acetic acid up to 300 mg ml^{-1}. It is important to note that the ionic precursors of apatite were dissolved in both, the collagen and the PEG solution. The global ionic strength (165.9 mmol L^{-1}) was kept constant throughout the process and was close to that described in physiological conditions. The flow of the collagen solution was controlled to maintain the same pressure on each side of the dialysis membrane. After complete collagen injection, dialysis was continued for 4 days in order to obtain homogeneous samples. Then, by increasing the pH in the range of 9 to 10 by NH_3 diffusion for 4 days, precipitation of collagen fibrils and mineral were simultaneously trigged. Finally, the matrices were then removed from the dialysis chamber and continuously washed with PBS (pH=7.4) in order to reach neutral pH. All the experiments were carried out at controlled temperature (19 ± 2 °C) in order to prevent collagen denaturation and sterility conditions were applied throughout the procedure.

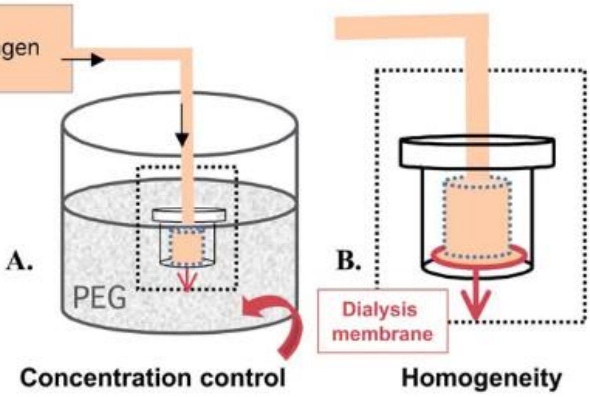

Figure 4.1 | Scheme of the process combining continuous injection and reverse dialysis. The collagen solution at low concentration (3 mg mL^{-1}) was continuously injected into a closed dialysis chamber against PEG solution (a). The final concentration of collagen in the chamber was controlled by the concentration of PEG (b). Dialysis was carried out by a dialysis membrane set at the bottom of the mold. The form of mold defines the 3D shape and the slow rate of injection in turn controls the homogeneous distribution of collagen molecules withing the matrix. Figure extracted with permission from Ref. 20, Copyright 2011 Royal Society of Chemistry.

4.2.4 | Bone sample

The sample was harvested from 2-year-old healthy French sheep. The study was reviewed and approved by Institutional Animal Care and Use Committee prior to starting.

4.2.5 | Sample Characterization

4.2.5.1 | Histological preparation for observations by microscopy

Samples were fixed in 4% paraformaldehyde (Merck France) in PBS for 24 h, dehydrated through successive ethanol baths (v/v 70%-24h, 95%-3h and 100%-3h) followed by 3 days bath in butan-1-ol and embedded in paraffin. Thick sections of 7 mm, transverse to the sample surface, were stained with picrosirius. This red staining is a useful tool to appraise collagen networks in normal and pathological tissues.

4.2.5.2 | Light microscopy under polarized light

Histological sections were observed with a Nikon E600 POL microscope between crossed polarizers. Images were taken using a Nikon CCD camera.

4.2.5.3 | Samples preparation for scanning and transmission electron microscopy

For SEM analysis the matrices were fixed in 3.6% glutaraldehyde in PBS (v/v) and dehydrated through successive ethanol baths (v/v 30%, 50%, 70%, 80%, 90%, 95% and 100%) for supercritical CO_2 drying performed on a BAL-TEC 030.

4.2.5.4 | Scanning and transmission electron microscopies

Samples coated with gold (10 nm layer) were studied by SEM using a Hitachi model S-3400N SEM at an accelerating voltage of 9 kV. For TEM observations, the samples were fixed with glutaraldehyde, dehydrated through successive ethanol baths (v/v 70%-24 h, 95%-3 h and 100%-3 h) and embedded in araldite. Ultrathin araldite sections (80 nm) were contrasted with uranyl acetate and analyzed with a FEI TECMAI G2 Spirit Twin electron microscope operating at 120 kV.

4.2.5.5 | Thermogravimetric analysis (TGA)

Experiments were performed on a thermo-microbalance instrument (TG 209 F1, Netzsch GmbH, Selb, Germany) with the air-dried sample. The measurement was performed from 20 °C to 800 °C in an air atmosphere with a heating rate of 10 °C min^{-1}.

4.2.6 | Cell culture experiments

4.2.6.1 | Cell viability – MTT assay

Osteoblastic lineage cells MC3T3-E1 (American Type Culture Collection-ATCCt) were cultured in a minimum essential medium (α-MEM, Gibco) supplemented with 10% fetal bovine serum and 1% (v/v) penicillin/streptomycin. This is a lineage with an osteoblastic phenotype that undergoes a proliferation–differentiation sequence, leading to the mineralization of bone-like extracellular matrix. The osteogenic medium was achieved by the addition of ascorbic acid and beta-glycerophosphate. Firstly, the collagen matrices were plated on the 24-well plates for 24 h to equilibrate with the culture medium. Then, the cells were seeded on the matrices at the density 2 x 10^4 cells per well and incubated in air at 37 °C with 5% CO_2. The culture medium was changed every two days. Cell viability was determined by the classic MTT assay after 7, 14 and 21 days of culture using the protocol described by Mosmann.[30] Cell viability was expressed as the percentage of the average of three experiments as compared to the control (Ct) without treatment for each day of culture (100%).

For the phosphate particles, the cells were first seeded on 24-well plates at the density 2.10^4 cells per well and incubated in air at 37 °C and 5% CO_2. The plated cells were then allowed to attach to the polystyrene well bottoms for 24h, followed by the replacement of the medium for a suspension of the particles at 1 μg mL^{-1} in the culture medium. The culture medium was changed every two days keeping constant the concentration of the particles. Cell viability was determined by MTT assay after 7 and 14 days of culture. Cell viability was expressed as the percentage of the average of three experiments as compared to the control (Ct) without treatment for each day of culture (100%).

4.2.6.2 | Alkaline phosphatase (ALP) activity

ALP activity was determined by quantifying the hydrolysis of the substrate p-nitrophenyl phosphate (PNPP) in the plasma membrane fraction extracted from cells after 7 and 14 days of culture, according to the protocol described elsewhere.[31] The enzymatic activity was normalized by the total protein content which was estimated in the presence of 2% (w/v) sodium dodecyl sulfate using bovine serum albumin as standard.

4.2.6.3 | Cell morphology

The cells cultured on the collagen matrices were fixed in 1.5% glutaraldehyde(v/v) at 4 ºC for 12 h, dehydrated through a series of ethanol concentrations (v/v, 20, 50, 70, 80, 90 and 100%) dried using super-critical CO_2 conditions and contrasted with osmium (Ribeirão Preto Medical School- University of São Paulo). After coated with gold the samples were observed on a Zeiss-EVO 50 SEM microscope under 20 kV accelerating voltage.

4.3 | Results and discussion

4.3.1 | Characterization of collagen matrices

The collagen matrices display a disk-shaped morphology provided by the dialysis chamber where the collagen solution was concentrated irrespective of their compostion (Figure 4.2.). Therefore, Sr^{2+} did not influence the macroscopic organization of the samples. According to the hydroxyproline titration, matrices with collagen concentrations of 250 mg mL^{-1} were obtained.

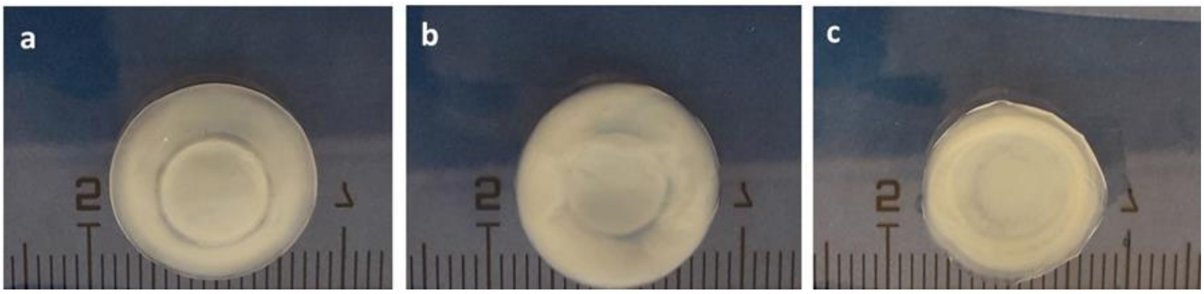

Figure 4.2 | Disk-shaped mineralized collagen matrices 0% Sr^{2+}(a), 10% Sr^{2+}(b) and 50% Sr^{2+}(c). The form of the mold controls the final shape of the matrix.

In the attempt of setting a bioinspired process, the ionic precursors of apatite (Ca^{2+}, CO_3^{2-}, PO_4^{3-} and Sr^{2+} salts) were added to the acidic collagen solution before the concentration process since the bone remodeling process occurs in an acidic front where the extracellular fluid baths the tissue.[32] At high concentrations in acidic solution, collagen molecules spontaneously assemble into liquid-crystal phases which is here cholesteric at the fixed PEG concentration (cf. methods).[33] The liquid crystal geometry of the molecules is stabilized *in vitro* by increasing the pH using ammonia vapor. Initially, the amino acids residues are positively charged in the acidic medium, thus the molecules of collagen are maintained in solution due to the repulsion between the chains. As the pH increases, the net charge of the collagen monomers decreases, and the hydrophobic interactions dominate. Hence, the triple-helices aggregate leading to the precipitation of the fibrils. This process involves the passage from the molecular to the fibrillar state by a sol-gel transition which takes place without disturbing the liquid crystal organization.[34] Additionally, the precipitation of the mineral phase is also triggered as the pH increases. Note that the chemical method of pH control is a suitable alternative to enzymatic control, which fails at producing fibrils at high concentration.[33]

The 0% Sr^{2+} matrix exhibits a dense network surface reaching dimensions above tens of micrometers due to the closely packed even sized parallel fibrils (Figure 4.3a[i]) resembling the pattern found in the sample of bone (Figure 4.3d). Transversal fracture of the matrix allows observations from the bulk revealing the alignment of collagen fibrils into periodic twisted plywood geometry over a long length scale (up to few cm) (Figure 4.3a[ii]). Such a specific arrangement of collagen fibrils supports the stabilization of cholesteric mesophase of the concentrated collagen solution during the fibrillogenesis.[33] This reminds the pattern found in transverse section of demineralized human bone.[14,35] The 10% Sr^{2+} matrix displays similarities in terms of organization to the 0% Sr^{2+} sample i.e. dense and organized fibrils at the surface and cholesteric domains in the bulk, suggesting that the hierarchical assembly of collagen was not affected at this degree of Ca^{2+} substitution by Sr^{2+} (Figure 4.3b[i-ii]). Unexpectedly, the typical arrangement of organized collagen fibrils become absent at surface of the 50% Sr^{2+} sample (Figure 4.4c[i]). Arrays of fibrils randomly oriented were found in the bulk rather than the regular long-range crimped architecture characteristic of dense connective tissues (Figure 4.4c[ii]).[36]

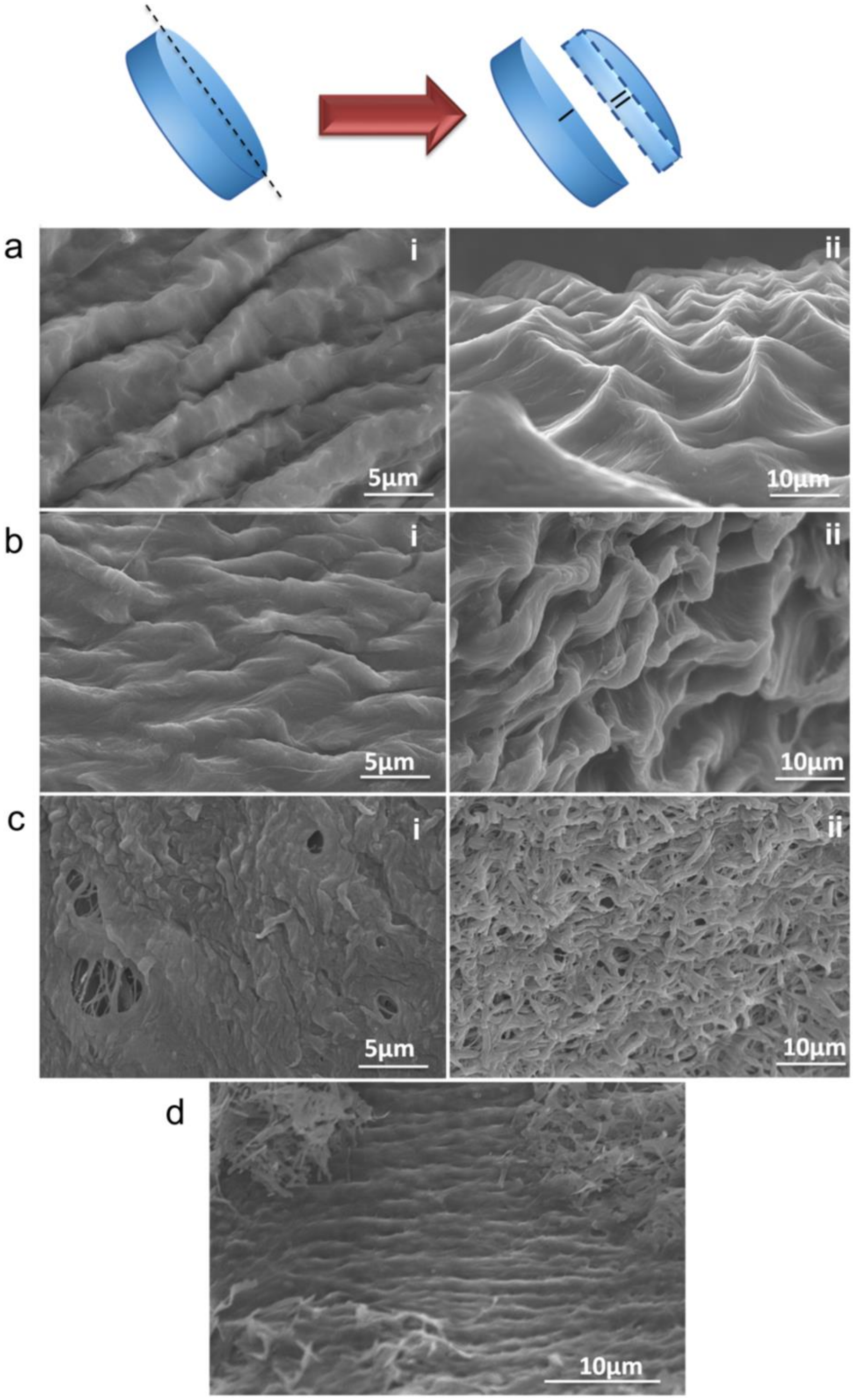

Figure 4.3 | SEM images of the mineralized collagen matrices 0%Sr^{2+} (a), 10%Sr^{2+} (b), 50%Sr^{2+} (c) and surface view of a bone sample (d). Examination of the surface (i) and transversally fractured matrix (ii). In the 0% Sr^{2+} and 10% Sr^{2+} matrices collagen fibrils are parallelly aligned at the surface and arranged in twisted plywood geometry in the interior as showed by the transversal fracture. In the 50%Sr^{2+} sample the collagen fibrils are randomly oriented at the surface and in the interior.

The strong optical birefringence throughout the thin sections of the 10%Sr^{2+} sample observed under polarized light microscopy confirms the alignment of collagen fibrils at the millimeter scale (Figure 4.4a). Some domains display alternating bright and dark bands (region indicated by *chol in the Figure 4.4b) which reveal the cholesteric organization of the collagen fibrils.[37] This motif can be tracked by rotating the sample stage and following the extinction of light specifically in areas where the collagen molecules lie parallel to the direction of the polarizers (Figure 4.4b and Figure 4.4c). These birefringent properties reflect the anisotropy of the matrices reassembling those found in human compact bone osteons.[35] Conversely, the 50%Sr^{2+} matrix displays weaker birefringence (two red asterisks in Figure 4.4d) as compared to the 10%Sr^{2+} matrix and regions in which the birefringence is absent (one red asterisk in Figure 4.4d). Moreover, cholesteric domains are not identified after a 45° rotation of the polarizers (Figure 4.4e and Figure 4.4f). This supports the destabilization of the supramolecular structure of collagen in the 50%Sr^{2+} matrix as suggested by SEM images.

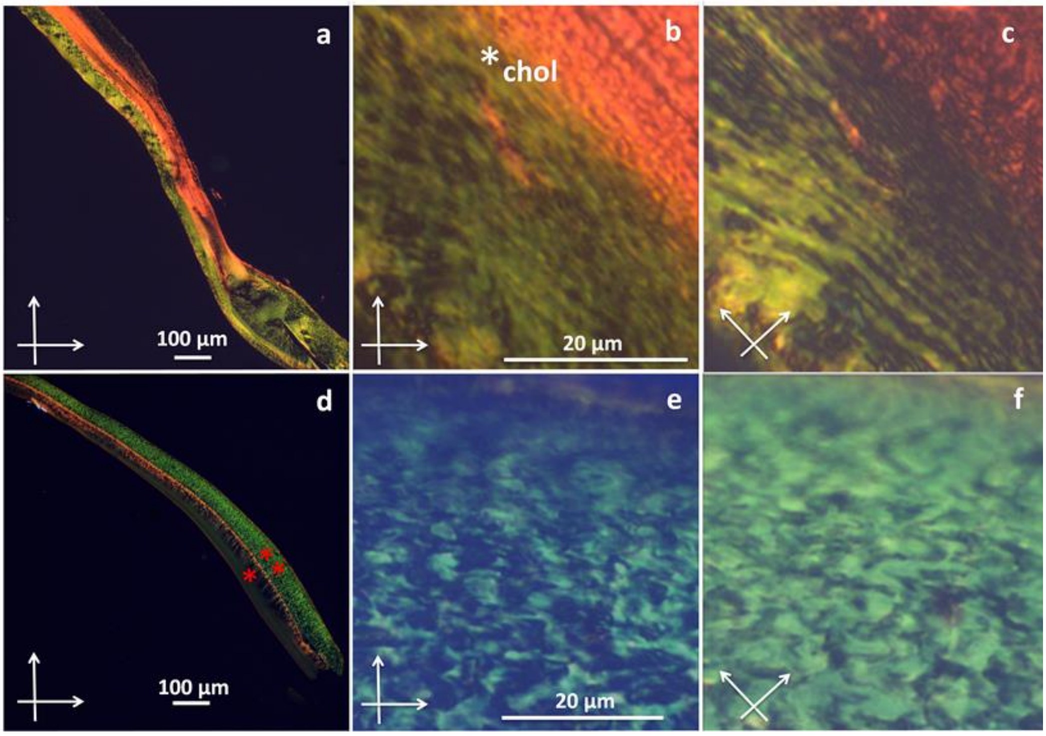

Figure 4.4 | Polarized light microscopy images of histological thin section of the mineralized collagen matrices containing 10%Sr^{2+} matrix (a-c) and 50%Sr^{2+}matrix (d-f) with the optical axis at 90° and 45° between the crossed polarizers.

Observations by TEM of the ultrathin sections of the 0% Sr^{2+} (Figure 4.5a[i]) and 10% Sr^{2+} collagen matrices (Figure 4.5b[i]) show dense areas comprising fibrils locally organized parallelly (white dashed lines) coexisting with domains of larger fibrils (white arrows). In addition, the presence of cross-striated fibrils with the typical d spacing of 67 nm confirms that the fibrillogenesis *in vitro* was successfully induced (Figure 4.5a[iii] and 4.5b[iii]). The coexistence of different organization domains i.e. parallel and non-oriented packing of fibrils is typical of the heterogeneity found in bone tissue.[38] The disappearance of banding pattern of the fibrils may reflect the intrafibrillar deposition of minerals.[14,39] The 50% Sr^{2+} matrix displays some fibrils without orientation thus strengthening the SEM and LPOM findings (Figure 4.5c[i-iii]).

From these results, it is clear that high doses of Sr^{2+} critically hind the ability of collagen to form long range ordered structures i.e. cholesteric suggesting unexpected impacts of Sr^{2+} on bone. A close related scenario was found in the dentin of rats receiving injections of strontium chloride solution where the mineralization, alignment and packing of collagen fibrils were disturbed.[40–42]

Dense collagen matrix with the fibrillar organization is the key structural parameter for the correct deposition namely crystal size, morphology and alignment of apatite in bone.[16] Moreover, the fibrillar structure of collagen provides tensile strength and flexibility to tissue, cartilage, and bone.[43,44] Consequently, disorders in collagen architectures are associated with specific pathological mineralization, i.e., osteogenesis imperfecta and fibrogenesis imperfecta.[45,46] In the cases of fibrogenesis imperfecta the organic matrix displays randomly oriented and distorted collagen fibrils being that the absence of birefringence under polarized light is the typical protocol to identify this abnormality.[47] Additionally, the organization of collagen is also deranged in osteoporotic bone strengthening the dependence of skeletal mechanical properties on collagen architecture.[48,49]

Sr^{2+} may interact with collagen by sites normally involved in the binding of Ca^{2+} during the initial steps of calcification or by displacing Ca^{2+} bound to the matrix.[8] Nevertheless, the possible involvement of this ion on the assembly of bone extracellular matrix remains unsolved so far. Our data rises the intriguing possibility that excess of Sr^{2+} plays a significant role in bone pathologies linked to the 3D organization of collagen matrix. Interestingly, although characterized as distinct clinical disorders osteomalacia usually develops in the cases of fibrogenesis imperfecta due to the local abnormalities in the collagen matrix impairing mineralization of bone.[50]

The examination of the sections using TEM also reveals nanometric apatite crystals embedded within the collagen fibrils and preferentially oriented along the fibril's axis suggesting a relationship between the mineral and the collagen network as found in bone (Figure 4.5a[ii] and Figure 4.5b[ii]). Interestingly, these crystals reassemble those found in the sample of bone (Figure 4.6) indicating that the 0%Sr^{2+} and 10%Sr^{2+} matrices guided biomimetic mineralization of apatite.[14] Another interesting aspect is that the structure of the apatite crystals formed in the presence of collagen contrast with those formed by homogeneous precipitation (as described in Chapter 2) which were characterized by bigger and non-oriented crystals (i.e., spherulites). This highlights the role played by the collagen matrix in the processes of nucleation, growth and crystallographic orientation of apatite in bone. Moreover, the small amount of crystals found at the surface of the fibrils is similar to that described at very early stages of *in vivo* calcification. As the mineralization proceeds the crystals span over the fibrils network.[38,51,52]

The role of collagen on the formation of bone apatite is mainly related to the effect of intra and interfibrillar confinement, however, at this point, we do not have evidences of intrafibrillar mineralization of the fibrils.[18,52] Further investigation using wide angle X-ray scattering will be performed to address this shortcoming.

Dense spheres are observed within the 50%Sr^{2+} matrix (indicated by white circles) suggesting the precipitation of an amorphous phase rather than biomimetic apatite crystals (Figure 4.5c[ii]).

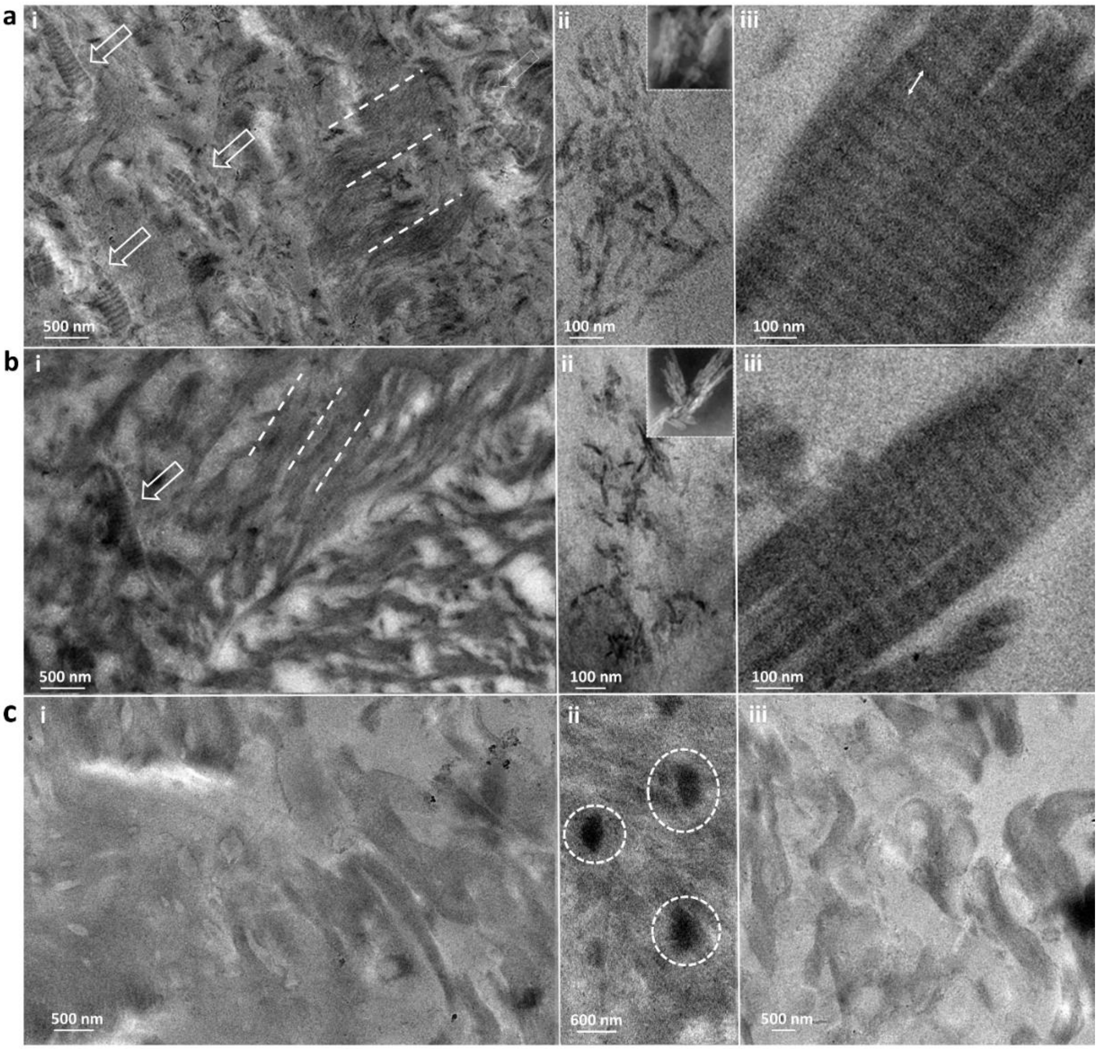

Figure 4.5 | TEM images of ultra-thin section of the (a) 0%Sr^{2+}, (b) 10%Sr^{2+} and (c)50% Sr^{2+} collagen matrices, showing collagen fibrils (i and iii) and minerals particles (ii).

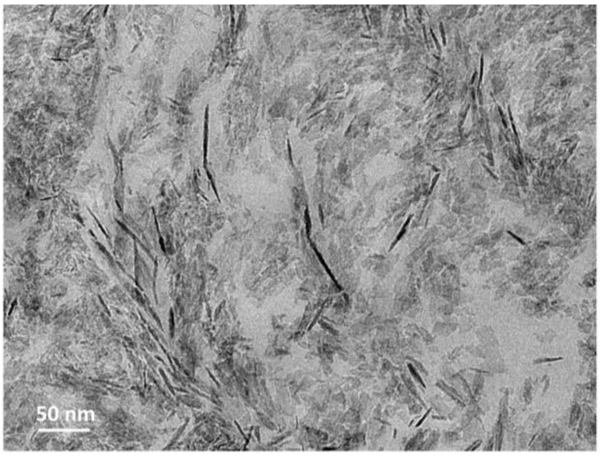

Figure 4.6 | TEM image of an ultra-thin section of bone sample showing apatite platelets.

TGA was performed on the collagen matrices to investigate their mineral content. The TGA and DTG curves reveal that matrices follow a multistage decomposition characterized by three thermal processes likewise the collagen in bone and dentine (Figure 4.7a and Figure 4.7b).[53,54]

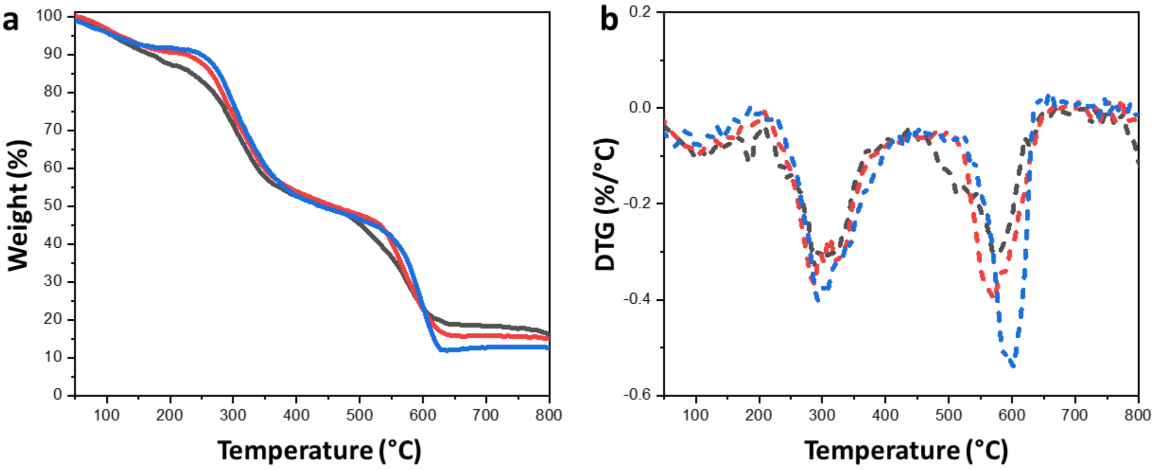

Figure 4.7 | TGA of the 0%Sr^{2+} (gray line), 10%Sr^{2+} (red line) and 50%Sr^{2+} (blue line) mineralized collagen matrices (a). The mineral contents (% wt.) of the matrices were determined by the ash content at 800 °C. DTG curves of the mineralized collagen matrices showing the occurrence of three thermal events as found in mineralized tissues (b).

The first weight loss in the TGA curves between 30 °C and 170 °C is assigned to the release of physiosorbed H_2O molecules, followed by the decomposition of collagens fibrils between 200 °C and 470 °C. This process comprises the release of structural water and products with low molecular weight. Finally, the combustion of the residual organic components takes place between 450 °C and 700 °C leading to the complete decomposition of collagen matrix.[55] The mineral content in the matrices was determined as the relative mass remaining after heating up to 800 °C. The transition temperatures and the corresponding percentage weight losses are summarized in the Table 4.1.

To exclude the possibility that the difference in final mineral weight percentage is caused by different levels of adsorbed water, the dry weight of each sample at T = 180 °C was normalized to 100%. Interestingly, the mineral content in the samples decreases from 20% in the 0%Sr^{2+} matrix to 13% in the 50%Sr^{2+} matrix. This result may be correlated to the effects of Sr^{2+} in hindering the nucleation and/or growth of apatite well illustrated in the cases of hypomineralized bone, dentine and enamel induced by high doses of Sr^{2+}.[56,40] Additionally, a shift towards lower values are observed in the combustion temperatures with the amount of Sr^{2+} in the samples (Figure 4.7 b). Several investigations have ascribed this change in the thermic behavior of collagen to the intrafibrillar deposition of minerals.[53,57] However, we believe that such assumption is not straightforward since other characterization techniques are needed to attest the infiltration of minerals within the collagen fibrils, as previously discussed. Overall, the thermogravimetric analysis somehow strengths the controlled deposition of minerals within the collagen matrices. Otherwise, the precipitation of a high mineral content at the surface would be obvious in the TGA curves.

Table 4.1 | Peak temperatures (T) and weight losses (W%) associated with the thermal processes detected by the TG-DGT plots of the mineralized collagen matrices 0%Sr^{2+}, 10%Sr^{2+} and 50%Sr^{2+}. The mineral content (wt. %) in the matrices was determined by the ash content at 800 °C considering (non-dried) or not (dried) the amount physiosorbed water within the matrices

Matrix	Peak 1		Peak 2		Peak3		Mineral content (%)	
	T_1(°C)	W_1(%)	T_2(°C)	W_2(%)	T_3(°C)	W_3(%)	Non-dried	Dried
0% Sr^{2+}	110	12	300	36	570	34	18	20
10% Sr^{2+}	110	11	300	39	575	35	15	17
50% Sr^{2+}	100	10	300	42	602	34	13	14

4.3.2 | Characterization of mineral formation within the collagen matrices

After characterizing the collagen assembly in the matrices, we moved towards the investigation of the mineral phase. It is important to highlight that due to the small amount and small size of crystals it is hard to analyze the mineral formed within the collagen matrices by means of X-ray diffraction. Moreover, the sample preparation for TEM analysis involves dehydration in ethanol what may induce the dissolution of possible amorphous particles as previously reported for calcium carbonate.[58] Therefore, we decided to rely on ^{31}P magic-angle spinning (MAS) solid-state nuclear magnetic resonance (ssNMR) to investigate the impact of Sr^{2+} on the mineral formed within the collagen matrices. This technique allows us to analyze fresh matrices samples without any previous treatment thus preventing specimen alteration and therefore misleading interpretations.

A single asymmetric resonance peak around 3 ppm, characteristic of carbonated apatite was detected in the 0%Sr^{2+} sample, confirming the precipitation of this mineral within the collagen matrix (Figure 4.8a, blue line).[14] The broadening of the resonance peak in the 10%Sr^{2+} sample reflects the increase in the distribution of chemical environments around the PO_4^{3-} ions (Figure 4.8a, green line). This result agrees with those described in the Chapter 2, thus confirming the Ca^{2+} substitution by Sr^{2+} in the lattice of the apatite precipitated within the matrix.[12] Such a broadening increases to the 50% Sr^{2+} matrix suggesting a higher amount of Sr^{2+} incorporated and consequently higher structural disorder in the mineral (Figure 4.8a, purple line). Noticeably, the ^{31}P resonance signal found in the spectrum of 50% Sr^{2+} collagen matrix matches with the typical signature of Sr(ACP) (Figure 4.8b). This shows that not only the supramolecular arrangement of collagen is disturbed at this Sr^{2+} concentration but also the apatitic phase. This may illustrate the case of impaired apatite mineralization found in bone disorders caused by high levels of Sr^{2+}.[59] Beyond this, alterations in the Sr/Ca balance in water have been associated with skeletal deformities in zebrafish and cod thus extending the side effects of excess of Sr^{2+} on bone mineralization towards different animals.[60,61]

These results show that the presence of a 3D-dense collagenous matrix does not overcome the structural disordering in biomimetic apatite caused by Sr^{2+} and the formation of Sr(ACP) may account to the destabilization of the supramolecular assembly of collagen fibrils. Although no temporal sequence has been established here and we have presented them as separated events, we believe that the effects of Sr^{2+} on the collagen matrix are intimately associated with the formation of this disordered mineral phase. Likewise, it is speculated that the collagen abnormality found in fibrogenesis imperfecta is possibly caused by the large amount of amorphous phosphate which could interfere with the assembly of fibrils.[62,63] However, the precise cause of poor molecular arrangement of collagen remains unknown. The high Sr/Ca ratios found in the plasma of patients with fibrogenesis imperfecta suggests a possible involvement of Sr^{2+} in this pathology, however there is not enough clinical evidences to support this assumption.[64,65]

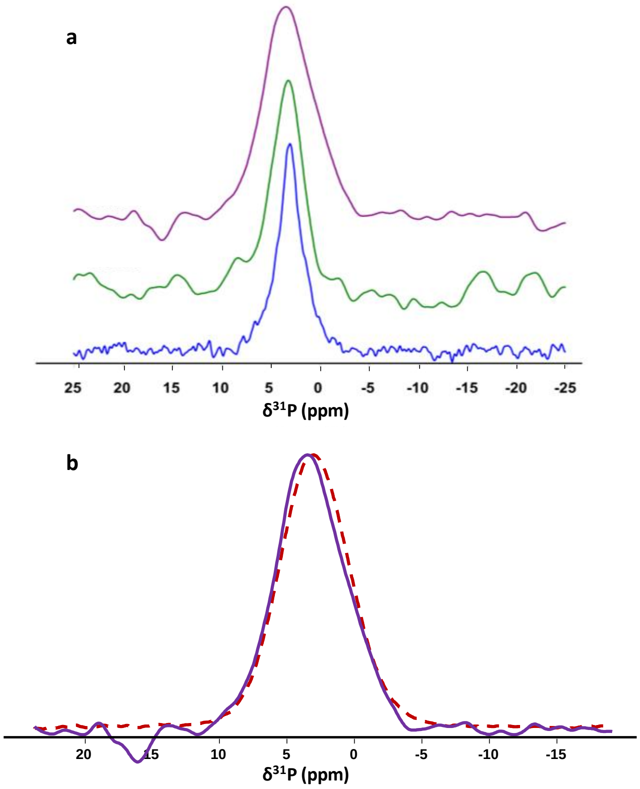

Figure 4.8 | ^{31}PMAS spectra of 0%Sr^{2+} (blue line), 10%Sr^{2+} (green line) and 50%Sr^{2+} (purple line) collagen matrices (a). Comparison between the ^{31}PMAS spectra of Sr(ACP) precipitated in the presence of 50 mol % Sr^{2+}in homogeneous medium and (red dashed line) and 50%Sr^{2+} mineralized collagen matrix (purple line) (b).

Because many other factors are involved *in vivo* (such as cells and non-collagenous proteins), it is difficult to determine the specific influence of Sr^{2+} on the processes of bone mineralization. However, on the basis of the present model and previous reports of the heterogeneous distribution of Sr^{2+} on bone, we propose that at high doses, Sr^{2+} locally inhibit apatite crystallization producing changes in the organic matrix leading to bone disorders.[40,66,50]

The exclusive evaluation of the effects of Sr^{2+} at the molecular level during collagen fibrillogenesis are beyond the scope of this study and X-ray scattering techniques should be undertaken to measure changes in the periodicity of the gap regions and the size of collagen fibrils as previously described for metallic species into collagen matrices.[67,68]

4.3.3 | Cell culture experiments

The architecture of the extracellular matrix is essential for bone formation since it provides the environmental cues to cells colonization and acts as template for mineral deposition and assembly.[69,70] Thus, we evaluated how the underlying structure of the Sr^{2+} bearing mineralized collagen matrices could affect osteoblasts behavior.

SEM images show that the MC3T3-E1 cells grew flatten on the $0\%Sr^{2+}$ and $10\%Sr^{2+}$ matrices displaying elongated morphology and high adhesion areas which suggest their strong anchoring and spreading on these matrices (Figure 4.9a).[71] Moreover, the cells elongation suggests that the anisotropic matrices provided physical cues to guide their unidirectional adhesion along the axis of the collagen fibrils (Figure 4.9b).[72,73] The suitable interaction between the cells and these substrates is further evidenced by the presence of filopodia contacting neighboring cells and extending along the matrices surface.[74] Conversely, the cells seeded onto the $50\%Sr^{2+}$ matrix display spherical morphology reflecting their limited affinity for the substrate namely attaching and spreading (Figure 4.9a-b).[75]

MTT assay revealed that the cells seeded on the $0\%Sr^{2+}$ and $10\%Sr^{2+}$ matrices maintained the viability until 14 days of culturing while decreased viability was found to cells cultured on the $50\%Sr^{2+}$ collagen matrix thus supporting the SEM observations (Figure 4.9c). After 7 days of culture, the ALP activity, an early marker for osteoblasts differentiation, was reduced for the cells cultured on the $50\%Sr^{2+}$ matrix suggesting that their evolution towards mature bone-forming osteoblasts was hindered as compared to the cells cultured on the hierarchically organized $0\%Sr^{2+}$ and $10\%Sr^{2+}$ matrices (Figure 4.9d, black bars). As expected, after 14 days of culture the ALP activity was also decreased for the cells seeded on the $50\%Sr^{2+}$ matrix indicating that the mineralization ability of the cells was also impaired as compared to the $0\%Sr^{2+}$ and $10\%Sr^{2+}$ matrices (Figure 4.9d, grey bars). Synthetic scaffolds displaying aligned fibers are shown to boost bone formation by enhancing ALP activity and expression of osteogenic genes while significant decrease in the ALP activity is often related to bone disorders such as osteomalacia.[22,76,77,]

These results point out that the possible physicochemical interference of Sr^{2+} with the bone tissue comprising the destabilization of apatite and collagen network directly impacts on cells activity (contact guidance, adhesion and proliferation) as found in pathologies related to Sr^{2+} accumulation.[22,78]

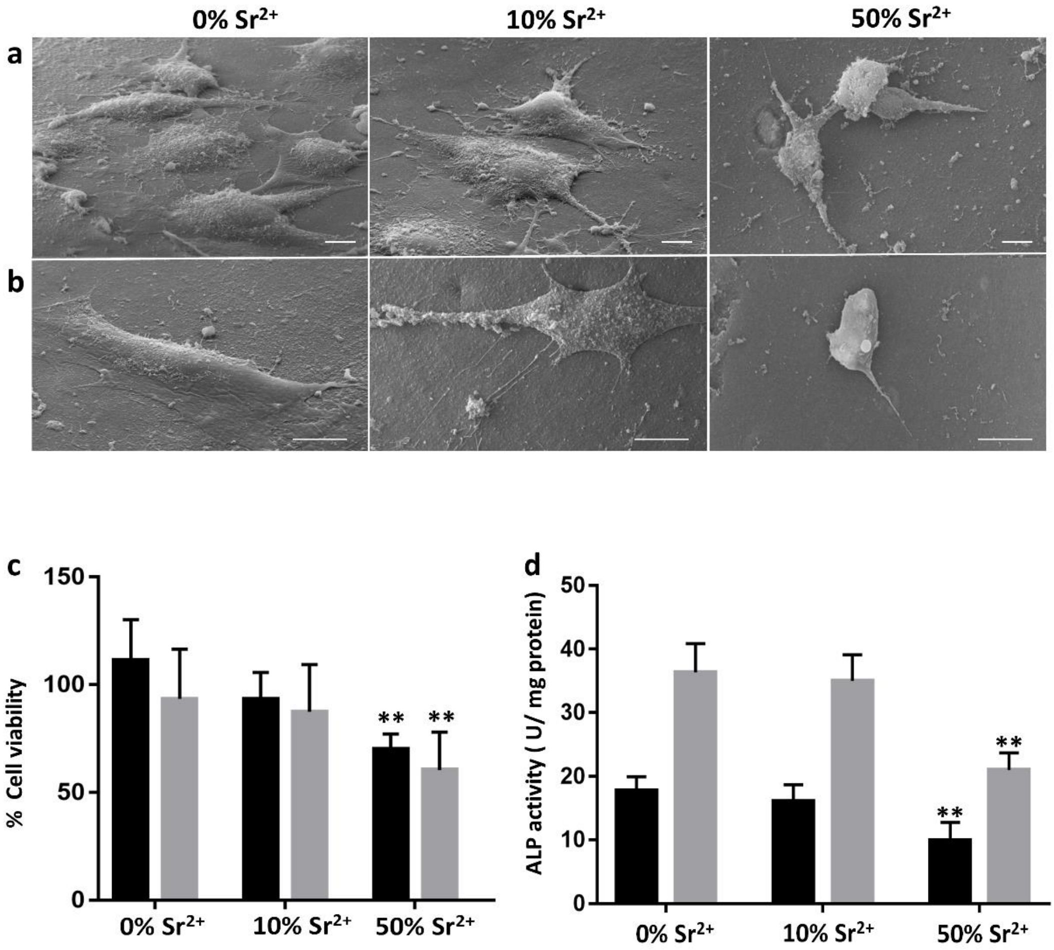

Figure 4.9 | MC3T3-E1 cells grown in the presence of the collagen matrices. (a-b) SEM images of MC3T3-E1 cells cultured for 14 days on the mineralized collagen matrices containing 0%Sr^{2+}, 10%Sr^{2+} and 50%Sr^{2+}. The images a, and b show different regions of the respective samples. Scale bars represent 10 μm. (c) % cell viability versus control measured by MTT assay after 7 days (black bars) and 14 days (grey bars) of culture and (d) activity of ALP in the osteoblasts' membrane fraction after 7 days (black bars) and14 days (grey bars) of culture. Results represent the mean values ± standard deviation for triplicate determination for one experiment. Multiple statistical comparisons were performed by one-way ANOVA, $^{**}p < 0.01$.

The fact that the phosphate particles formed in the absence of collagen did not display toxicity towards MC3T3-E1 cells further suggests that the origin of these results lie mainly on the collagen matrix assembly rather than on the mineral phase (Figure 4.10). The suitable interaction between osteoblasts and the extracellular matrix is an essential requirement for the production of structural components and enzymes in bone tissue.[79] Indeed, local defects in the bone matrix lead to impaired osteoblasts migration and maturation which in turn prevent mineralization to proceed normally.[47,80] Hence, the model of bone adopted in this investigation reproduce the dose-dependent effects of Sr^{2+} in the several levels as previously observed *in vivo*.[26,79,81,82]

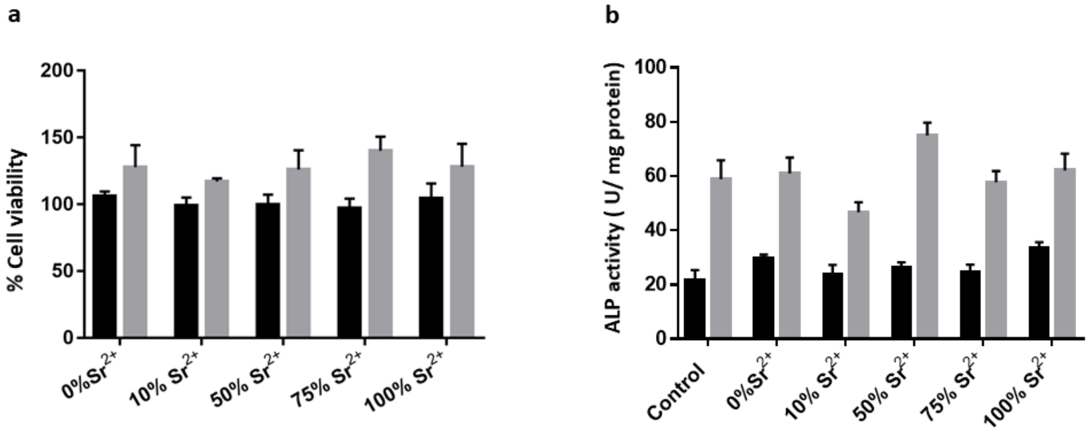

Figure 4.10 | MC3T3-E1 cells grown in the presence of the phosphate particles. (a) % cell viability versus control measured by MTT assay after 7 days (black bars) and 14 days (grey bars) of culture and (b) activity of ALP in the osteoblasts' membrane fraction after 7 days (black bars) and14 days (grey bars) of culture. Results represent the mean values ± standard deviation for triplicate determination for one experiment.

4.4 | Conclusions

Biomimetic mineralized collagen matrices displaying the hierarchical architecture of bone were set as model to investigate the impacts of Sr^{2+} on the organic/inorganic interface of this tissue. At physiological concentration (10 mol% Sr^{2+}), the organization of the matrices was maintained in terms of fibrils tridimensional arrangement and apatite crystals morphology. In a situation of pathological accumulation of Sr^{2+} (50 mol% Sr^{2+}) the supramolecular structure of the matrix was deranged resulting in fibrils randomly oriented and mineral phase characterized as Sr(ACP). Thus, in this case Sr^{2+} led to the simultaneously destabilization of collagen network and apatite. This illustrates the clinical reports of pathological mineralization driven by Sr^{2+} accumulation in bone, i.e, rickets and osteomalacia. This was further supported by decreased viability and metabolic activity of osteoblasts seeded on the 50 mol% Sr^{2+} matrices. Therefore, we present a model able to reproduce the *in vivo* observations of the different impacts of Sr^{2+} according to the dose comprising the multiple levels of bone: organic matrix, mineral and cells. To sum up, these observations improve the current understanding about the multiple effects of Sr^{2+} on bone from a physicochemical point-of-view.

4.5 | References

(1) Bonnelye, E.; Chabadel, A.; Saltel, F.; Jurdic, P. Dual Effect of Strontium Ranelate: Stimulation of Osteoblast Differentiation and Inhibition of Osteoclast Formation and Resorption in Vitro. *Bone* **2008**, *42* (1), 129–138.

(2) Zhang, W.; Shen, Y.; Pan, H.; Lin, K.; Liu, X.; Darvell, B. W.; Lu, W. W.; Chang, J.; Deng, L.; Wang, D.; et al. Effects of Strontium in Modified Biomaterials. *Acta Biomater.* **2011**, *7* (2), 800–808.

(3) Marie, P. J.; Ammann, P.; Boivin, G.; Rey, C. Mechanisms of Action and Therapeutic Potential of Strontium in Bone. *Calcif. Tissue Int.* **2001**, *69* (3), 121–129.

(4) D'Haese, P. C.; Schrooten, I.; Goodman, W. G.; Cabrera, W. E.; Lamberts, L. V.; Elseviers, M. M.; Couttenye, M. M.; De Broe, M. E. Increased Bone Strontium Levels in Hemodialysis Patients with Osteomalacia. *Kidney Int.* **2000**, *57* (3), 1107–1114.

(5) Couttenye, M. M.; D'Haese, P. C.; Verschoren, W. J.; Behets, G. J.; Schrooten, I.; De Broe, M. E. Low Bone Turnover in Patients with Renal Failure. *Kidney Int. Suppl.* **1999**, *56* (73), 70–76.

(6) Anderson, I.; Campbell, A. E. R.; Dunn, A.; Runciman, J. B. M. Osteomalacia in Elderly Women. *Scott. Med. J.* **1966**, *11* (12), 429–435.

(7) Dahl, S. G.; Allain, P.; Marie, P. J.; Mauras, Y.; Boivin, G.; Ammann, P.; Tsouderos, Y.; Delmas, P. D.; Christiansen, C. Incorporation and Distribution of Strontium in Bone. *Bone* **2001**, *28* (4), 446–453.

(8) Frankær, C. G.; Raffalt, A. C.; Stahl, K. Strontium Localization in Bone Tissue Studied by X-Ray Absorption Spectroscopy. *Calcif. Tissue Int.* **2014**, *94* (2), 248–257.

(9) Reginster, J. Y.; Seeman, E.; De Vernejoul, M. C.; Adami, S.; Compston, J.; Phenekos, C.; Devogelaer, J. P.; Curiel, M. D.; Sawicki, A.; Goemaere, S.; et al. Strontium Ranelate Reduces the Risk of Nonvertebral Fractures in Postmenopausal Women with Osteoporosis: Treatment of Peripheral Osteoporosis (TROPOS) Study. *J. Clin. Endocrinol. Metab.* **2005**, *90* (5), 2816–2822.

(10) Rossi, A. L.; Moldovan, S.; Querido, W.; Rossi, A.; Werckmann, J.; Ersen, O.; Farina, M. Effect of Strontium Ranelate on Bone Mineral: Analysis of Nanoscale Compositional Changes. *Micron* **2014**, *56*, 29–36.

(11) Li, Z. Y.; Lam, W. M.; Yang, C.; Xu, B.; Ni, G. X.; Abbah, S. a; Cheung, K. M. C.; Luk, K. D. K.; Lu, W. W. Chemical Composition, Crystal Size and Lattice Structural Changes after Incorporation of Strontium into Biomimetic Apatite. *Biomaterials* **2007**, *28* (7), 1452–1460.

(12) Bussola Tovani, C.; Gloter, A.; Azaïs, T.; Selmane, M.; Ramos, A. P.; Nassif, N. Formation of Stable Strontium-Rich Amorphous Calcium Phosphate: Possible Effects on Bone Mineral. *Acta Biomater.* **2019**, *92*, 315–324.

(13) Reznikov, N.; Bilton, M.; Lari, L.; Stevens, M. M.; Kröger, R. Fractal-like Hierarchical Organization of Bone Begins at the Nanoscale. *Science* **2018**, *360,* 388.

(14) Wang, Y.; Azaïs, T.; Robin, M.; Vallée, A.; Catania, C.; Legriel, P.; Pehau-Arnaudet, G.; Babonneau, F.; Giraud-Guille, M. M.; Nassif, N. The Predominant Role of Collagen in the Nucleation, Growth, Structure and Orientation of Bone Apatite. *Nat. Mater.* **2012**, *11* (8), 724–733.

(15) Buckwalter, J. A.; Glimcher, M. J.; Cooper, R. R.; Recker, R. Bone Biology. *Instr. Course Lect.* **1996**, *45*, 371–386.

(16) Landis, W. J. The Strength of a Calcified Tissue Depends in Part on the Molecular Structure and Organization of Its Constituent Mineral Crystals in Their Organic Matrix. *Bone* **1995**, *16* (5), 533–544.

(17) Eyre, D. R.; Weis, M. A. Bone Collagen: New Clues to Its Mineralization Mechanism from Recessive Osteogenesis Imperfecta. *Calcif. Tissue Int.* **2013**, *93* (4), 338–347.

(18) Chen, J.; Burger, C.; Krishnan, C. V.; Chu, B.; Hsiao, B. S.; Glimcher, M. J. *In Vitro* Mineralization of Collagen in Demineralized Fish Bone. *Macromol. Chem. Phys.* **2005**, *206* (1), 43–51.

(19) Nassif, N.; Gobeaux, F.; Seto, J.; Belamie, E.; Davidson, P.; Panine, P.; Mosser, G.; Fratzl, P.; Giraud Guille, M. M. Self-Assembled Collagen-Apatite Matrix with Bone-like Hierarchy. *Chem. Mater.* **2010**, *22* (11), 3307–3309.

(20) Wang, Y.; Silvent, J.; Robin, M.; Babonneau, F.; Meddahi-Pellé, A.; Nassif, N.; Giraud Guille, M. M. Controlled Collagen Assembly to Build Dense Tissue-like Materials for Tissue Engineering. *Soft Matter* **2011**, *7* (20), 9659–9664.

(21) Oste, L.; Bervoets, A. R.; Behets, G. J.; Dams, G.; Marijnissen, R. L.; Geryl, H.; Lamberts, L. V.; Verberckmoes, S. C.; Van Hoof, V. O.; De Broe, M. E.; et al. Time-Evolution and Reversibility of Strontium-Induced Osteomalacia in Chronic Renal Failure Rats. *Kidney Int.* **2005**, *67* (3), 920–930.

(22) Francis, R. M.; Selby, P. L. Osteomalacia. *Baillieres. Clin. Endocrinol. Metab.* **1997**, *11* (1), 145–163.

(23) Felsenfeld, A. J.; Gutman, R. A.; Llach, F.; Harrelson, J. M. Osteomalacia in Chronic Renal Failure: A Syndrome Previously Reported Only with Maintenance Dialysis. *Am. J. Nephrol.* **1982**, *2* (3), 147–154.

(24) Schrooten, I.; Behets, G. J. S.; Cabrera, W. E.; Vercauteren, S. R.; Lamberts, L. V.; Verberckmoes, S. C.; Bervoets, A. J.; Dams, G.; Goodman, W. G.; De Broe, M. E.; et al. Dose-Dependent Effects of Strontium on Bone of Chronic Renal Failure Rats. *Kidney Int.* **2003**, *63* (3), 927–935.

(25) D'Haese, P. C.; Schrooten, I.; Goodman, W. G.; Cabrera, W. E.; Lamberts, L. V.; Elseviers, M. M.; Couttenye, M. M.; De Broe, M. E. Increased Bone Strontium Levels in Hemodialysis Patients with Osteomalacia. *Kidney Int.* **2000**, *57* (3), 1107–1114.

(26) Doublier, A.; Farlay, D.; Bala, Y.; Boivin, G. Strontium Does Not Affect the Intrinsic Bone Quality at Tissue and BSU Levels in Iliac Samples from Macaca Fascicularis Monkeys. *Bone* **2014**, *64*, 18–24.

(27) Gobeaux, F.; Belamie, E.; Mosser, G.; Davidson, P.; Panine, P.; Giraud-Guille, M. M. Cooperative Ordering of Collagen Triple Helices in the Dense State. *Langmuir* **2007**, *23* (11), 6411–6417.

(28) Bergman, I.; Loxley, R. Two Improved and Simplified Methods for the Spectrophotometric Determination of Hydroxyproline. *Anal. Chem.* **1963**, *35* (12), 1961–1965.

(29) Mosser, G.; Anglo, A.; Helary, C.; Bouligand, Y.; Giraud-Guille, M. M. Dense Tissue-like Collagen Matrices Formed in Cell-Free Conditions. *Matrix Biol.* **2006**, *25* (1), 3–13.

(30) Mosmann, T. Rapid Colorimetric Assay for Cellular Growth and Survival: Application to Proliferation and Cytotoxicity Assays. *J. Immunol. Methods* **1983**, *65* (2), 55–63.

(31) Simão, A. M. S.; Beloti, M. M.; Rosa, A. L.; de Oliveira, P. T.; Granjeiro, J. M.; Pizauro, J. M.; Ciancaglini, P. Culture of Osteogenic Cells from Human Alveolar Bone: A Useful Source of Alkaline Phosphatase. *Cell Biol. Int.* **2007**, *31* (11), 1405–1413.

(32) Baron, R. Molecular Mechanisms of Bone Resorption by the Osteoclast. *Anat. Rec.* **1989**,

224 (2), 317–324.

(33) Besseau, L.; Giraud-Guille, M. M. Stabilization of Fluid Cholesteric Phases of Collagen to Ordered Gelated Matrices. *J. Mol. Biol.* **1995**, *251* (2), 197–202.

(34) Belamie, E.; Mosser, G.; Gobeaux, F.; Giraud-Guille, M. M. Possible Transient Liquid Crystal Phase during the Laying out of Connective Tissues: α-Chitin and Collagen as Models. *J. Phys. Condens. Matter* **2006**, *18* (13), S115.

(35) Giraud-Guille, M. M.; Besseau, L.; Martin, R. Liquid Crystalline Assemblies of Collagen in Bone and *in Vitro* Systems. *J. Biomech.* **2003**, *36* (10), 1571–1579.

(36) Belamie, E.; Mosser, G.; Gobeaux, F.; Giraud-Guille, M. M. Possible Transient Liquid Crystal Phase during the Laying out of Connective Tissues: α-Chitin and Collagen as Models. *J. Phys. Condens. Matter* **2006**, *18* (13), S115–S129.

(37) Giraud-Guille, M. M. Twisted Liquid Crystalline Supramolecular Arrangements in Morphogenesis. *Int. Rev. Cytol.* **1996**, *166*, 59–101.

(38) Weiner, S.; Wagner, H. D. The Material Bone: Structure-Mechanical Function Relations. *Annu. Rev. Mater. Sci.* **1998**, *28* (1), 271–298.

(39) Nudelman, F.; Pieterse, K.; George, A.; Bomans, P. H. H.; Friedrich, H.; Brylka, L. J.; Hilbers, P. A. J.; De With, G.; Sommerdijk, N. A. J. M. The Role of Collagen in Bone Apatite Formation in the Presence of Hydroxyapatite Nucleation Inhibitors. *Nat. Mater.* **2010**, *9* (12), 1004–1009.

(40) Ogawa, Y.; Ishida, T.; Yagi, T. Ultramicroscopy of Hypomineralized Responses in Rat Incisor Dentine to Injected Strontium. *Arch. Oral Biol.* **1981**, *26* (3), 229–236.

(41) Eisenmann, D. R.; Yaeger, J. A. Alterations in the Formation of Rat Dentine and Enamel Induced by Various Ions. *Arch. Oral Biol.* **1969**, *14* (9), 1045-IN13.

(42) Grady, J. E.; Yager, J. A. Polarizing Microscopy of Abnormal Dentine Produced By Injections Of. *Arch. Oral Biol.* **1965**, *10* (1), 175–178.

(43) Pendleton, M. M.; Emerzian, S. R.; Liu, J.; Tang, S. Y.; O'Connell, G. D.; Alwood, J. S.; Keaveny, T. M. Effects of Ex Vivo Ionizing Radiation on Collagen Structure and Whole-Bone Mechanical Properties of Mouse Vertebrae. *Bone* **2019**, *128* (3), 115043.

(44) Rossetti, L.; Kuntz, L. A.; Kunold, E.; Schock, J.; Müller, K. W.; Grabmayr, H.; Stolberg-Stolberg, J.; Pfeiffer, F.; Sieber, S. A.; Burgkart, R.; et al. The Microstructure and Micromechanics of the Tendon-Bone Insertion. *Nat. Mater.* **2017**, *16* (6), 664–670.

(45) Bhadada, S. K.; Dhaliwal, R.; Dhiman, V.; Rao, S. D. Fibrogenesis Imperfecta Ossium. *Calcif. Tissue Int.* **2019**, *104* (5), 561–569.

(46) Misof, K.; Landis, W. J.; Klaushofer, K.; Fratzl, P. Collagen from the Osteogenesis Imperfecta Mouse Model (Oim) Shows Reduced Resistance against Tensile Stress. *J. Clin. Invest.* **1997**, *100* (1), 40–45.

(47) Barron, M. L.; Rybchyn, M. S.; Ramesh, S.; Mason, R. S.; Fiona Bonar, S.; Stalley, P.; Khosla, S.; Hudson, B.; Arthur, C.; Kim, E.; et al. Clinical, Cellular, Microscopic, and Ultrastructural Studies of a Case of Fibrogenesis Imperfecta Ossium. *Bone Res.* **2017**, *5* (20), 1–14.

(48) Xi, L.; De Falco, P.; Barbieri, E.; Karunaratne, A.; Bentley, L.; Esapa, C. T.; Terrill, N. J.; Brown, S. D. M.; Cox, R. D.; Davis, G. R.; et al. Bone Matrix Development in Steroid-Induced Osteoporosis Is Associated with a Consistently Reduced Fibrillar Stiffness Linked to Altered Bone Mineral Quality. *Acta Biomater.* **2018**, *76*, 295–307.

(49) Acerbo, A. S.; Kwaczala, A. T.; Yang, L.; Judex, S.; Miller, L. M. Alterations in Collagen and Mineral Nanostructure Observed in Osteoporosis and Pharmaceutical Treatments

Using Simultaneous Small- and Wide-Angle X-Ray Scattering. *Calcif. Tissue Int.* **2014**, *95* (5), 446–456.

(50) Gerald W. Chodak, Ronald A. Thisted, Glenn S. Gerber, Jan-Erik Johansson, Jan Adolfsson, George W. Jones, Geoff D. Chisholm, Boaz Moskovitz, Pinhas M. Livne, and J. W. Fibrogenesis Imperfecta Ossium a Collagen Defect Causing Osteomalacia. *N. Engl. J. Med.* **1994**, *330* (4), 242–248.

(51) Rey, C.; Combes, C.; Drouet, C.; Glimcher, M. J. Bone Mineral: Update on Chemical Composition and Structure. *Osteoporos. Int.* **2009**, *20* (6), 1013–1021.

(52) Su, X.; Sun, K.; Cui, F. Z.; Landis, W. J. Organization of Apatite Crystals in Human Woven Bone. *Bone* **2003**, *32* (2), 150–162.

(53) Lozano, L. F.; Peña-Rico, M. A.; Heredia, A.; Ocotlán-Flores, J.; Gómez-Cortés, A.; Velázquez, R.; Belío, I. A.; Bucio, L. Thermal Analysis Study of Human Bone. *J. Mater. Sci.* **2003**, *38* (23), 4777–4782.

(54) De Dios Teruel, J.; Alcolea, A.; Hernández, A.; Ruiz, A. J. O. Comparison of Chemical Composition of Enamel and Dentine in Human, Bovine, Porcine and Ovine Teeth. *Arch. Oral Biol.* **2015**, *60* (5), 768–775.

(55) Bigi, A.; Ripamonti, A.; Cojazzi, G.; Pizzuto, G.; Roveri, N.; Koch, M. H. J. Structural Analysis of Turkey Tendon Collagen upon Removal of the Inorganic Phase. *Int. J. Biol. Macromol.* **1991**, *13* (2), 110–114.

(56) Grynpas, M. D.; Marie, P. J. Effects of Low Doses of Strontium on Bone Quality and Quantity in Rats. *Bone* **1990**, *11* (5), 313–319.

(57) Thula, T. T.; Rodriguez, D. E.; Lee, M. H.; Pendi, L.; Podschun, J.; Gower, L. B. In Vitro Mineralization of Dense Collagen Substrates: A Biomimetic Approach toward the Development of Bone-Graft Materials. *Acta Biomater.* **2011**, *7* (8), 3158–3169.

(58) Blondeau, M.; Sachse, M.; Boulogne, C.; Gillet, C.; Guigner, J.-M.; Skouri-Panet, F.; Poinsot, M.; Ferard, C.; Miot, J.; Benzerara, K. Amorphous Calcium Carbonate Granules Form Within an Intracellular Compartment in Calcifying Cyanobacteria. *Front. Microbiol.* **2018**, *9, 1768.*

(59) Verberckmoes, S. C.; De Broe, M. E.; D'Haese, P. C. Dose-Dependent Effects of Strontium on Osteoblast Function and Mineralization. *Kidney Int.* **2003**, *64* (2), 534–543.

(60) Pasqualetti, S.; Banfi, G.; Mariotti, M. The Effects of Strontium on Skeletal Development in Zebrafish Embryo. *J. Trace Elem. Med. Biol.* **2013**, *27* (4), 375–379.

(61) Polak-Juszczak, L. Impact of Strontium on Skeletal Deformities in Baltic Cod (Gadus Morhua Callaris L.). *Chemosphere* **2011**, *83* (4), 486–491.

(62) Ralphs, J. R.; Stamp, T. C. B.; Dopping-Hepenstal, P. J. C.; Ali, S. Y. Ultrastructural Features of the Osteoid of Patients with Fibrogenesis Imperfecta Ossium. *Bone* **1989**, *10* (4), 243–249.

(63) Sissons, H. A. Fibrogenesis Imperfecta Ossium (Baker's Disease): A Case Studied at Autopsy. *Bone* **2000**, *27* (6), 865–873.

(64) Smith, B. J.; Eveson, J. W. Paget's Disease of Bone with Particular Reference to Dentistry. *J. Oral Pathol. Med.* **1981**, *10* (4), 233–247.

(65) Dow, E. C.; Stanbury, J. B. Strontium and Calcium Metabolism in Metabolic Bone Diseases. *J. Clin. Invest.* **1960**, *39*, 885–903.

(66) Thomas Jr, W. C. and Moore T. H. Fibrinogenesis imperfecta ossium. *Trans. Am. Clinic. Climat. Assoc.* **1969,** 80, 54.

(67) Zhang, Y.; Mansel, B. W.; Naffa, R.; Cheong, S.; Yao, Y.; Holmes, G.; Chen, H. L.;

Prabakar, S. Revealing Molecular Level Indicators of Collagen Stability: Minimizing Chrome Usage in Leather Processing. *ACS Sustain. Chem. Eng.* **2018**, *6* (5), 7096–7104.

(68) Parmar, A. S.; Xu, F.; Pike, D. H.; Belure, S. V.; Hasan, N. F.; Drzewiecki, K. E.; Shreiber, D. I.; Nanda, V. Metal Stabilization of Collagen and de Novo Designed Mimetic Peptides. *Biochemistry* **2015**, *54* (32), 4987–4997.

(69) Chung, W. J.; Oh, J. W.; Kwak, K.; Lee, B. Y.; Meyer, J.; Wang, E.; Hexemer, A.; Lee, S. W. Biomimetic Self-Templating Supramolecular Structures. *Nature* **2011**, *478* (7369), 364–368.

(70) Okada, S.; Ito, H.; Nagai, A.; Komotori, J.; Imai, H. Adhesion of Osteoblast-like Cells on Nanostructured Hydroxyapatite. *Acta Biomater.* **2010**, *6* (2), 591–597.

(71) Zhu, X.; Chen, J.; Scheideler, L.; Reichl, R.; Geis-Gerstorfer, J. Effects of Topography and Composition of Titanium Surface Oxides on Osteoblast Responses. *Biomaterials* **2004**, *25* (18), 4087–4103.

(72) Driscoll, M. K.; Sun, X.; Guven, C.; Fourkas, J. T.; Losert, W. Cellular Contact Guidance through Dynamic Sensing of Nanotopography. *ACS Nano* **2014**, *8* (4), 3546–3555.

(73) Lowe, C. J.; Reucroft, I. M.; Grota, M. C.; Shreiber, D. I. Production of Highly Aligned Collagen Scaffolds by Freeze-Drying of Self-Assembled, Fibrillar Collagen Gels. *ACS Biomater. Sci. Eng.* **2016**, *2* (4), 643–651.

(74) Stachewicz, U.; Qiao, T.; Rawlinson, S. C. F.; Almeida, F. V.; Li, W. Q.; Cattell, M.; Barber, A. H. 3D Imaging of Cell Interactions with Electrospun PLGA Nanofiber Membranes for Bone Regeneration. *Acta Biomater.* **2015**, *27*, 88–100.

(75) Khalili, A. A.; Ahmad, M. R. A Review of Cell Adhesion Studies for Biomedical and Biological Applications. *Int. J. Mol. Sci.* **2015**, *16* (8), 18149–18184.

(76) Madhurakkat Perikamana, S. K.; Lee, J.; Ahmad, T.; Jeong, Y.; Kim, D. G.; Kim, K.; Shin, H. Effects of Immobilized BMP-2 and Nanofiber Morphology on in Vitro Osteogenic Differentiation of HMSCs and in Vivo Collagen Assembly of Regenerated Bone. *ACS Ap. Mat. Int*. 2015, 7(16) 8798–8808.

(77) Zhuang, J.; Lin, S.; Dong, L.; Cheng, K.; Weng, W. Magnetically Assisted Electrodeposition of Aligned Collagen Coatings. *ACS Biomater. Sci. Eng.* **2018**, *4* (5), 1528–1535.

(78) Verberckmoes, S. C.; De Broe, M. E.; D'Haese, P. C. Dose-Dependent Effects of Strontium on Osteoblast Function and Mineralization. *Kidney Int.* **2003**, *64* (2), 534–543.

(79) Clarke, B. Normal Bone Anatomy and Physiology. *Clin. J. Am. Soc. Nephrol.* **2008**, *3(3)*, 131–139.

(80) Young, M. F. Bone Matrix Proteins: Their Function, Regulation, and Relationship to Osteoporosis. *Osteoporos. Int.* **2003**, *14 (3)*, 35–42.

(81) Storey, E. Strontium " rickets " : bone, calcium and strontium changes. *Australas. Ann. Med.* **1961**, *10* (3), 213–222.

(82) Schrooten, I.; Elseviers, M. M.; Lamberts, L. V.; De Broe, M. E.; D'Haese, P. C. Increased Serum Strontium Levels in Dialysis Patients: An Epidemiological Survey. *Kidney Int.* **1999**, *56* (5), 1879–1885.

CHAPTER 5

Using confinement to study the crystallization pathway of calcium phosphate in the presence of Sr^{2+}

Abstract

Confined spaces control the formation of biominerals in several levels since the early stages of nucleation until the arrangement of the basic building-blocks, giving rise to functional materials with controlled morphology, orientation and polymorphism. Given the great significance of the physical environment in biomineralization, in this chapter we present for the first time a systematic investigation of the effects of both Sr^{2+} content and confinement in the precipitation of calcium phosphate. To this end, the cylindrical pores of polycarbonate track-etch membranes were used as model of confined environment. We found that apatite is the main product precipitated in bulk and confinement in the absence of Sr^{2+}. Likewise, Sr^{2+}-substituted apatite was precipitated at up to 10 mol% of Sr^{2+} in bulk solution. However, Sr^{2+} and confinement when combined stabilize Sr(ACP) at physiological conditions. Relying on the pathway of apatite formation *in vitro* and previous findings, we hypothesize that Sr^{2+} acts as a temporary stabilizing agent of ACP during apatite formation. This result gives insights into the involvement of Sr^{2+} in the nucleation and evolution of bioapatite, thus highlighting the importance of confinement on biomineralization. In a second moment we evaluate the in vitro the biological response of the particles. The Sr^{2+} released from the particles reduced the differentiation and activity of osteoclasts in a Sr^{2+}-concentration dependent manner while osteoblast maturation and mineralization were supported without eliciting any cytotoxicity. These results were achieved at strikingly low concentrations of Sr^{2+} that is crucial to avoid its side effects. Overall, these results open a simple and promising pathway to develop a new generation of calcium phosphate-based ceramics active in tissue regeneration.

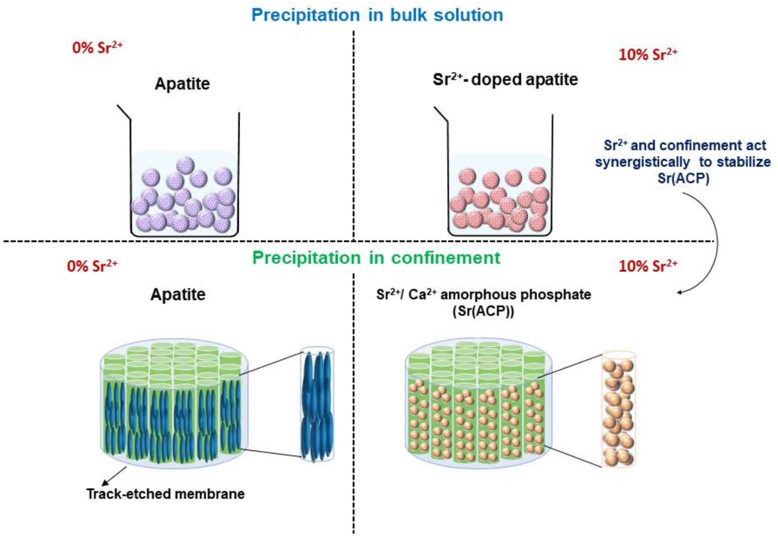

5.1 | Introduction

Calcium phosphate (CaP) is the main inorganic constituent of bone and teeth and one of the most studied biominerals.[1] Given their suitable biocompatibility, synthetic CaP are of great importance for materials science, especially hard tissue engineering.[2] Indeed, biomaterials containing CaP moieties are shown to promote osteogenic differentiation of stem cells and foster *in vivo* bone tissue formation.[3] Particularly nanorod-like hydroxyapatite crystals found in tooth enamel, the hardest tissue in the body, have inspired the synthesis of one-dimensional particles.[4,5] In fact, such intricate architecture is found across the species from all geological eras and seems to play a key role in determining the unique physicochemical properties of enamel, regardless its composition.[6,7,8] Hence, the use of CaP rod-like particles seems to be a promising strategy to enhance the mechanical stability of cements, bone scaffolds and dental implants.

Despite the outstanding features of CaP, achieving control over composition, size and morphology in synthetic materials is still challenging and of paramount importance since the structure and biological performance are intimately related.[9] The process by which natural materials are formed shed light on how overcome such a challenge.[10] For instance, mineralized organisms control the extend of crystallization processes in a masterly manner forming multifunctional hybrid structures with enhanced mechanical resistance and distinctive optical properties as compared to their synthetic counterparts.[11] This is greatly exemplified by calcite in sea urchin, aragonitic corals, bone apatite and tooth enamel in which the hierarchical architectures have widely inspired scientists from several fields *i.e.* photonics, tissue engineering, catalysis.[12]

Notably, all these biogenic minerals share a common characteristic: they are formed in confined spaces rather than in bulk solution.[13,14] Therefore, it is proposed that organisms may exploit confinement to control several features including crystal size, morphology, orientation, single crystal/polycrystal structure and more recently polymorphism.[15–17] Indeed, in bone and teeth mineralization, the confined environment provided by the gaps in the collagen fibrils controls apatite platelets deposition at the atomic scale defining their size and three-dimensional distribution over larger length scales.[18,19] However, it is often difficult to reproduce such microenvironment, so confinement effects have been neglected in materials science and mineralization investigations.

Herein, we propose the use of confinement to design one dimensional phosphate particles with controlled size and morphology aiming at bone regeneration and osteoporosis treatment. In this scenario, Sr^{2+} has shown to enhance biomaterials performance either by increasing their resorption rate or regulating the unbalanced cellular metabolism.[20] Unlike most of the osteoporosis therapies, Sr^{2+} based medicines exert a twofold effect on bone, increasing osteoblast metabolism while inhibiting osteoclasts activity thereby boosting bone regeneration.[21] Hence, extensive studies have been undertaken to design platforms to locally delivery Sr^{2+}including Ti implants, mico/nanoparticles and polymeric membranes.[22,23] Unfortunately, most of them lack the composition and the intrinsic micro/nanoscale architecture which determine the biological functions of mineralized tissues.[1] Consequently, these platforms may find limitations towards the regeneration of osteoporotic bone.

Although the role of Sr^{2+} in bone metabolism is assumed, its involvement in the nucleation and evolution of bioapatite remains elusive so far. Inspired by the presumed effects of confinement in biomineralization this study is twofold. Firstly, to gain insights towards bone mineral formation in the presence of Sr^{2+}, we evaluated how Sr^{2+} affects apatite mineralization within delimited spaces offered by cylindrical pores of polycarbonate track-etched membranes. In a second moment, we extended this approach to design bioinspired one-dimensional Sr^{2+}- loaded phosphate particles to be used as bioactive Sr^{2+} platforms. By showing that Sr^{2+} and confinement act in synergism to stabilize amorphous Sr^{2+}/Ca^{2+} phosphate Sr(ACP), our results pave the way to understand the mechanisms governing the formation of bone mineral in the presence of Sr^{2+}. Going further, this study gives clues to address the ongoing request of designing bioactive particles with controlled size and morphology.

5.2 | Experimental procedure

5.2.1 | Precipitation of rod-like phosphate particles in confinement

Biomimetic precipitation of phosphates containing different amount of Sr^{2+} was carried out within the cylindrical pores of polycarbonate track-etched membrane (Millipore) by modifying the approach developed by Lost et al.[14] Briefly, poly(acrylic acid) (PAA) (0.1% wt., Sigma MW1800 $g\,mol^{-1}$) was dissolved in aqueous solutions containing H_3PO_4 (0.006 mol L^{-1}, Sigma), $CaCl_2$(Merck P.A.), $SrCl_2$(Synth P.A.), or a mixture of these salts containing different Sr^{2+} molar percentages (0, 10, 50, and 100%) in relation to the total number of mols of divalent cations Ca^{2+} and Sr^{2+}. The total $[Ca^{2+}] + [Sr^{2+}]$ concentrations was 0.01 mol L^{-1}. The (Ca + Sr)/P molar ratio was kept constant and equal to 1.67 and the pH ~3.5. PAA is shown to enhance significantly the ability of the mineral to infiltrate into the membrane pores leading to higher synthesis yield.[24] Poly(carbonate) membranes with pore sizes measuring 200 nm were initially plasma cleaned (Harrick-plasma chamber) using N_2(g) for 2 min. In the sequence they were immersed into the PAA/salt solution for 12 h allowing the solution penetration within the pores of the membrane. So, they were subsequently placed between two glass slides and put into a desiccator containing $(NH_4)_2CO_3$ at room temperature for 12h. The $(NH_4)_2CO_3$ decomposition generates CO_2(g) and NH_3(g) that diffuse into the aqueous solutions, thus reacting with $Ca^{2+}$and Sr^{2+} triggering precipitation within the pores of the membrane. After precipitation, the surface of the membranes was scraped using filter paper to remove the crystals that were not precipitated within the pores. In the sequence, the particles were isolated by dissolving the membranes with chloroform followed by centrifugation (11000 rpm) three times. The particles were then rinsed with ethanol and characterized.

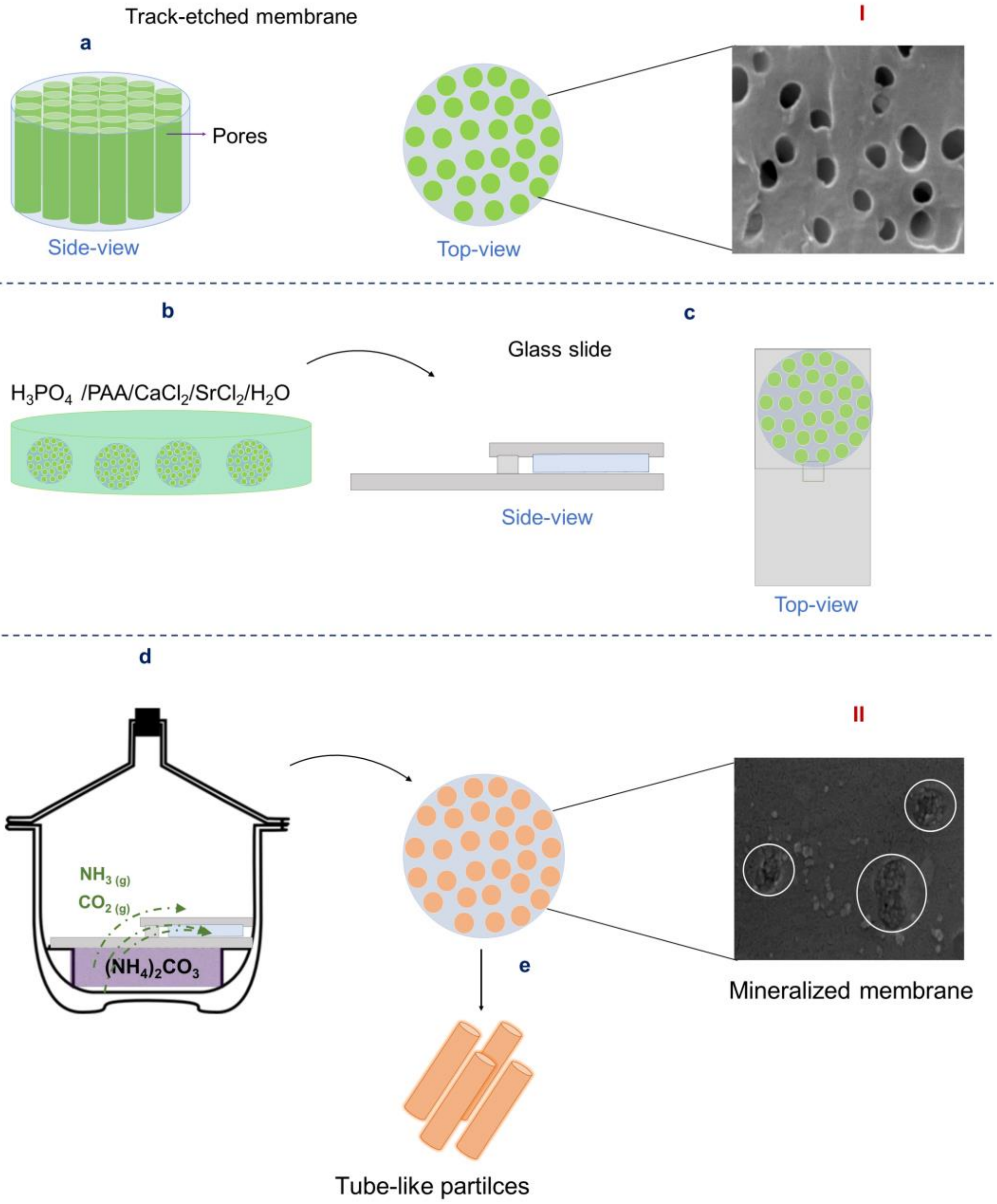

Figure 5.1 | Scheme of the formation of rod-like phosphate particles in confinement. (a) The membranes (b) are immersed into the PAA/salt solution for 12 h and then (c) placed between two glass slides. (d) For mineralization the membranes are placed in a desiccator containing $(NH_4)_2CO_3$. (e) Finally, the particles are isolated by dissolving the membranes with chloroform followed by centrifugation. I and II are representations with SEM images of a track-etched polycarbonate membrane before and after mineralization, respectively

5.2.2 | Precipitation from the bulk

Precipitation from bulk solution was carried out as control experiments. To this end 50-mL flasks containing 20 mL of the PAA/salt starting solutions were placed in a closed desiccator under identical reaction conditions used for the intramembrane precipitation, *i.e.* precursors concentration, temperature, dissector volume and reaction time. The precipitates were centrifugated, rinsed with ethanol and dried at room temperature.

5.2.3 | Biomimetic mineralization ability *in vitro*

The particles were suspended in simulated body fluid (SBF) at 37°C for 5 days to evaluate their ability to induce biomimetic precipitation of apatite in physiological environment. The SBF composition in described in the Chapter 3.

5.2.4 | Characterization of the samples

The morphology of the gold-coated particles was investigated by scanning electron microscopy (SEM) using a Zeiss-EVO 50 microscope under 20 kV accelerating voltage (Chemistry Department- University of São Paulo/RP)). For transmission electron microscopy (TEM) analysis, the samples were dispersed in ethanol and some drops were deposited on a lacey carbon film on copper grid. Energy dispersive spectroscopy (EDS) mapping of Ca, Sr and P was obtained on a single particle using a TEM microscope FEI TECNAI G2 F20 HRTEM operating at 200 kV (Department of Materials Engineering, Federal University of São Carlos/São Carlos-SP). TEM images and single particle selected area electron diffraction (SAED) patterns were acquired using a TEM microscope JEOL 2011 operating at 100 keV (LPS-Orsay, France). The chemical groups were identified by Fourier-transform infrared spectroscopy (FTIR) coupled with an attenuated total reflectance (ATR) accessory (Shimadzu-IRPrestige-21), with a resolution of 2 cm^{-1} (Chemistry Department- University of São Paulo/RP). The X-ray diffraction patterns were acquired with a Bruker-AXS D5005 diffractometer using Cu-K_α radiation at 40 kV and 30 mA (Chemistry Department-FFCLRP). The diffraction peaks were indexed based on the databank of the Joint Committee on Powder Diffraction.

5.2.5 | Release of Sr^{2+}

The amount of Sr^{2+}released from the particles after immersion in cell culture medium for 12 hours, 1, 3, 7, 14 and 21 days was determined by atomic absorption spectrometry with atomization by acetylene-air flame in the equipment ContrAA 700 (Analytik Jena AG, Jena, Germany) (Chemistry Department-University of São Paulo/RP)). Absorbance was read at 460 and 733 nm, and the samples were supplemented with La^{3+} (10 g L^{-1}) and K^{+} (1 g L^{-1}).

5.2.6 | Cellular response *in vitro*

Osteoblastic lineage cells MC3T3-E1 (American Type Culture Collection-ATCC) were cultured in a minimum essential medium (α-MEM, Gibco) supplemented with 10% fetal bovine serum and 1% (v/v) penicillin/streptomycin. This is a lineage with an osteoblastic phenotype that undergoes a proliferation–differentiation sequence, leading to the mineralization of bone-like extracellular matrix. The osteogenic medium was achieved by the addition of ascorbic acid and β-glycerophosphate. Briefly the cells were seeded on 24-well plates at the density 2.10^4 cells per well and incubated in air at 37 °C and 5% CO_2. The plated cells were then allowed to attach to the polystyrene well bottoms for 24h, followed by the replacement of the medium for a suspension of the particles at 1 μg mL^{-1} in the culture medium. The culture medium was changed every two days keeping constant the concentration of the particles. Cell viability was determined by MTT assay after 7, 14 and 21 days of culture using the protocol described by Mosmann.[25] Cell viability was expressed as the percentage of the average of three experiments as compared to the control (Ct) without treatment for each day of culture (100%).

5.2.7 | Alkaline phosphatase (ALP) activity and mineralized nodule quantification

ALP activity was determined by quantifying the hydrolysis of the substrate p-nitrophenyl phosphate (PNPP) in the plasma membrane fraction extracted from cells after 7 and 14 days of culture, according to the protocol described elsewhere.[26] The enzymatic activity was normalized by the total protein content which was estimated in the presence of 2% (w/v) sodium dodecyl sulfate using bovine serum albumin as standard. After culturing for 21 days the mineralized extra-cellular matrix was assessed by Alizarin Red staining (ARS).[27] To this end the wells were rinsed with PBS to remove possible precipitated phosphate particles.

5.2.8 | Cell morphology

SEM and confocal microscopy were applied to investigate cell morphology. The cells cultured on the polystyrene discs were fixed in 1.5% glutaraldehyde(v/v) at 4 ºC for 12 h, dehydrated through a series of ethanol concentrations (v/v, 20, 50, 70, 80, 90 and 100%) dried using super-critical CO_2 conditions and contrasted with OsO_4 (Ribeirão Preto Medical School- University of São Paulo/RP). After coated with gold the samples were observed on a Zeiss-EVO 50 SEM microscope under 20 kV accelerating voltage. The attached cells were stained with acridine orange (5 μg mL^{-1}) and then visualized using a confocal laser scanning microscopy a Leica TCS SP5 microscope. This fluorophore binds to the osteoblast nucleic acids (RNA in red; DNA in green) then providing a contrasted image. To visualize DNA, the sample was excited with the 488 nm line of an argon laser, and emission was collected between 499 and 541 nm. RNA was visualized by exciting the sample with the 458 nm line of an argon laser, and emission was collected between 642 and 682 nm.

5.2.9 | Osteoclasts differentiation and resorption activity

Bone marrow macrophages (BMMs) were isolated from long bone of 6- to 8-wk-old C57BL/6 mice and were cultured in α-MEM (GIBCO, Invitrogen) supplemented with 10 wt% fetal bovine serum (FBS; Sigma-Aldrich), 1 vol% penicillin-streptomycin, and 30 $ng.mL^{-1}$ M-CSF (R&D Systems). After 3 days, adherents BMMs were collected, seeded at a density of 2.10^4 cells/well in 96-well plates or hydroxyapatite-coated plates. Cells were cultured for 2 days in osteoclastogenic medium condition: M-CSF (30 $ng.mL^{-1}$) and RANKL (10 $ng.mL^{-1}$). Then, the osteoclastogenic medium was replaced by 1 μg mL^{-1} dispersion of the of rod-like particles Sr(CaP) containing 0, 10, 50, 100 mol% Sr^{2+} in the culture medium. Osteoclast-differentiated cells on day 4 were confirmed by tartrate-resistant acid phosphatase (TRAP) staining (Sigma-Aldrich 387A kit). The osteoclast number (TRAP-positive cells containing 3 or more nuclei) was analyzed in 5 wells per group using ImageJ software (National Institutes of Health). Resorption area was measured in hydroxyapatite-coated 96 well plate (OsteoAssay-Corning) on day 5 of culture. The results are representative of two independent experiments.

5.3 | Results and discussion

5.3.1 | Sr^{2+} and confinement act in synergism to stabilize Sr(ACP)

Precipitation into the pores of polycarbonate membranes was performed to evaluate how Sr^{2+} impacts on the formation of CaP in confinement. The effects of both Sr^{2+} content (mol%) and the physical environment were distinguished by comparison with control experiments in which the precipitation was carried out in bulk solution.

Polydisperse spherical particles were formed in the control (Figure 5.2a [i-iv]), while rod-like particles regular in size and morphology, displaying diameters from 200 to 250 nm were precipitated within the 200 nm-pores of the membranes, regardless the amount of Sr^{2+}(Figure 5.2b[i-iv]). The Sr^{2+}incorporation in the solids was proportional to its concentration in the starting solutions as determined by TEM-EDS (Table 5.1).

Table 5.1 | Sr^{2+} molar percentages (% Sr^{2+}) in relation to the total number of mols of divalent cations (Ca^{2+} + Sr^{2+}) in the starting solutions and in the products formed in bulk and in confinement, determined by TEM-EDS

%Sr^{2+} in the solution	**%Sr^{2+} bulk prodcuts**	**%Sr^{2+} confinement products**
0	0	0
10	10	10
50	47	45
100	98	97

In the absence of Sr^{2+} a mixture of apatite and others calcium phosphates *i.e.* ocatacalcium phosphate (JPDCS 26–1056) was formed in the control (Figure 5.2c[i]) while apatite was the main product formed within the membrane pores (and Figure 5.2d[i]) as evidenced by XRD. The addition of 10 mol% of Sr^{2+} in the control lead to increased strain in the crystalline structure of apatite as suggested by the broaden diffraction patterns (Figure 5.2c[ii]). Moreover, the displacement of the 002 peak towards lower values of 2θ supports the Ca^{2+} replacement by Sr^{2+} in the apatite lattice. Conversely, an amorphous phosphate phase (Sr(ACP)) was formed within the membrane pores at 10 mol% of Sr^{2+} (Figure 5.2d[ii]). At 50 mol% of Sr^{2+}, Sr(ACP) was precipitated in the control experiments as indicated by the characteristic humps at around $2\theta = 30°$ (Figure 5.2c[iii]), in agreement with the results from the Chapter 2.[28] Additionally, some peaks assigned to strontianite ($SrCO_3$, JPDCS 01-071-4899) were also detected.[29] This was expected as the reaction was carried out by the decomposition of $(NH_4)_2CO_3$. In contrast, diffraction peaks were not observed for the samples containing 50 mol% of Sr^{2+} formed within the membrane pores thus suggesting that confinement promotes the amorphization of both phosphate and carbonate (Figure 5.2d[iii]). Hence, this sample may be formed by a mixture of amorphous calcium/strontium phosphate (Sr(ACP)) and amorphous calcium/strontium carbonate (Sr(ACC)). Increased amount of Sr^{2+} up to 100 mol% resulted in the precipitation of strontium hydrogen phosphate in the control, while strontium apatite was formed in confinement (Figure 5.2c[iv] and Figure 5.2d[iv]).

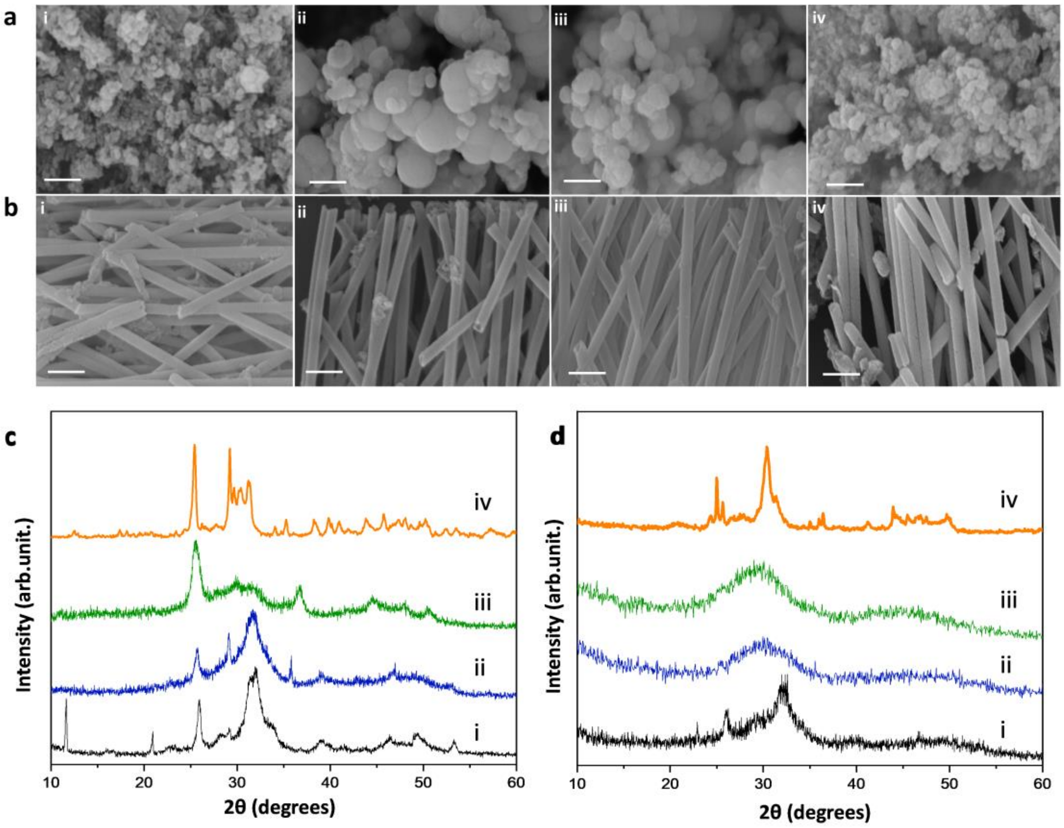

Figure 5.2| SEM images of the phosphate particles formed in the bulk solution (a) and in confinement (b). XRD pattern of the particles synthesized in homogeneous media (c) and in confinement (d). The samples where synthesized at different Sr^{2+} concentrations (mol%): 0% (i), 10% (ii), 50% (iii) and 100% (iv). Scale bar represents 1 µm. The diffractograms (ci), (cii) and (di) were indexed with the hydroxyapatite structure (JCPDS 9-432). The diffractograms (civ) and (div) were indexed as strontium hydrogen phosphate (JCPDS 23-105026) and strontium hydroxyapatite (JPDCS 33-1348), respectively.

Additional characterization of the intramembrane products was carried out using TEM and SAED (Figure 5.3). The rod-like particles obtained in absence of Sr^{2+} are polycrystalline composed of platelets of about 10 nm (Figure 5.3a and Figure 5.3b). Their apatite nature was confirmed by the typical SAED patterns (Figure 5.3c). The samples containing 10 mol% and (Figure 5.3d and Figure 5.3e) and 50 mol% of Sr^{2+} (Figure 5.3g and Figure 5.3h) are hollow and the absence of crystalline reflections in the SAED (Figure 5.3f and Figure 5.3i) confirms their amorphous nature depicted by XRD. The sample containing 100 mol% Sr^{2+} is formed by the homogenous distribution of nanometric particles (Figure 5.3j and Figure 5.3k). Finally, elementary TEM mapping results show that the elements Ca, and Sr, are homogeneously distributed within the Sr(ACP) particles containing 10%Sr^{2+} and 50%Sr^{2+} (Figure 5.4m and Figure 5.4n respectively).

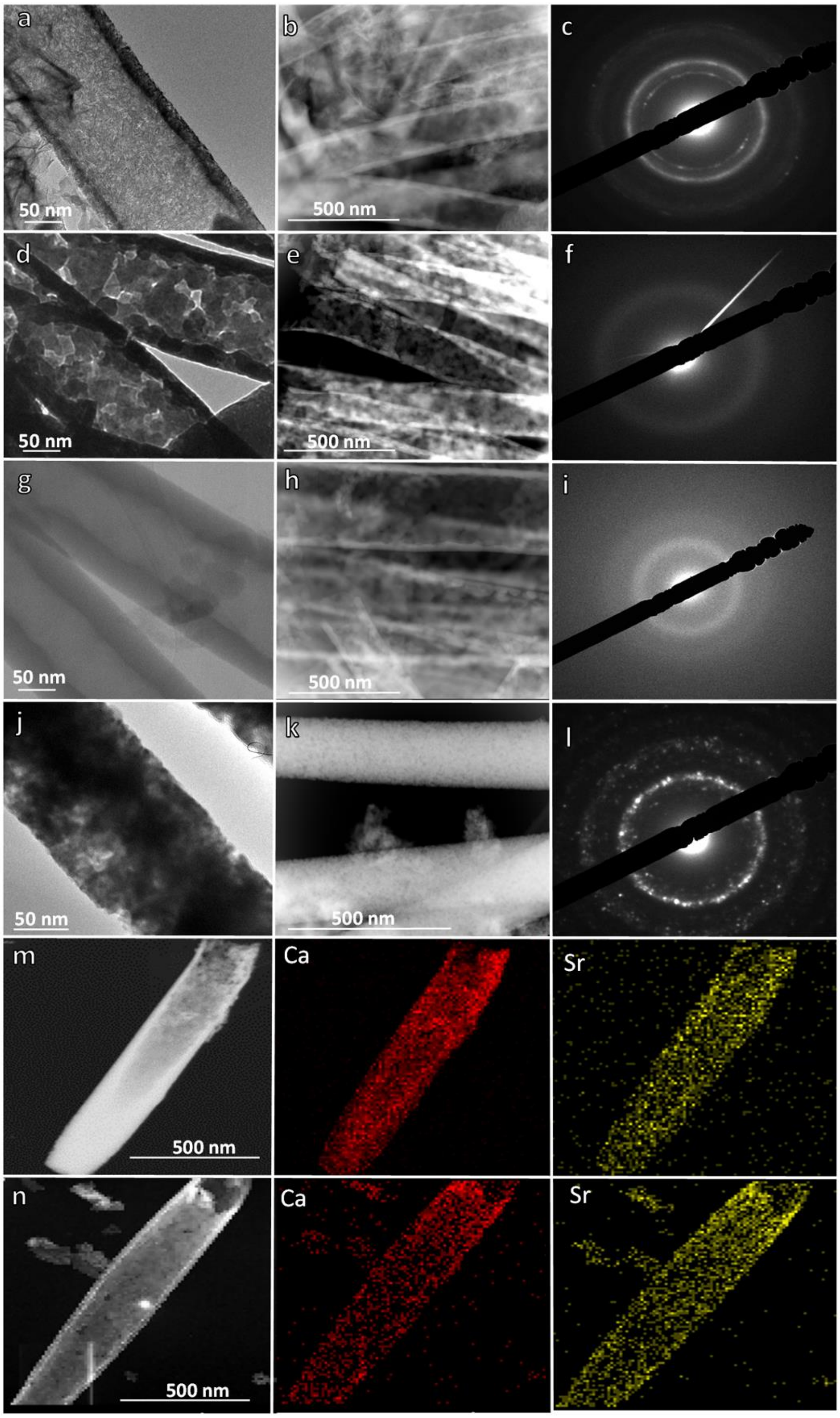

Figure 5.3 | TEM-BF (a,d,g,j) and, STEM-HAADF (b,e,h,k) images of the samples 0%Sr^{2+} (a,b), 10%Sr^{2+} (d,e), 50%Sr^{2+} (g,h) and 100%Sr^{2+} (j,k). SAED patterns of the samples 0%Sr^{2+} (c), 10%Sr^{2+} (f), 50%Sr^{2+} (i) and 100%Sr^{2+} (l). Dark field images with EDS mapping showing the Ca and Sr distribution over the samples 10%Sr^{2+} (m) and 50%Sr^{2+} (n).

From these results it can be clearly seen that both, Sr^{2+} content and physical environment have marked effects over CaP formation in terms of size, morphology and phase selection. For instance, while ACP is mostly reported with spherical morphology, here we were able to tailor the shape of Sr(ACP) into rod-like particles thanks to the boundaries offered by the membrane pores which in turn direct the mineral growth.[28] Likewise, the crystals of the apatite sample (0%Sr^{2+}) were assembled into rod-like, rather than the usually reported spherulitic morphology.[30] Precipitation within confined environments *i.e.* chitin frames and collagen fibrils, is a common strategy of mineralized organisms, that results in exquisite morphologies.[31] Such control offered by confinement has been strengthened *in vitro* by molding calcite crystals into the morphology found in urchin skeletal plate and apatite particles with similar spatial orientation found in bone mineral.[13,32]

Sr(ACP) was formed at 10 mol% of Sr^{2+} using intramembrane precipitation, while the same concentration led to the formation of apatite in bulk solution. Moreover, the comparison with the results obtained in absence of Sr^{2+} reveals that under the reaction conditions investigated herein, confinement by itself is not enough to stabilize ACP. Hence, beyond the sum of the effects observed in each system, Sr^{2+} and confinement act in synergism to stabilize Sr(ACP). Recently, we have shown that the biomimetic precipitation of Sr(ACP) in homogeneous media starts when the degree of Ca^{2+} substitution by Sr^{2+} reaches 25 mol% in the reactional medium.[28] However, this amorphous phase was stable in the reaction medium only at higher degrees of Sr^{2+} substitution, namely 50 and 75 mol%. Strikingly, here by controlling the physical environment where the precipitation takes place, we were able to precipitate Sr(ACP) at 10 mol% Sr^{2+}, that is the maximum percentage found in the bone tissue.[33]

Relying on the pathway of apatite formation *in vitro* and previous findings, we hypothesize that Sr^{2+} acts as a temporary stabilizing agent of ACP during apatite formation.[34,35] Hence, the spatial confinement provided by the membrane pores may avoid the contact of Sr(ACP) with the solution which in turn hinds the redissolution and reprecipitation processes towards crystallization.[16] In fact, the study of the lifetime of different amorphous minerals within limited volumes revealed several mechanisms by which confinement may affect the kinetics of precipitation, including slower transport of ions and reduced convection.[36,37]

The stabilization of Sr(ACP) in confinement at Sr^{2+} content close to that found in the tissue of animals raises interesting questions concerning its impacts on bone biomineralization. Previous observations have pointed out that amorphous phosphate infiltrates within the confines of the gap zone in the collagen to form bone mineral.[18,38] Notably, higher Sr^{2+} concentrations are found in young bone which is reported to be less crystalline as compared to the long term bone.[39,40] On account of that, our results bring the notion that Sr^{2+} may impact on the early stages of bone mineralization as proposed for Zn^{2+} and non-collagenous proteins.[41,42] Therefore, the action of Sr^{2+} on bone apatite may be further than a simple hetero-ionic exchange with Ca^{2+} or physical adsorption in the mature mineral, as usually described.[43] However, it is important to note that the mineralization in biological systems is much more complex than *in vitro* models and that a multitude of specialized molecules and cells are involved in this process.

Given the high controlled physicochemical features displayed by the rod-like particles described herein, we propose their application as osteogenic materials. Therefore, their ability in inducing the precipitation of bone-like apatite under physiological condition as well as their osteogenic properties was also investigated.

5.3.2 | Conversion into bone-like apatite

Aiming at bone tissue regeneration, the osteoconductive ability of the rod-like particles was assessed *in vitro* by immersion in SBF, a solution which mimics the body fluid in terms of ionic composition and pH. This is a standard assay to give insights towards the bone forming ability of biomaterials *in vitro* under physiological conditions.[44]

After 5 days of immersion in SBF, the particles were covered by a newly rough layer formed by nanometric platelets indicating the deposition biomimetic apatite (Figure 5.4a). X-ray diffraction confirms that these precipitates on the surface of the particles are nanocrystalline apatite with typical broad diffractions peaks (Figure 5.4b). It should be noted that the addition of 50%Sr^{2+} sample led also to the formation of $SrCO_3$ after exposure to SBF, as indicated by the diffraction peaks at $2\theta = 25°$ and $35°$. As discusses above this sample is likely formed by a mixture of Sr(ACP) and Sr(ACC). Therefore, in SBF these phases undergo crystallization leading to the formation of apatite and $SrCO_3$. Interestingly, $SrCO_3$ is also a potential biomaterial to osteoporosis treatments, thus, the present experimental conditions and setup could constitute an alternative procedure to precipitate such mixed phases *in vitro*.[29,45]

The fact that the rod-like morphology of the particles was maintained after the exposure to SBF suggests that their surface acted as template for the nucleation of the new phase *i.e* biomimetic apatite. It is proposed that Ca^{2+} and PO_4^{3-} from SBF accumulate at the surface of templates leading to the formation of ACP which is converted into apatite the most thermodynamically stable phase of CaP at physiological conditions.[18,34] Then, apatite grows spontaneously by consuming the templating particles and the ions from the medium including Na^+, Mg^{2+} and CO_3^{2-} thus evolving towards a bone-like mineral in terms of structure and composition.[46] The incorporation of Sr^{2+} did not disturb the apatite-forming ability of the rod-like particles during the time of exposure investigated herein, in agreement with previous findings.[47] This is regarded as an important evidence that the biomaterial will interact with the living tissue avoiding the formation of a fibrous layer between the implant and the living tissue thus leading to osteointegration.[48] Hence, these results confirm the potential ability of these particles to stimulate bone formation in an implant scenario.

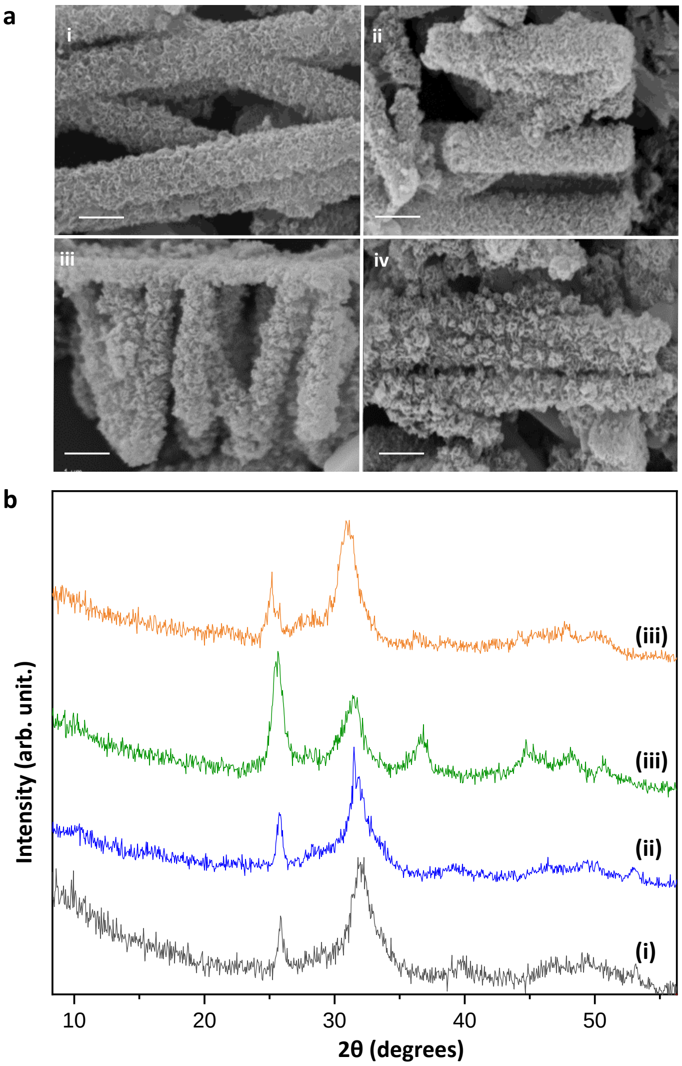

Figure 5.4 | SEM images (a) and X-ray diffraction patterns (b) of the rod-like particles after 5 days of immersion into SBF: (i) 0%Sr^{2+}; (ii) 10%Sr^{2+}; (iii) 50%Sr^{2+} and (iv) 100%Sr^{2+}. Scales bars in the SEM images correspond to 1 μm. The diffractograms were indexed with the hydroxyapatite structure (JCPDS 9-432).

The ability of the particles release Sr^{2+} in physiological media was evaluated for periods of 12 hours, 1, 3, 7, 14 and 21 days (Figure 5.5). The amount of Sr^{2+} released from the particles increased with the time suggesting the sustained and controlled delivery of the ion for long periods. This is an important result as most of the materials are reported to release the total amount of Sr^{2+} within few days. It noteworthy that the sample containing 50 mol% Sr^{2+} released higher amount of Sr^{2+} than the sample containing 100%Sr^{2+} until the 7th day. This may be ascribed to the amorphous nature of the 50%Sr^{2+} sample which may be more soluble than the highly crystalline 100%Sr^{2+} sample. Moreover, the concentrations found in the solutions fall within the values reported to enhance bone healing *in vivo*.[49]

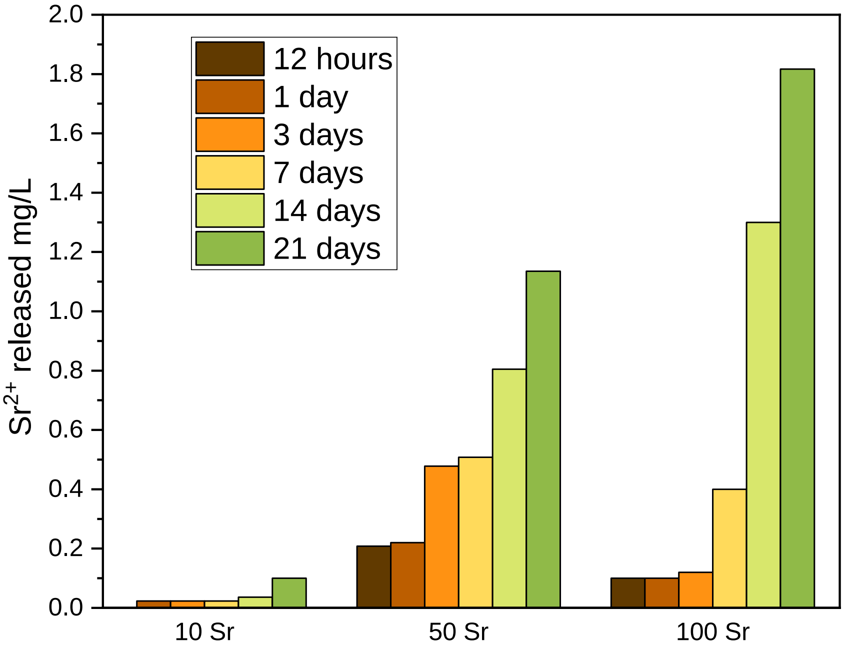

Figure 5.5 | Sr^{2+}released from the 10%Sr^{2+}, 50%Sr^{2+} and 100%Sr^{2+} phosphate particles immersed in the cell culture medium at 37 °C for 12 hours, 1, 3, 7, 14 and 21 days.

5.3.3 | *In vitro* assessment of biocompatibility and osteogenic ability of the rod-like particles

It is well-kwon that an imbalance in the activity of osteoblasts and osteoclasts leads to bone diseases, in special osteoporosis. In this sense, the biological response of the particles was assessed *in vitro* by using pre-osteoblastic cells and osteoclasts differentiation protocols.[50]

Confocal microscopy images obtained after 7 days of culture confirm that the pre-osteoblasts reached confluence displaying a polygonal shape typical from osteoblasts

(Figure 5.6a).[51] The cells remained attached at the substrate even after long term culture (21 days) with flattened and elongated morphology forming continuous monolayers typical from mature osteoblasts thus suggesting that the particles support cells adhesion and subsequent proliferation(Figure 5.6b).[52]

The MTT assays revealed that the particles did not significantly influence MC3T3-E1 proliferation, attesting their negligibly toxicity towards osteoblasts even after long exposure periods (14 and 21 days) (Figure 5.6c).

We further investigated the impacts of the rod-like particles on the ALP activity, an important early stage marker of cells differentiation, osteogenic activity and therefore bone formation.[53] After 7 days of culturing the ALP activity was higher to the 10%Sr^{2+} and 50%Sr^{2+} samples while there were no differences between the 0%Sr^{2+} and 100%Sr^{2+} samples and the control (Figure 5.6d). This agrees with *in vivo* and *in vitro* studies showing that Ca^{2+} and Sr^{2+} mixed may led to an ideal microenvironment where these ions act synergistically to stimulate osteoblast metabolism.[45,54] Indeed, the synergism between Sr and other elements such Si, Fe and Cu in promoting bone mineral formation has been demonstrated.[55–57] However, it is noteworthy that, the 10%Sr^{2+} and 50%Sr^{2+} samples are amorphous and may display enhanced degradability and consequently availability of PO_4^{3-} and Ca^{2+} in the cellular environment.[58] In this regard, it has been speculated that the biological effects of Sr^{2+} in apatite arise from the formation of an ion-rich environment conducive for osteogenesis.[59,54] Thus, it is difficult to ascertain whether the increase in the ALP activity comes from the Sr^{2+} availability in the cell culture medium or there is a synergism with other ions such as Ca^{2+} and PO_4^{3-} .[60,61] Overall, the fact that ALP activity was sustained for a long time in the presence of the particles irrespective of the Sr^{2+} concentration attests their ability to support MC3T3-E1 cells evolution towards mature bone-forming osteoblasts. Finally, in agreement with ALP results, ARS revealed that the mineralization of extracellular matrix by osteoblasts was not negatively affected by the presence of the particles (Figure 5.6e).

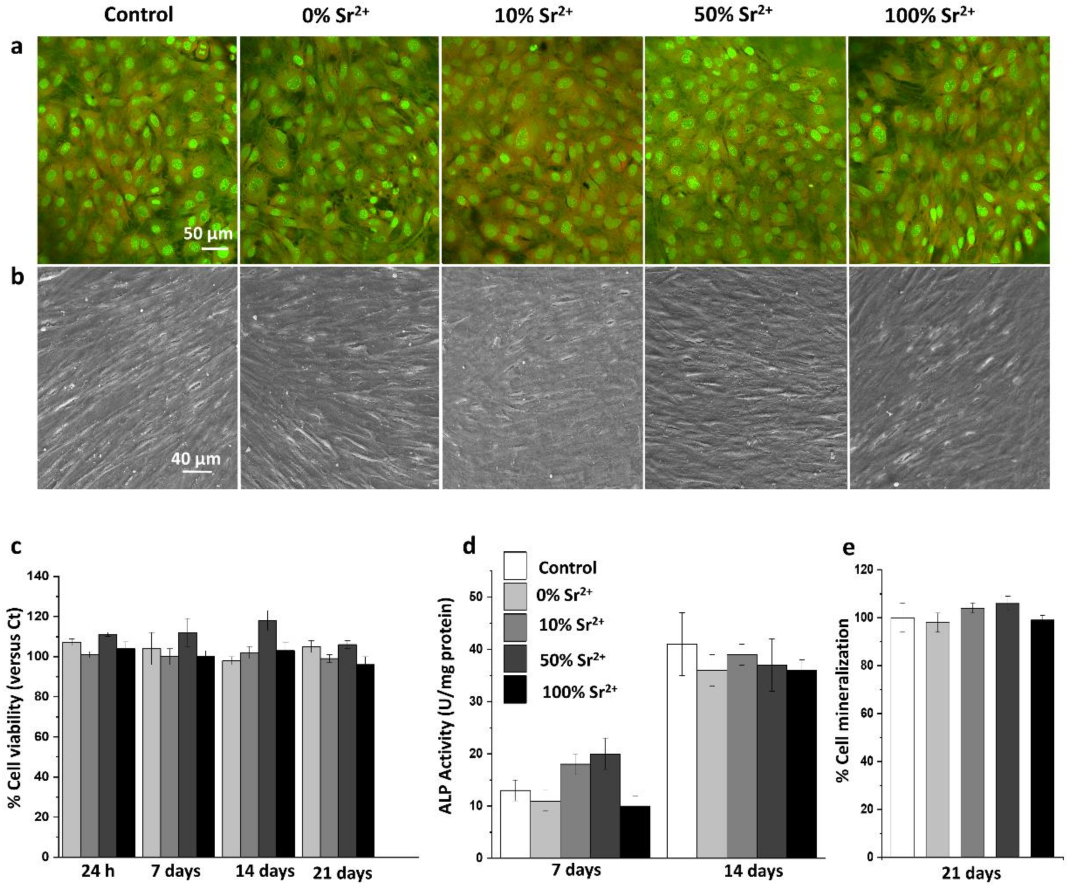

Figure 5.6 | Confocal microscopy (a) and SEM (b) images of MC3T3-E1 cells cultured for 7 and 21 days respectively, in the absence (control) and in the presence of phosphate particles containing 0% Sr^{2+}, 10% Sr^{2+}, 50% Sr^{2+} and 100% Sr^{2+}. % cell viability versus control measured by MTT assay after 24 h, 7, 14 and 21 days of culture (c), activity of ALP in the osteoblasts' membrane fraction after 7 and14 days of culture (d) and quantification of mineralized nodules formed in the wells after 21 days of culture (e). Results represent the mean values ± standard deviation for triplicate determination for one experiment.

Next, we evaluated the impact of the particles on osteoclasts differentiation and function. Bone marrow-derived monocytes/macrophages (BMMs) were cultured under osteoclastogenic condition medium in the presence of the 0,10, 50 and 100 mol% Sr^{2+} particles and TRAP staining was performed to identify osteoclasts differentiation. The formation of multinucleated osteoclasts was inhibited by the Sr^{2+} loaded particles whereas no significant differences in relation to the control were found to the 0%Sr^{2+} particles (Figure 5.7a). Quantitative measurement confirmed that the number of TRAP positive cells was reduced as the Sr^{2+} concentration increased in the particles (Figure 5.7b).

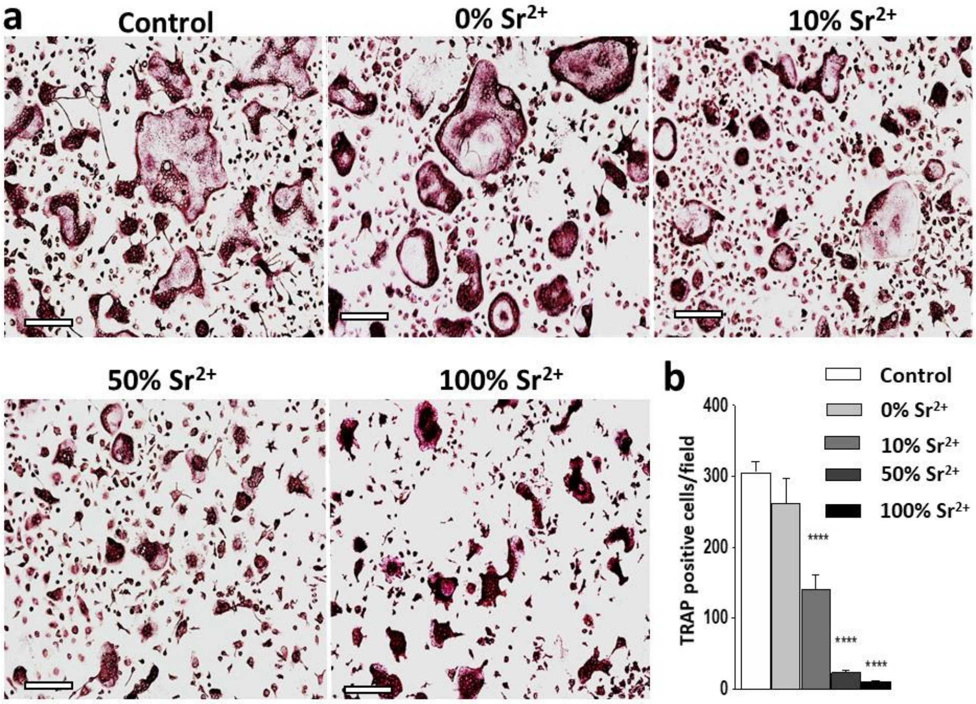

Figure 5.7 | Representative images (a) and quantification (b) of TRAP-positive osteoclasts cultured for 4 days. Bone marrow macrophages (BMMs) was cultured under M-CSF and RANKL stimulation, in the absence (control) and in the presence of the CaP tubes containing 0% Sr^{2+}, 10% Sr^{2+}, 50% Sr^{2+} and 100% Sr^{2+}. Results represent the mean value ± standard deviation (n=5) representative of two independent experiments. One-way ANOVA, followed by Tukey's post-test.****$p< 0.001$, compared to control. Scales bars represent 100 μm.

To evaluate the ability of the particles to inhibit bone resorption, osteoclasts were cultured on hydroxyapatite-coated plates. The formation of demineralization pits was prevented by the Sr^{2+} loaded particles (Figure 5.8a). Quantification of the areas of the pits confirmed that the demineralization capacity of osteoclasts was significantly reduced by the 10% Sr^{2+} particles or completely inhibited in the case of the 50% Sr^{2+} and 100% Sr^{2+} particles (Figure 5.8b).

Overall, these results are in agreement with previous investigations which demonstrated that Sr^{2+} released from biomaterials and particles inhibit osteoclast differentiation and resorption activities. Nevertheless, Sr^{2+} levels much higher (88 mg L^{-1}) than those found in the serum of patients treated with strontium ranelate (10 mg L^{-1}) are usually described for eliciting such anti-osteoclastogenic effects.[62] Herein, a striking low amount of Sr^{2+} (less than 0.2 mg L^{-1}) was enough to significantly hinder osteoclast activity and differentiation. Interestingly, the % Sr^{2+} incorporated in these particles is the physiological percentage found in bone tissue (10% mol with respect to Ca^{2+}).[63] Even the highest Sr^{2+} concentration used here (0.7 mg L^{-1}) was lower than that used in other investigations reporting on bioglasses able to delivery Sr^{2+} within the range described as efficient to trigger antiosteoporotic effects in vivo (~5 mg L^{-1}).[63] This is an important feature, as the side effects of Sr^{2+} accumulation in bone cannot be overlooked;. although high doses decrease differentiation and metabolism of osteoclasts it may also lead to pathological mineralization.[64] Actually, the regulation of bone cells metabolism by Sr^{2+} is quite ambiguous. Several studies have demonstrated that osteoblasts response to Sr^{2+} might be a question of optimal environment rather than a concentration driven effect.[65]

On the basis of our results and the literature presented in this discussion, we believe that tuning the Sr^{2+} and Ca^{2+} concentrations is crucial for the design of materials aiming at bone regeneration and our approach provides an effective way to do this.

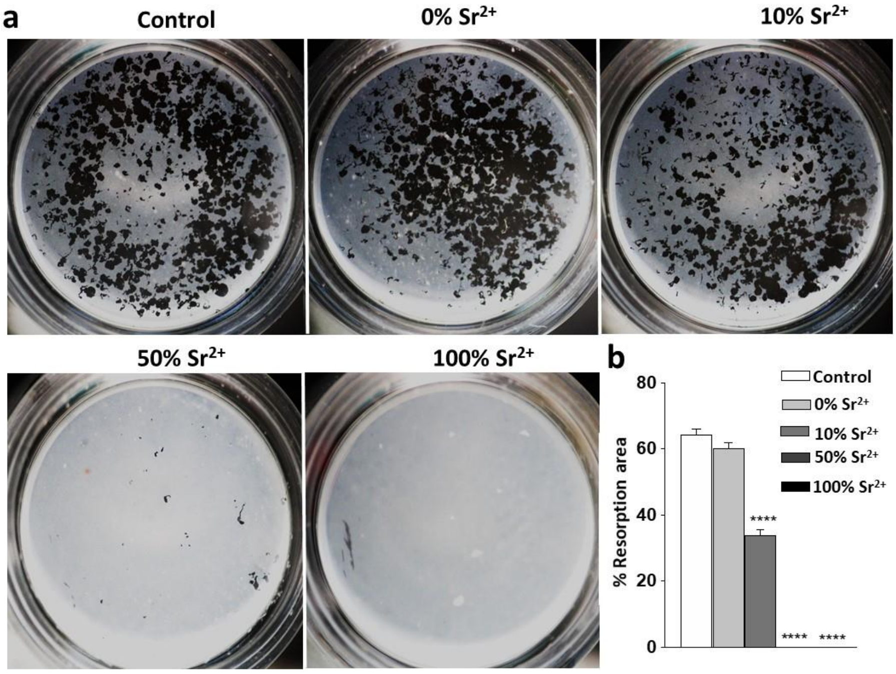

Figure 5.8 | Representative images (a) and quantification of resorption area (b) induced by osteoclasts cultured in hydroxyapatite-coated plates for 5 days. Bone marrow macrophages (BMMs) was cultured under M-CSF and RANKL in hydroxyapatite-coated plates, in the absence (control) and in the presence of CaP tubes containing 0% Sr^{2+}, 10% Sr^{2+}, 50% Sr^{2+} and 100% Sr^{2+}. Results represent the mean value ± standard deviation (n=5) representative of two independent experiments. One-way ANOVA, followed by Tukey's post-test.****$p < 0.001$, compared to control.

5.4 | Conclusions

The use of confinement allowed to investigate the role played by Sr^{2+} on the early stages of apatite precipitation and the synthesis of particles with controlled size, morphology and Sr^{2+} content. This investigation showed that Sr^{2+} and confinement act in synergism to stabilize amorphous calcium phosphate, an important precursor of bone apatite. This suggests that Sr^{2+} may be involved during the steps of the infiltration of the amorphous precursor within the gap zones of collagen. Moreover, the particles were not toxic to osteoblasts sustaining is maturation and mineralization. Specially the samples containing Ca^{2+} and Sr^{2+} mixed were shown to increase the ALP activity at the early stages. The rod-like particles displayed controlled and sustained release of Sr^{2+} until 21 days which is an important feature for *in vivo* platforms. By showing that Sr^{2+} can be effective at low concentrations when combined with calcium CaPs, this investigation reconciliates the reports of pathological mineralization at excess of Sr^{2+} with its therapeutic effects. Going further, this investigation provides a facile strategy to produce a new generation of biomimetic ceramics with relevant biological responses.

5.5 | References

(1) Weiner, S.; Wagner, H. D. The Material Bone: Structure-Mechanical Function Relations. *Annu. Rev. Mater. Sci.* **1998**, *28* (1), 271–298.

(2) Zhou, H.; Lee, J. Acta Biomaterialia Nanoscale Hydroxyapatite Particles for Bone Tissue Engineering. *Acta Biomater.* **2011**, 7 (7), 2769–2781.

(3) Jiang, N.; Guo, Z.; Sun, D.; Li, Y.; Yang, Y.; Chen, C.; Zhang, L.; Zhu, S. Promoting Osseointegration of Ti Implants through Micro/Nanoscaled Hierarchical Ti Phosphate/Ti Oxide Hybrid Coating. *ACS Nano* **2018**, *12* (8), 7883–7891.

(4) Wei, J.; Ping, H.; Xie, J.; Zou, Z.; Wang, K.; Xie, H.; Wang, W.; Lei, L.; Fu, Z. Bioprocess-Inspired Microscale Additive Manufacturing of Multilayered TiO 2 / Polymer Composites with Enamel-Like Structures and High Mechanical Properties. *Adv. Funct. Mater.* **2019**, *1904880*, 1–9.

(5) Chen, Z.; Miao, Z.; Zhang, P.; Xiao, H.; Liu, H.; Ding, C.; Tan, H.; Li, J. Bioinspired Enamel-like Oriented Minerals on General Surfaces : Towards Improved Mechanical. *J. Mater. Chem. B* **2019**, 7 (3), 5237–5244.

(6) Hwang, S. H. The Evolution of Dinosaur Tooth Enamel Microstructure. *Biol. Rev.* **2011**, *86*, 183–216.

(7) Qu, Q.; Haitina, T.; Zhu, M.; Ahlberg, P. E. New Genomic and Fossil Data Illuminate the Origin of Enamel. *Nature* **2015**, *526* (7571), 108.

(8) Yeom, B.; Sain, T.; Lacevic, N.; Bukharina, D.; Cha, S. H.; Waas, A. M.; Arruda, E. M.; Kotov, N. A. Abiotic Tooth Enamel. *Nature* **2017**, *543* (7643), 95–98.

(9) Ramos, A. P., Cruz, M. A.E.; Tovani, C.B., Ciancaglini, P. Biomedical Applications of Nanotechnology. *Biophys. Rev.* **2017**, *9* (2), 79–89.

(10) Greil, B. P. Advanced Materials Progress Report on Microporous and Mesoporous Material. *Adv. Mater.* **2002**, *14* (10), 709–716.

(11) Weiner, S.; Addadi, L. Design Strategies in Mineralized Biological Materials. *J. Mater. Chem.* **1997**, 7 (5), 689–702.

(12) Nudelman, F.; Sommerdijk, N. a J. M. Biomineralization as an Inspiration for Materials Chemistry. *Angew. Chem. Int. Ed. Engl.* **2012**, *51* (27), 6582–6596.

(13) Cantaert, B.; Beniash, E.; Meldrum, F. C. Nanoscale Confinement Controls the Crystallization of Calcium Phosphate: Relevance to Bone Formation. *Chem. - A Eur. J.* **2013**, *19* (44), 14918–14924.

(14) Loste, E.; Park, R. J.; Warren, J.; Meldrum, F. C. Precipitation of Calcium Carbonate in Confinement. *Adv. Funct. Mater.* **2004**, *14* (12), 1211–1220.

(15) Schenk, A. S.; Albarracin, E. J.; Kim, Y. Y.; Ihli, J.; Meldrum, F. C. Confinement Stabilises Single Crystal Vaterite Rods. *Chem. Commun.* **2014**, *50* (36), 4729–4732.

(16) Wang, Y. W.; Christenson, H. K.; Meldrum, F. C. Confinement Increases the Lifetimes of Hydroxyapatite Precursors. *Chem. Mater.* **2014**, *26* (20), 5830–5838.

(17) Zeng, M.; Kim, Y. Y.; Anduix-Canto, C.; Frontera, C.; Laundy, D.; Kapur, N.; Christenson, H. K.; Meldrum, F. C. Confinement Generates Single-Crystal Aragonite Rods at Room Temperature. *Proc. Natl. Acad. Sci. U. S. A.* **2018**, *115* (30), 7670–7675.

(18) Lotsari, A.; Rajasekharan, A. K.; Halvarsson, M.; Andersson, M. Transformation of Amorphous Calcium Phosphate to Bone-like Apatite. *Nat. Commun.* **2018**, *9* (1), 4170.

(19) Kim, D.; Lee, B.; Thomopoulos, S.; Jun, Y. S. The Role of Confined Collagen Geometry

in Decreasing Nucleation Energy Barriers to Intrafibrillar Mineralization. *Nat. Commun.* **2018**, *9* (1), 962.

(20) Marie, P. J. Strontium as Therapy for Osteoporosis. *Curr. Opin. Pharmacol.* **2005**, *5* (6), 633–636.

(21) Bonnelye, E.; Chabadel, A.; Saltel, F.; Jurdic, P. Dual Effect of Strontium Ranelate: Stimulation of Osteoblast Differentiation and Inhibition of Osteoclast Formation and Resorption in Vitro. *Bone* **2008**, *42* (1), 129–138.

(22) Schumacher, M.; Gelinsky, M. Strontium Modified Calcium Phosphate Cements - Approaches towards Targeted Stimulation of Bone Turnover. *J. Mater. Chem. B* **2015**, *3* (23), 4626–4640.

(23) Xin, Y.; Jiang, J.; Huo, K.; Hu, T.; Chu, P. K. Bioactive SrTiO 3 Nanotube Arrays: Strontium Delivery Platform on Ti-Based Osteoporotic Bone Implants. *ACS Nano* **2009**, *3* (10), 3228–3234.

(24) Kim, Y. Y.; Hetherington, N. B. J.; Noel, E. H.; Kröger, R.; Charnock, J. M.; Christenson, H. K.; Meldrum, F. C. Capillarity Creates Single-Crystal Calcite Nanowires from Amorphous Calcium Carbonate. *Angew. Chemie - Int. Ed.* **2011**, *50* (52), 12572–12577.

(25) Mosmann, T. Rapid Colorimetric Assay for Cellular Growth and Survival: Application to Proliferation and Cytotoxicity Assays. *J. Immunol. Methods* **1983**, *65* (2), 55–63.

(26) Simão, A. M. S.; Beloti, M. M.; Rosa, A. L.; de Oliveira, P. T.; Granjeiro, J. M.; Pizauro, J. M.; Ciancaglini, P. Culture of Osteogenic Cells from Human Alveolar Bone: A Useful Source of Alkaline Phosphatase. *Cell Biol. Int.* **2007**, *31* (11), 1405–1413.

(27) Gregory, C. A.; Gunn, W. G.; Peister, A.; Prockop, D. J. An Alizarin Red-Based Assay of Mineralization by Adherent Cells in Culture: Comparison with Cetylpyridinium Chloride Extraction. *Anal. Biochem.* **2004**, *329* (1), 77–84.

(28) Bussola Tovani, C.; Gloter, A.; Azaïs, T.; Selmane, M.; Ramos, A. P.; Nassif, N. Formation of Stable Strontium-Rich Amorphous Calcium Phosphate: Possible Effects on Bone Mineral. *Acta Biomater.* **2019**, *92*, 315–324.

(29) Tovani, C. B.; Oliveira, T. M.; Gloter, A.; Ramos, A. P. Sr2+-Substituted CaCO3Nanorods: Impact on the Structure and Bioactivity. *Cryst. Growth Des.* **2018**, *18* (5), 2932–2940.

(30) Nassif, N.; Martineau, F.; Syzgantseva, O.; Gobeaux, F.; Willinger, M.; Coradin, T.; Cassaignon, S.; Azaïs, T.; Giraud-Guille, M. M. In Vivo Inspired Conditions to Synthesize Biomimetic Hydroxyapatite. *Chem. Mater.* **2010**, *22* (12), 3653–3663.

(31) Addadi, L.; Joester, D.; Nudelman, F.; Weiner, S. Mollusk Shell Formation: A Source of New Concepts for Understanding Biomineralization Processes. *Chem. - A Eur. J.* **2006**, *12* (4), 980–987.

(32) Park, R. J.; Meldrum, F. C. Synthesis of Single Crystals of Calcite with Complex Morphologies. *Adv. Mater.* **2002**, *14* (16), 1167–1169.

(33) Farlay, D.; Boivin, G.; Panczer, G.; Lalande, A.; Meunier, P. J. Long-Term Strontium Ranelate Administration in Monkeys Preserves Characteristics of Bone Mineral Crystals and Degree of Mineralization of Bone. *J. Bone Miner. Res.* **2005**, *20* (9), 1569–1578.

(34) Wang, X.; Yang, J.; Andrei, C. M.; Soleymani, L.; Grand, K. Biomineralization of Calcium Phosphate Revealed by in Situ Liquid-Phase Electron Microscopy. *Commun. Chem.* **2018**, *1* (1), 80.

(35) Shih, Y. R. V.; Hwang, Y.; Phadke, A.; Kang, H.; Hwang, N. S.; Caro, E. J.; Nguyen, S.; Siu, M.; Theodorakis, E. A.; Gianneschi, N. C.; et al. Calcium Phosphate-Bearing Matrices

Induce Osteogenic Differentiation of Stem Cells through Adenosine Signaling. *Proc. Natl. Acad. Sci. U. S. A.* **2014**, *111* (3), 990–995.

(36) Ihli, J.; Wang, Y.-W.; Cantaert, B.; Kim, Y.-Y.; Green, D. C.; Bomans, P. H. H.; Sommerdijk, N. A. J. M.; Meldrum, F. C. Precipitation of Amorphous Calcium Oxalate in Aqueous Solution. *Chem. Mater.* **2015**, *27* (11), 3999–4007.

(37) Anduix-Canto, C.; Kim, Y. Y.; Wang, Y. W.; Kulak, A.; Meldrum, F. C.; Christenson, H. K. Effect of Nanoscale Confinement on the Crystallization of Potassium Ferrocyanide. *Cryst. Growth Des.* **2016**, *16* (9), 5403–5411.

(38) Akiva, A.; Kerschnitzki, M.; Pinkas, I.; Wagermaier, W.; Yaniv, K.; Fratzl, P.; Addadi, L.; Weiner, S. Mineral Formation in the Larval Zebra Fi Sh Tail Bone Occurs via an Acidic Disordered Calcium Phosphate Phase. *J. Am. Chem. Soc.* **2016**, *138* (43), 14481–14487.

(39) Li, C.; Paris, O.; Siegel, S.; Roschger, P.; Paschalis, E. P.; Klaushofer, K.; Fratzl, P. Strontium Is Incorporated into Mineral Crystals Only in Newly Formed Bone during Strontium Ranelate Treatment. *J. Bone Miner. Res.* **2010**, *25* (5), 968–975.

(40) Chamberlain, T.; Handbook, S. E. Infrared Analysis of Rat Bone : Age Dependency Of. *Science* **1966**, *153* (3743), 1523–1525.

(41) Cantaert, B.; Beniash, E.; Meldrum, F. C. The Role of Poly(Aspartic Acid) in the Precipitation of Calcium Phosphate in Confinement. *J. Mater. Chem. B* **2013**, *1* (48), 6586–6595.

(42) Procopio, A.; Malucelli, E.; Pacureanu, A.; Cappadone, C.; Farruggia, G.; Sargenti, A.; Castiglioni, S.; Altamura, D.; Sorrentino, A.; Giannini, C.; et al. Chemical Fingerprint of Zn–Hydroxyapatite in the Early Stages of Osteogenic Differentiation. *ACS Cent. Sci.* **2019**, *5* (8), 1449–1460.

(43) Frankær, C. G.; Raffalt, A. C.; Stahl, K. Strontium Localization in Bone Tissue Studied by X-Ray Absorption Spectroscopy. *Calcif. Tissue Int.* **2014**, *94* (2), 248–257.

(44) Kokubo, T.; Takadama, H. How Useful Is SBF in Predicting in Vivo Bone Bioactivity? *Biomaterials* **2006**, *27* (15), 2907–2915.

(45) Cruz, M. A. E.; Zanatta, M. B. T.; da Veiga, M. A. M. S.; Ciancaglini, P.; Ramos, A. P. Lipid-Mediated Growth of SrCO 3 /CaCO 3 Hybrid Films as Bioactive Coatings for Ti Surfaces. *Mater. Sci. Eng. C* **2019**, *99* , 762–769.

(46) Kim, H. M.; Himeno, T.; Kokubo, T.; Nakamura, T. Process and Kinetics of Bonelike Apatite Formation on Sintered Hydroxyapatite in a Simulated Body Fluid. *Biomaterials* **2005**, *26* (21), 4366–4373.

(47) Leite, Á. J.; Gonçalves, A. I.; Rodrigues, M. T.; Gomes, M. E.; Mano, J. F. Strontium-Doped Bioactive Glass Nanoparticles in Osteogenic Commitment. *ACS Appl. Mater. Interfaces* **2018**, *10* (27), 23311–23320.

(48) Zhao, W.; Michalik, D.; Ferguson, S.; Hofstetter, W.; Lemaître, J.; von Rechenberg, B.; Bowen, P. Rapid Evaluation of Bioactive Ti-Based Surfaces Using an in Vitro Titration Method. *Nat. Commun.* **2019**, *10* (1), 1–11.

(49) Marie, P. J.; Ammann, P.; Boivin, G.; Rey, C. Mechanisms of Action and Therapeutic Potential of Strontium in Bone. *Calcif. Tissue Int.* **2001**, *69* (3), 121–129.

(50) Jilka, R. L. Biology of the Basic Multicellular Unit and the Pathophysiology of Osteoporosis. *Med. Pediatr. Oncol.* **2003**, *41* (3), 182–185.

(51) Uggeri, J.; Guizzardi, S.; Scandroglio, R.; Gatti, R. Adhesion of Human Osteoblasts to Titanium: A Morpho-Functional Analysis with Confocal Microscopy. *Micron* **2010**, *41* (3), 210–219.

(52) Suphasiriroj, W.; Yotnuengnit, P.; Surarit, R.; Pichyangkura, R. The Fundamental Parameters of Chitosan in Polymer Scaffolds Affecting Osteoblasts (MC3T3-E1). *J. Mater. Sci. Mater. Med.* **2009**, *20* (1), 309–320.

(53) Sifert, R. S. The Role of Alkaline Phosphatase in Osteogenesis. *J. Exp. Med.* **1951**, *93* (5), 415–426.

(54) Xie, H.; Gu, Z.; He, Y.; Xu, J.; Xu, C.; Li, L.; Ye, Q. Microenvironment Construction of Strontium-Calcium-Based Biomaterials for Bone Tissue Regeneration: The Equilibrium Effect of Calcium to Strontium. *J. Mater. Chem. B* **2018**, *6* (15), 2332–2339.

(55) Li, K.; Dai, F.; Yan, T.; Xue, Y.; Zhang, L.; Han, Y. Magnetic Silicium Hydroxyapatite Nanorods for Enhancing Osteoblast Response in Vitro and Biointegration in Vivo. *ACS Biomater. Sci. Eng.* **2019**, *5*, 2208–2221.

(56) Basu, S.; Ghosh, A.; Barui, A.; Basu, B. (Fe/Sr) Codoped Biphasic Calcium Phosphate with Tailored Osteoblast Cell Functionality. *ACS Biomater. Sci. Eng.* **2018**, *4* (3), 857–871.

(57) Weng, L.; Boda, S. K.; Teusink, M. J.; Shuler, F. D.; Li, X.; Xie, J. Binary Doping of Strontium and Copper Enhancing Osteogenesis and Angiogenesis of Bioactive Glass Nanofibers While Suppressing Osteoclast Activity. *ACS Appl. Mater. Interfaces* **2017**, *9* (29), 24484–24496.

(58) Deng, Y.; Liu, M.; Chen, X.; Wang, M.; Li, X.; Xiao, Y.; Zhang, X. Enhanced Osteoinductivity of Porous Biphasic Calcium Phosphate Ceramic Beads with High Content of Strontium-Incorporated Calcium-Deficient Hydroxyapatite. *J. Mater. Chem. B* **2018**, *6* (41), 6572–6584.

(59) Boda, S. K.; Thrivikraman, G.; Panigrahy, B.; Sarma, D. D.; Basu, B. Competing Roles of Substrate Composition, Microstructure, and Sustained Strontium Release in Directing Osteogenic Differentiation of HMSCs. *ACS Appl. Mater. Interfaces* **2017**, *9* (23), 19389–19408.

(60) Cai, X.; Han, B.; Liu, Y.; Tian, F.; Liang, F.; Wang, X. Chlorhexidine-Loaded Amorphous Calcium Phosphate Nanoparticles for Inhibiting Degradation and Inducing Mineralization of Type i Collagen. *ACS Appl. Mater. Interfaces* **2017**, *9* (15), 12949–12958.

(61) Yu, W.; Sun, T. W.; Qi, C.; Ding, Z.; Zhao, H.; Chen, F.; Chen, D.; Zhu, Y. J.; Shi, Z.; He, Y. Strontium-Doped Amorphous Calcium Phosphate Porous Microspheres Synthesized through a Microwave-Hydrothermal Method Using Fructose 1,6-Bisphosphate as an Organic Phosphorus Source: Application in Drug Delivery and Enhanced Bone Regeneration. *ACS Appl. Mater. Interfaces* **2017**, *9* (4), 3306–3317.

(62) Gentleman, E.; Fredholm, Y. C.; Jell, G.; Lotfibakhshaiesh, N.; O'Donnell, M. D.; Hill, R. G.; Stevens, M. M. The Effects of Strontium-Substituted Bioactive Glasses on Osteoblasts and Osteoclasts in Vitro. *Biomaterials* **2010**, *31* (14), 3949–3956.

(63) Lao, J.; Jallot, E.; Nedelec, J. M. Strontium-Delivering Glasses with Enhanced Bioactivity: A New Biomaterial for Antiosteoporotic Applications? *Chem. Mater.* **2008**, *20* (15), 4969–4973.

(64) D'Haese, P. C.; Schrooten, I.; Goodman, W. G.; Cabrera, W. E.; Lamberts, L. V.; Elseviers, M. M.; Couttenye, M. M.; De Broe, M. E. Increased Bone Strontium Levels in Hemodialysis Patients with Osteomalacia. *Kidney Int.* **2000**, *57* (3), 1107–1114.

(65) Cruz, M. A. E.; Zanatta, M. B. T.; da Veiga, M. A. M. S.; Ciancaglini, P.; Ramos, A. P. Lipid-Mediated Growth of SrCO 3 /CaCO 3 Hybrid Films as Bioactive Coatings for Ti Surfaces. *Mater. Sci. Eng. C* **2019**, *99* (February), 762–769

CHAPTER 6

Sr^{2+}-substituted $CaCO_3$ rod-like particles: structural characterization and in vitro osteogenic activity

Abstract

Besides bone apatite, strontium is also a natural trace element in aragonitic corals. Even though Ca^{2+} substitution for Sr^{2+} has been described in many phosphate minerals, the impact of such substitution on bioactivity and structure in pure carbonate phases has not been explored. Therefore, here we used a bioinspired approach to synthesize carbonate particles with controlled size in which Ca^{2+} was progressively substituted for Sr^{2+}. Through structural investigation by X-ray diffraction, Raman spectroscopy, electron microscopy techniques including high resolution transmission electron microscopy and electron diffraction we studied the precipitation mechanism of Sr-substituted $CaCO_3$ nanorods showing that increased Sr^{2+} content lead to stabilization of strontianite, a mineral from aragonite group. *In vitro* assays attested that the bioactivity of the particles was maintained even at high Sr^{2+} concentrations. Moreover, pre-osteoblastic cells proliferated and mineralized in the presence of the particles highlighting their potential application in bone regeneration. These outcomes are fundamental for proper evaluation of the role that Sr^{2+} plays in carbonate-based biomaterials properties and biomineralization. Overall, this investigation constitutes a starting point to explore (Ca,Sr)CO_3 particles as bioactive materials for bone replacement.

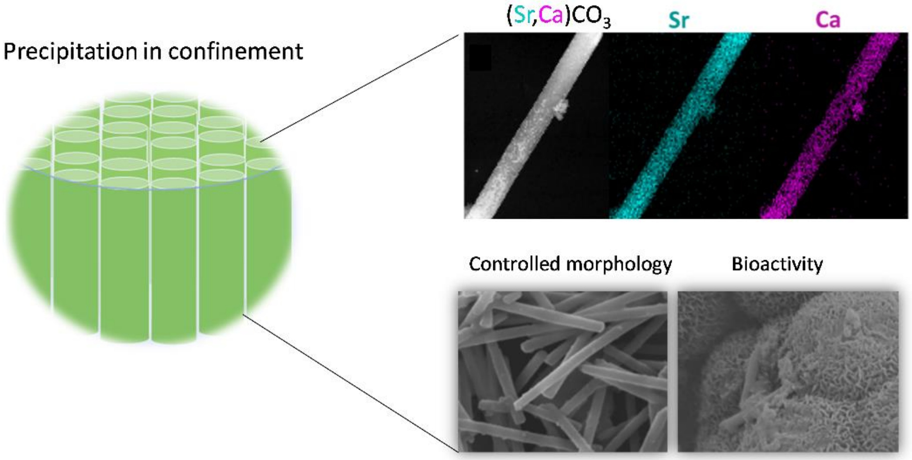

The results presented in this chapter are reproduced in part with permission from: Tovani, C. B.; Oliveira, T. M.; Gloter, A.; Ramos, A. P. Sr^{2+}-Substituted $CaCO_3$ Nanorods: Impact on the Structure and Bioactivity. Cryst. Growth Des. ***2018****, 18 (5), 2932–2940.* Copyright 2018 American Chemical Society.

6.1 | Introduction

The major challenge in the field of bone regeneration is to obtain a biomaterial with suitable bioactivity, biocompatibility and osteoconduction. The bioactivity, the ability of a biomaterial to induce apatite precipitation in biological medium, is essential to biomaterial performance *in vivo*.[1] The apatite layer formed at the biomaterial/tissue interface guides the first steps of the osteoconduction process.[2] In this sense, among the countless materials that have been applied to achieve this goal, biominerals have proven to be a promising choice.[3,4,5]

Biominerals are hybrid materials with outstanding mechanical properties.[6] Their organic component consists mainly of proteins and polysaccharides, whereas the most common inorganic phases are calcium carbonate ($CaCO_3$), hydroxyapatite ($Ca_{10}(PO_4)_6(OH)_2$, (designated HA), and silica (SiO_2).[7]

Although the use of apatite to build bone replacement implants is well established, $CaCO_3$ has been increasingly studied for this purpose, not to mention that the CO_3^{2-} ion is the main substitute in bone apatite (B-type substitution).[8,9,10] This substitution underlies many properties of biological apatite such as the high reactivity and enhanced collagen deposition and resorption of young bones as compared to stoichiometric HA or HA bearing A-type substitution (OH group).[11,12] This fact has motivated numerous studies regarding the conversion of $CaCO_3$-based materials to calcium phosphate minerals.[13,14] Some studies of our group have pointed out the bioactivity of $CaCO_3$ based materials in the form of films and particles.[15,16,17]

Sr^{2+} can substitute Ca^{2+} in the carbonate crystal structure, and the former element occurs in aragonitic coral skeletons and carbonate rocks.[18,19,20] The mineral $SrCO_3$ has been synthesized for application in the fields of optics and catalysis.[21,22] This mineral has also been used as a model to examine aragonite mineralization since $SrCO_3$ is an isostructure of this $CaCO_3$ polymorph, which is present in natural systems like nacre, pearls, and corals.[21,22]

In vitro and *in vivo* studies have shown that Sr^{2+} administration has dual action: it increases osteoblast activity and diminishes osteoclast activity, resulting in enhanced bone mineral density and mechanical properties.[23,24] Unlike oral administration, the strategy of Sr^{2+} incorporation in the material that will be contacting the tissue thought the interface offers the advantage of direct Sr^{2+} delivery at the specific bone site defect, at a desired dosage.[24] In this regard, special attention has been devoted to substituting Ca^{2+} for Sr^{2+} in biomaterials to boost bone healing.[25,26,27]

In this context, $SrCO_3$ particles have been used to produce Sr^{2+}-rich phosphate cements.[28,29] The presence of Sr^{2+} in the phosphate lattice leads to physical-chemical changes that directly impact the cement features, including mechanical resistance, cellular response, and bioactivity.[30] However, the lack of consistent characterization of the final materials has caused contradictory reports about Sr^{2+} participation in the biomaterial performance.[31] To draw general conclusions about the role that Sr^{2+} plays in biomaterial performance, it is crucial to obtain materials with controlled size, crystallinity, and composition. Therefore, the synthesis of a series of Sr^{2+}-substituted carbonate particles with controlled features can be an important starting point to evaluate the role that Sr^{2+} has in the properties of the biomaterials and to clarify some issues such as its impact on bioactivity and crystalline structure of carbonates.

Even though Ca^{2+} substitution for Sr^{2+} has been described in many phosphate structures, such substitution has not been explored in pure carbonate phases.[32,33,34] To address this shortcoming, here we used a bioinspired approach to synthesize particles in which Ca^{2+} was progressively substituted for Sr^{2+} in the carbonate structure. The approach involved precipitating mineral particles in confined media, to mimic biomineralization. Apart from synthesizing $(Ca,Sr)CO_3$ particles for application in the field of bone regeneration, we also conducted a systematic study about how the Sr^{2+} content affected the structural properties of carbonates in order to extract useful information concerning the biological role that Sr^{2+} plays in biomineralization.

6.2 | Experimental procedure

6.2.1 | Preparation of (Ca,Sr)CO_3 rod-like particles

The rod-like particles were synthesized by a modified method described by Loste et al.[35] Polycarbonate membranes with pore sizes measuring 50, 100, 200, and 400 nm were used as templates for rod particle growth. Poly(acrylic acid) (PAA) (0.1% wt., Sigma MW 1800 g mol^{-1}) was dissolved in aqueous solutions containing $CaCl_2$ (Merck P.A.), $SrCl_2$ (Synth P.A.), or a mixture of these salts containing %Sr^{2+} in relation to the total number of mols of divalent cations (Ca^{2+} + Sr^{2+}) ranging from 0 to 100. The total (Ca^{2+}) + (Sr^{2+}) concentration was 0.10 mol L^{-1}. After 12 h under stirring, the final solution was filtered through a Millipore® cellulose ester membrane (0.45-μm pore size). The polycarbonate membranes were cleaned in a plasma cleaner system (Harrick Plasma PDC-32G) for 30 s, to unblock the pores and to increase hydrophilicity. Next, the membranes were immersed in the PAA solution containing the salts and left under vacuum for 30 s. This helped the polymer chains bound to the Ca^{2+} and Sr^{2+} ions to diffuse into the pores, to form nucleation centers for the mineralization process. The membranes were maintained in this solution for 12 h. All the solutions and washing steps were carried out with ultrapure deionized water from a Milli-Q® system (resistance = 18.2 MΩ cm and surface tension = 72.3 mN m^{-1}). The modified membranes were placed between two glass slides, and some drops of initial PAA solution containing Ca^{2+} and/or Sr^{2+} were added between the slides and the membrane. This system was placed in a sealed desiccator containing $(NH_4)_2CO_{3(s)}$ (Vetec) and left to stand at room temperature for 12 h. $(NH_4)_2CO_3$ decomposition at room temperature produced CO_2(g), which reacted with the Ca^{2+} and Sr^{2+} ions and the water present in the membrane pores, to give the mineral carbonate. Then, the membrane surfaces were cleaned with filter paper to remove the crystals which were not inside the membrane. The templates were removed by washing with $CHCl_3$ (Sigma), which was followed by five-minute centrifugation (11.000 rpm). The supernatant was discarded, and the precipitate was isolated. The washing step was repeated three times.

6.2.2 | Evaluation of the bioactivity

The experiments were performed as described in the experimental section in the Chapter 5.

6.2.3 | Sr^{2+}release from the (Ca,Sr)CO_3 particles

The experiments were performed as described in the experimental section in the Chapter 5.

6.2.4 | Particles characterization

The morphology of the gold-coated particles was investigated by scanning electron microscopy (SEM) on a Zeiss-EVO 50 microscope under 20-kV accelerating voltage. A transmission electron microscope (TEM) FEI TECNAI G^2 F20 HRTEM operating at 200 kV was used to obtain the selected area TEM images and electron diffraction (SAED) patterns. High-resolution imaging (HRTEM) and energy dispersive spectroscopy (EDS) mapping of the elements Ca and Sr were obtained on a single particle. The chemical groups were identified by Fourier-transform infrared spectroscopy (FTIR) coupled with an attenuated total reflectance (ATR) accessory (Shimadzu-IRPrestige-21), with resolution of 2 cm^{-1}. The X-ray diffraction patterns were acquired with a Bruker-AXS D5005 diffractometer with Cu Kα radiation. The peaks were indexed on the basis of the databank of the Joint Committee on Powder Diffraction. The coherent domain length was estimated in the direction of the planes (111) and (021) in the $2\theta = 25\text{-}27^{\circ}$ region, according to the Scherrer equation. This length was also estimated by HRTEM. Interplanar distances (d values) allowed us to calculate the crystal lattice parameters and Mindat database was used to obtain the lattice parameters to the mineral strontianite. The Raman spectra were recorded on a MicroRaman LabRAM HR (HORIBA Jobin–Yvon, New Jersey, USA) combined with an Olympus microscope. A He/Ne laser operating at $\lambda_0 = 632.81$ nm was employed as the excitation source. The Digital Micrograph (Gatan) program was used to process the images.

6.2.5 | Experiments of cell culture

The experiments were performed as described in the experimental section in the Chapter 5.

6.3 | Results and discussion

6.3.1 | Formation and chemical analysis of the particles

The (Ca,Sr)CO_3 particles were precipitated by means of the entrapment of Ca^{2+}, Sr^{2+} ions and PAA inside the pores of the membranes used as templates. The positively charged Ca^{2+} and Sr^{2+} ions bound electrostatically to the negatively charged PAA chains. The polymer in turn carrying the ions penetrate the membrane pores, to form an organic matrix for subsequent mineralization. $(NH_4)_2CO_3$ decomposition at room temperature produce CO_2(g), which react with Ca^{2+} and Sr^{2+} ions and water entrapped in the pores to give (Ca,Sr)CO_3 according to the reaction:

$$(NH_4)_2CO_3(s) \rightarrow 2NH_3(g) + CO_2(g) + H_2O(l)$$
$$Ca^{2+}(aq) + CO_2(g) + H_2O(l) \rightarrow CaCO_3(s) + 2H^+(aq)$$

Table 6.1 summarizes the content of Sr^{2+} in the final particles as evaluated by EDS coupled to a TEM. The Sr^{2+} molar fraction in the synthesized particles agreed with the Ca^{2+} and Sr^{2+} content in the starting solution and attested to incorporation of these ions in the rod-like particles.

Table 6.1 | Molar percentage of Sr^{2+} in the starting solutions and in the final particles as evaluated by EDS

%Sr^{2+} in the solution	**%Sr^{2+} in the product**
0	0
10	9
25	20
50	50
75	80
100	100

SEM images reveal that the particles display well-defined rod-like morphology and diameter tuned by the size of membranes pores used as template (Figure 6.1).

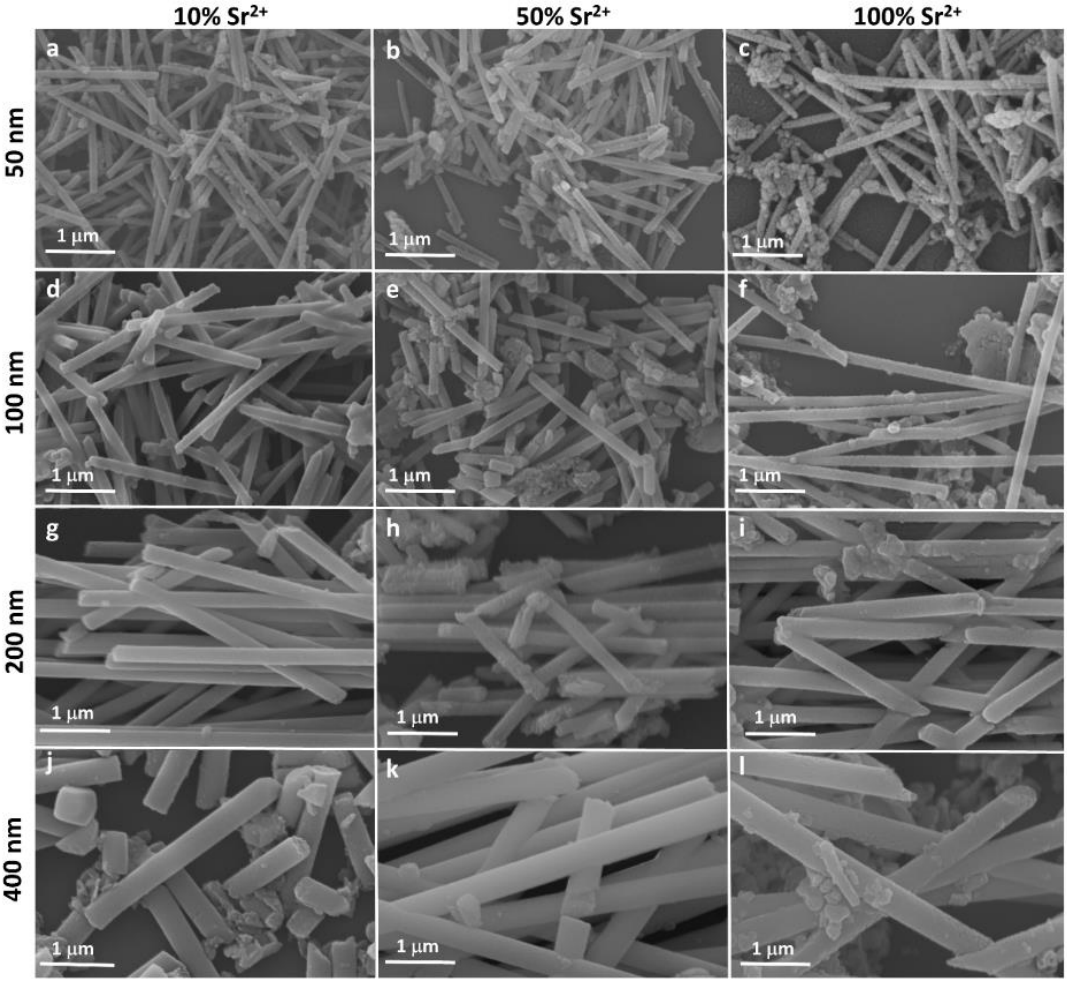

Figure 6.1 | SEM images of rod carbonate particles with different sizes (horizontal lines), 50 nm (a-c), 100 nm (d-f), 200 nm (g-i), and 400 nm (j-l), and different Sr^{2+} contents (mol%) (vertical lines), 10% Sr^{2+} (a-j), 50% Sr^{2+} (b-k), and 100% Sr^{2+} (c-l).

The Ca^{2+} and Sr^{2+} distribution over the particle surface was homogeneous, thus indicating that the elements did not segregate into different phases (Figure 6.2).

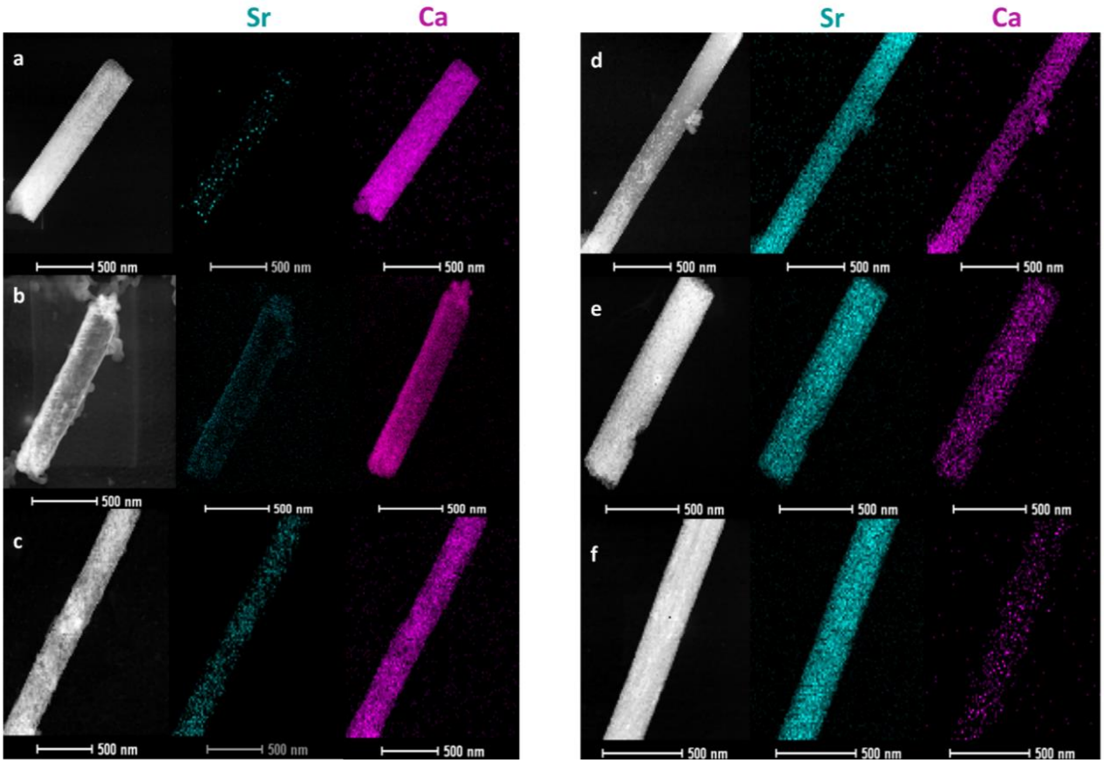

Figure 6.2 | Dark field TEM images and EDS mapping of the 200-nm-diameter particles containing different Sr^{2+} amounts (mol%): 0%Sr^{2+}(a), 10%Sr^{2+}(b), 25%Sr^{2+}(c), 50%Sr^{2+}(d), 75%Sr^{2+}(e), and 100%Sr^{2+}(f). The purple and green dots corresponded to Ca^{2+} and to Sr^{2+}, respectively.

6.3.2 | Structural analysis

Figure 6.3 shows the X-ray diffraction patterns obtained for the series of samples 0%-100% Sr^{2+}. Accordingly, a mixture of calcite and vaterite was formed in the 0% Sr^{2+} and 10% Sr^{2+} samples. The peaks related to vaterite are broader than the peaks relative to calcite indicating smaller particle size and poorer crystallinity. This may be related to the mechanism by which the particles are formed. As proposed by Ostwald, in nature, carbonate particles arise from a sequence of precipitation and re-precipitation steps.[38] The first step involves formation of a transient unstable amorphous precursor that is subsequently dissolved and re-precipitated in the vaterite phase, which will be later converted to calcite, the most thermodynamically stable $CaCO_3$ polymorph.[39] In this sense, the broader peaks verified for vaterite may be due to its partial conversion to calcite. Although the mineralization of $CaCO_3$ is accompanied by the competition between its different polymorphs, the XRD pattern of the series of sample 25%Sr^{2+}-100%Sr^{2+} display only one crystalline phase indexed as strontianite which is isomorphic with the aragonite structure.[40]

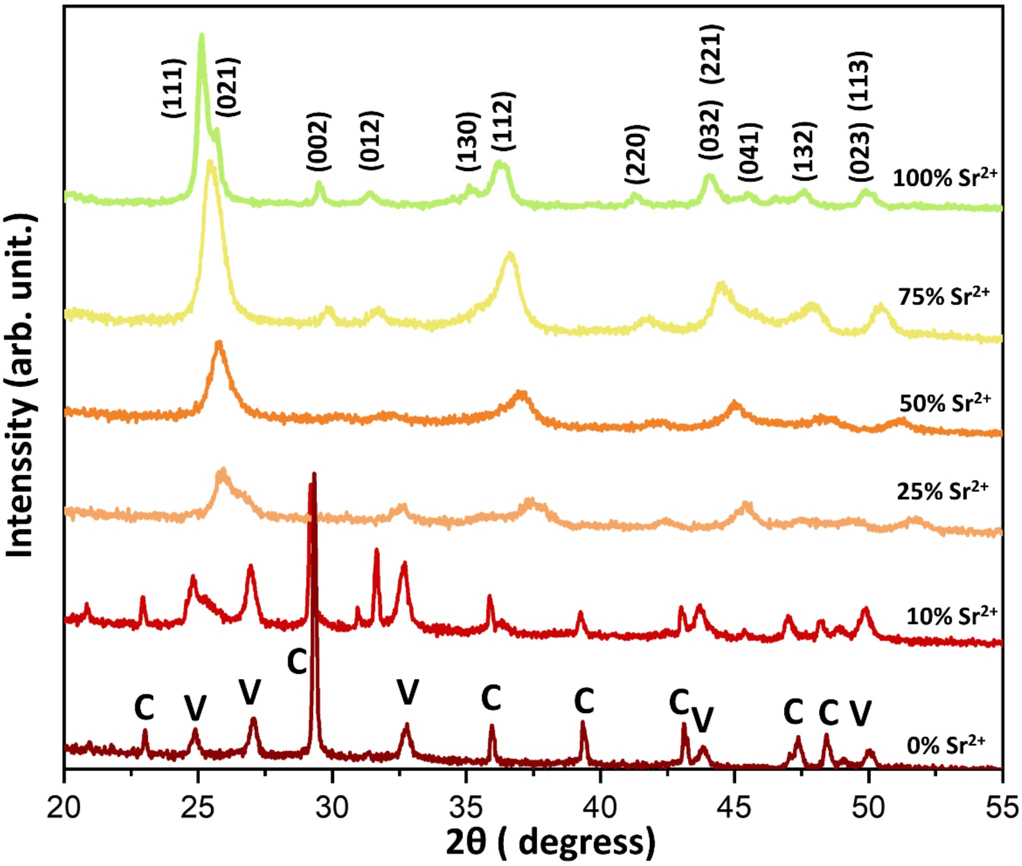

Figure 6.3 | XRD patterns for the Sr^{2+}-substituted $CaCO_3$ particles with 200-nm diameter. The Sr^{2+} content (mol%) ranged from 0 to 100%. The captions S, V, and C indicate the peaks assigned to the polymorphs strontianite (JPDCS 01-071-4899), vaterite (JPDCS 01-074-1867), and calcite (JPDCS 00-005-0586), respectively.

In the aragonite structure, Ca^{2+} ions coordinate to nine oxygen atoms, whereas these ions coordinate to six oxygen atoms in the calcite and from 6 up to 8 in vaterite structures (Figure 6.4).[40,41] The presence of Sr^{2+} ions, which have larger ionic radius as compared to Ca^{2+}, favors coordination to nine oxygen atoms. For this reason, aragonite is the most stable structure for $SrCO_3$.[42] The 0%Sr^{2+}, 10%Sr^{2+} and 100%Sr^{2+}samples display better defined and sharper peaks as compared to the samples containing strong admixture of Ca^{2+} and Sr^{2+} ions, which attested to the reduced degree of crystallinity in the latter samples. Moreover, the 75%Sr^{2+} and 100%Sr^{2+} samples display better resolved peaks as compared to the 25%Sr^{2+} and 50%Sr^{2+} samples suggesting that crystallinity improved with higher Sr^{2+} content in the samples with aragonite structure.

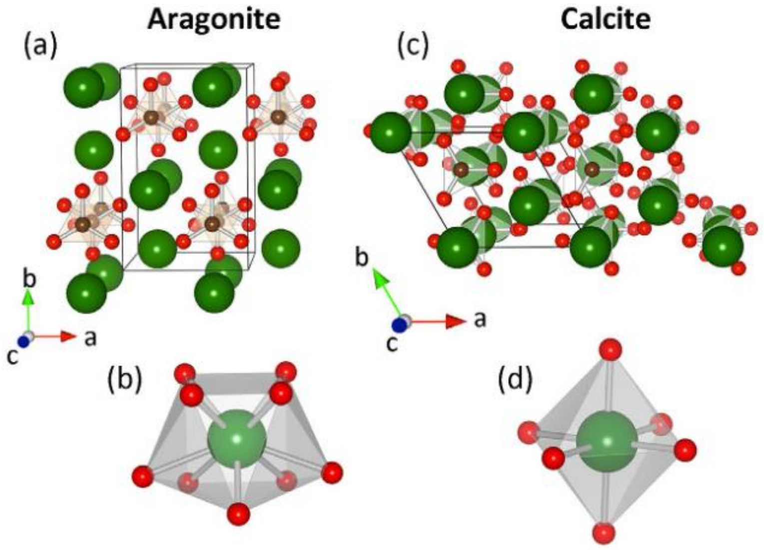

Figure 6.4 | Schematic representation of crystal structure of the $CaCO_3$ polymorphs aragonite and calcite. Aragonite (a) has a crystal structure with orthorhombic symmetry where the Ca-site is nine-fold coordinated by O as shown in (b). Strontianite is isostructural with aragonite. The crystal structure of calcite (c) is trigonal and calcium is octahedrally coordinated by O. Ca is represented by green spheres and oxygen by red spheres. Image reprinted with permission from Ref.51, Copyright 2016 Springer Nature.

According to the Scherrer equation, the coherent domains had typical size of ca. 10 nm for the series 25%Sr^{2+}-50%Sr^{2+} samples and ca. 17 nm for the 100%Sr^{2+} sample. The diffraction peak shift to lower 2θ values in the case of the samples with aragonitic structure is a consequence of larger *d*-spacing and lattice parameters due to incorporation of the larger Sr^{2+} ions. Increased Sr^{2+} content expanded the lattice parameters of the aragonite-strontianite structure by *ca.* 3 % on the basis of the (111) and (021) peak shifts, becoming similar to the values described in literature to strontianite (Table 6.2).

Table 6.2 | Interplanar distance (*d*-spacing), crystallite size (d), lattice parameter (a), and unity cell volume (V) obtained from the XRD patterns of the particles with 200-nm diameter and Sr^{2+} content (mol%) ranging from 25 to 100 with strontianite structure

%Sr^{2+}	**d (nm)**	**d spacing (Å)**	**a (Å)**	**V (Å^3)**
25	10	3.45	4.99	240
50	10	3.47	5.02	245
75	11	3.50	5.06	251
100	17	3.55	5.13	261
Strontianite	-	-	5.11	260

The SAED obtained for the nanorods with different content of Sr^{2+} confirmed the XRD measurements (Figure 6.5). Lattice expansion and higher crystallinity were observed by increasing the content of Sr^{2+}. For instance, the planes (002), (012), which were not visible in the 25%Sr^{2+} sample, became clear for the 75%Sr^{2+} and 100%Sr^{2+} samples, in agreement with the XRD patterns.

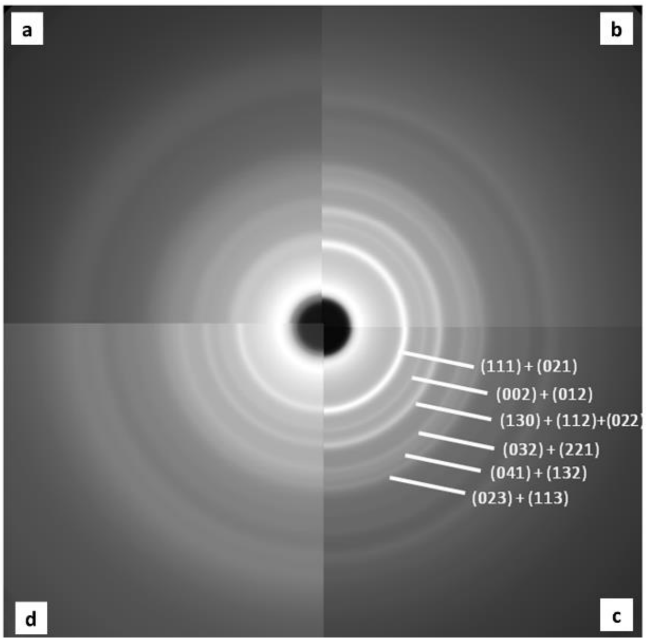

Figure 6.5 | Rotational average of the selected area diffraction pattern for the samples containing different amounts of Sr^{2+} (mol%): (a) 25%Sr^{2+}, (b) 50%Sr^{2+}, (c) 75%Sr^{2+} and (d) 100%Sr^{2+}. The corresponding diffraction rings indexed for a *Pmcn* aragonite-strontianite structure.

Figure 6.6(a-d) and Figure 6.6(e-h) show the bright and the dark field TEM images recorded for the 200-nm-diameter rod-like particles. The dark field image of the 25% Sr^{2+} sample (Figure 6.6e) revealed a rather homogeneous contrast. The HRTEM image of this sample (Figure 6.6i) confirmed that these particles are formed by crystalline domains measuring around 10 nm. Figure 6.6b and Figure 6.6f contain the TEM images of the 50%Sr^{2+} sample. The dark field image (Figure 6.6f) show some well-diffracted nanocrystals with typical size in the range of tens of nanometers. In accordance with the XRD measurements, the dark field images of the 75% Sr^{2+}(Figure 6.6g) and 100% Sr^{2+} samples (Figure 6.6h) are typical of particles with higher crystallinity. The dark field contrast extended over the whole particles, with some heterogeneous intensity changes arising due to local texture misorientation. The HRTEM image of the 100%Sr^{2+} sample (Figure 6.6j) exhibits crystalline domains that extended over several tens of nanometer. This Figure also reveals the presence of disorders such as lattice distortions, grain boundaries, and some dislocations. Such defect also explained why the XRD peaks of the 75%Sr^{2+} and 100%Sr^{2+} samples are still rather broad despite their improved crystallinity.

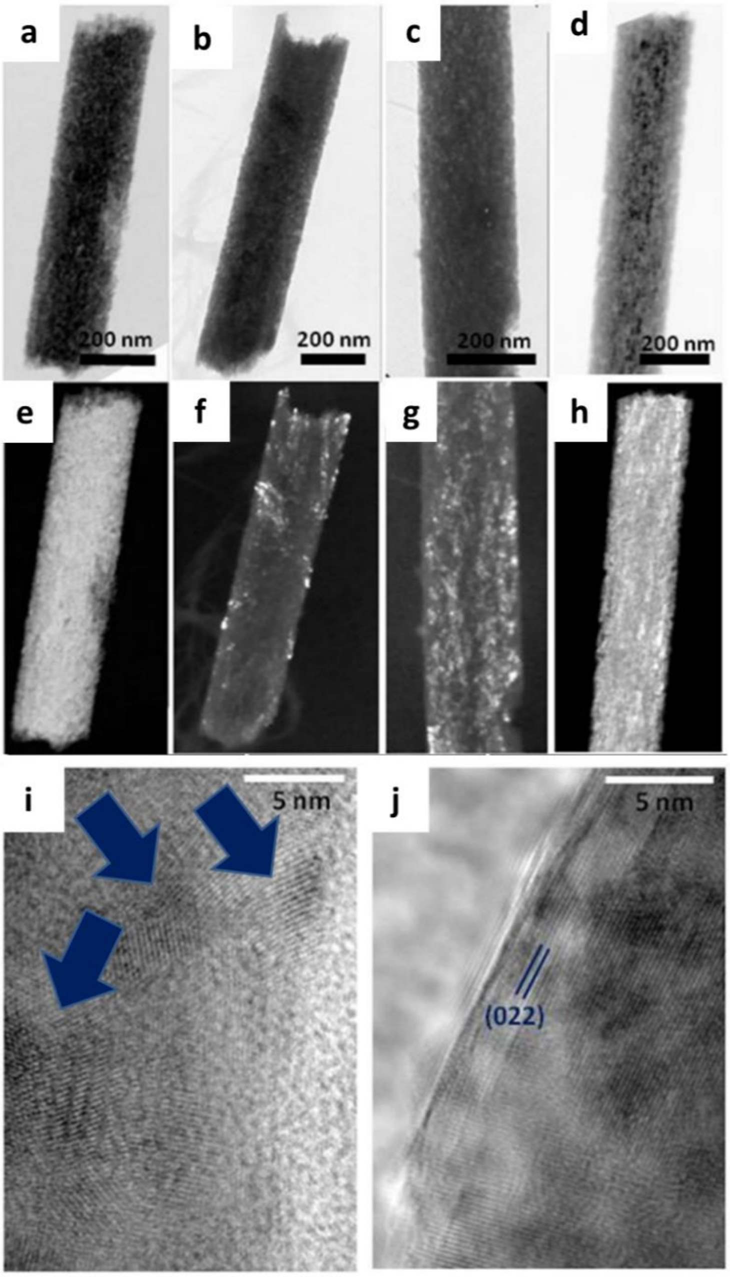

Figure 6.6 | TEM bright field (a-d) and TEM dark field (e-h) images of particles containing 25%Sr^{2+}(a and e), 50%Sr^{2+}(b and f), 75%Sr^{2+} (c and g) and 100%Sr^{2+}(d and h). HRTEM images of samples containing 25%Sr^{2+} (i) and 100%Sr^{2+} (j). The blue arrows indicate the crystalline domains in the HRTEM image.

Given the high sensitivity to the crystalline structure, Raman spectroscopy is a powerful technique to investigate polymorphs. Specially, the lattice phonon region (Raman active vibrational modes below 400 cm^{-1}) represents the fingerprint of the atomic crystalline lattice.[43] Therefore, we also evaluated these spectral signatures to identify the crystalline structure of the particles.

Figure 6.7a displays the Raman spectra of the series of samples 0-100%Sr^{2+}. Two bands at 275 and 150 cm^{-1} typical of calcite are observed in the spectrum of the 0%Sr^{2+} sample whereas the series of samples 25%Sr^{2+}-100%Sr^{2+} exhibit bands at 150 and 175 cm^{-1}, confirming the formation of aragonite/strontianite, in accordance with the XRD data.[44] Because the band assigned to vaterite overlapped with the band assigned to calcite at 281 cm^{-1}, we were not able to identify the presence of this polymorph in the Raman spectrum of the 0%Sr^{2+} sample. The ν_4 band at 680-750 cm^{-1} is ascribed to the out-of-plane bending mode of CO_3^{2-}. The main Raman band around 1100 cm^{-1}, assigned to the symmetric stretching of CO_3^{2-} shifted linearly to lower wavenumbers with increased content of Sr^{2+} (Figure 6.7b). Since the frequency of Raman bands depends on the weight of the atoms/ions and the bond strength, the increase of Sr^{2+} content in the samples results in a general shift to lower wavenumbers.

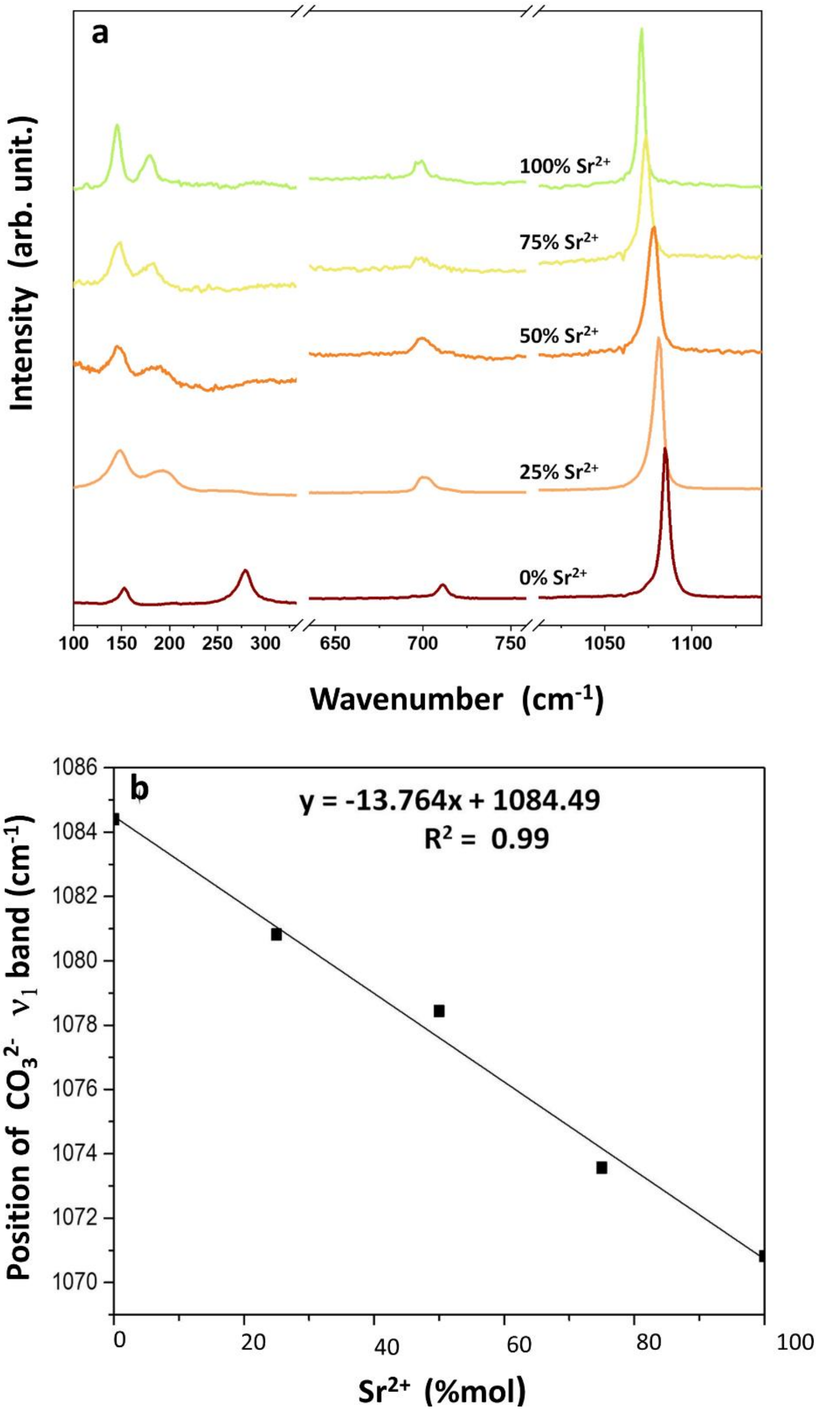

Figure 6.7 | Raman spectra of the Sr^{2+}-substituted CaCO$_3$ particles with Sr^{2+} content (mol%) ranging from 0 to 100%(a) and Position of the CO$_3^{2-}$ bands as a function of Sr^{2+} content (b).

6.3.3 | Bioactivity test *in vitro*

SEM images reveal that all the particles, irrespective of size or content of Sr^{2+}, induced precipitation of a new mineral phase consisting of spherical agglomerates of needle-like particles typical of apatite (Figure 6.8).

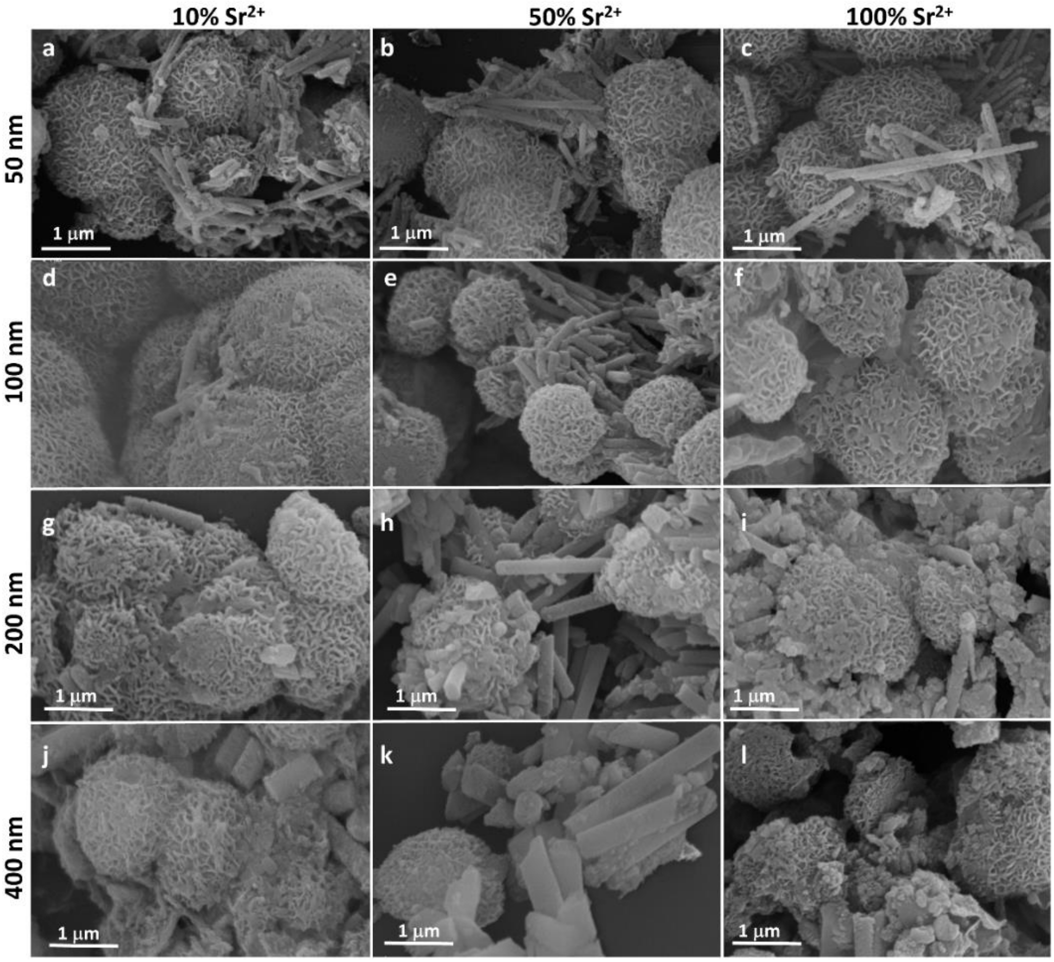

Figure 6.8 | SEM images of the carbonate particles with 50 nm (a-c), 100 nm (d-f), 200 nm (g-i) and 400 nm (j-l) containing (a-j) 10%Sr^{2+}, (b-k) 50%Sr^{2+} and (c-l) 100%Sr^{2+} after 5 days SBF exposure.

Figure 6.9 shows the FITR spectra of the 200-nm diameter particles containing (a)10%Sr^{2+}, (b)50%Sr^{2+} and (c)100%Sr^{2+}, before (black line) and after (red line) exposure to SBF. All the spectra displayed bands ascribed to the presence of the CO_3^{2-} group at 1400 cm^{-1} (asymmetric stretching) and 860 cm^{-1} (out-of-plane bending vibration), confirming $CaCO_3$ formation. The presence of a narrow intense band at 1100 cm^{-1}, assigned to n_3 stretching of the PO_4^{3-} group after exposure to SBF, confirmed that the needle-like particles corresponded to phosphate-minerals. Due to the low amount of sample it was not possible to confirm the mineral phase by means of XRD.

It is proposed that the mechanism throughout apatite precipitates involves an interfacial dissolution-reprecipitation.[45] Carbonate dissolution at the surface raised the local Ca^{2+} and Sr^{2+} concentration and favored PO_4^{3-} and Ca^{2+} migration from SBF leading to apatite precipitation. The apatite crystallization in SBF is a complex phenomenon and its formation is thermodynamically favored in such conditions.[36,46] This is because SBF is strongly supersaturated with respect to HA and not with respect to carbonates and other phosphates phases.[47]

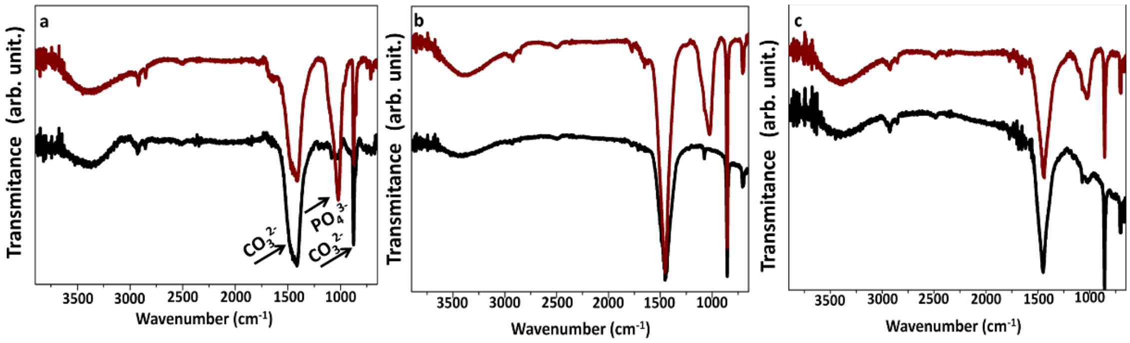

Figure 6.9 | FTIR spectra of the rod carbonate particles with 200-nm diameter containing 10%Sr^{2+}(a), 50%Sr^{2+} (b) and 100%Sr^{2+}(c), before (black line) and after (red line) five days of exposure to SBF.

We also investigated the ability of the particles to release Sr^{2+} in physiological media (Fig. 6.10). As can be observed, the amount of Sr^{2+} (mg L^{-1}) released by the particles increased as a function of the Sr^{2+} substitution, and also as a function of time. Interestingly, the 50%Sr^{2+} and 100% Sr^{2+} samples displayed comparable release of Sr^{2+} until the day 14. This may be explained by the high structural disorder in the 50%Sr^{2+} which may impact on its solubility. Moreover, the concentrations found in the solutions is in the range of the pharmacological doses of Sr^{2+} used for osteoporosis treatment described in the literature.[48] This finding evidences the possibility of controlling the concentration of Sr^{2+} delivered by the particles and therefore its possible applications as biomaterials for bone regeneration.

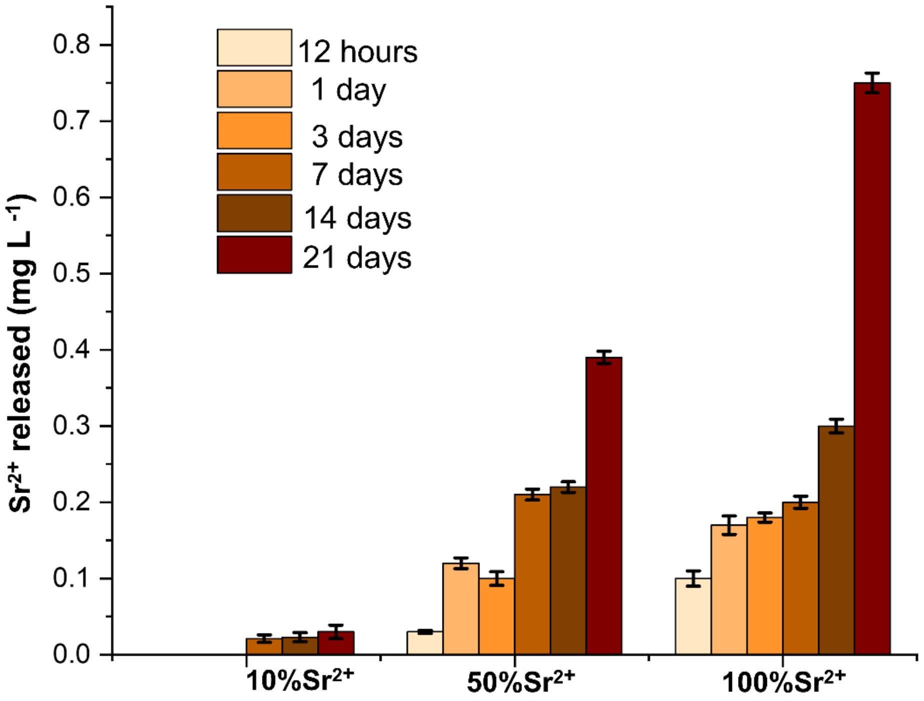

Figure 6.10 | Sr^{2+}released from the 10% Sr^{2+}, 50% Sr^{2+} and 100% Sr^{2+} particles immersed in the cell culture medium at 37 °C for 12 hours, 1, 3, 7, 14 and 21 days.

6.3.4 | Osteoblast culture

The osteogenic response of the particles was assessed *in vitro*. As observed in Fig. 6.11a, the particles were not toxic to osteoblasts irrespective of the content of Sr^{2+}. Moreover, the ALP activity increased from the 7th day of culture up to the 14th day and decreased at the 21st day (Fig. 6.11b). This behavior is typical for osteoblast and indicates that the cells were able to mineralize, as evidenced in the Fig.6.11c. The absence of differences in osteoblasts proliferation and mineralization unrespect to the concentration of Sr^{2+} is expected since the effect this ion is related to the sustainment of osteoblasts activity, while reducing osteoclasts activity.[49] Further assays will be conducted in order to investigate the effect of the particles in osteoclasts cultures. Confocal images after 7 days of culture show that the cells attached well onto the substrate and proliferate normally reaching confluence with a polygonal shape typical of osteoblasts.[50]

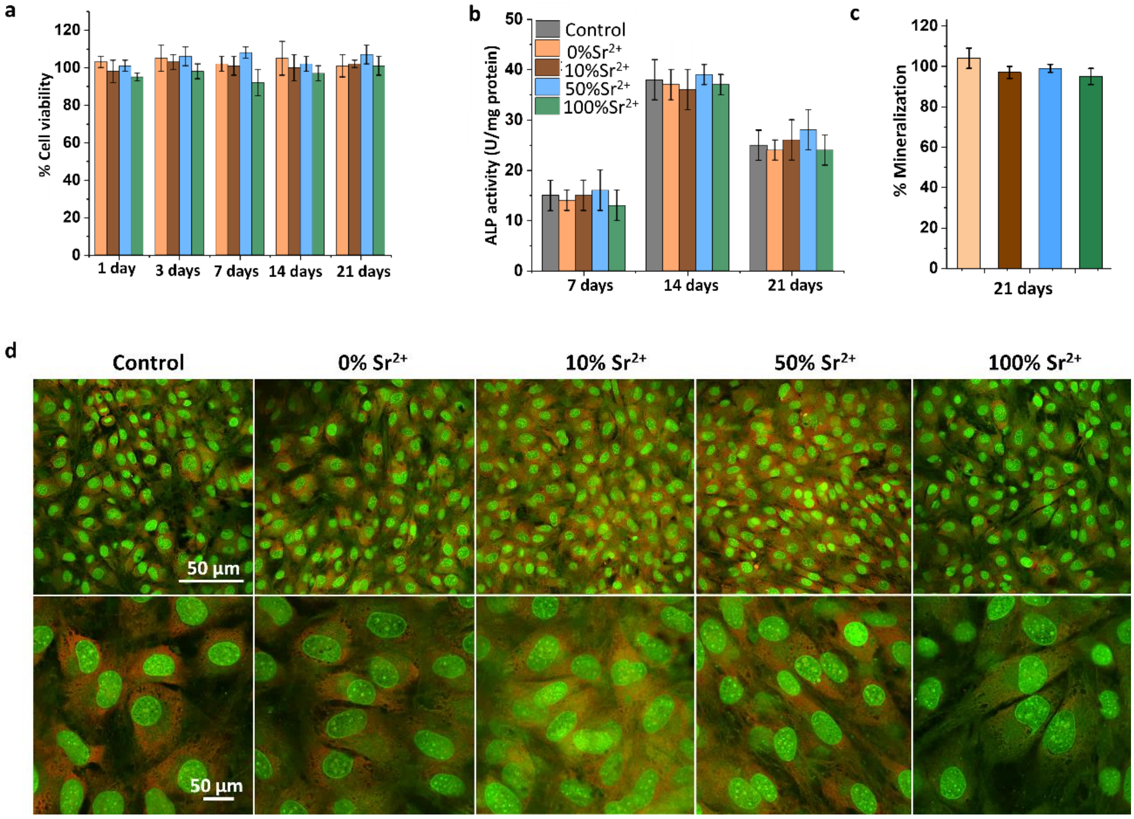

Figure 6.11 | *In vitro* osteogenic response of (Sr,Ca)CO_3 rod-like particles containing different amounts of Sr^{2+} (mol%), namely 0, 10, 50 and 100%. (a) % Cell viability versus control measured by the MTT assay after 1, 3, 7,14 and 21 days of culture. (b) ALP activity of osteoblasts after 7, 14 and 21 days of culture. (c) % Cell mineralization versus control measured by Alizarin Red S staining. (d) Confocal microscopy images of MC3T3-E1 cells cultured for 7 days in the absence (control) and in the presence of the particles.

6.4 | Conclusions

We have described the synthesis of a series of Sr^{2+}-substituted rod-like $CaCO_3$ particles in order to better understand the role played by Sr^{2+} on the mineralization of carbonates. The use of confined medium allowed to study the formation of the minerals in a biomimetic environment rather than bulk solution as usually described in the literature. Moreover, this also led to the formation of cylindrical and monodisperse particles with tuned diameters. A detailed structural characterization confirmed that Sr^{2+} and Ca^{2+} were homogeneously incorporated into the particles. Overall, crystallinity and lattice parameters augmented with rising the Sr^{2+} concentration in the carbonate particles. *In vitro* bioactivity and cell culture assays confirmed the potential application of these particles as platform for the delivery of pharmacological doses of Sr^{2+}. To sum up, high control over the physicochemical features of the synthesized particles could be useful in a further detailed *in vitro* and *in vivo* investigation into the role played by Sr^{2+} on biomineralization.

6.5 | References

(1) Hench, L. L. Biomaterials: A Forecast for the Future. In *Biomaterials*; Elsevier Sci Ltd, **1998**, 19,1419–1423.

(2) Blokhuis, T. J.; Arts, J. J. C. Bioactive and Osteoinductive Bone Graft Substitutes: Definitions, Facts and Myths. *Injury* **2011**, *42*, .

(3) Fujihara, K.; Kotaki, M.; Ramakrishna, S. Guided Bone Regeneration Membrane Made of Polycaprolactone/Calcium Carbonate Composite Nano-Fibers. *Biomaterials* **2005**, *26* (19), 4139–4147.

(4) Cruz, M. A. E.; Zanatta, M. B. T.; da Veiga, M. A. M. S.; Ciancaglini, P.; Ramos, A. P. Lipid-Mediated Growth of $SrCO_3$ /$CaCO_3$ Hybrid Films as Bioactive Coatings for Ti Surfaces. *Mater. Sci. Eng. C* **2019**, *99*, 762–769.

(5) de Souza, I. D.; Cruz, M. a E.; de Faria, A. N.; Zancanela, D. C.; Simão, A. M. S.; Ciancaglini, P.; Ramos, A. P. Formation of Carbonated Hydroxyapatite Films on Metallic Surfaces Using Dihexadecyl Phosphate-LB Film as Template. *Colloids Surf. B. Biointerfaces* **2014**, *118*, 31–40.

(6) Currey, J. D. Hierarchies in Biomineral Structures. *Science* **2005**, 8, 253–254.

(7) Nudelman, F.; Sommerdijk, N. a J. M. Biomineralization as an Inspiration for Materials Chemistry. *Angew. Chem. Int. Ed. Engl.* **2012**, *51* (27), 6582–6596.

(8) Jiang, N.; Guo, Z.; Sun, D.; Li, Y.; Yang, Y.; Chen, C.; Zhang, L.; Zhu, S. Promoting Osseointegration of Ti Implants through Micro/Nanoscaled Hierarchical Ti Phosphate/Ti Oxide Hybrid Coating. *ACS Nano* **2018**, *12* (8), 7883–7891.

(9) Kim, S.; Park, C. B. Mussel-Inspired Transformation of $CaCO_3$ to Bone Minerals. *Biomaterials* **2010**, *31* (25), 6628–6634.

(10) Nitiputri, K.; Ramasse, Q. M.; Autefage, H.; McGilvery, C. M.; Boonrungsiman, S.; Evans, N. D.; Stevens, M. M.; Porter, A. E. Nanoanalytical Electron Microscopy Reveals a Sequential Mineralization Process Involving Carbonate-Containing Amorphous Precursors. *ACS Nano* **2016**, *10* (7), 6826–6835.

(11) Landi, E.; Sprio, S.; Sandri, M.; Celotti, G.; Tampieri, A. Development of Sr and CO_3 Co-Substituted Hydroxyapatites for Biomedical Applications. *Acta Biomater.* **2008**, *4* (3), 656–663.

(12) Redey, S. A.; Razzouk, S.; Rey, C.; Bernache-Assollant, D.; Leroy, G.; Nardin, M.; Cournot, G. Osteoclast Adhesion and Activity on Synthetic Hydroxyapatite, Carbonated Hydroxyapatite, and Natural Calcium Carbonate: Relationship to Surface Energies. *J. Biomed. Mater. Res.* **1999**, *45* (2), 140–147.

(13) Jeong, N.; Park, S. C.; Jang, M. S.; Kim, S. I. Direct Growth of Graphitic Carbon-Encapsulating Carbonate Apatite Nanowires from Calcium Carbonate. *Cryst. Growth Des.* **2018**, *18* (9), 4920–4928.

(14) Verwilghen, C.; Chkir, M.; Rio, S.; Nzihou, A.; Sharrock, P.; Depelsenaire, G. Convenient Conversion of Calcium Carbonate to Hydroxyapatite at Ambient Pressure. *Mater. Sci. Eng. C* **2009**, *29* (3), 771–773.

(15) Tovani, C. B.; Zancanela, D. C.; Faria, A. N.; Ciancaglini, P.; Ramos, A. P. Bio-Inspired Synthesis of Hybrid Tube-like Structures Based on $CaCO_3$ and Type I-Collagen. *RSC Adv.* **2016**, *6* (93), 90509–90515.

(16) Tovani, C. B.; Faria, A. N.; Ciancaglini, P.; Ramos, A. P. Collagen-Supported $CaCO_3$

Cylindrical Particles Enhance Ti Bioactivity. *Surf. Coatings Technol.* **2019**, *358*, 858–864.

(17) Cruz, M. A. E.; Ruiz, G. C. M.; Faria, A. N.; Zancanela, D. C.; Pereira, L. S.; Ciancaglini, P.; Ramos, A. P. Calcium Carbonate Hybrid Coating Promotes the Formation of Biomimetic Hydroxyapatite on Titanium Surfaces. *Appl. Surf. Sci.* **2016**, *370*, 459–468.

(18) Weber, J. N. Incorporation of Stontium into Reef Coral Skeletal Carbonates. *Geochim. Cosmochim. Acta* **1973**, *37* (1971), 2173–2190.

(19) Allison, N.; Finch, A. A.; Sutton, S. R.; Newville, M. Strontium Heterogeneity and Speciation in Coral Aragonite: Implications for the Strontium Paleothermometer. *Geochim. Cosmochim. Acta* **2001**, *65* (16), 2669–2676.

(20) Littlewood, J. L.; Shaw, S.; Peacock, C. L.; Bots, P.; Trivedi, D.; Burke, I. T. Mechanism of Enhanced Strontium Uptake into Calcite via an Amorphous Calcium Carbonate Crystallization Pathway. *Cryst. Growth Des.* **2017**, *17* (3), 1214–1223.

(21) Wu, X. F.; Li, H.; Sun, L. S.; Su, J. Z.; Zhang, J. R.; Zhang, W. G.; Zhang, M.; Sun, G. W.; Zhan, L.; Zhang, M. One-Step Hydrothermal Synthesis of Visible-Light-Driven In2.77S4/$SrCO_3$ Heterojunction with Efficient Photocatalytic Activity for Degradation of Methyl Orange and Tetracycline. *Appl. Phys. A Mater. Sci. Process.* **2018**, *124* (9), 584.

(22) Hu, Z.; Li, Y.; Zhang, C.; Ao, B. Structural, Electronic, Optical and Bonding Properties of Strontianite, $SrCO_3$: First-Principles Calculations. *J. Phys. Chem. Solids* **2016**, *98*, 65–70.

(23) Marie, P. J. Strontium as Therapy for Osteoporosis. *Curr. Opin. Pharmacol.* **2005**, *5* (6), 633–636.

(24) Bonnelye, E.; Chabadel, A.; Saltel, F.; Jurdic, P. Dual Effect of Strontium Ranelate: Stimulation of Osteoblast Differentiation and Inhibition of Osteoclast Formation and Resorption in Vitro. *Bone* **2008**, *42* (1), 129–138.

(25) Ding, X.; Li, X.; Li, C.; Qi, M.; Zhang, Z.; Sun, X.; Wang, L.; Zhou, Y. Chitosan/Dextran Hydrogel Constructs Containing Strontium-Doped Hydroxyapatite with Enhanced Osteogenic Potential in Rat Cranium. *ACS Biomater. Sci. Eng.* **2019**, *5* (9), 4574–4586.

(26) Zhang, W.; Shen, Y.; Pan, H.; Lin, K.; Liu, X.; Darvell, B. W.; Lu, W. W.; Chang, J.; Deng, L.; Wang, D.; et al. Effects of Strontium in Modified Biomaterials. *Acta Biomater.* **2011**, 7 (2), 800–808.

(27) Li, K.; Dai, F.; Yan, T.; Xue, Y.; Zhang, L.; Han, Y. Magnetic Silicium Hydroxyapatite Nanorods for Enhancing Osteoblast Response in Vitro and Biointegration in Vivo. *ACS Biomater. Sci. Eng.* **2019**, *5* (5), 2208–2221.

(28) Montesi, M.; Panseri, S.; Dapporto, M.; Tampieri, A.; Sprio, S. Sr-Substituted Bone Cements Direct Mesenchymal Stem Cells, Osteoblasts and Osteoclasts Fate. *PLoS One* **2017**, *12* (2), e0172100.

(29) Schumache, M.; Henß, A.; Rohnke, M.; Gelinsky, M. A Novel and Easy-to-Prepare Strontium(II) Modified Calcium Phosphate Bone Cement with Enhanced Mechanical Properties. *Acta Biomater.* **2013**, *9* (7), 7536–7544.

(30) Landi, E.; Tampieri, A.; Celotti, G.; Sprio, S.; Sandri, M.; Logroscino, G. Sr-Substituted Hydroxyapatites for Osteoporotic Bone Replacement. *Acta Biomater.* **2007**, *3* (6), 961–969.

(31) Schumacher, M.; Gelinsky, M. Strontium Modified Calcium Phosphate Cements-Approaches towards Targeted Stimulation of Bone Turnover. *J. Mater. Chem. B* **2015**, 15 (12),*4626*-4640.

(32) Bigi, A.; Boanini, E.; Capuccini, C.; Gazzano, M. Strontium-Substituted Hydroxyapatite Nanocrystals. *Inorganica Chim. Acta* **2007**, *360* (3), 1009–1016.

(33) Capuccini, C.; Torricelli, P.; Sima, F.; Boanini, E.; Ristoscu, C.; Bracci, B.; Socol, G.; Fini, M.; Mihailescu, I. N.; Bigi, A. Strontium-Substituted Hydroxyapatite Coatings Synthesized by Pulsed-Laser Deposition: In Vitro Osteoblast and Osteoclast Response. *Acta Biomater.* **2008**, *4* (6), 1885–1893.

(34) Li, Z. Y.; Lam, W. M.; Yang, C.; Xu, B.; Ni, G. X.; Abbah, S. a; Cheung, K. M. C.; Luk, K. D. K.; Lu, W. W. Chemical Composition, Crystal Size and Lattice Structural Changes after Incorporation of Strontium into Biomimetic Apatite. *Biomaterials* **2007**, *28* (7), 1452–1460.

(35) Loste, E.; Meldrum, F. C. Control of Calcium Carbonate Morphology by Transformation of an Amorphous Precursor in a Constrained Volume. *Chem. Commun.* **2001**,10, 901–902.

(36) Zhao, W.; Michalik, D.; Ferguson, S.; Hofstetter, W.; Lemaître, J.; von Rechenberg, B.; Bowen, P. Rapid Evaluation of Bioactive Ti-Based Surfaces Using an in Vitro Titration Method. *Nat. Commun.* **2019**, *10* (1), 1–11.

(37) Kokubo, T.; Takadama, H. How Useful Is SBF in Predicting in Vivo Bone Bioactivity? *Biomaterials* **2006**, *27* (15), 2907–2915.

(38) Cantor, B.; H Chang, I. T.; Knight, P.; B Vincent, A. J.; Sci, M. References and notes. *Met. Mater. Trans. A* **2004**, *6*, 817–822.

(39) Addadi, L.; Raz, S.; Weiner, S. Taking Advantage of Disorder: Amorphous Calcium Carbonate and Its Roles in Biomineralization. *Advanced Materials*. **2003,** 15(12)8 959–970.

(40) Ye, Y.; Smyth, J. R.; Boni, P. Crystal Structure and Thermal Expansion of Aragonite-Group Carbonates by Single-Crystal X-Ray Diffraction. *Am. Mineral.* **2012**, *97* (4), 707–712.

(41) Maslen, E. N.; Streltsov, V. A.; Streltsova, N. R. X-ray Study of the Electron Density in Calcite, CaCo3. *Acta Crystallogr. Sect. B* **1993**, *49* (4), 636–641.

(42) Antao, S. M.; Hassan, I. The orthorhombic structure of $CaCO_3$, $SrCO_3$, $PbCO_3$ and $BaCO_3$ *Can. Mineral.* **2009**, *47*, 1245–1255.

(43) Carteret, C.; Dandeu, A.; Moussaoui, S.; Muhr, H.; Humbert, B.; Plasari, E. Polymorphism Studied by Lattice Phonon Raman Spectroscopy and Statistical Mixture Analysis Method. Application to Calcium Carbonate Polymorphs during Batch Crystallization. *Cryst. Growth Des.* **2009**, *9* (2), 807–812.

(44) Kontoyannis, C. G.; Vagenas, N. V. Calcium Carbonate Phase Analysis Using XRD and FT-Raman Spectroscopy. *Analyst* **2000**, *125* (2), 251–255.

(45) Kim, S.; Park, C. B. Mussel-Inspired Transformation of $CaCO_3$ to Bone Minerals. *Biomaterials* **2010**, *31* (25), 6628–6634.

(46) Dey, A.; Bomans, P. H. H.; Müller, F. A.; Will, J.; Frederik, P. M.; De With, G.; Sommerdijk, N. A. J. M. The Role of Prenucleation Clusters in Surface-Induced Calcium Phosphate Crystallization. *Nat. Mater.* **2010**, *9* (12), 1010–1014.

(47) Shi, D.; Jiang, G.; Bauer, J. The Effect of Structural Characteristics on Thein Vitro Bioactivity of Hydroxyapatite. *J. Biomed. Mater. Res.* **2002**, *63* (1), 71–78.

(48) Marie, P. J.; Ammann, P.; Boivin, G.; Rey, C. Mechanisms of Action and Therapeutic Potential of Strontium in Bone. *Calcif. Tissue Int.* **2001**, *69* (3), 121–129.

(49) Cruz, M. A. E.; Tovani, C. B.; Favarin, B. Z.; Soares, M. P. R.; Fukada, S. Y.; Ciancaglini, P.; Ramos, A. P. Synthesis of Sr-Morin Complex and Its: In Vitro Response: Decrease in Osteoclast Differentiation While Sustaining Osteoblast Mineralization Ability. *J. Mater. Chem. B* **2019**, 7 (5), 823–829.

(50) Uggeri, J.; Guizzardi, S.; Scandroglio, R.; Gatti, R. Adhesion of Human Osteoblasts to

Titanium: A Morpho-Functional Analysis with Confocal Microscopy. *Micron* **2010**, *41* (3), 210–219.

(51) Soldati, A. L.; Jacob, D. E.; Glatzel, P.; Swarbrick, J. C.; Geck, J. Element Substitution by Living Organisms: The Case of Manganese in Mollusc Shell Aragonite. *Sci. Rep.* **2016**, *6* (1), 22514.

CHAPTER 7

Conclusions and final considerations

In this thesis we have developed biomimetic models to understand the fundamental mechanisms behind the different effects *i.e* therapeutic and pathological of Sr^{2+} on bone. By using a biomimetic model of bone mineral, we success in reproducing the limit of 10 mol% of Sr^{2+} incorporation in bioapatite during osteoporosis treatments. In a situation of pathological accumulation of Sr^{2+}, *i.e,* 50 mol% and 75 mol%, we observed the destabilization of apatite giving rise to an amorphous phase Sr(ACP). The detection of Sr(ACP) may be an evidence of the physicochemical interference of Sr^{2+} on the formation of apatite and consequently its adverse effects at the regime of high doses observed *in vivo* and in cell cultured *in vitro*. Different from the usual amorphous phosphates, at 75 mol% Sr^{2+} Sr(ACP) displayed high stability towards crystallization in physiological environment raising the possibility of its existence in bone. One step further, a dense and organized type-I collagen matrix mineralized with biomimetic apatite was set as model to investigate the impacts of Sr^{2+} at the organic/inorganic interface of bone. By doing so, we found that Sr(ACP) is formed at 50 mol% Sr^{2+} leading to the destabilization of the supramolecular arrangement of collagen fibrils. This evidenced that the effects of high Sr^{2+} content in the mineral extends also to the organic matrix. These results agree with the clinical reports of bone disorders at high doses of this element, therefore validating the biomimetic models adopted in this study. These biomimetic models were able to overcome the challenge of reproducing the whole effect of Sr^{2+} on bone tissue.

The use of confined environment allowed us to investigate the impact of Sr^{2+} on the early stages of apatite formation, showing that the presence of Sr^{2+} and confinement act synergistically to increase the stability of Sr(ACP). The mineralization of the calcium carbonates polymorphs calcite and aragonite was also affected by the presence of Sr^{2+}. Increased Sr^{2+} content stabilized aragonite/strontianite mineral phases, while in the absence of this ion calcite was preferred precipitated.

We also focused our attention on how to apply the principle of biomineralization to the design of bioactive particles with controlled morphology, size, and Sr^{2+} content. The particles precipitated in confinement displayed bioactivity and controlled release of Sr^{2+} suggesting their possible application in bone regenerative therapies. In this sense, this thesis integrated material and biological science.

Overall, these results question the current understanding of Sr^{2+} incorporation in bone mineral that limits its action to the mature bone mineral discarding its possible involvement on the early stages of bone formation. Moreover, we believe the findings presented herein provide a fundamental understanding to the development of bone regenerative therapies and inspire future investigation in both biomineralization and materials science. Our results encourage the investigation of Sr(ACP) in the bone tissue of patients with osteomalacia and rickts.

Appendix

Curriculum Vitæ

Camila Bussola Tovani
Born 22th February 1991 at Junqueirópolis, Brazil

Academic formation

2015: Graduation in Chemistry at University of São Paulo; Ribeirão Preto, Brazil

Complementary formation

2017 June-July: Short term collaboration at Université Paris Sud, Laboratoire de Physique des Solides, Orsay, France, advised by Dr. Alexandre Gloter **(Project: Characterization of Sr^{2+}-substituted carbonates and phosphates by transmission electron microscopy, Scholarship: FAPESP)**

2018-2019: Research internship at Sorbonne Université, CNRS, Collège de France, Laboratoire Chimie de la Matière Condensée de Paris, advised by Dr. Nadine Nassif (**Exploring the synergistic effect between collagen and Sr^{2+} in the process of apatite formation in bone mineralization, Scholarship: BEPE, FAPESP)**

2019 April-July: Short term collaboration at Sorbonne Université, CNRS, Collège de France, Laboratoire Chimie de la Matière Condensée de Paris, advised by Dr. Nadine Nassif (**Synthesis and characterization of tissue-like collagen matrices, Scholarship: Foundation College de France)**

Teaching experience

University of São Paulo, Ribeirão Preto, SP (Brazil)

Graduate monitor, Chemistry Department

•General Chemistry (2014, 2015, 2016)

•Physical Chemistry I: Thermodynamics (2017)

•Physical Chemistry IV: Statics Thermodynamics (2018)

Awards

2014: Best poster at 4th Meeting on Self Assembly Structures in Solution and at Interfaces-Langmuir and American Chemical Society.

2017 : *Bernhard Gross Award* (Best Oral presentation) at XVI Brazilian MRS (Material Research Society).

Publications

1. Tovani, C. B., Ferreira, C. R., Simão, A. M. S., Bolean, M., Coppeta, L., Rosato, N., Bottini, M., Ciancaglini, P., and Ramos, A. P. Characterization of the in Vitro Osteogenic Response to Submicron TiO_2 Particles of Varying Structure and Crystallinity. *ACS omega* **2020**, *5* (27), 16491–16501.

2. Tovani, C. B., Gloter, A., Azaïs, T., Selmane, M., Ramos, A. P., and Nassif, N. Formation of stable strontium-rich amorphous calcium phosphate: Possible effects on bone mineral. *Acta biomaterialia* **2019**, 92, 315-324.

3. Cruz, M. A., Tovani, C. B., Favarin, B. Z., Soares, M. P., Fukada, S. Y., Ciancaglini, P., and Ramos, A. P. Synthesis of Sr–morin complex and its *in vitro* response: decrease in osteoclast differentiation while sustaining osteoblast mineralization ability. *Journal of Materials Chemistry B* **2019**, 7 (5), 823–829.

4. Tovani, C. B., Faria, A. N., Ciancaglini, P., and Ramos, A. P. Collagen-supported $CaCO_3$ cylindrical particles enhance Ti bioactivity. *Surface and Coatings Technology* **2019**, 358, 858-864.

5. Tovani, C. B., Oliveira, T. M., Gloter, A., and Ramos, A. P. Sr^{2+}-substituted $CaCO_3$ nanorods: impact on the structure and bioactivity. *Crystal Growth & Design* **2018**, 18, 2932-2940.

6. Simão, A. M. S., Bolean, M., Favarin, B. Z., Veschi, E. A., Tovani, C. B., Ramos, A. P.and Ciancaglini, P. Lipid microenvironment affects the ability of proteoliposomes harboring TNAP to induce mineralization without nucleators. *Journal of bone and mineral metabolism*, **2019**, 3, 607-613.

7. Ramos, A. P., Cruz, M. A., Tovani, C. B., and Ciancaglini, P. Biomedical applications of nanotechnology. *Biophysical reviews* **2017**, 9, 79-89.

8. Paterlini, T. T., Nogueira, L. F., Tovani, C. B., Cruz, M. A., Derradi, R., and Ramos, A. P. The role played by modified bioinspired surfaces in interfacial properties of biomaterials. *Biophysical reviews* **2017**, 9, 683-698.

9. Tovani, C. B., Zancanela, D. C., Faria, A. N., Ciancaglini, P., and Ramos, A. P. Bio-inspired synthesis of hybrid tube-like structures based on $CaCO_3$ and type I-collagen. *RSC Advances* **2016**, 6, 90509-90515.

10. Tovani, C. B., de Souza, J. F. V., de Souza Cavallini, T., Demets, G. J. F., Ito, A., Barioni, M. B.and Zaniquelli, M. E. D. Comparison between cucurbiturils and β-cyclodextrin interactions with cholesterol molecules present in Langmuir monolayers used as a biomembrane model. *Colloids and Surfaces B: Biointerfaces* **2013**, 111, 398-406.

Review for scientific journals

Journal of Materials Science (Springer)

Orbital: The Electronic Journal of Chemistry (UFMT, Brazil)

Languages

Portuguese (native language)

English

French